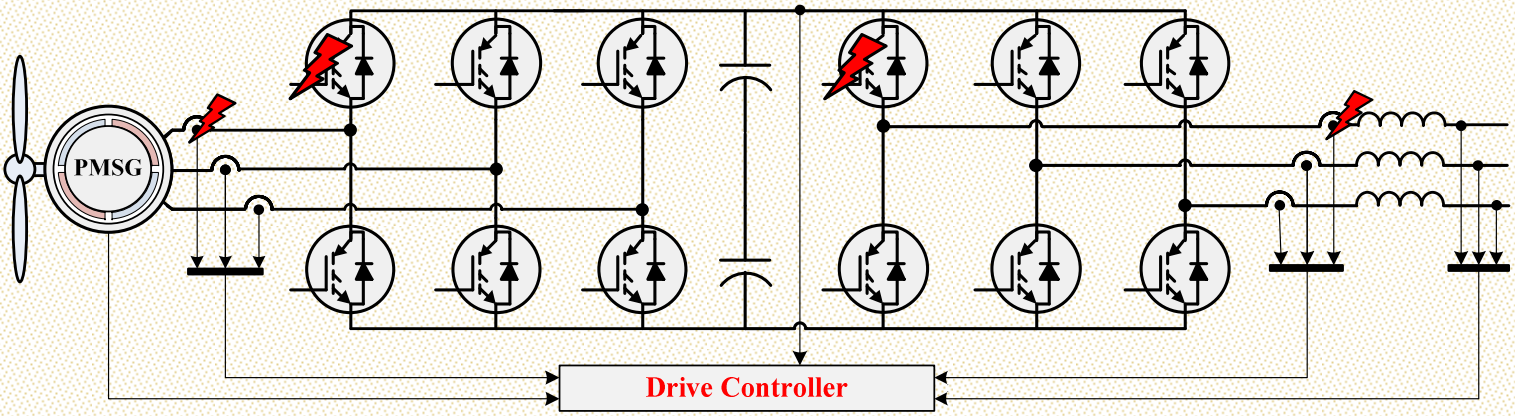

Nuno Miguel Amaral Freire

Fault-Tolerant Permanent Magnet Synchronous Generator Drives for Wind Turbine Applications

Doctor of Philosophy Thesis in Electrical and Computer Engineering supervised by Professor António João Marques Cardoso and presented in the Electrical and Computer Engineering Department of the Faculty of Sciences and Technology of the University of Coimbra

Coimbra
September 2013

· U C ·

Universidade de Coimbra

This work was supported by the Portuguese Foundation for Science and Technology (FCT) under the project nº SFRH/BD/70868/2010.

Acknowledgments

I want to express my sincere gratitude to Professor António João Marques Cardoso for is guidance, valuable corrections suggested throughout this work, and provided working conditions.

I am very grateful to Jorge Estima who was always available to discuss technical issues and to contribute with possible solutions. I also have to thank his contagious enthusiasm for laboratory experiments, which I now share, and his help on all the steps that this thesis involved.

To Eunice and Silvia I thank all and the valuable experience transmitted as well as the friendly ambience created by them in the laboratory.

I acknowledge the ceaseless support and love of Sofia and my parents, to whom I dedicate this work.

Finally, I acknowledge the financial support of the Portuguese Foundation for Science and Technology (FCT) under fellowship SFRH/BD/70868/2010.

Nuno Freire

Abstract

This thesis intends to present new solutions for extending the reliability and availability levels of wind energy conversion systems based on permanent magnet synchronous generator (PMSG) drives. Therefore, fault-tolerant power converters for PMSG drives with the ability to handle open-circuit faults and current sensor faults are developed and proposed. By considering distinct control strategies, diagnostic techniques and converter topologies for post-fault operation, a wide range of solutions for fault-tolerant PMSG drive can be adopted with the contribution of this work.

Firstly, taking into account that a standard PMSG drive is composed of two power converters in a back-to-back topology, four of the most broadly adopted control strategies for each converter are addressed in detail and their normal and faulty operation is analyzed by means of simulation and experimental results, permitting to verify the merits of each strategy under normal operation and to evaluate the fault impact.

Having recognized that currents and reference voltages are suitable quantities to perform fault diagnosis, current- and voltage-based approaches are proposed in a total of six algorithms for open-circuit fault diagnosis and one algorithm for current sensor fault diagnosis. These techniques demonstrate high effectiveness and robustness, without requiring additional measurements or high computational effort.

With the aim to handle open-circuit faults by employing non-redundant converters, alternative converter topologies and respective control strategies are necessary for post-fault operation. Accordingly, four topologies for post-fault operation are chosen and studied, and suitable control strategies are proposed. Once again, various control strategies are considered for each converter topology, and their performance is evaluated and compared by means of simulations and experiments.

Finally, three fully-integrated fault-tolerant PMSG drives are suggested by taking into consideration their design, control system and real-time response.

Resumo

Neste trabalho apresentam-se novas soluções para melhorar os níveis de fiabilidade e disponibilidade dos sistemas de conversão de energia eólica baseados em geradores síncronos de ímanes permanentes. Neste contexto, são propostos e desenvolvidos conversores de potência tolerantes a falhas com a capacidade de lidar com avarias de circuito aberto e avarias dos sensores de corrente. Considerando diferentes estratégias de controlo, técnicas de diagnóstico de avarias e topologias de conversores para funcionamento pós-falha, uma ampla gama de soluções para accionamentos baseados em geradores síncronos de ímanes permanentes tolerantes a falhas pode ser adoptada com a contribuição deste trabalho.

Primeiramente, tendo em conta que um accionamento convencional baseado em geradores síncronos de ímanes permanentes é composto por dois conversores de potência, quatro das estratégias de controlo mais amplamente adoptados para cada conversor são abordadas em detalhe e o seu desempenho em funcionamento normal e em avaria é analisado através de resultados de simulação e experimentais, permitindo verificar os méritos de cada estratégia em funcionamento normal e também avaliar a influência das avarias.

Tendo reconhecido que as correntes e tensões de referência são grandezas adequadas para efectuar o diagnóstico de avarias, abordagens baseadas nas correntes e tensões são propostas num total de seis algoritmos para diagnóstico de avarias de circuito aberto e um algoritmo para o diagnóstico de avarias em sensores de corrente. Estas técnicas demonstram elevada eficácia e robustez, sem sensores adicionais nem um elevado esforço computacional.

Com o objectivo de lidar com avarias de circuito aberto usando conversores não redundantes, topologias alternativas e respectivas estratégias de controlo são necessários para o funcionamento pós-falha. Consequentemente, quatro topologias para operação pós-falha são escolhidas e estudadas, e estratégias de controlo adequadas são propostas. Diversas estratégias de controlo são considerados para cada topologia e o seu desempenho é avaliado e comparado com base em resultados de simulação e experimentais.

Finalmente, três accionamentos tolerantes a falhas baseados em geradores síncronos de ímanes permanentes são sugeridos, tendo em consideração o dimensionamento dos componentes, o sistema de controlo integrado no controlador do accionamento, e a resposta em tempo real.

Contents

Acknowledgments i
Abstract iii
Resumo v
Contents xi
Nomenclature xvii

1 Introduction **1**
1.1 Main Contributions 3
1.2 Structure of the Thesis 3

2 PMSG Drive and Converter Control Strategies **5**
2.1 Drive Description 8
2.1.1 Mathematical Models 8
2.1.2 Experimental Setup 11
2.2 Control Strategies for the PMSG-Side Converter 12
2.2.1 Vector Control - Rotor Field Oriented Control 13
2.2.1.1 RFOC with HCC 13
2.2.1.2 RFOC with SVM 14
2.2.2 Direct Torque Control 18
2.2.2.1 Conventional DTC 19
2.2.2.2 DTC with SVM 21
2.3 Control Strategies for the Grid-Side Converter 22
2.3.1 Vector Control - Voltage Oriented Control 22
2.3.1.1 VOC with HCC 23
2.3.1.2 VOC with SVM 23
2.3.1.3 VOC with Vector-based HCC 23
2.3.2 Direct Power Control 25
2.4 Simulation Results 28
2.4.1 Control Strategies for the PMSG-Side Converter 28
2.4.2 Control Strategies for the Grid-Side Converter 29

2.5 Experimental Results . . . 29
2.5.1 Control Strategies for the PMSG-Side Converter . . . 31
2.5.2 Control Strategies for the Grid-Side Converter . . . 31
2.6 Summary . . . 33

3 Faulty Operation Analysis **39**
3.1 Power Switch Open-Circuit Faults . . . 40
3.1.1 Simulation Results . . . 41
3.1.2 Experimental Results . . . 42
3.2 Current Sensor Faults . . . 43
3.2.1 Simulation Results . . . 43
3.2.2 Experimental Results . . . 44
3.3 Summary . . . 44

4 Fault Diagnosis **51**
4.1 Power Switch Open-Circuit Fault Diagnosis . . . 52
4.1.1 Current Park's Vector Phase . . . 54
4.1.2 Current Polarity . . . 57
4.1.3 Errors of the Normalized Currents Average Absolute Values Using the Park's Vector Modulus as Normalization Quantity . . . 58
4.1.4 Errors of the Normalized Currents Average Absolute Values Using the Instantaneous Maximum Value of the Currents Absolute Values as Normalization Quantity . . . 60
4.1.5 Average Values of the Normalized Reference Voltages and Average Values of the Normalized Voltage Errors . . . 62
4.1.5.1 Average Values of the Normalized Reference Voltages . . . 62
4.1.5.2 Average Values of the Normalized Voltage Errors . . . 63
4.1.5.3 Voltage Estimation . . . 64
4.1.5.4 Theoretical Considerations . . . 65
4.2 Current Sensor Fault Diagnosis and Fault Tolerance . . . 67
4.2.1 Normalized Currents Average Absolute Values . . . 68
4.2.2 Current Sensor Fault Tolerance . . . 72
4.3 Simulation and Experimental Results - Open-Circuit Fault Diagnosis . . . 73
4.3.1 Current Park's Vector Phase, Current Polarity and Errors of the Normalized Currents Average Absolute Values Methods Using the Park's Vector Modulus as Normalization Quantity . . . 73
4.3.1.1 Simulation Results . . . 73
4.3.1.2 Experimental Results . . . 75

4.3.2 Errors of the Normalized Currents Average Absolute Values Using the Instantaneous Maximum Value of the Currents Absolute Values as Normalization Quantity . . . 79
4.3.2.1 Simulation Results . . . 79
4.3.2.2 Experimental Results . . . 80
4.3.3 Average Values of the Normalized Reference Voltages and Average Values of the Normalized Voltage Errors . . . 81
4.3.3.1 Simulation Results . . . 82
4.3.3.2 Experimental Results . . . 82
4.4 Simulation and Experimental Results - Current Sensor Fault Diagnosis and Fault Tolerance . . . 88
4.4.1 Normalized Currents Average Absolute Values . . . 88
4.4.1.1 Simulation Results . . . 88
4.4.1.2 Experimental Results . . . 88
4.5 Detection Times and Performance Comparison of the Open-Circuit Fault Diagnostic Methods . . . 91
4.6 Summary . . . 95

5 Alternative Converter Topologies and Control Strategies for Post-Fault Operation 97
5.1 Three-Switch Three-Phase Rectifier for the PMSG-Side Converter . . . 99
5.1.1 RFOC with HCC . . . 101
5.1.2 RFOC with SVM . . . 104
5.1.3 Conventional DTC . . . 105
5.1.4 DTC with SVM . . . 108
5.1.5 Simulation Results . . . 109
5.1.6 Experimental Results . . . 110
5.2 Four-Switch Three-Phase Converter with a Phase Connected to DC Bus Midpoint for the Grid-Side Converter . . . 114
5.2.1 VOC with HCC . . . 115
5.2.2 VOC with SVM . . . 116
5.2.3 VOC with Vector-based HCC . . . 118
5.2.4 DPC . . . 119
5.2.4.1 Control of the Capacitor Voltage Offset . . . 121
5.2.5 Simulation Results . . . 123
5.2.6 Experimental Results . . . 123
5.3 Four-Switch Three-Phase Converter with the Transformer Neutral Point Connected to DC Bus Midpoint for the Grid-Side Converter . . . 128
5.3.1 VOC with HCC . . . 131

5.3.1.1 Capacitor Voltage Balancing 132
5.3.2 Simulation Results 134
5.3.3 Experimental Results 134
5.4 Five-Leg Converter with a Shared-Leg Connected to the Transformer Neutral Point 139
5.4.1 HCC 140
5.4.2 S-PWM 141
5.4.3 Simulation Results 142
5.4.4 Experimental Results 143
5.5 Summary 143

6 Fault-Tolerant Converters for PMSG Drives: Design Considerations, Control System and Real-Time Response 147
6.1 Fault-Tolerant Converter Topology I 148
6.1.1 Design Considerations 148
6.1.2 Control System 150
6.1.3 Real-Time Response 151
6.1.3.1 Real-Time Response to a Fault in the Grid-Side Converter . . 151
6.1.3.2 Real-Time Response to a Fault in the PMSG-Side Converter 153
6.2 Fault-Tolerant Converter Topology II 153
6.2.1 Design Considerations 154
6.2.2 Control System 155
6.2.3 Real-Time Response 156
6.2.3.1 Real-Time Response to a Fault in the Grid-Side Converter . . 156
6.2.3.2 Real-Time Response to a Fault in the PMSG-Side Converter . 157
6.3 Fault-Tolerant Converter Topology III 157
6.3.1 Design Considerations 158
6.3.2 Control System 160
6.3.3 Real-Time Response 161
6.3.3.1 Real-Time Response to a Fault in the Grid-Side Converter . . 162
6.3.3.2 Real-Time Response to a Fault in the PMSG-Side Converter . 162
6.4 Summary 162

7 Conclusions and Future Work 165
7.1 Conclusions 165
7.2 Future Work 167

Bibliography 169

A Experimental Setup Details **189**
A.1 Experimental Setup Pictures 189
A.1.1 Autotransformer and Transformer 189
A.1.2 Power Converter 190
A.1.3 Test Bench 192
A.1.4 PMSG Parameters 192

Nomenclature

α	Angle between the reference voltage vector and the basic adjacent vector (rad)
$\Delta u_{dc,max}$	Maximum absolute value of the capacitor voltage deviation
Δu_{dc}	Capacitor voltage deviation
δ	Load angle (rad)
$\hat{}$	Estimated value
$\langle x \rangle$	Average value of the variable x
ω	Fundamental electrical frequency (rad/s)
ω_g	Grid fundamental electrical frequency (rad/s)
ω_r	PMSG mechanical speed (rad/s)
ω_s	Synchronous electrical frequency (rad/s)
ϕ	Currents initial phase angle (rad)
ψ_{PM}	Rotor magnets flux linkage (Wb)
$\psi_{s\alpha}$, $\psi_{s\beta}$	Stator flux in the $\alpha\beta$ stationary reference frame (Wb)
ψ_s	Stator flux space vector (Wb)
ψ_{sd}, ψ_{sq}	Stator flux linkages in the dq synchronous reference frame (Wb)
θ_r	Rotor flux electrical position (rad)
*	Reference value
B_i	Current control loop bandwidth (Hz)
B_{hcc}	Hysteresis band (A)

D	Damping coeficient (Nms/rad)
d_k, d'_k	Diagnostic variables
d_{PMSG}, d_{Grid}	Detection variables
e_n	Errors of the normalized currents average absolute values
f_s	Sampling frequency (Hz)
f_{PWM}	PWM Carrier frequency (Hz)
i_A, i_B, i_C	Grid phase currents (A)
i_a, i_b, i_c	PMSG phase currents (A)
I_m	Current amplitude (A)
$i_{g\alpha}$, $i_{g\beta}$	Grid phase currents in the $\alpha\beta$ stationary reference frame (A)
i_{gd}, i_{gq}	Grid phase currents in the dq synchronous reference frame (A)
i_{nN}	Normalized phase currents
i_N	Grid transformer neutral current (A)
i_n	Measured phase currents (A)
I_{rated}	Rated phase current amplitude (A)
$i_{s\alpha}$, $i_{s\beta}$	Stator phase currents in the $\alpha\beta$ stationary reference frame (A)
i_{sd}, i_{sq}	Stator phase currents in the dq synchronous reference frame (A)
$I_{C,rms}$	Capacitor maximum rms current (A)
J	Moment of inertia (Kgm^2)
k_d, k_s, k_t	Threshold values
K_P, T_I	PI controller gains
L_d, L_q	Stator inductances in the dq synchronous reference frame (H)
L_f	Grid filter inductance (H)
L_s	Synchronous inductance (H)

l_n	Localization variables
p	Pole pairs number
p_g	Grid instantaneous active power
P_n, N_n	Localization variables for the CP method
q_g	Grid instantaneous reactive power
R_f	Grid filter resistance (Ω)
R_s	Stator winding per-phase resistance (Ω)
S_A, S_B, S_C	Swiching states of grid-side converter
S_a, S_b, S_c	Swiching states of PMSG-side converter
T_e	Electromagnetic torque (Nm)
T_L	Load torque (Nm)
T_s	Sampling period (s)
t_x, t_y, t_0	Time values for the voltage reference vector syntetization (s)
T_{dGrid}, T_{dPMSG}	Threshold values for the CPVP method
T_{lGrid}	Threshold value for the CP method
u_{A0}, u_{B0}, u_{C0}	Grid phase-to-zero voltages (V)
u_{a0}, u_{b0}, u_{c0}	PMSG phase-to-zero voltages (V)
u_{AN}, u_{BN}, u_{CN}	Grid phase-to-neutral voltages (V)
u_{an}, u_{bn}, u_{cn}	PMSG phase-to-neutral voltages (V)
$u_{c\alpha}$, $u_{c\beta}$	Converter voltages in the $\alpha\beta$ stationary reference frame (V)
u_d^c, u_q^c	Decoupling voltage components in the dq synchronous reference frame (V)
u_f^*	Reference voltage generated by a fault (V)
$u_{g\alpha}$, $u_{g\beta}$	Grid phase voltages in the $\alpha\beta$ stationary reference frame (V)
u_{gd}, u_{gq}	Grid phase voltages in the dq synchronous reference frame (V)

U_g	Grid phase voltage amplitude (V)
u_{N0}	Grid neutral-to-zero voltage (V)
u_{n0}	PMSG neutral-to-zero voltage (V)
$u_{s\alpha}$, $u_{s\beta}$	Stator phase voltages in the $\alpha\beta$ stationary reference frame (V)
u_{sd}, u_{sq}	Stator phase voltages in the dq synchronous reference frame (V)
u_{dc1}, u_{dc2}	Voltages of capacitors C_1 and C_2
V_c	Converter voltage space vector (V)
V_{dc}	DC bus voltage (V)
V_m^*	Reference voltage amplitude (V)
V_{ph}	Phase-to-neutral voltage amplitude (V)
x	Arbitrary variable
AC	Alternating current
AVNRV	Average values of the normalized reference voltages
AVNVE	Average values of the normalized voltage errors
CP	Current polarity
CPVP	Current Park's Vector phase
DC	Direct current
DFIG	Doubly fed induction generator
DPC	Direct power control
DSP	Digital signal processor
DTC	Direct torque control
ENCAAV-CMax	Errors of the normalized currents average absolute values using the instantaneous maximum value of the currents absolute values as normalization quantity
ENCAAV-CPVM	Errors of the normalized currents average absolute values using the Park's Vector modulus as normalization quantity

FLC	Five-leg converter
FOC	Field oriented control
FPGA	Field programmable gate array
FSTPC	Four-switch three-phase converter
HCC	Hysteresis current control
IGBTs	Insulated gate bipolar transistors
LPF	Low-pass filter
NCM	Neutral to capacitors midpoint
PCM	Phase to capacitors midpoint
PI	Proportional-Integral
PLL	Phase locked loop
PMSG	Permanent magnet synchronous generator
PMSM	Permanent magnet synchronous machine
PWM	Pulsewidth modulation
RFOC	Rotor field oriented control
rpm	Revolutions per minute
S-PWM	Sinusoidal pulsewidth modulation
SCIG	Squirrel-cage induction generator
SSTPC	Six-switch three-phase converter
SVM	Space vector modulation
THD	Total harmonic distortion
TRIAC	Triode for alternating current
TSTPR	Three-switch three-phase rectifier
TWO	Total waveform oscillation
VOC	Voltage oriented control
WECS	Wind energy conversion systems

Chapter 1

Introduction

All over the world there is a need for clean, affordable, reliable and quick to install power generation systems, in order to support a sustainable growth. Therefore, among renewable energies, wind power generation appears to have the greatest potential. Accordingly, ambitious targets have been set by the European Wind Energy Association, 16% of wind energy penetration in 2020 and 50% in 2050 [1]. During the first half of 2013, offshore capacity has registered the highest increase ever in Europe, a trend that is expected to continue.

Although wind energy has been being exploited for approximately four decades, there are several issues, essential for its rapid spread, still driving the scientific research in this field, such as grid integration (grid codes, energy quality, fault ride-through capability), and efficiency and reliability of the wind energy conversion systems (WECS).

Competitiveness and economic viability require cost reduction of the generated wind energy, so that highly reliable and available wind turbines are demanded, reducing downtimes as well as operation and maintenance costs, which is of prime importance in offshore installations where maintenance interventions are very costly and time consuming. Consequently, robust technologies, condition monitoring and fault-tolerant systems should be adopted for WECS, contributing to an optimized schedule of maintenance operations and avoiding unforeseen stoppages. As a result, value-added solutions are obtained, with features that go beyond the standard ones.

Permanent magnet synchronous generator (PMSG) drives are a promising technology [2] and, lately, have been adopted by the major wind turbine manufacturers (for example Siemens, GE, Alstom, Gamesa and Vestas [3]-[7]) due to various advantageous features, such as high efficiency, operation at low temperatures (hence extending lubrication intervals and increasing bearing life-time), compact design, low rated speed (as a consequence of a high number of magnetic poles) permitting to avoid the gearbox that is usually considered the most problematic component due to long downtimes for maintenance [8]-[9]. Thus, modern PMSG drives have become the solution for offshore applications, and their research and development is ongoing up to the multi-megawatt range. In such a drive, power converters are mandatory [2], which have seen increased their flex-

ibility and performance together with the development of semiconductor power devices and DSP and FPGA technologies. In this particular area of research, the development of advanced control solutions has achieved prominence, in order to enhance energy conversion efficiency and dynamic performance [10]-[11].

However, the power converter required in a PMSG drive is linked to a high failure rate in wind turbines, higher than in other applications [8]. Statistical studies on failures have concluded that the aggregate failure rate of generators and converters in direct drive systems is greater than the aggregate failure rate of gearboxes, generators and converters in indirect drive ones. So, a direct drive system does not have an inherent reliability higher than the indirect one, but its availability should be greater, because a converter failure has a shorter average time of repair than a gearbox failure. An investigation on converter failures in wind turbines reported in [12] found that, non-switching IGBTs (power switch open-circuit fault) and faulty sensors are the main causes for power converter outage. Thus, despite being scarce data on power converter failures, all the available studies seem to identify power switch open-circuit faults and sensor faults as major causes. Having recognized that direct drive wind turbines have shown a reliability lower than expected, with a significant contribution of power converter faults [13], the industry demands a solution to such critical issues [14].

In this context, the development of fully-integrated fault-tolerant converters with capability to maintain their operation after an internal fault occurrence until a maintenance operation can be scheduled is of both academia and industry interest. Even though fault-tolerant systems have traditionally been applied in critical applications, such as aircrafts, due to safety reasons and to prevent danger to human life, they also have applicability when reliability and availability assume paramount importance due to economical reasons.

Fault tolerance in power converters involves the following main subjects: (1) accurate and fast fault diagnosis; (2) remedial actions to compensate fault-induced performance degradation; (3) design and trade-off between cost and post-fault performance; and (4) integration and automation for real-time implementation. These subjects are extensively discussed in this thesis concerning a PMSG drive intended to tolerate power switch open-circuit faults and current sensor faults. This work aims to propose and analyze different solutions for endowing PMSG drives with fault-tolerant capabilities, contributing to extend their reliability and availability . Two fault types are considered: power switch open-circuit faults and current sensor faults. On the one hand, only one approach is proposed to handle current sensor faults. On the other hand, in order to handle open-circuit faults, various diagnostic techniques, and converter topologies and respective control strategies for post-fault operation are proposed and compared.

1.1 Main Contributions

The review of the state of the art in fault-tolerant PMSG drives shows lack of research in suitable and cost-effective fault-tolerant power converters for wind turbine applications. Moreover, power converters have shown to be a significant contributor to the overall failure rate of modern wind turbines. Taking this into account and concerning power switch open-circuit faults and current sensor faults, this thesis analyzes the PMSG drive faulty operation, fault diagnosis, and alternative converter topologies and control strategies for post-fault operation, seeking different solutions of fully-integrated fault-tolerant PMSG drives.

The faulty operation analysis intends to motivate the development of fault diagnostic methods and fault-tolerant PMSG drives by verifying the degraded operation forced by the fault occurrences, and also to be a preliminary study of the suitable quantities for fault diagnosis and of the extent of hardware and software modifications needed for post-fault operation.

In a fault-tolerant system, timely and accurate transition from faulty operation to post-fault operation is mandatory, such task is ensured by a fault diagnostic technique, which must be independent of the operating conditions, robust to transients, and fast. However, there is lack of reliable fault diagnostic techniques that are also able to meet the requirements for real-time implementation and integration into the drive controller, namely, lack of need for extra hardware, simple implementation and low computational requirements. Accordingly, six fault diagnostic algorithms for open-circuit faults and one algorithm for current sensor faults have been developed and proposed in this thesis.

Regarding open-circuit faults, post-fault operation of non-redundant converters is characterized by the adoption of an alternative converter topology and respective control strategy. Accordingly, four alternative converter topologies and their operating limits are studied and new control strategies are proposed. Both vector control and direct control strategies with different modulations techniques are addressed, offering a wide range of fault-tolerant solutions for PMSG drives.

Finally, three fully-integrated fault-tolerant PMSG drives are suggested and their design, control system and real-time response are analyzed. Concerning component design, the dc bus capacitor bank is the main focus. The real-time response of the algorithms and remedial procedures integrated into the drive controller are analyzed by means of experimental results.

1.2 Structure of the Thesis

The content of this thesis is divided into seven chapters. This first chapter is restricted to a brief introduction to the subjects related to this thesis in order to contextualize the presented work and to elucidate its relevance. Furthermore, the main contributions and the structure of the thesis are succinctly described. All the remaining chapters start with an introduction to the subject under analysis, including a revision of the state of the art, and finish with experimental validation and a

summary of the chapter.

Chapter 2 starts with the description of the PMSG drive and its mathematical models. Then, control strategies proposed in the literature for controlling the PMSG- and grid-side converters under normal operation are addressed in detail, namely, four control strategies are considered for each converter side, including both vector control and direct control. Their performance under normal operating conditions is analyzed and compared by means of simulation and experimental results. Such variety of strategies is considered to propose later on different fault-tolerant solutions.

The drive faulty operation as a consequence of open-circuit faults and current sensor faults is analyzed in Chapter 3 through simulation and experimental results, always concerning the two converter sides and the distinct control strategies addressed in Chapter 2.

Chapter 4 is dedicated to fault diagnosis of the two fault types considered, six algorithms are proposed for open-circuit fault diagnosis and one is proposed for current sensor fault diagnosis. Simulation and experimental results verify the merits of the proposed methods, and the tolerance to current sensor faults is experimentally verified. To finish with, the six algorithms for open-circuit fault diagnosis are evaluated and compared by using key evaluation parameters, such as detection times, computational burden, and implementation and tuning effort.

Chapter 5 presents alternative converter topologies and control strategies for post-fault operation of the PMSG drive. All topologies are classified as non-redundant, one topology is proposed for post-fault operation of the PMSG-side converter and three are proposed for post-fault operation of the grid-side converter. First of all, each converter topology operation is analyzed theoretically, then, different control strategies are formulated, and, finally, their performance is evaluated by means of simulations and experiments.

Three fully-integrated fault-tolerant converter topologies for PMSG drives are proposed in Chapter 6, together with the analysis of their design, control system, and real-time response. Some of the diagnostic methods and control strategies proposed in chapters 4 and 5 are taken as examples for the experimental validation.

In Chapter 7 the main conclusions of this thesis are drawn, and some topics for future research in this field are pointed out.

Chapter 2

PMSG Drive and Converter Control Strategies

For the rapid spread of the wind power generation, there is the need for efficient, flexible, reliable and cost-effective wind energy conversion systems (WECS). As a result, a considerable diversity of drive concepts have been adopted for wind turbine applications, varying the employed generator, and the possible inclusion of a gearbox and a power converter [15]-[16].

Three generator types are commonly employed in wind turbine applications, the squirrel-cage induction generator (SCIG), the doubly-fed induction generator (DFIG), and the synchronous generators, with the PMSG being the most used. Induction generators are characterized by high rated speeds, and so a gearbox is required for their application in wind turbines. On the other hand, as the main advantage of PMSGs, they can be designed to have low rated speeds, and then avoiding the gearbox, which are designated as direct-drive. A hybrid concept can be composed of a PMSG and an one stage gearbox, which may increase the overall drive power density. SCIG are usually found in the obsolete fixed-speed wind turbines directly connected to the grid (without the presence of a power converter). Variable-speed concepts are required in order to enhance the harness of the wind power and to comply with grid codes, hence they have become widely adopted. With the use of a partial-scale power converter, the DFIG drive is economically attractive, and nowadays this concept dominates the wind market. However, with the decreasing cost of the converters and the increasing demand of grid codes, DFIG drives are also expected to become obsolete in the future [17]. Therefore, PMSG drives turn out to be the most promising technology [18], in which a full-power converter is mandatory. In addition to the variable speed operation, the full-power converter allows the turbine to fully fulfill the grid connection requirements, such as fault ride-through capability and reactive power control.

The main advantages of a PMSG drive for WECS can be summarized as follows: higher efficiency, improved thermal characteristics, absence of gearboxes and slip rings, higher power density. Some disadvantages usually pointed out are: high cost of permanent magnets material, demagne-

tization at high temperatures, and the fact that it is not a mature technology, so some difficulties in the generators manufacture may exist. Due to PMSG drives advantages concerning efficiency and reliability, future offshore installations tend to be dominated by large PMSGs.

A transformer for each wind turbine is commonly used to step-up voltage, since low-voltage two-level voltage source converters are usually used [2],[19], and to galvanically isolate the drive from the grid, also contributing to attenuate PWM harmonics together with the output filter. The transformer might be excluded if a medium-voltage multilevel converter is considered, which is still not the most common option nowadays.

The most common converter topology in high-power WECS is the back-to-back two level voltage source converter [2],[16],[19], and their parallel connection is the solution for high currents adopted by Gamesa and Siemens [21]-[20], designated as modular converters. Diode rectifiers are only suitable for low power applications because the high harmonic distortion of the stator currents lead to low efficiency and high torque ripple. Multilevel converters are a valid option for medium voltage applications, with neutral-point diode clamped, flying capacitor clamped, and cascaded converter cells being the most studied structures [22].

With regard to PMSG drives, a back-to-back converter is controlled with the aims of extracting the maximum power from the wind and delivering it to the grid with the best quality possible. The first task is performed by the generator-side converter by adjusting the generator speed, whereas the second one is accomplished by the grid-side converter by controlling the dc-link voltage, regulating the power factor, and ensuring low harmonic distortion in compliance with the grid codes. Such goals require powerful control schemes with fast dynamic response in order to accomplish the control targets and to quickly compensate sudden load changes [23], which have become available due to the continuous developments in power electronics and controlled electrical drives during the last decades [11]. As a consequence, open-loop schemes (known as Volt/Hertz or scalar control), with no feedback signals, are not suitable for a PMSG drive. Closed-loop schemes, such as vector control and direct control strategies, are then the obvious choice to obtain the desired high performance. The development of control techniques for high-performance AC drives started aiming to replace maintenance demanding DC motors with robust AC motors. Thus, control methods for AC machines were firstly developed, and then analogous techniques were proposed for the control of grid-connected converters. Vector control (Field Oriented Control - FOC) was proposed by Hasse and Blaschke [24]-[25] with the aim to control torque and flux independently, emulating the separately excited DC machine operating principle. Although in a three-phase AC machine flux and torque control are coupled in the stator current, it was demonstrated that the decoupled control of these quantities can be achieved by transforming the natural reference frame abc into a rotating reference frame dq, as a consequence coordinate transformations are of prime importance in vector control schemes.

Alternatively, direct torque control (DTC) was proposed by Takahashi and Noguchi [26] to

control torque and flux directly, which attracted a lot of attention due to its simpler structure and excellent dynamic performance. A similar approach was proposed by Depenbrock and called Direct Self Control [27]. Afterwards, a lot of work has been done to improve DTC performance [28]-[30].

Concerning the control of a grid-connected converter, voltage oriented control (VOC) [31] and direct power control (DPC) [32]-[33] are analogous to FOC and DTC, respectively, provided that independent control of active and reactive power is intended. Comparative studies of vector control and direct control have been reported by several authors. In summary, both are considered viable schemes, with direct control techniques being preferred for high dynamic applications and vector control techniques being preferred for superior steady-state performance (low harmonic distortion, low torque/power ripple). It is also worth noting that some improvements to the conventional direct control schemes may lead to lose their main merits, namely, simplicity and fast response [28],[30],[34]-[35].

Another important topic correlated with the control schemes is the adopted modulation technique, which, finally, dictates the switching pattern, allowing the converter to generate a voltage waveform with variable amplitude and frequency. Accordingly, it has a great impact on the performance of the converter, since the switching frequency, the switching losses, the harmonic distortion and the dynamic response depend on the chosen modulation. Moreover, the choice of a different modulation technique may carry changes to the control method, such as additional control loops, coordinate transformations or switching tables, this will be explained in detail later on in this chapter for the considered PMSG drive. Generally speaking, modulation techniques can be classified as variable switching frequency methods, carrier-based PWM methods, space vector modulation (SVM), and harmonic control modulation [36].

Variable switching frequency methods are well known for their superior dynamic response and, usually, simple implementation, as a result of the lack of need for a voltage modulator. In this category are included hysteresis control (hysteresis current control or hysteresis control with switching tables) and model predictive control. However, these techniques lead to a spread harmonic content, which makes difficult the filter design for harmonic and noise attenuation. As opposed to simple hysteresis control, model predictive control involves complex algorithms, using models of both load and converter in order to predict the system behavior as a function of the available switching states. Nowadays, predictive schemes tend to be more and more adopted in demanding applications, since they offer increased flexibility concerning the fulfillment of distinct control objectives through the modification of a cost function [37]-[38].

Carrier-based PWM techniques [39]-[40] are based on the comparison of a reference/modulation signal (with variable frequency and amplitude) and a carrier signal (with fixed frequency and amplitude), from which results the converter switching pattern. The betterment of the dc-link voltage utilization can be achieved through the injection of a third harmonic in the sinusoidal reference voltage, extending up to 15% the linear modulation range. Different performance tradeoffs are

achieved by choosing different injected harmonics, as concluded in [41] the use of discontinuous zero-sequence components reduces the number of commutations.

Alternatively, the widely employed SVM, invented by Busse and Holtz [42], uses a vector representation of the phase to neutral converter voltages and the reference voltage is generated as a combination of three switching vectors over the switching period. SVM techniques vary according to the defined voltage vector sequence, which can be optimized as a function of a given control target such as common-mode voltage elimination, current ripple reduction and switching losses minimization [36].

Reviews and comparisons of distinct modulation techniques can be found in [39]-[40],[43]-[47]. It is worth noting that a proper choice of the third harmonic injection in carrier-based PWM yields a switching pattern similar to the one obtained with SVM through a simpler algorithm.

In this chapter, control strategies are broadly divided into two major groups: vector control and direct control. Both are considered for the control of the generator- and grid-side converters of the PMSG drive under study together with a variety of modulation techniques, which leads to the analysis of four control schemes for each converter side. First of all, the PMSG drive is described in detailed and simplified mathematical models of both PMSG and grid are presented. Then, the considered control schemes are presented, and their formulation and implementation discussed. To finish with, simulation and experimental results are presented and the performance of the different control strategies is compared.

2.1 Drive Description

The PMSG drive under study (Figure 2.1) is composed of a PMSG, two typical three-phase voltage source converters in a back-to-back topology, each one comprising six IGBTs (Insulated Gate Bipolar Transistors) with the respective antiparallel diodes, a dc-link capacitor bank, an output chocke inductance, and several sensors (current, voltage and speed sensors). The generator speed is controlled by the PMSG-side converter operating as a rectifier, while the torque is determined by the load. The grid-side converter, operating as an inverter, controls the dc-link voltage and the power factor at the grid connection point, ensuring power balance between the PMSG- and grid-side. Different control strategies intended to achieve these control targets are analyzed later on in this chapter.

2.1.1 Mathematical Models

Mathematical models of both PMSG and grid are needed to formulate and theoretically analyze the control strategies for the PMSG drive as well as to allow the whole system to be computationally simulated by using simulation tools like Matlab/Simulink. In this case, the most complex and

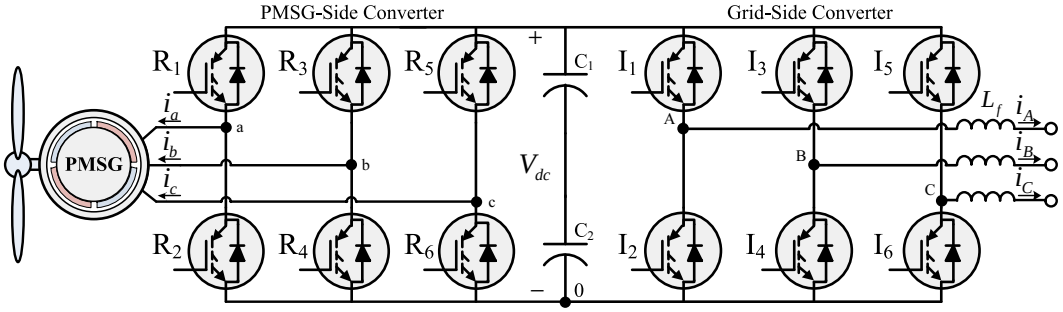

Figure 2.1: Schematic diagram of the PMSG drive under study.

accurate models are not the best suited neither for fast simulation nor for real-time implementation, so that simplifications are acceptable in order to reduce complexity and computational demand.

Therefore, based on the space vector theory, dynamic models in a two-phase coordinate reference frame, rotating at an arbitrary speed, are extensively used for control and simulation purposes as alternative to the real three-phase abc frame. Taking as an example the synchronous dq reference frame (with one of the axes aligned with the rotor flux or grid voltage space vectors), sinusoidal quantities in the abc frame appear as dc quantities in the dq frame under steady-state operation. In addition to the mathematical simplification, obtaining linear equations, it becomes feasible the decoupled control of torque and flux or active power and reactive power in three-phase systems.

The state variables in the stationary *abc* reference frame are transformed to the rotating *dq*0 reference frame by using the following transformation matrix:

$$\begin{bmatrix} x_d \\ x_q \\ x_0 \end{bmatrix} = \frac{2}{3} \begin{bmatrix} \cos(\theta) & \cos\left(\theta - \frac{2\pi}{3}\right) & \cos\left(\theta + \frac{2\pi}{3}\right) \\ -\sin(\theta) & -\sin\left(\theta - \frac{2\pi}{3}\right) & -\sin\left(\theta + \frac{2\pi}{3}\right) \\ 1/2 & 1/2 & 1/2 \end{bmatrix} \begin{bmatrix} x_a \\ x_b \\ x_c \end{bmatrix} \tag{2.1}$$

where θ is the angle between the stator phase a and the *d*-axis. Inversely, the state variables in the rotating $dq0$ reference frame are transformed to the stationary *abc* reference using:

$$\begin{bmatrix} x_a \\ x_b \\ x_c \end{bmatrix} = \begin{bmatrix} \cos(\theta) & -\sin(\theta) & 1 \\ \cos\left(\theta - \frac{2\pi}{3}\right) & -\sin\left(\theta - \frac{2\pi}{3}\right) & 1 \\ \cos\left(\theta + \frac{2\pi}{3}\right) & -\sin\left(\theta + \frac{2\pi}{3}\right) & 1 \end{bmatrix} \begin{bmatrix} x_d \\ x_q \\ x_0 \end{bmatrix} \tag{2.2}$$

Furthermore, it is worthwhile to point out that the state variables in the stationary $\alpha\beta$ reference frame are obtained with $\theta = 0$, and that the transformations between the rotating dq reference frame and the stationary $\alpha\beta$ reference frame are given by the following matrixes:

$$\begin{bmatrix} x_d \\ x_q \end{bmatrix} = \begin{bmatrix} \cos(\theta) & \sin(\theta) \\ -\sin(\theta) & \cos(\theta) \end{bmatrix} \begin{bmatrix} x_\alpha \\ x_\beta \end{bmatrix} \tag{2.3}$$

$$\begin{bmatrix} x_\alpha \\ x_\beta \end{bmatrix} = \begin{bmatrix} \cos(\theta) & -\sin(\theta) \\ \sin(\theta) & \cos(\theta) \end{bmatrix} \begin{bmatrix} x_d \\ x_q \end{bmatrix} \tag{2.4}$$

The most widely used PMSG model neglects the stator core losses, the hysteresis losses, the magnetic the saturation and the skin effect, while the electromotive force is assumed sinusoidal. If the *dq* axes rotate at an arbitrary speed ω, the PMSG voltage equations are given by:

$$u_{sd} = R_s i_{sd} + L_d \frac{di_{sd}}{dt} - \omega \psi_{sq} \tag{2.5}$$

$$u_{sd} = R_s i_{sq} + L_q \frac{di_{sq}}{dt} + \omega \psi_{sd} \tag{2.6}$$

If the *dq* axes rotate at the synchronous speed and the *d*-axis is aligned with the rotor flux space vector, the stator flux components are given by:

$$\psi_{sd} = L_d i_{sd} + \psi_{PM} \tag{2.7}$$

$$\psi_{sq} = L_q i_{sq} \tag{2.8}$$

As a result, the voltage equations in the *dq* synchronous reference frame are given as follows:

$$u_{sd} = R_s i_{sd} + L_d \frac{di_{sd}}{dt} - \omega_s L_q i_{sq} \tag{2.9}$$

$$u_{sq} = R_s i_{sq} + L_q \frac{di_{sq}}{dt} + \omega_s L_d i_{sd} + \omega \psi_{PM} \tag{2.10}$$

It should be noticed the cross-coupling in equations (2.9) and (2.10), in other words the *d*-axis voltage component does not only depend on the *d*-axis current component but also it depends on the *q*-axis current component.

The electromagnetic torque as a function of the stator current in the *dq* axes is given by:

$$T_e = \frac{3}{2} p \left[\psi_{PM} i_{sq} + (L_d - L_q) i_{sd} i_{sq} \right] \tag{2.11}$$

If a surface-mounted PMSG is considered, the previous equation for T_e can be further simplified since $L_d = L_q$:

$$T_e = \frac{3}{2} p \psi_{PM} i_{sq} \tag{2.12}$$

Accordingly, i_{sq} is called the torque producing current component.

The modeling of the PMSG is completed by the equation of motion given by:

$$\frac{d\omega_r}{dt} = \frac{1}{J}\left(T_e - D\omega_r - T_L\right) \tag{2.13}$$

where

$$\frac{d\theta_r}{dt} = \omega_s = \omega_r p \tag{2.14}$$

The resulting PMSG model is a second order system, where the rotor flux is a constant parameter of the machine. A slightly more complex and accurate model of the PMSG was implemented for the computational simulation in Matlab/Simulink by taking into account stator iron losses [48]-[49].

Similarly, the dynamic model of the grid-side system in the dq reference frame can be derived [50]-[51]. In the $\alpha\beta$ stationary reference frame, the grid-side converter voltages are given as:

$$u_{c\alpha} = R_f i_{g\alpha} + L_f \frac{di_{g\alpha}}{dt} + u_{g\alpha} \tag{2.15}$$

$$u_{c\beta} = R_f i_{i\beta} + L_f \frac{di_{g\beta}}{dt} + u_{g\beta} \tag{2.16}$$

In the *dq* synchronous reference frame, with the *dq*-axes rotating at the grid voltage frequency and the *q*-axis aligned with the grid voltage space vector, the grid-side converter voltages are given as:

$$u_{cd} = R_f i_{gd} + L_f \frac{di_{gd}}{dt} - \omega_g L_f i_{gq} \tag{2.17}$$

$$u_{cq} = R_f i_{gq} + L_f \frac{di_{gq}}{dt} + \omega_g L_f i_{gd} + u_{gq} \tag{2.18}$$

Once again, it can be noticed the cross coupling in the voltage equations (2.17) and (2.18). The similarity between these equation and equations (2.9) and (2.10) justifies the analogy between vector control for the PMSG- and grid-side converters (RFOC and VOC).

2.1.2 Experimental Setup

The experimental setup comprises a 2.2 kW PMSG coupled to a four-quadrant test bench (Figure 2.2), two Semikron SKiiP three-phase two-level voltage source converters in a back-to-back topology, a dSPACE DS1103 digital controller, two precision power analyzers Yokogawa WT3000, a dc bus capacitor bank of 1.1 mF and an output filter of 5 mH. The experimental setup is depicted in Figure 2.3. Throughout this work two different machines were used, both 2.2 kW Yaskawa surface-mounted magnet machines with equal rated speed and torque but with different rated current and voltage, their parameters are given in Appendix A. Moreover, an autotransformer was

always used to adjust the grid voltage, and a transformer was used only when the access to neutral point was a requirement (chapters 5 and 6). Together with Matlab/Simulink and dSPACE ControlDesk software, the DS1103 controller provides real-time control and monitoring of the overall system with a sampling time of 50 µs. The rotor position is obtained by an incremental encoder with 1024 pulses per revolution. All the experimental results in this chapter were carried out at a grid phase-to-phase voltage of 135 V and a reference dc link voltage of 250 V.

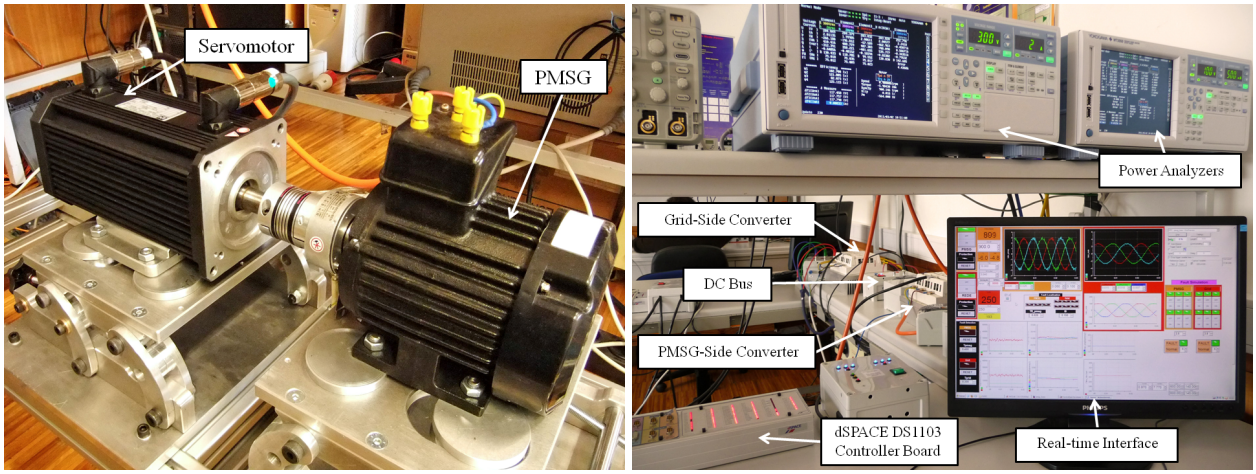

(a) (b)

Figure 2.2: Laboratory setup: (a) detail of the PMSG coupled to the servo machine; (b) general view of the power and control stages.

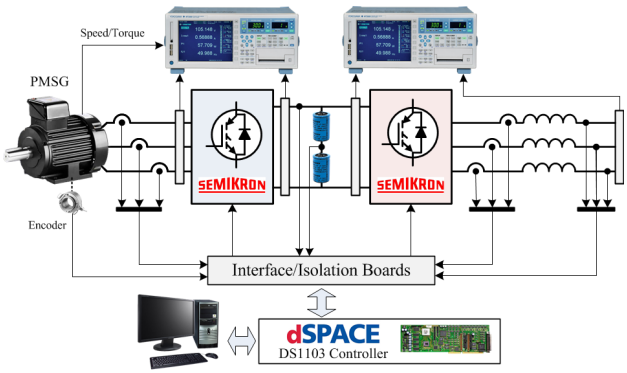

Figure 2.3: Schematic diagram of the experimental setup.

2.2 Control Strategies for the PMSG-Side Converter

A control strategy for the PMSG-side converter aims to control separately flux and torque (through the control of generator phase currents), which can be achieved directly by using DTC or

indirectly by using RFOC [52]-[53]. The knowledge of the initial rotor position is a requirement for both DTC and RFOC when applied to a PMSG. Afterwards, the rotor position is necessary for speed control, which can be obtained in a sensor or sensorless basis. An encoder for speed measurement is always used in this work. The following sections present the operating principles of RFOC and DTC, together with two distinct modulation techniques, namely, hysteresis control and space vector modulation.

2.2.1 Vector Control - Rotor Field Oriented Control

Vector control is based on the use of the dq reference frame, whose direct axis is fixed to the rotor flux space vector. As a result, considering a constant magnet flux, the electromagnetic torque is proportional to the q-axis stator current component (equation 2.12). Therefore, the maximum torque per ampere in a surfaced mounted PMSG is obtained with $i_{sd} = 0$.

The stator current components can be directly or indirectly controlled, hysteresis current control and SVM are the considered examples, respectively.

2.2.1.1 RFOC with HCC

HCC (also called on-off or bang-bang control) is classified as a nonlinear controller (variable switching frequency method), which intends to control directly the converter current by using hysteresis comparators to generate the switching pattern. The block diagram of the RFOC strategy with HCC for the PMSG-side converter is depicted in Figure 2.4. The reference torque-producing current component (i^*_{sq}) is generated by a PI speed controller, while i^*_{sd} is fixed to zero to achieve the maximum torque per ampere. Therefore, the reference current components in the rotor reference frame are transformed to natural abc reference frame and three hysteresis comparators are used to generate the converter gate command signals, having as input the error between the reference currents and the actual ones. The digital implementation of two-level hysteresis comparators can expressed as:

$$S_n = \begin{cases} 1 & \text{if } i^*_n > i_n + B_{hcc}/2 \\ 0 & \text{if } i^*_n < i_n - B_{hcc}/2 \end{cases} \tag{2.19}$$

where B_{hcc} stands for the width of the hysteresis band and $n = a,\ b,\ c$. S_n stands for the switching state of the upper switch of each phase (ON: 1, OFF: 0), while the bottom assumes the complementary state. Thus, current error compensation and PWM generation are carried out together [50], since the phase switching state changes when the current error ($i^*_j - i_j$) exceeds the hysteresis band. The tracking capability of the HCC is defined by the hysteresis bandwidth, in other words the smaller the hysteresis bandwidth, the closer to the reference current the actual current will be. However, a high sampling frequency (f_s) is required, otherwise the tracking capability would be

limited by f_s instead.

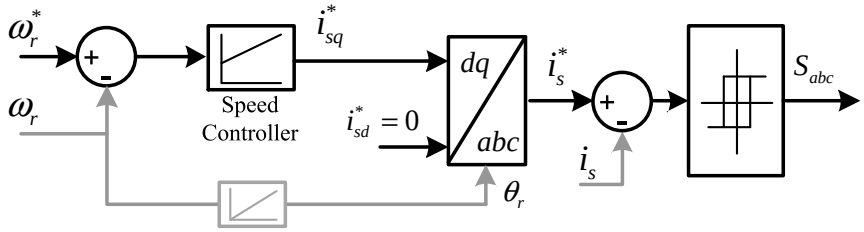

Figure 2.4: Block diagram of the RFOC strategy with HCC applied to the PMSG-side converter.

The HCC main advantages are simplicity, robustness, stability, independence of the system parameters and very fast response. The extremely fast dynamic response results from the lack of a voltage modulator and cross coupling, thus, high amplitude voltages are instantaneously applied when the current error exceeds the defined band. This allows HCC to show a superior performance for applications in which dynamic response is of prime importance, active power filters are one example [54].

Some drawbacks of HCC are variable switching frequency (spread harmonic spectrum), requirement of a high sampling frequency, and band violation up to twice of the defined bandwidth due to interphases dependency. Different solutions based on HCC have been proposed to overcome such issues, for example by implementing HCC in the dq or $\alpha\beta$ reference frame [43] or by using variable hysteresis band [55]-[56]. Due to the aforementioned disadvantages, for a fully digital implementation, PWM linear controllers are the most common choice for current control of voltage source converters, which are analyzed next.

2.2.1.2 RFOC with SVM

In a linear current controller, the current is indirectly controlled by means of a voltage PWM modulator. In contrast to the HCC, current error compensation and voltage modulation are performed separately [43]. The most common implementation uses PI controllers in the synchronous reference frame for the internal current control loops in order to perform current error compensation. The resultant reference voltage is fed to a modulator, SVM for instance, which finally generates the switching sequence. The block diagram of the RFOC strategy with SVM for the PMSG-side converter is shown in Figure 2.5, elucidating the differences between SVM and HCC (Figure 2.4). It becomes evident that a more complex algorithm is obtained, also with a more demanding tuning, since a dedicated modulator (SVM) and two additional PI controllers are included.

Moreover, attempting to improve the dynamic performance, feed-forward signals should be added to the output of the current controllers in order to eliminate the cross coupling between the d-axis and the q-axis voltages expressed in equations (2.9) and (2.10). Therefore, the decoupling system is introduced in a feed-forward manner:

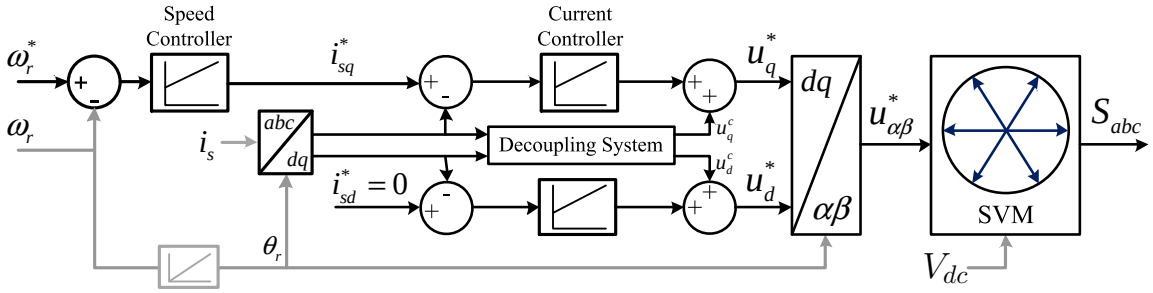

Figure 2.5: Block diagram of the RFOC strategy with SVM applied to the PMSG-side converter.

$$u_d^c = -\omega_s L_q i_{sq} \tag{2.20}$$

$$u_q^c = \omega_s L_d i_{sd} + \omega \psi_{PM} \tag{2.21}$$

whose accuracy depends on the parameters estimation. Consequently, the PI controllers operate independently from each other, and the decoupled control of i_d and i_q intended by the vector control can be achieved. The design of the PI current controllers is conventionally based on a simplified open-loop transfer function, by considering the transfer functions of the controller and the simplified machine model (Figure 2.6), and cancelling the pole of the machine with the zero of the controller, the PI controller gains (K_P, T_I) can be simply given by:

$$K_P = \frac{L_s}{R_s T_I}; \tag{2.22}$$

$$T_I = \frac{1}{R_s 2\pi B_i}; \tag{2.23}$$

where L_s=L_d=L_q stands for the synchronous inductance of a surface-mounted PMSG and B_i stands for the current control loop bandwidth. A more accurate tuning can be performed by taking into account all the time delays introduced by the hardware (converter and sampling process) [57]. Among a great variety of tuning methods [58]-[59], a fast and stable closed-loop response can be obtained by using the Magnitude Optimum method. Alternatively, performance measures (for instance, the phase margin) can be also used as PI tuning parameters.

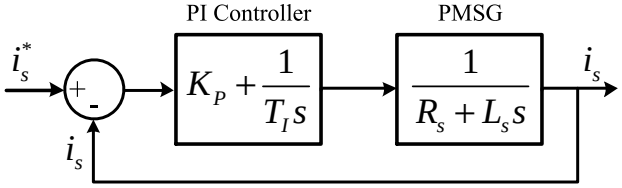

Figure 2.6: Block diagram of the current control loop.

Before the reference voltages being fed to the modulator, they are transformed from the synchronous *dq* reference frame (u_d^*, u_q^*) to the stationary $\alpha\beta$ reference frame (u_α^*, u_β^*). Finally, the modulator uses the reference voltages to define the switching pattern.

The voltage modulator considered in this work is the widely used SVM, which aims to determine (for a given sampling interval) a switching pattern that ensures an average output phase voltage equal to the reference voltages fed to the modulator. As opposed to carrier-based PWM techniques, a separate modulator for each phase are not used. Instead, the reference voltage space vector is processed as a whole [39]. The converter voltage space vectors are defined by:

$$V_c = \frac{2}{3}\left(u_{an} + u_{bn}e^{j2\pi/3} + u_{cn}e^{j4\pi/3}\right) = u_{c\alpha} + ju_{c\beta} \tag{2.24}$$

where u_{an}, u_{bn} and u_{cn} stand for the phase-to-neutral voltages, which can be expressed as function of the phase-to-zero (u_{a0}, u_{a0}, u_{c0}) and neutral-to-zero (u_{n0}) voltages:

$$u_{an} = u_{a0} - u_{n0};\ u_{bn} = u_{b0} - u_{n0};\ u_{cn} = u_{c0} - u_{n0};\ u_{n0} = \frac{u_{a0} + u_{b0} + u_{c0}}{3} \tag{2.25}$$

In turn the phase-to-zero (u_{a0}, u_{bO}, u_{c0}) voltages are defined by the switching states:

$$u_{a0} = V_{dc}S_a;\ u_{b0} = V_{dc}S_b;\ u_{c0} = V_{dc}S_c \tag{2.26}$$

and substituting (2.26) in (2.25), the phase voltages are given by:

$$\begin{bmatrix} u_{an} \\ u_{bn} \\ u_{cn} \end{bmatrix} = \frac{V_{dc}}{3}\begin{bmatrix} 2 & -1 & -1 \\ -1 & 2 & -1 \\ -1 & -1 & 2 \end{bmatrix}\begin{bmatrix} S_a \\ S_b \\ S_c \end{bmatrix} \tag{2.27}$$

Finally, by substituting (2.27) in (2.24), eight voltage vectors are obtained, which are expressed in $\alpha\beta$ axes as:

$$\begin{cases} u_{c\alpha} = \dfrac{2}{3}V_{dc}\left(S_a - \dfrac{S_b + S_c}{2}\right) \\ u_{c\beta} = \dfrac{1}{\sqrt{3}}V_{dc}\left(S_b - S_c\right) \end{cases} \tag{2.28}$$

The eight voltage vectors are composed of six active vectors (V_1 to V_6) and two null vectors (V_0 and V_7), which are represented in Table 2.1 and Figure 2.7. Thus, the active vectors are displaced by 60º and the area between two adjacent active vectors defines a sector, dividing the complex plane into six sectors, according to Figure 2.7.

In order to synthesize the reference voltage vector (V_c^*), the two converter voltage vectors adjacent to V_c^* are chosen to be applied and their on-durations during a sampling period T_s are

Table 2.1: Voltage vectors synthesized by the six-switch three-phase converter.

$V_c(S_a,S_b,S_c)$	$V_0(000)$	$V_1(100)$	$V_2(110)$	$V_3(010)$	$V_4(011)$	$V_5(001)$	$V_6(101)$	$V_7(111)$
u_α	0	$\frac{2}{3}V_{dc}$	$\frac{1}{3}V_{dc}$	$-\frac{1}{3}V_{dc}$	$\frac{2}{3}V_{dc}$	$-\frac{1}{3}V_{dc}$	$\frac{1}{3}V_{dc}$	0
u_β	0	0	$\frac{1}{\sqrt{3}}V_{dc}$	$\frac{1}{\sqrt{3}}V_{dc}$	0	$-\frac{1}{\sqrt{3}}V_{dc}$	$-\frac{1}{\sqrt{3}}V_{dc}$	0

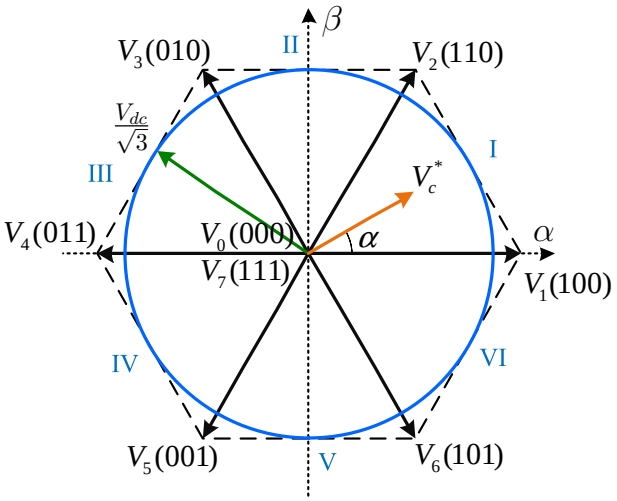

Figure 2.7: Representation of the voltage space vectors in the complex plane and sector definition for the SVM.

calculated ($T_{PWM} = 2T_s$). If the active vectors are applied during a time period shorter than T_s (linear modulation range), the null vectors are applied during the remaining time. Taking as an example V_c^* in sector I, this can be elucidated by:

$$T_s V_c^* = t_x V_1 + t_y V_2;\ T_s = t_x + t_y + t_0 \tag{2.29}$$

Therefore, having obtained the modulus $|V_c^*|$ and phase angle α of the reference voltage vector from u_α^* and u_β^*, the switching times for the active $(t_x,\ t_y)$ and null (t_0) vectors are calculated as follows:

$$\begin{cases} t_x = & \frac{\sqrt{3}\,|V_c^*|}{V_{dc}} T_s \sin\left(\frac{\pi}{3} - \alpha\right) \\ t_y = & \frac{\sqrt{3}\,|V_c^*|}{V_{dc}} T_s \sin\left(\alpha\right) \\ t_0 = & T_s - t_x - t_y \end{cases} \tag{2.30}$$

where α stands for the angle between the immediately previous basic vector and the reference vector. For instance, in sector I, α is the angle between V_1 and V_c^*.The relationships in equation (2.30) are

valid for all the six sectors.

The maximum amplitude of the reference voltage vector is $V_{dc}/\sqrt{3}$, which corresponds to the radius of the largest circle inscribed within the hexagon of Figure 2.7.

Finally, an adequate vectors sequence has to be chosen. One of the most common choices intends to minimize the number of commutations, in such a way that a switching state change implies the switching of only one converter leg [60]. This can be accomplished if the switching sequence (during T_s) starts and ends with null vectors, with t_0 being equally divided by V_0 and V_7, and the active vectors are symmetrically distributed as shown in Table 2.2. In addition to the vectors sequence, Table 2.2 includes the on-duration of each voltage vector for a PWM period. It is worth noting that the sampling frequency ($1/T_s$) is twice as high as the PWM frequency ($1/(2T_s)$).

Table 2.2: SVM voltage vectors sequence and timing plan for the SSTPC.

Sector	Voltage Vector Sequence	Voltage Vector Timing
I	$V_0 \rightarrow V_1 \rightarrow V_2 \rightarrow V_7 \rightarrow V_2 \rightarrow V_1 \rightarrow V_0$	$t_0/2 \rightarrow t_x \rightarrow t_y \rightarrow t_0 \rightarrow t_y \rightarrow t_x \rightarrow t_0/2$
II	$V_0 \rightarrow V_3 \rightarrow V_2 \rightarrow V_7 \rightarrow V_2 \rightarrow V_3 \rightarrow V_0$	$t_0/2 \rightarrow t_y \rightarrow t_x \rightarrow t_0 \rightarrow t_x \rightarrow t_y \rightarrow t_0/2$
III	$V_0 \rightarrow V_3 \rightarrow V_4 \rightarrow V_7 \rightarrow V_4 \rightarrow V_3 \rightarrow V_0$	$t_0/2 \rightarrow t_x \rightarrow t_y \rightarrow t_0 \rightarrow t_y \rightarrow t_x \rightarrow t_0/2$
IV	$V_0 \rightarrow V_5 \rightarrow V_4 \rightarrow V_7 \rightarrow V_4 \rightarrow V_5 \rightarrow V_0$	$t_0/2 \rightarrow t_y \rightarrow t_x \rightarrow t_0 \rightarrow t_x \rightarrow t_y \rightarrow t_0/2$
V	$V_0 \rightarrow V_5 \rightarrow V_6 \rightarrow V_7 \rightarrow V_6 \rightarrow V_5 \rightarrow V_0$	$t_0/2 \rightarrow t_x \rightarrow t_y \rightarrow t_0 \rightarrow t_y \rightarrow t_x \rightarrow t_0/2$
VI	$V_0 \rightarrow V_1 \rightarrow V_6 \rightarrow V_7 \rightarrow V_6 \rightarrow V_1 \rightarrow V_0$	$t_0/2 \rightarrow t_y \rightarrow t_x \rightarrow t_0 \rightarrow t_x \rightarrow t_y \rightarrow t_0/2$

Therefore, RFOC with SVM allows the PMSG-side converter to operate at constant switching frequency and with reduced current harmonic distortion. Moreover, SVM allows well-defined harmonic spectrum (concentrated around the switching frequency), good utilization of the dc-link voltage, and reduced switching losses. Accordingly, SVM offers a better steady state performance but its dynamic performance is inferior to that of the HCC, and it is not inherently stable.

Despite SVM increased complexity when compared to HCC, thanks to its advantages and due to microprocessor advances, SVM is widely used in industrial applications.

2.2.2 Direct Torque Control

The main distinctive features of the conventional DTC are [52]-[53]: direct control of stator flux and electromagnetic torque; indirect control of stator currents; high current and torque ripple; reduced torque oscillations; excellent torque dynamics; and variable switching frequency. When compared to vector control strategies, the main advantages of the conventional DTC are simplicity and fast dynamic response, which result from the absence of: coordinate transformations, separate voltage modulator, decoupling system, and current controllers.

Disadvantages of the conventional DTC such as variable switching frequency and high current and torque ripple can be overcome by including SVM. As a consequence, a more complex algorithm

is obtained and the dynamic performance is degraded.

The following sections address the implementation of the conventional DTC and DTC with SVM.

2.2.2.1 Conventional DTC

In the conventional DTC, direct and independent control of flux and torque is achieved by the selection of the optimum voltage vector in a switching table. This choice is based on the outputs of the flux and torque hysteresis controllers and the sector where the stator flux space vector is located. The block diagram of the conventional DTC is shown in Figure 2.8, which is intended to control the generator speed (ω_r), imposing a fixed reference flux (ψ_s^*) and employing two-level hysteresis comparators with outputs $d\psi$ and dT_e.

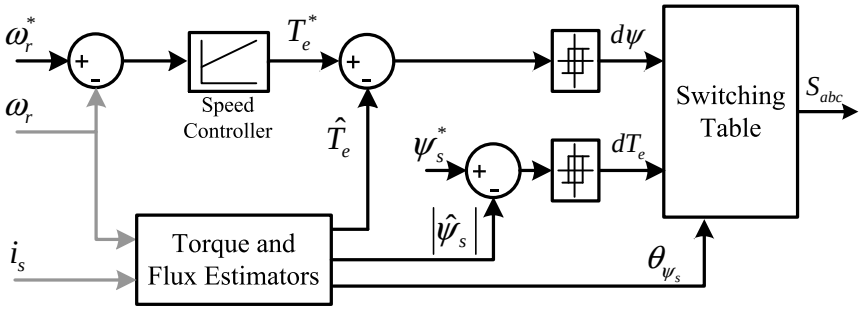

Figure 2.8: Block diagram of the conventional DTC strategy applied to the PMSG-side converter.

Flux and torque estimation is a crucial task in a DTC drive, demanding a model of the machine and accurate knowledge of its parameters. Through the mathematical model of a surface-mounted PMSG in the stationary reference frame, the stator flux (ψ_s) and the electromagnetic torque (T_e) are given by:

$$\psi_{s\alpha} = \int_0^t (u_{s\alpha} - R_s i_{s\alpha})\, dt + \psi_{s\alpha|t=0};\ \psi_{s\beta} = \int_0^t (u_{s\beta} - R_s i_{s\beta})\, dt + \psi_{s\beta|t=0} \tag{2.31}$$

$$\psi_{s\alpha} = L_s i_{s\alpha} + \psi_{PM} \cos\theta_r;\ \psi_{s\beta} = L_s i_{s\beta} + \psi_{PM} \sin\theta_r \tag{2.32}$$

$$T_e = \frac{3}{2} p \left(\psi_{s\alpha} i_{s\beta} - \psi_{s\beta} i_{s\alpha}\right) \tag{2.33}$$

$$T_e = \frac{3}{2} p \frac{|\psi_s|\, \psi_{PM}}{L_s} \sin\delta \tag{2.34}$$

Thus, the stator flux can be estimated by integrating the generator terminal voltage reduced by the ohmic losses in the stator windings resistance (R_s), known as voltage model based flux estimator

(2.31). However, at low frequencies, large errors can occur due to the variation of R_s, integrator drift and noise. Alternatively, a current model based flux estimator can be used (2.32), which requires the phase currents, the mechanical speed in order to obtain the rotor angular position θ_r, and the values of L_s and ψ_{PM}. Various improved flux estimators can be found in the literature [61], using observers or model adaptive reference systems, with the aim to reduce the sensitivity of flux models to errors in the parameters estimation. After having estimated the stator flux, the electromagnetic torque (T_e) calculation is straightforward by using equation (2.33).

According to (2.31), the application of a given voltage vector leads to the variation of the stator flux, while in (2.34) it is expressed that the electromagnetic torque can be controlled through the angle between the stator and rotor flux vectors (δ). Therefore, regulating the position of the stator flux vector by applying the appropriate voltage vector allows the torque to be quickly controlled, which is the basic principle of DTC.

In order to explain the formulation of the switching table (Table 2.3), the stator flux should be seen as the torque control quantity, since the torque production results from the angle between the stator flux and the rotor flux (2.34). Considering that R_s can be neglected, ψ_s moves in the direction of the applied converter voltage vector (2.31). If a null voltage vector is applied, it turns out that ψ_s keeps its position. Accordingly, and supposing that the rotor flux rotates in the anticlockwise direction, the torque is increased by any voltage vector that moves ψ_s away from ψ_r, whereas the torque is decreased by any voltage vector that leads to the decrease of the angle δ (including the null vectors). A null vector leads the torque to decrease because the rotor flux keeps moving towards the stator flux, while this is fixed, and as a result δ decreases.

Table 2.3: Conventional DTC switching table.

$d\psi$	dTe	Sector					
		I	II	III	IV	V	VI
+	+	V_2 (110)	V_3 (010)	V_4 (011)	V_5 (001)	V_6 (101)	V_1 (100)
	-	V_6 (101)	V_1 (100)	V_2 (110)	V_3 (010)	V_4 (011)	V_5 (001)
-	+	V_3 (010)	V_4 (011)	V_5 (001)	V_6 (101)	V_1 (100)	V_2 (110)
	-	V_5 (001)	V_6 (101)	V_1 (100)	V_2 (110)	V_3 (010)	V_4 (011)

Therefore, by dividing the complex plane into six sectors as depicted in Figure 2.9 and taking into account the eight voltage vectors that a six-switch three-phase converter (SSTPC) is able to synthesize, Table 2.3 is formulated with the optimum voltage vector intended to increase (+) or decrease (-) flux and torque in each sector. Additionally, only the voltage vectors that lead to the same effects in flux and torque throughout the sector are selected, for instance, in sector I, voltage vectors V_1 and V_4 are not used.

Alternatively, by employing three-level torque hysteresis comparators, null voltage vectors can be included [26].

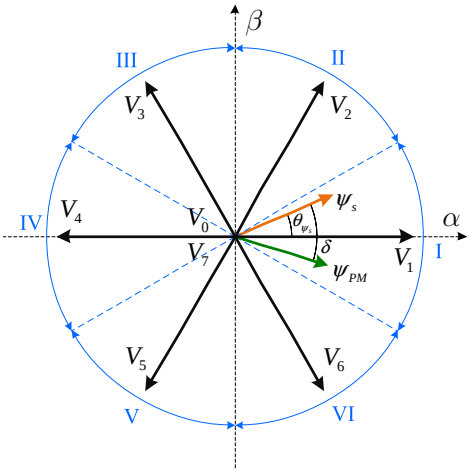

Figure 2.9: Voltage vectors synthesized by an SSTPC and sector definition according to the stator flux vector for the conventional DTC.

2.2.2.2 DTC with SVM

DTC with SVM has been proposed with the aim to overcome conventional DTC drawbacks, allowing DTC to operate at a constant switching frequency. Among the different DTC schemes with SVM that can be found in the literature [28], [62]-[64], it is the DTC scheme of Figure 2.10 [65]-[66], in which the hysteresis torque and flux controllers and the switching table are replaced by PI controllers and a voltage modulator (SVM). The PI controllers use the flux and torque errors to generate reference voltages in the stator flux reference, which in turn are transformed to the stationary reference frame (using the stator flux angular position θ_{ψ_s}) and then fed to the SVM block. The implemented SVM is the one previously analyzed in section 2.2.1.2.

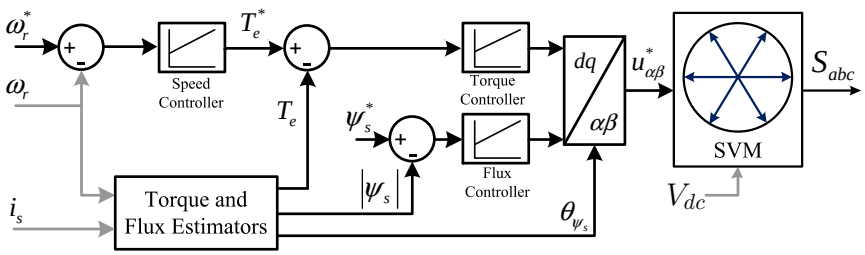

Figure 2.10: Block diagram of the DTC strategy with SVM applied to the PMSG-side converter.

2.3 Control Strategies for the Grid-Side Converter

A control strategy for the grid-side converter aims to control separately active and reactive power, which can be achieved directly, using DPC, or indirectly, using VOC. The main control tasks devoted to the grid-side converter are dc-link voltage control, in order to achieve power balance between the generator and the grid, and reactive power control (power factor control). Inherently, the converter has to ensure synchronization with the grid voltage and high power quality (low current harmonic distortion). Independently of the selected control strategy, the dc-link voltage must be always higher than the amplitude of the sum of the phase-to-phase grid voltage and the voltage drop in output filter.

The following sections present the operating principles of VOC and DPC, and their implementation for the grid-side converter of the PMSG drive.

2.3.1 Vector Control - Voltage Oriented Control

Once again, it is worth reinforcing that vector control is based on the use of the dq reference frame, in the particular case of VOC, the choice of a reference frame rotating at the angular speed of the grid voltage with the q-axis aligned with the grid voltage space vector (equations (2.17) and (2.18)) allows decoupled control of active and reactive power. Consequently, the calculation of active and reactive powers:

$$p_g = \frac{3}{2}\left(u_{gd}i_{gd} + u_{gq}i_{gq}\right) \tag{2.35}$$

$$q_g = \frac{3}{2}\left(u_{gq}i_{gd} - u_{gd}i_{gq}\right) \tag{2.36}$$

is simplified when imposing $u_{gd} = 0$:

$$p_g = \frac{3}{2}u_{gq}i_{gq} \tag{2.37}$$

$$q_g = \frac{3}{2}u_{gq}i_{gd} \tag{2.38}$$

As a result, the active power is controlled independently through i_{gq} , while the reactive power is controlled through i_{gd} .

The required information about the phase angle of the grid voltage to perform the coordinate transformation can be obtained by means of a phase locked loop (PLL).

2.3.1.1 VOC with HCC

The block diagram of the VOC strategy with HCC is depicted in Figure 2.11, which brings to the fore its simplicity as well as its similarity with the RFOC startegy with HCC. Thus, the implementation issues involved have already been discussed in section 2.2.1.1. In addition, it is worth noting that i^*_{gd} is fixed to zero in order to imposed an unity power factor ($q_g = 0$), while i^*_{gq} is generated by the dc-link voltage controller.

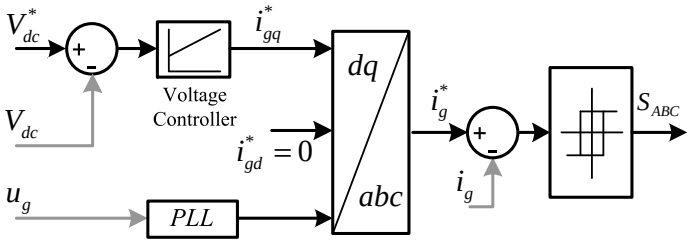

Figure 2.11: Block diagram of the VOC strategy with HCC applied to the grid-side converter.

2.3.1.2 VOC with SVM

All the advantages of the inclusion of SVM as voltage modulator (section 2.2.1.2) are also desired for the control of the grid-side converter. Therefore, when performing the control in the dq frame, PI controllers are the most adopted solution. However, when the control is performed in the stationary $\alpha\beta$ frame, resonant and deadbeat controllers assume prominence because PI controllers are inefficient in removing the steady-state error [67]-[68].

Figure 2.12 shows the block diagram of the VOC strategy with SVM. As a consequence of the cross coupling verified in equations (2.17) and (2.18), feed-forward compensation terms should be included to improve the control dynamic performance:

$$u^c_d = -\omega_g L_f i_{gq} \tag{2.39}$$

$$u^c_q = \omega_g L_f i_{gd} + u_{gq} \tag{2.40}$$

2.3.1.3 VOC with Vector-based HCC

Vector-based HCC [69]-[71], has been proposed to overcome some disadvantages of the conventional HCC – high switching frequency and band violation up to twice of the defined bandwidth due to interphases dependency – but retaining its main advantages – simplicity of implementation, fast transient response, and parameters independence. Concerning HCC practical implementation for SSTPCs, the conventional HCC requires three two-level hysteresis comparators, so that each one controls a converter phase. Thus, the state change in one phase - that leads to a different voltage

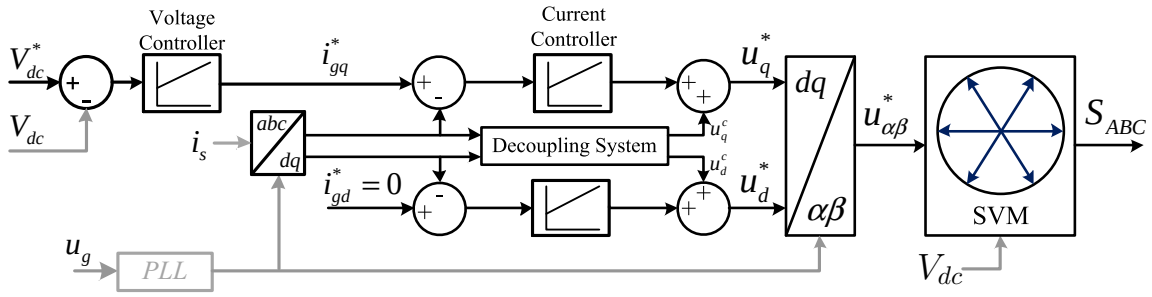

Figure 2.12: Block diagram of the VOC strategy with SVM applied to the grid-side converter.

space vector - does not take into account its influence on the remaining phases (interphases dependency). On the other hand, the vector-based HCC in the stationary reference frame uses multilevel hysteresis comparators (three or four levels) and a switching table to control the currents in $\alpha\beta$ axes. Thus, a voltage space vector is selected in the switching table accordingly to the current error information of all phases, eliminating the issue of interphases dependency and reducing significantly the switching frequency. Additionally, the use of null voltage vectors permits further decrease of the switching frequency. The basic principle of the vector-based HCC can be illustrated through the equivalent mathematical model of the grid-side in the stationary reference frame (equations (2.15) and (2.16)). Therefore, by neglecting the filter resistance (R_f), it is obtained that the sign of the current variation only depends on the applied voltage space vector and the grid voltage:

$$\frac{di_{g\alpha}}{dt} = \frac{1}{L}\left(u_{c\alpha} - u_{g\alpha}\right) \tag{2.41}$$

$$\frac{di_{g\beta}}{dt} = \frac{1}{L}\left(u_{c\beta} - u_{g\beta}\right) \tag{2.42}$$

Accordingly, with the knowledge of the eight available voltage vectors (2.28), the switching table can be easily formulated, since the current increase (or decrease) in a given axis (α or β) is accomplished by applying a voltage vector with the respective axis component positive (or negative). For instance, if i_α is intended to increase a voltage vector with positive u_α should be selected (V_1,V_2,V_6). Adopting three-level hysteresis comparators [70], the switching table (Table 2.4) can be formulated by substituting (2.28) in (2.41) and (2.42).

A three-level hysteresis controller can be implemented by adding the output of two two-level comparators (2.19) with different widths for the hysteresis bands, which leads to three possible actions: decrease (0), hold (1) or increase (2) the respective current component. As a result, the choice of the voltage vector is unequivocal only if both three-level comparators have as output 0 or 2. If a comparator assumes the output 1 (indicating a null voltage vector as the best suited), the control priority is attributed to the other comparator. Finally, a null voltage vector is only selected when both comparators assume the output 1. The number of commutations are reduced by selecting the null vector according to the previously applied vector, namely, the selection of V_0 is preceded

Table 2.4: Vector-based HCC switching table for the SSTPC.

		dI_β		
		0	1	2
dI_α	0	V_5 (001)	V_4 (011)	V_3 (010)
	1	V_5/V_6	V_0/V_7 (000)/(111)	V_2/V_3
	2	V_6 (101)	V_1 (100)	V_2 (110)

by the application of V_0, V_1,V_3 or V_5.

The block diagram of the VOC strategy with vector-based HCC applied to the grid-side converter is shown in Figure 2.13.

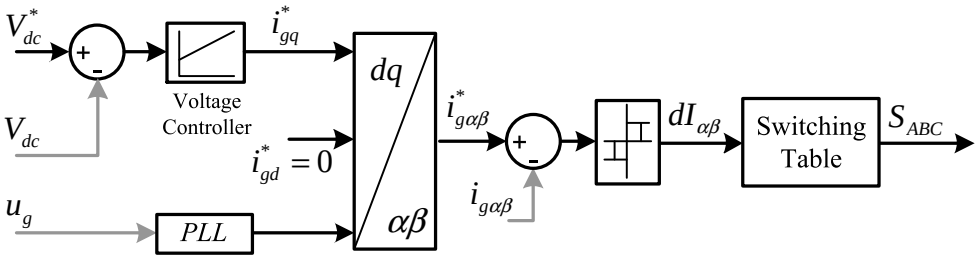

Figure 2.13: Block diagram of the VOC strategy with vector-based HCC applied to the grid-side converter.

2.3.2 Direct Power Control

The conventional DPC [32] is based on the idea of directly and independently controlling the active and reactive powers by selecting the optimum voltage vector in a switching table, in a similar way to the conventional DTC. As a consequence, the main features of the conventional DTC are common to the table-based DPC, namely, simplicity, fast dynamic response, variable switching frequency, and the requirement of a high sampling frequency. A noticeable variety of approaches have been proposed seeking to improve the performance of DPC [33],[72]-[75], largely driven by the growing need to connect renewable sources to the grid. Some examples are the introduction of virtual flux estimation with the aim to avoid voltage sensors (sensorless operation) [76], the use space vector modulation (SVM) in order to operate the converter with constant switching frequency [77] and predictive approaches [78]-[79].

In order to formulate enhanced switching tables for DPC of a SSTPC, the instantaneous power derivatives were used in [72]-[73]. This approach is adopted in this thesis to deduce the switching tables proposed for the DPC. Using the pq theory, for a three-phase three-wire system, the grid active and reactive instantaneous powers are calculated from the instantaneous grid voltages ($u_{g\alpha}$, $u_{g\beta}$) and currents ($i_{g\alpha}$, $i_{g\beta}$) in $\alpha\beta$ axes as follows:

$$p_g = u_{g\alpha} i_{g\alpha} + u_{g\beta} i_{g\beta} \tag{2.43}$$

$$q_g = u_{g\beta} i_{g\alpha} - u_{g\alpha} i_{g\beta} \tag{2.44}$$

Therefore, the instantaneous power derivatives are given by:

$$\frac{dp_g}{dt} = u_{g\alpha} \frac{di_{g\alpha}}{dt} + i_{g\alpha} \frac{du_{g\alpha}}{dt} + u_{g\beta} \frac{di_{g\beta}}{dt} + i_{g\beta} \frac{du_{g\beta}}{dt} \tag{2.45}$$

$$\frac{dq_g}{dt} = u_{g\beta} \frac{di_{g\alpha}}{dt} + i_{g\alpha} \frac{du_{g\beta}}{dt} - u_{g\alpha} \frac{di_{g\beta}}{dt} - i_{g\beta} \frac{du_{g\alpha}}{dt} \tag{2.46}$$

To obtain the derivatives of the grid voltages and currents, the grid voltages can be expressed as:

$$u_{g\alpha} = u_{c\alpha} - R_f i_{g\alpha} - L_f \frac{di_{g\alpha}}{dt} = U_g \sin(\omega t) \tag{2.47}$$

$$u_{g\beta} = u_{c\beta} - R_f i_{g\beta} - L_f \frac{di_{g\beta}}{dt} = -U_g \cos(\omega t) \tag{2.48}$$

that results from considering the equivalent circuit of the system grid connection and assuming perfectly balanced three-phase sinusoidal grid voltages. From (2.47) and (2.48) current and voltage derivatives are then easily obtained:

$$\frac{di_{g\alpha}}{dt} = \frac{u_{c\alpha} - u_{g\alpha} - R_f i_{g\alpha}}{L_f};\ \frac{di_{g\beta}}{dt} = \frac{u_{c\beta} - u_{g\beta} - R_f i_{g\beta}}{L_f} \tag{2.49}$$

$$\frac{du_{g\alpha}}{dt} = -\omega u_{g\beta};\ \frac{du_{g\beta}}{dt} = \omega u_{g\alpha} \tag{2.50}$$

Finally, by substituting (2.49) and (2.50) in (2.45) and (2.46), neglecting R_f and considering both p_g and q_g as null (initial conditions), the instantaneous power derivatives can be simply expressed as a function of the filter inductance and grid and converter voltages:

$$\frac{dp_g}{dt} = -\frac{1}{L_f} \left({u^2}_{g\alpha} + {u^2}_{g\beta} - u_{g\alpha} u_{c\alpha} - u_{g\beta} u_{c\beta} \right) \tag{2.51}$$

$$\frac{dq_g}{dt} = \frac{1}{L_f} \left(u_{g\beta} u_{c\alpha} - u_{g\alpha} u_{c\beta} \right) \tag{2.52}$$

By substituting each voltage vector that the SSTPC can synthesize (Table 2.1) in equations (2.51) and (2.52), the instantaneous active and reactive power variations caused by the application of each voltage vector over a period of the grid voltage are shown in Figure 2.14.

The block diagram of the DPC strategy is shown in Figure 2.15. In order to control the dc bus

voltage and the grid power factor, dc bus voltage and reactive power references are imposed (V_{dc}^*, q_g^*) by the user, while the active power reference (p_g^*) is generated through a proportional-integral controller. The power errors are restricted by employing two-level hysteresis comparators and selecting the optimum voltage vector in a switching table, according to the grid voltage vector angle. The hysteresis comparators outputs (dP, dQ) define whether the instantaneous active and reactive powers are intended to increase (+) or decrease (-). Since the switching table is intended to choose which converter voltage space vector leads, in a more effective way, to the desired variation in the instantaneous powers, a comprehensive analysis of the power derivatives forced by each converter voltage vector (Figure 2.14) allows us to define the most appropriate switching table. First of all, the complex plane is divided into six sectors according to the grid voltage vector angle (as illustrated in Figure 2.14 and identically to the sector definition for the DTC - Figure 2.9). Then, for each sector, an appropriate vector is selected to conduct the action defined by the hysteresis controllers output. However, in some cases, the desired action can be accomplished by different voltage vectors with different absolute values of the respective power derivatives. For instance, in sector I, both V_3 and V_4 can be chosen in order to decrease p_g and increase q_g (-dP/+dQ). Table 2.5 is formulated selecting always the voltage vector responsible for the largest variation in p_g, i.e., the voltage vector associated to the highest absolute value of the active power derivative. Taking advantage of the above mentioned redundancy, modified switching tables can be adopted [73].

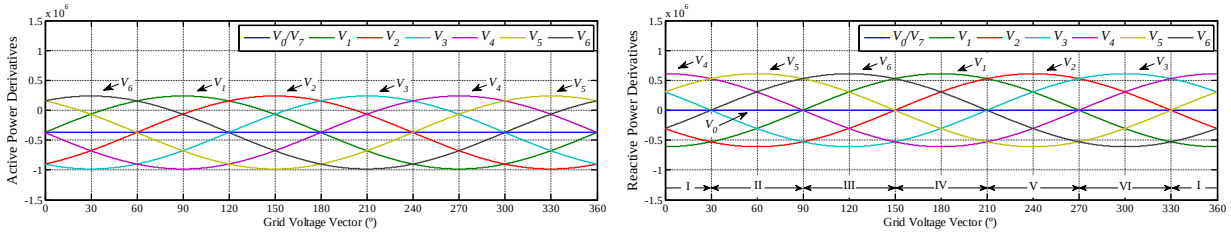

Figure 2.14: Instantaneous active and reactive power derivatives imposed by the SSTPC.

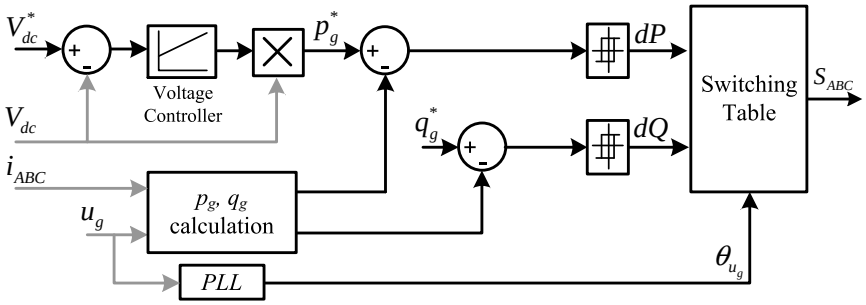

Figure 2.15: Block diagram of the DPC strategy applied to the grid-side converter.

Table 2.5: DPC switching table for the SSTPC.

dP	dQ	Sector					
		I	II	III	IV	V	VI
+	+	V_5	V_6	V_1	V_2	V_3	V_4
	-	V_6	V_1	V_2	V_3	V_4	V_5
-	+	V_3	V_4	V_5	V_6	V_1	V_2
	-	V_2	V_3	V_4	V_5	V_6	V_1

2.4 Simulation Results

Simulation results are presented in order to validate and evaluate the studied control strategies from a theoretical point of view. The simulations were carried out in the Matlab/Simulink environment, in association with the SimPowerSystems blockset software toolbox. Throughout this thesis a reduced number of simulation results are presented, only accompanied by a succinct analysis. This option was made in order to minimize the repetition of results, leaving space for a detailed analysis of the experimental results.

Concerning the commissioning of the different control strategies, widths of the hysteresis bands and carrier frequency for the SVM need to be defined. For HCC-based strategies the hysteresis band is imposed to 0.2 A ($B_{hcc} = 0.2$ A), i.e., approximately 2% of the rated current. For the conventional DTC, torque and flux hysteresis bands were set to 2% and 1% of the torque and flux rated values, respectively. For the DPC, hysteresis bands corresponding to 0.5% of the PMSG rated power were chosen. A carrier frequency of 5 kHz was selected for the SVM.

The following simulation results were obtained at a grid phase-to-phase voltage of 135 V and a reference dc link voltage of 250 V. The PMSG parameters are given in Appendix A - Table A.1.

2.4.1 Control Strategies for the PMSG-Side Converter

Figure 2.16 shows the PMSG phase currents when applying the four control strategies considered for the PMSG-side converter, under the same operating conditions: a reference speed of 600 rpm and a load torque equivalent to 50% of the PMSG rated torque.

It can be seen that all the control strategies are able to control the generator speed providing approximately sinusoidal phase currents. However, it is clear that the generated harmonic content varies, with RFOC with HCC and Conventional DTC presenting larger current ripple. As expected, when employing SVM a better performance under steady-state operation is achieved, since current harmonic distortion is reduced leading to a smother torque production.

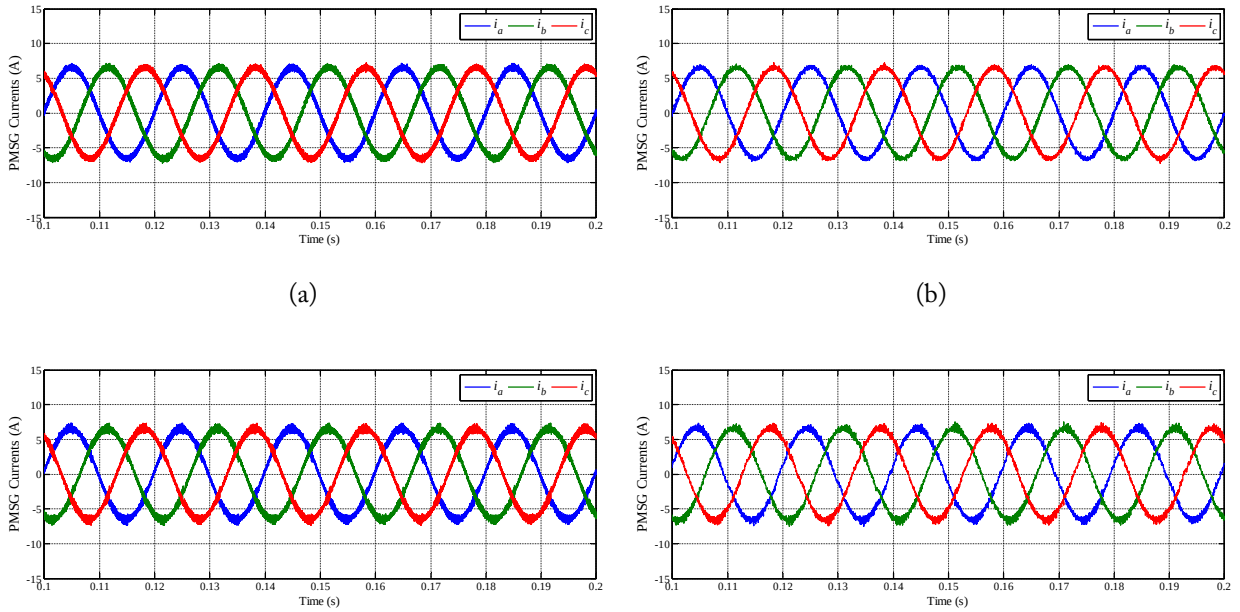

Figure 2.16: Simulation results regarding the time-domain waveforms of the PMSG phase currents with: (a) RFOC strategy with HCC, (b) RFOC strategy with SVM; (c) Conventional DTC strategy; (d) DTC strategy with SVM.

2.4.2 Control Strategies for the Grid-Side Converter

Regarding the control for the grid-side converter, the time-domain waveforms of the grid phase currents for the four control strategies considered are presented in Figure 2.17, assuming a reference speed of 1200 rpm and a load torque equivalent to 75% of the PMSG rated torque (51% of the PMSG rated mechanical power). For all the control strategies, it is verified that the dc-link voltage is kept constant at the reference value of 250 V and, simultaneously, approximately unit power factor and sinusoidal currents are obtained. Although the performance of the control strategies seems to be very similar by analyzing the phase currents in Figure 2.17, a deeper analysis of the corresponding THD values and active and reactive power oscillation elucidates that SVM tends to provide lower ripple.

2.5 Experimental Results

The experimental setup is described in section 2.1.2 and all the control parameters are identical to those presented in section 2.4. The PMSG parameters are given in Appendix A - Table A.1.

In order to quantify the distortion of the phase currents the Total Harmonic Distortion (THD) is used, according to IEEE standards [80]:

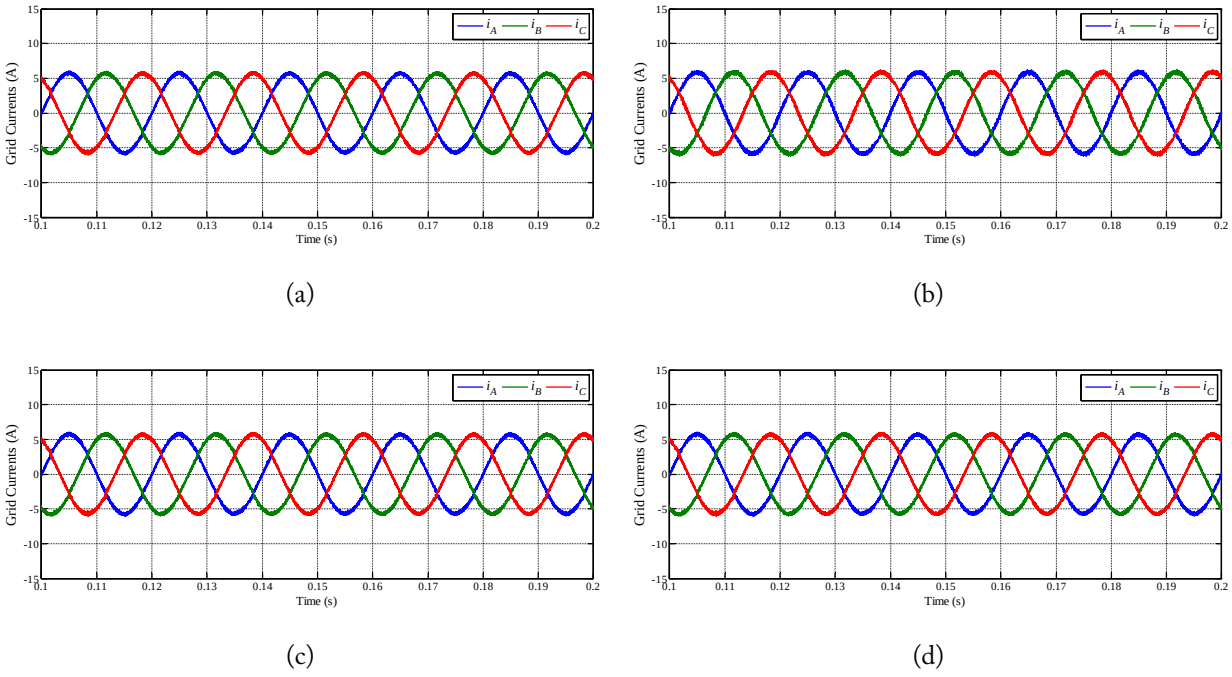

Figure 2.17: Simulation results regarding the time-domain waveforms of the grid phase currents with: (a) VOC strategy with HCC; (b) VOC strategy with SVM; (c) VOC strategy with vector-based HCC; (d) DPC strategy.

$$\text{THD} = \frac{\sqrt{\sum_{n=2}^{\infty} X_{h_{rms}}^2}}{X_{1_{rms}}} \times 100\% \tag{2.53}$$

where $X_{h_{rms}}$ and $X_{1_{rms}}$ stand for the rms values of the h order harmonic and fundamental component, respectively. Concerning the three phases, an equivalent THD is considered:

$$THD_{eq} = \frac{\sqrt{THD_a^2 + THD_b^2 + THD_c^2}}{3} \tag{2.54}$$

The oscillation of a given quantity can be evaluated by the Total Waveform Oscillation (TWO):

$$\text{TWO} = \frac{\sqrt{X_{e_{\text{rms}}}^2 - X_{e_{\text{dc}}}^2}}{|X_{e_{\text{dc}}}|} \times 100\% \tag{2.55}$$

where $X_{e_{rms}}$ and $X_{e_{dc}}$ stand for the *rms* and average values, respectively.

Finally, efficiency values obtained through the precision power analyzers Yokogawa WT3000 are compared.

2.5.1 Control Strategies for the PMSG-Side Converter

The experimental results in Figure 2.18 reproduce the operating conditions of the simulation results in Figure 2.16, with a reference speed of 600 rpm and a load torque equivalent to 50% of the PMSG rated torque. Additionally, the electromagnetic torque is estimated by using equation (2.33), allowing a more detailed performance evaluation by taking into account that the torque production is desired to be as smooth as possible.

Therefore, in good agreement with the simulation results, RFOC and DTC strategies with SVM present low torque oscillation, verified by the TWO values obtained (Table 2.6). As a consequence, they are characterized by a slower dynamic response. Despite showing higher torque ripple, RFOC with HCC and conventional DTC have a quite acceptable performance under steady-state operation and are endowed with extremely fast dynamic response and robustness, thus, being considered viable schemes for controlling a PMSG drive.

Efficiency measurements of the generator-side (overall efficiency of the PMSG and converter) are presented in Figure 2.19. The PMSG efficiency tends to increase with the load increase, which is generally verified in Figure 2.19. These results also elucidate that higher PMSG efficiency values are reached with SVM-based strategies (DTC with SVM and RFOC with SVM), mainly due to the application of voltages with lower rms values, reducing the iron losses. Concerning the converter efficiency, it appears to have less influence on the overall efficiency, since its range of variation is expected to be shorter (1% to 2% of variation was verified for the considered load torque variation from 25% to 100% of the rated load torque). However, it should be noticed that the converter efficiency is strongly linked to the switching losses, accordingly variable switching control strategies may show higher or lower efficiency than SVM whether the switching frequency is lower or higher, respectively.

Table 2.6: Electromagnetic torque TWO values.

Control Strategy	Torque TWO
RFOC HCC	16.9 %
RFOC SVM	10.6 %
Conventional DTC	16.7 %
DTC SVM	10.9 %

2.5.2 Control Strategies for the Grid-Side Converter

In addition to grid phase currents, Figure 2.20 shows the instantaneous active and reactive powers. In this experiments, a reference speed of 1200 rpm and a load torque equivalent to 75% of the PMSG rated torque were imposed, corresponding to approximately 50% of the PMSG rated

power. From Figure 2.20, it can be concluded that all the control strategies allow the grid-side converter to shape approximately sinusoidal currents and to achieve unit power factor (null instantaneous reactive power). With the aim to analyze the performance of the control strategies in more detail, the grid current THD values and the active power TWD values can be calculated (Table 2.7). Table 2.7 indicates that the lowest current THD is reached with VOC with HCC and DPC strategies. In comparison to the VOC with HCC, VOC with vector-based HCC leads to higher current distortion as a consequence of the switching frequency reduction, which has a positive influence on the converter efficiency (Figure 2.21). Strangely, SVM shows the highest THD value. Despite being an unexpected result, this can be explained by the dSPACE hardware limitations, which force a fully digital implementation of the voltage modulator (SVM) and, consequently, the gate signals generation through digital outputs. In this case, the minimum pulse width is equal to the sampling period (T_s), resulting in a low resolution of the PWM outputs and extra harmonic content in the generated voltages.

Regarding the active power oscillation, the TWO values in Table 2.7 are practically in concordance with the THD values. DPC is the exception, since it presents the highest active power TWO value and a low THD value. The low current THD results from a good control of the reactive power, which compensates the increased ripple in the active. The high active power ripple is a direct consequence of the selected switching table (section 2.3.2), which uses the voltage vectors associated to the largest variation of the active power.

Table 2.7: Grid current THD values and active power TWO values.

Control Strategy	Grid Current THD	Active Power TWO
VOC HCC	2.2 %	5.6 %
VOC SVM	6.1 %	7.3 %
VOC VHCC	5.1 %	6.7 %
DPC	4.1 %	8.3 %

To finish with, the efficiency results for the grid-side converter under four distinct operating conditions are presented in Figure 2.21, corresponding to the overall efficiency of the converter and the output filter. The highest efficiency values are presented by the VOC strategy with vector-based HCC, due to a lower switching frequency. Thus, it is proved that an effective reduction of the switching frequency can be achieved by replacing HCC with vector-based HCC, with a significant influence on the converter efficiency. The lowest efficiency is presented by the VOC with HCC and DPC strategies, being more noticeable for low load levels due to the increase of the switching frequency and harmonic distortion.

2.6 Summary

After having briefly presented the state of the art in electrical drives for wind energy conversion systems and control strategies for power converters, some of the most widely used control strategies for two-level voltage source converters were selected taking into account their suitability for controlling the power converters of a PMSG drive as well as for being later on endowed with fault-tolerant capabilities.

Therefore, for each converter side (PMSG- and grid-sides), four control strategies were presented, focusing their basic operating principles, real-time implementation issues, advantages and drawbacks.

The presented simulation and experimental results verify the application feasibility of all the control strategies and their main features. In short, SVM-based strategies tend to present a better performance under steady-state operation, minimizing the ripple of the controlled quantities and enhancing efficiency. However, they are outperformed by variable switching frequency strategies in simplicity of implementation and tuning, robustness to the variation of the system parameters, and dynamic response.

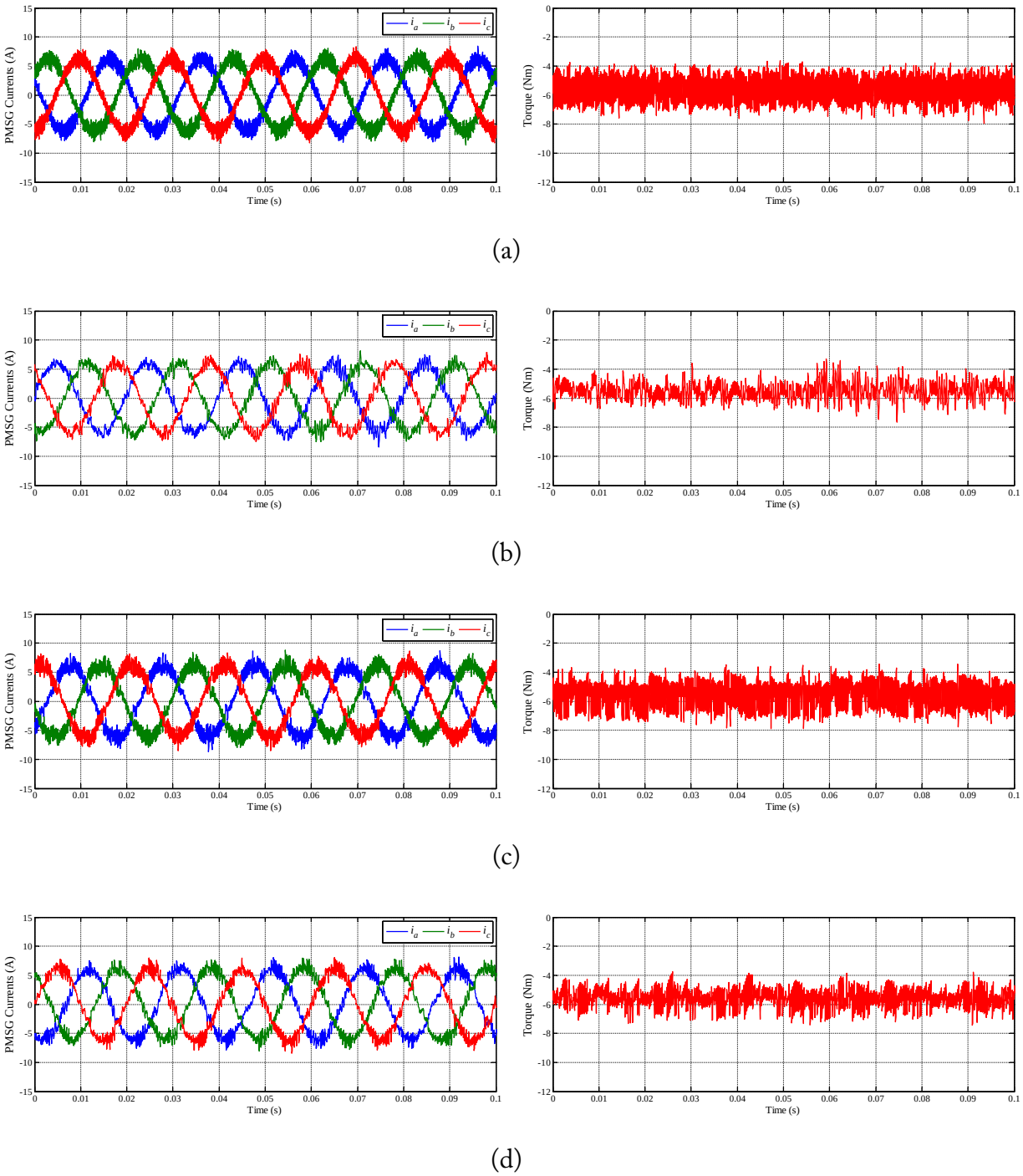

Figure 2.18: Experimental results regarding the time-domain waveforms of the PMSG phase currents and estimated electromagnetic torque with: (a) RFOC strategy with HCC; (b) RFOC strategy with SVM; (c) Conventional DTC strategy; (d) DTC strategy with SVM.

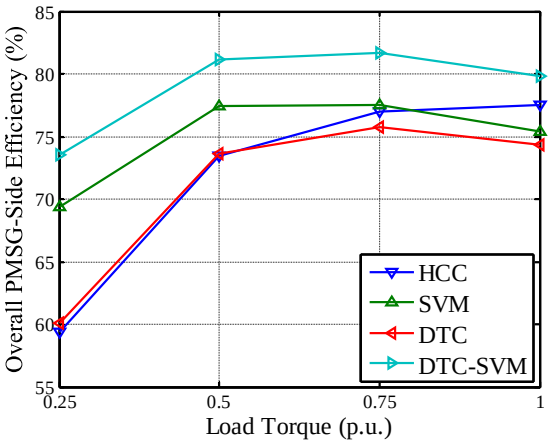

Figure 2.19: Experimental results regarding the overall efficiency of the PMSG-side system (PMSG + Converter) at a reference speed of 1200 rpm for four distinct load levels (25%, 50%, 75% and 100% of the PMSG rated torque) with: (HCC) RFOC strategy with HCC; (SVM) RFOC strategy with SVM; (DTC) Conventional DTC strategy; (DTC-SVM) DTC strategy with SVM.

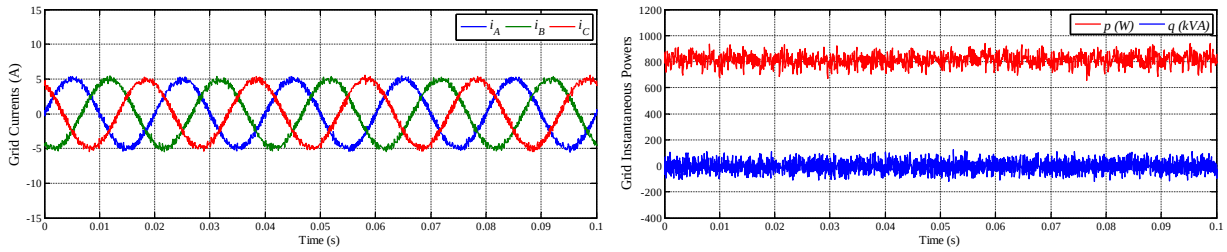

(a)

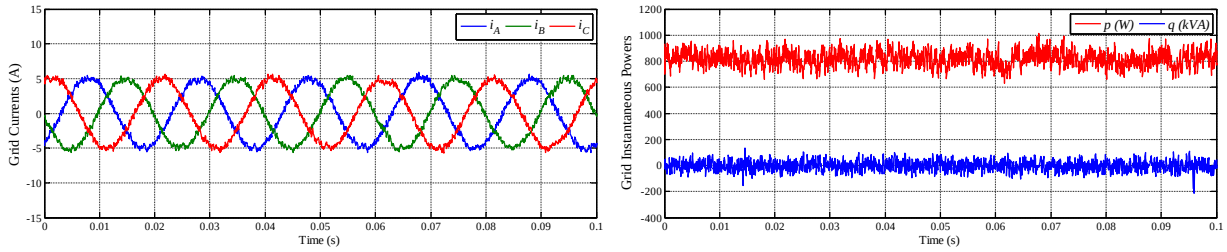

(b)

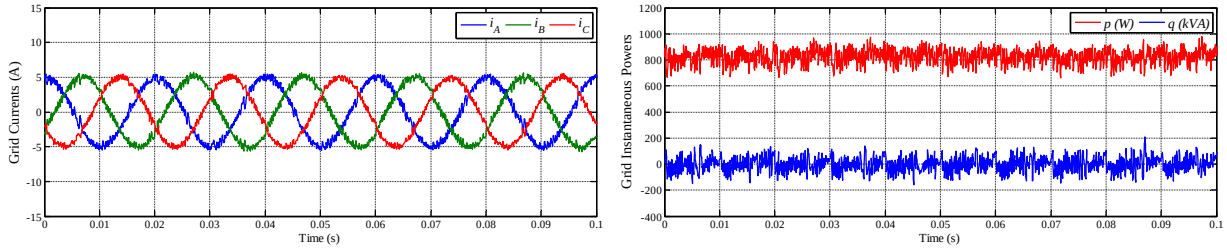

(c)

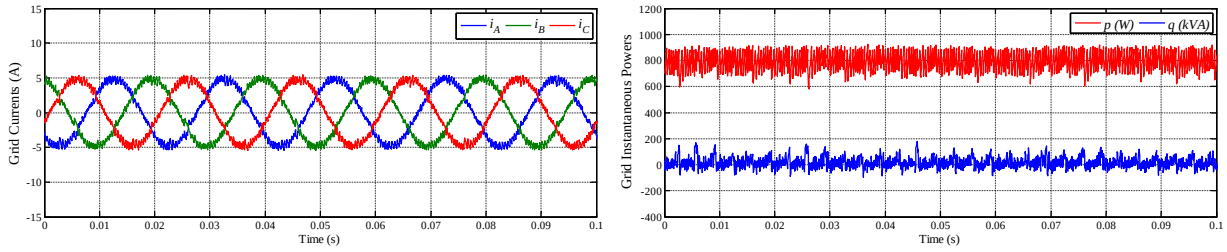

(d)

Figure 2.20: Experimental results regarding the time-domain waveforms of the grid phase currents and the instataneous active and reactive powers with: (a) VOC strategy with HCC; (b) VOC strategy with SVM; (c) VOC strategy with vector-based HCC; (d) DPC strategy.

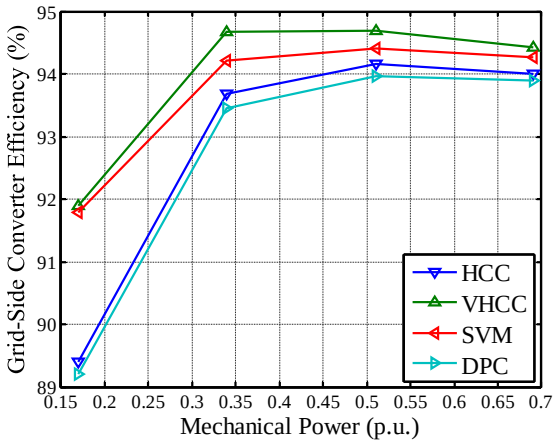

Figure 2.21: Experimental results regarding the overall efficiency of the grid-side system (converter + output filter) for four distinct load levels (17%, 34%, 51% and 69% of the PMSG rated mechanical power) with: (HCC) VOC strategy with HCC; (SVM) VOC strategy with SVM; (VHCC) VOC strategy with vector-based HCC; (DPC) DPC strategy.

Chapter 3

Faulty Operation Analysis

Electric drives are prone to suffer several kinds of electrical faults, namely, those affecting the following components: machine, capacitors, power converter, and sensors. Among them, power converter faults are the most frequent, which are usually related to semiconductor or control circuit failures. This is reported in some statistical studies [8], [13], where such faults are attributed to 60% of the power devices failures (26% of printed circuit boards failures, 21% of semiconductor failures, and 13% of solder failures). As an elucidative example, the investigation on converter failures in wind turbines reported in [12] found that in a sample of four replaced converters, three presented non-switching IGBTs (with healthy diodes) and one presented faulty sensors (current and temperature sensors).

The knowledge of a system behavior in the presence of faults is extremely important in order to evaluate its design, protections and fault-tolerant capabilities. Moreover, the drive faulty operation analysis permits to determine the fault severity, to select suitable quantities for fault diagnosis, and to assess the extent of hardware and software modifications for allowing post-fault operation without endangering the drive.

Therefore, taking into consideration that the study of the drive faulty operation mandatorily precedes the improvement of its reliability, several studies are found in the literature regarding the fault analysis of different variable speed drives.

Faults modes such as ground faults and power switch short-circuit and open-circuit faults in an induction motor drive are investigated in [81]. It is pointed out that open-circuit faults may not trigger typical drive protections and that they cause pulsating torque.

Several fault conditions, including power-switch open-circuit faults, were analyzed in [82] considering the flux weakening operation of a PMSM drive. The analysis of a PMSM drive response to a single phase open-circuit fault was addressed in [83]-[84]. A theoretical analysis of several fault types is presented in [85], establishing fault models. A fault model for switch open-circuit faults is also derived in [86]. The impact of inverter power switch open-circuit faults in the overall performance of a PMSM drive was addressed in vector controlled and direct controlled PMSM

drives [87]-[90]. It was concluded that the drive operates with a degraded performance and that a single phase open-circuit fault has a greater negative impact on the drive performance than a single power switch open-circuit failure.

As far as the back-to-back converter is concerned, a few works have been published. The performance of a back-to-back and a matrix converter induction motor drive under the presence of open-circuit faults is compared in [91]; the results show that the back-to-back converter is less affected due to the presence of the dc-link bank. It is also verified that a fault in the rectifier stage is less severe than a fault in inverter stage. A performance evaluation of a PMSG drive under several open-circuit fault combinations is reported in [92], concluding that the faults in one converter practically do not influence the variables on the other converter and that an open-circuit fault in an IGBT of the grid-side converter is more severe than one in the PMSG-side. The influence of the modulation technique's choice under faulty operation is investigated in [93], comparing HCC and SV-PWM. It was verified that the HCC presents considerable lower electromagnetic torque oscillation in the presence of a open-circuit fault in the PMSG-side converter. It was also concluded that a software reconfiguration could be sufficient to achieve post-fault operation of the PMSG-side converter, whereas for the grid-side converter a hardware reconfiguration would be certainly required.

The analysis of current measurement errors in vector-controlled AC motor drives is presented in [94]-[95]; it is demonstrated that offset and scaling errors lead to torque oscillations at the fundamental stator current frequency and twice the fundamental stator current frequency, respectively. As a consequence, the performance of the speed control is deteriorated and unnecessary mechanical stress is imposed, which can lead to the failure of several machine components, such as bearings, shafts and gear transmissions.

This section intends to introduce the fault types under study in this thesis - power switch open-circuit faults and current sensor faults - and their impact on the PMSG drive operation. Simulation and experimental results under faulty operating conditions are presented with the aim to motivate the development of fault diagnostic methods and fault-tolerant PMSG drives. Taking this into account an extensive analysis of the drive performance under faulty operating conditions is not the goal. This can be found in [93], [96] through the analysis of several performance parameters, such as the current rms and distortion values, power factor, dc link voltage and electromagnetic torque oscillation, and the overall drive efficiency.

3.1 Power Switch Open-Circuit Faults

An open-circuit fault is considered to result from the inability of the power switch to turn on, which may occur as a consequence of a semiconductor or gate control circuit failure. However, it is always considered that the antiparallel diode remains connected and healthy. Thus, IGBT

open-circuit faults are introduced by removing their corresponding gate command signals. All the simulation and experimental results presented next are obtained under the same operating conditions, an open-circuit fault in IGBT R1 (PMSG-side converter) or IGBT I1 (grid-side converter), a reference dc-link voltage of 250 V, a reference speed of 600 rpm, and a load torque equivalent to 50% of the PMSG rated torque.

3.1.1 Simulation Results

The PMSG phase currents in the presence of an open-circuit fault in IGBT R1 of the PMSG-side converter are shown in Figure 3.1, for the four considered control strategies. As a consequence of the fault, the currents become unbalanced and a sinusoidal current system cannot be achieved. Naturally, such distorted current system leads to undesirable electromagnetic torque oscillation, which is later on verified by means of experimental results. In addition, it can be seen that the RFOC strategy with HCC is the one less affected by the fault (Figure 3.1a), such tolerance to the fault results from the independent control of each converter leg, indicating that this control strategy may allow acceptable post-fault operation with reduced modifications. It is worthwhile emphasizing that the PMSG-side converter operates as rectifier, thus, the diodes assume an important rule. Despite the fact that IGBT R1 is unable to turn on, the phase a current flows in positive direction due to the path offered by the diode R2 (non-controlled operation of phase a).

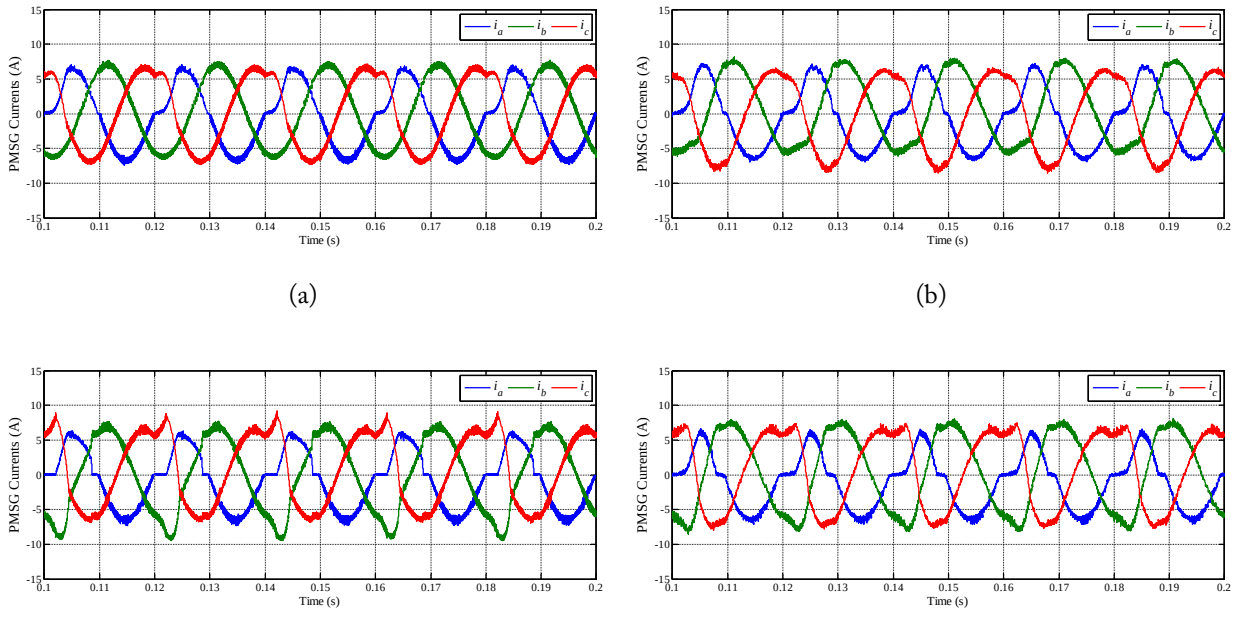

Figure 3.1: Simulation results regarding the time-domain waveforms of the PMSG phase currents with an open-circuit fault in IGBT R1 of the PMSG-side converter: (a) RFOC strategy with HCC; (b) RFOC strategy with SVM; (c) Conventional DTC strategy; (d) DTC strategy with SVM.

Figure 3.2 shows the grid phase currents in the presence of an open-circuit fault in IGBT I1 of the grid-side converter, for the four control strategies considered. As opposed to the fault effect under rectifier operation, since the grid-side converter operates as an inverter, there is no alternative path for the phase A current flow in the positive direction, so phase A current assumes only negative values. Consequently, under faulty operation, the converter generates a highly distorted and unbalanced current system, and the current rms values of the healthy phases increase significantly in order to keep the control of the dc-link voltage and the power flow between the dc-link and the grid. For the considered operating conditions, the converter is still able to control the dc-link voltage, in spite of considerable oscillations.

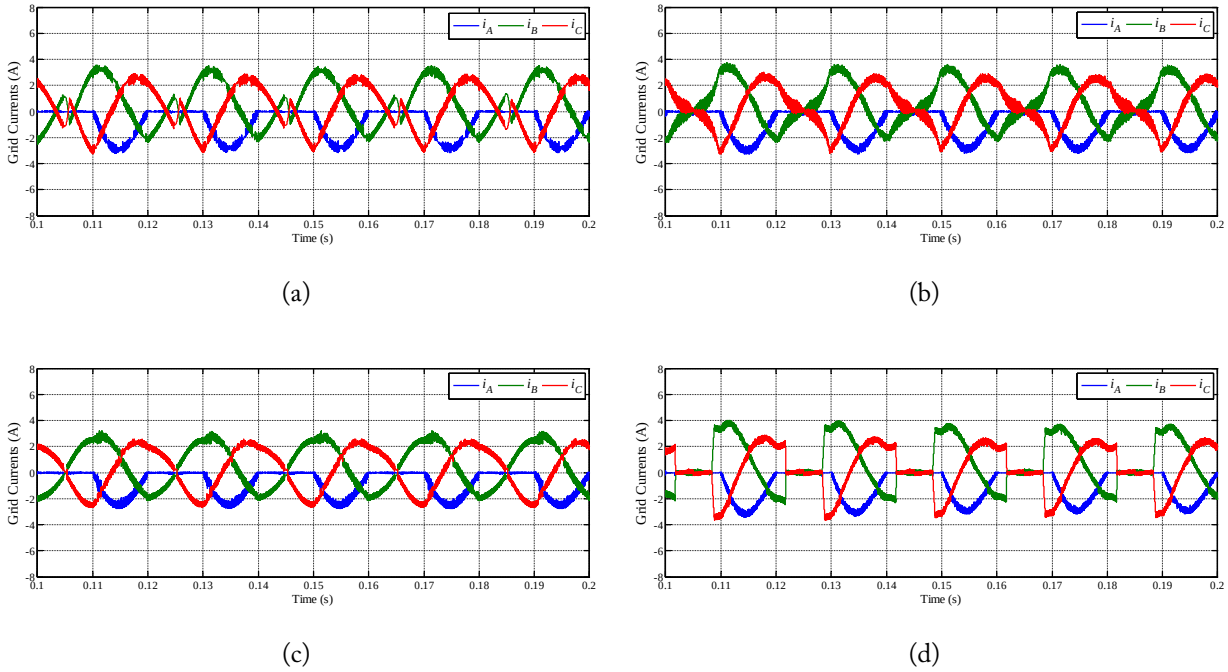

Figure 3.2: Simulation results regarding the time-domain waveforms of the grid phase currents with an open-circuit fault in IGBT I1 of the grid-side converter: (a) VOC strategy with HCC; (b) VOC strategy with SVM; (c) VOC strategy with vector-based HCC; (d) DPC strategy.

3.1.2 Experimental Results

The experimental results obtained for an open-circuit fault in IGBT R1 of the PMSG-side converter are shown in Figure 3.3, including the estimated electromagnetic torque. The time-domain waveforms of the PMSG phase currents are in good agreement with the simulation results (Figure 3.1). For the considered operating conditions, the speed control is always maintained, despite the oscillations forced by the produced electromagnetic torque. Analysing the electromagnetic torque in Figure 3.3, a pulsating behavior at the fundamental frequency of the phase currents is observed for all the control strategies. However, the amplitude of the torque oscillation differs between control

strategies, with the strategies with SVM showing the largest oscillation amplitudes. The conventional DTC shows the electromagnetic torque with less pronounced oscillating nature, which is a consequence of directly controlling the torque, allowing to counteract the oscillations introduced by the fault.

Figure 3.4 shows the experiments in the presence of an open-circuit fault in IGBT I1 of the grid-side converter, for the four control strategies considered. Once again in good agreement with the simulation results, despite being possible to keep the dc-link voltage close to its reference, the phase A current assumes only negative values and the required sinusoidal and balanced three-phase current system cannot be obtained. Accordingly, and similarly for all the control strategies, both active and reactive powers present a high oscillating behavior at the grid fundamental frequency. Such operating conditions may endanger the converter, due to the excessive stress imposed to the healthy power switches, and the power system voltage stability, due to the large power variations.

3.2 Current Sensor Faults

The considered current sensor faults are those that lead to a null sensor output, corresponding to the worst case scenario of a scaling error. Such faults may result from sensor disconnection or supply failure. Current sensor faults are introduced by setting the sensor output to zero via software. It is worth noting that each phase has a current sensor. All the simulation and experimental results presented next are obtained under the same operating conditions, a current sensor fault in phase a (PMSG-side converter) or phase A (grid-side converter), a reference dc-link voltage of 250 V, a reference speed of 600 rpm, and a load torque equivalent to 50% of the PMSG rated torque. The following results do not include the RFOC strategy with HCC and the VOC strategy with HCC, because high current spikes are generated in response to a current sensor fault, triggering the converter over-current protections. Moreover, due to similarity of results between all the other control strategies only two case scenarios for each converter side are selected for illustrating the effects of a current sensor fault, namely, RFOC with SVM and conventional DTC for the PMSG-side converter, and VOC with vector-based HCC and DPC for the grid-side converter.

3.2.1 Simulation Results

Figures 3.5 and 3.6 show the phase currents of the PMSG- and grid-side converters with a current sensor fault in phase a and phase A, respectively. It is immediatly concluded that the effects of a current sensor fault are identical for all the case scenarios. It shoul be noted that the presented phase currents correspond to their actual values, while the control system sees the current of the faulty phase equal to zero ($i_a = 0$ or $i_A = 0$).

Taking the comparison of Figures 3.5 and Figure 2.16 (simulation results under normal operation) as an example, it is confirmed that, as a response to the fault, the current amplitude of the

healthy phases remains practically unchanged, while the current amplitude of the faulty phase is $\sqrt{3}$ times higher. Furthermore, the phase displacement is changed, with the displacement of 120º between phases not being respected. Therefore, based on these results, it is concluded that a current sensor fault leads to the increase of the current in the faulty phase and subsequent increase of the losses.

3.2.2 Experimental Results

Figure 3.7 presents the PMSG phase currents and estimated electromagnetic torque with a current sensor fault in phase a of the PMSG-side converter, for the RFOC strategy with SVM and the conventional DTC strategy. The estimated electromagnetic torque shows the main problem introduced by a current sensor fault; large torque oscillations at twice the fundamental frequency of the phase currents are introduced, which may increase the stress in the mechanical components drastically. To better understand the control system response, the electromagnetic torque estimated by the control system with the erroneous information from the faulty current sensor is shown in Figure 3.8 for the conventional DTC strategy (corresponding to Figure 3.7b). Figure 3.8 shows that, from the control system point of view, an approximately constant torque is achieved with its amplitude reduced by a given factor (when compared to the normal operation), which, indeed, does not correspond to the actual torque (Figure 3.7b). It is known that the same current space vector obtained with three phase currents displaced by 120º can be obtained with two phase currents displaced by 60º with their amplitude increased by a factor of $\sqrt{3}$ if the neutral point is available [97]. Accordingly, the control system forces the currents of the healthy phases to be displaced by 60º, but there is lack of need for increasing their amplitudes. Thus, it is easy to deduce that the estimated electromagnetic torque appears to be constant and with a reduced amplitude. In fact, the actual current of phase a is different from zero ($i_a = -i_b - i_c$) and a current space vector with oscillating modulus is generated, leading to an oscillating torque. Naturally, in order to maintain the speed control, the average value of the developed torque has to be the same under normal and faulty operating conditions.

In addition to the increase of the phase A current amplitude, Figure 3.9 shows that a current sensor fault in the grid-side converter leads to high oscillations of both active and reactive powers at twice the grid fundamental frequency.

3.3 Summary

In this chapter the PMSG drive operation in the presence of open-circuit faults and current sensor faults was analyzed. From this analysis, it was verified that typical converter protections (such as over-current and dc link over-voltage or under-voltage protections) are not triggered by the fault types under study, allowing the drive to maintain its operation with a degraded performance.

However, such operating conditions lead to noticeable torque or power oscillations, which might endanger the whole system and cause secondary faults due to excessive stress imposed over electrical and mechanical components.

An open-circuit fault has different impacts on the drive behavior, depending on the affected converter side as well as on the employed control strategy. A fault in PMSG-side converter (rectifier stage) is less severe than a fault in grid-side converter (inverter stage), since the diodes offer an alternative path for the current flow. On the other hand, with a fault in a given phase of the grid-side converter, the current is only able to flow in one direction, which means that the current becomes null during half-cycle.

In relation to a current sensor fault, it has similar repercussions in both converter sides independently of the control strategy, with the exception of the HCC that does not tolerate this fault condition. Thus, HCC should not be employed to achieve a fault-tolerant PMSG drive with regards to current sensor faults.

Regarding the effects of both fault types in the electromagnetic torque and grid powers, a single open-circuit fault introduces oscillations at the fundamental frequency of the phase currents, whereas a current sensor fault introduces torque and power oscillation at twice the fundamental current frequency.

The conducted analysis also intends to obtain useful information for fault diagnosis and remedial procedures for post-fault operation. Concerning fault diagnosis, current-based techniques appear as straightforward approaches, since the phase currents are noticeably affected. Despite this, an open-circuit fault in the PMSG-side converter might be difficult to diagnose, due to its small impact on the phase currents. Finally, concerning post-fault operation, the lack of path for the current flow as a consequence of an open-circuit fault in the grid-side converter indicates that there is a need for hardware reconfiguration. On the other hand, for an open-circuit fault in the PMSG-side converter, control reconfiguration may provide an acceptable performance under post-fault operation. Provided that there is a current sensor per phase, a simple software reconfiguration also permits proper operation after the occurrence of a current sensor fault.

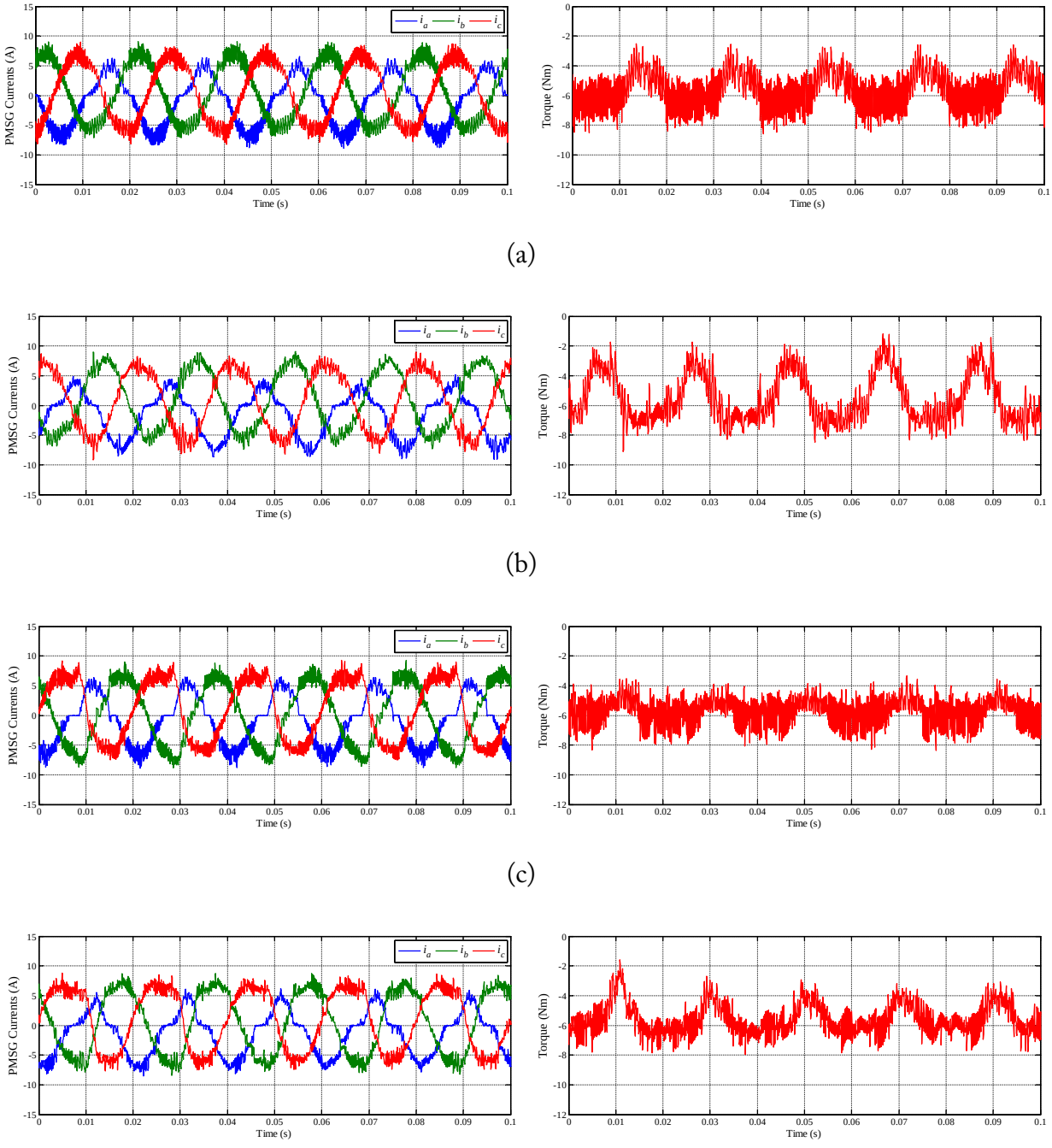

Figure 3.3: Experimental results regarding the time-domain waveforms of the PMSG phase currents and estimated electromagnetic torque with an open-circuit fault in IGBT R1 of the PMSG-side converter: (a) RFOC strategy with HCC; (b) RFOC strategy with SVM; (c) Conventional DTC strategy; (d) DTC strategy with SVM.

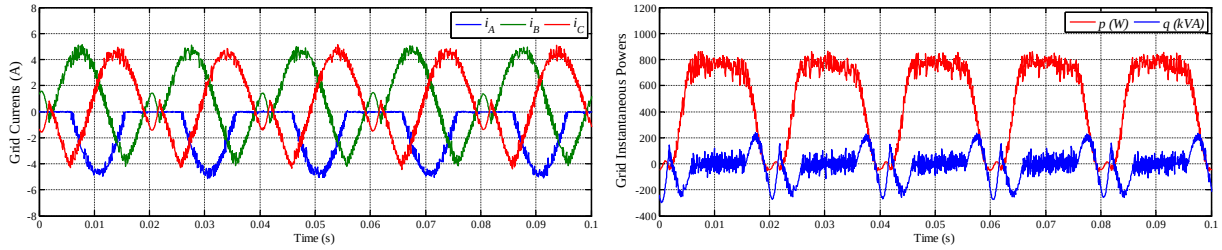

(a)

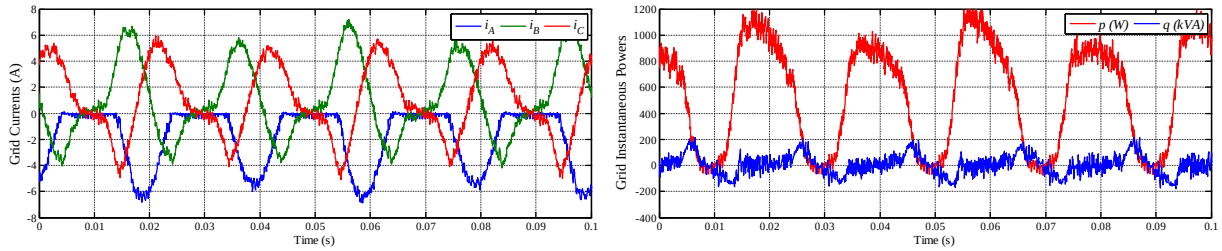

(b)

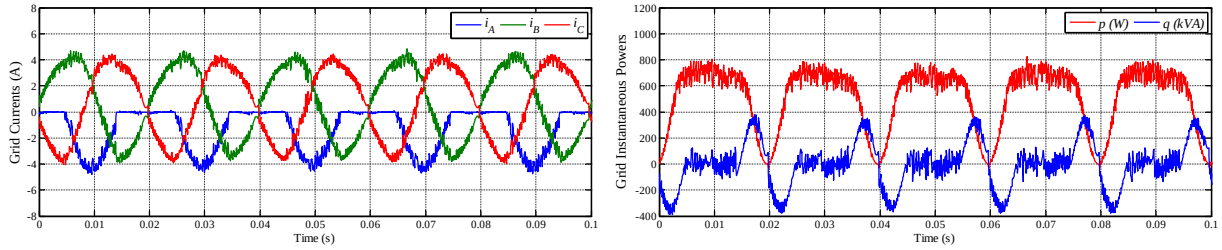

(c)

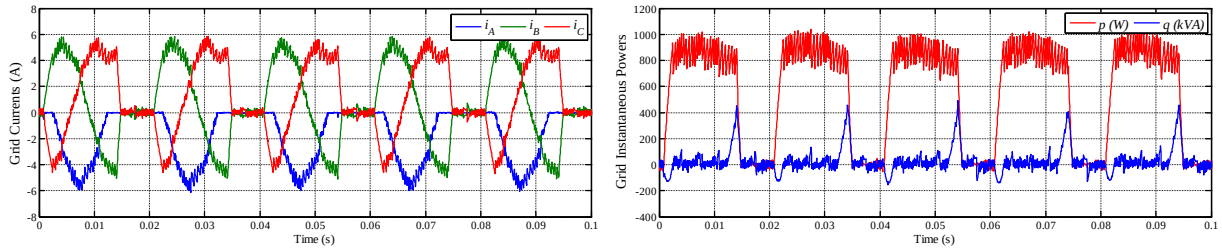

(d)

Figure 3.4: Experimental results regarding the time-domain waveforms of the grid phase currents and the instataneous active and reactive powers with an open-circuit fault in IGBT I1 of the grid-side converter: (a) VOC strategy with HCC; (b) VOC strategy with SVM; (c) VOC strategy with vector-based HCC; (d) DPC strategy.

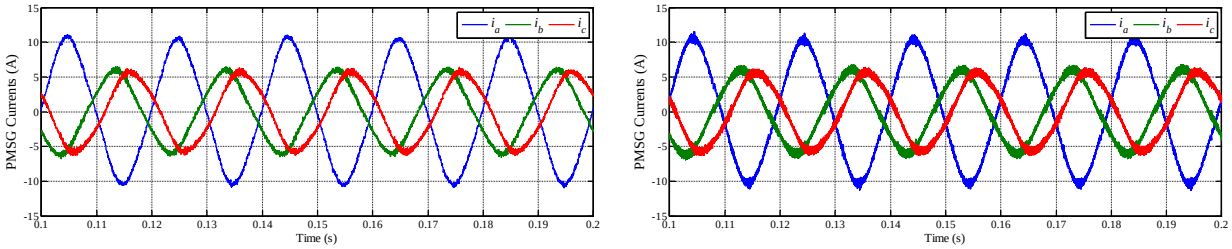

(a) (b)

Figure 3.5: Simulation results regarding the time-domain waveforms of the PMSG phase currents with a current sensor fault in phase a of the PMSG-side converter: (a) RFOC strategy with SVM; (b) Conventional DTC strategy.

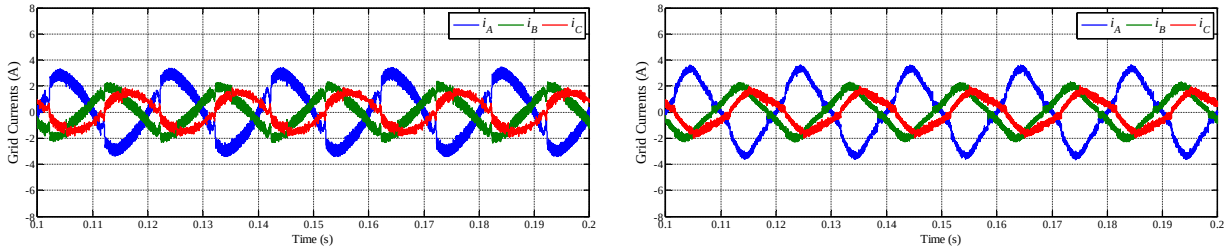

(a) (b)

Figure 3.6: Simulation results regarding the time-domain waveforms of the grid phase currents with a current sensor fault in phase A of the grid-side converter: (a) VOC strategy with vector-based HCC; (b) DPC strategy.

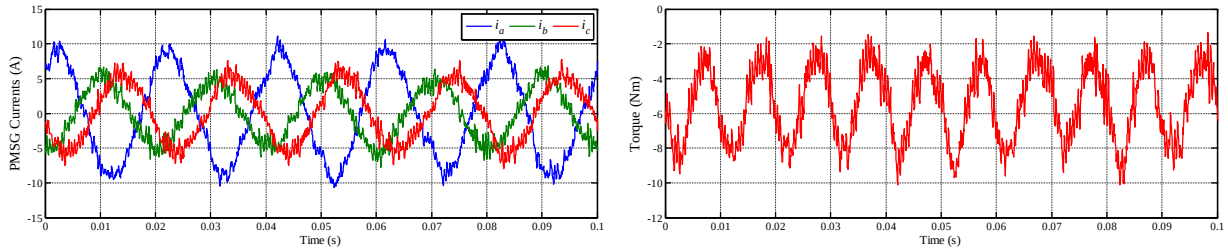

(a)

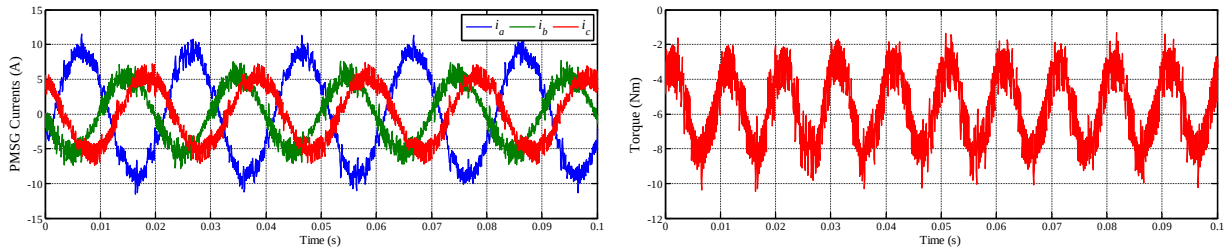

(b)

Figure 3.7: Experimental results regarding the time-domain waveforms of the grid phase currents and estimated electromagnetic torque with a current sensor fault in phase a of the PMSG-side converter: (a) RFOC strategy with SVM; (b) Conventional DTC strategy.

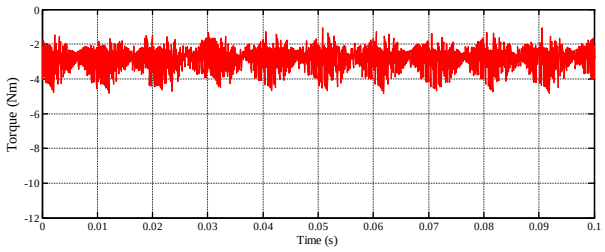

(a)

Figure 3.8: Experimental results regarding the electromagnetic torque estimated by the control system with a current sensor fault in phase a of the PMSG-side converter, for the conventional DTC strategy.

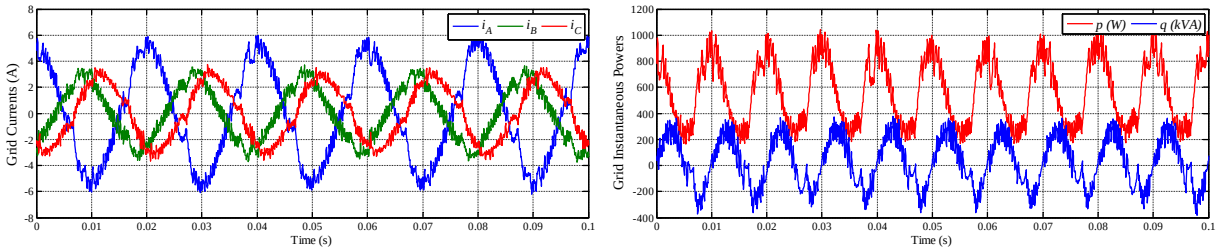

(a)

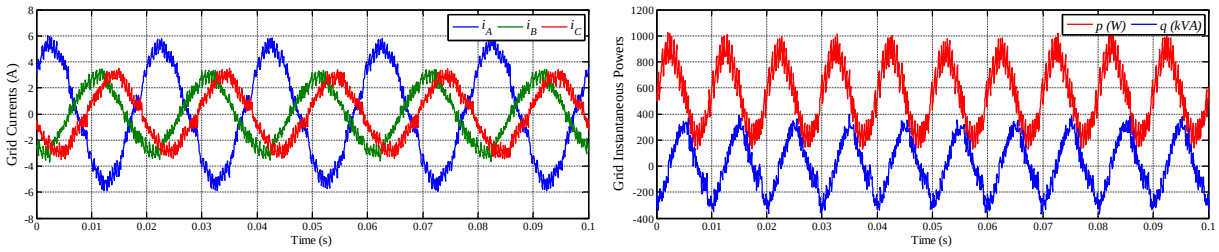

(b)

Figure 3.9: Experimental results regarding the time-domain waveforms of the grid phase currents and the instataneous active and reactive powers with a current sensor fault in phase A of the grid-side converter: (a) VOC strategy with vector-based HCC; (b) DPC strategy.

Chapter 4

Fault Diagnosis

Reliability and availability of wind conversion systems have gained attention, being seen as key parameters to assess their economic viability. Consequently, the condition monitoring and fault diagnosis of these systems is considered an effective tool to detect incipient failures and generate early fault alarms [98], assuming a paramount importance in reducing operational and maintenance costs and permitting to reduce the wind energy cost.

Faults in a wind turbine are mainly imputed to rotor blades, pitch and yaw control, bearings, gearbox, shaft, generator and power converter. After identifying the components that are prone to fail, it is necessary to choose suitable quantities to be monitored, which are commonly the vibration, torque, lubrication oils, temperature, acoustic emission, and electrical quantities [99]. Although mechanical sensors have been widely used for condition monitoring of wind turbines [100]-[101], they are expensive, sometimes difficult to install, and their signal analysis is computationally demanding. Hence, electrical quantities are currently suggested for a cost-effective condition monitoring strategy [102]-[104].

Power converters tend to be a great contributor to failure rates in modern wind turbines [8], with semiconductor and control circuit faults being the most common ones. Power switch failures can be broadly classified as short-circuit faults and open-circuit faults. Such faults can result from excessive electrical and thermal stress, lifting of the bonding wires or a failure in the gate control circuits. Typical power converter protections include protection against short-circuits, but they do not include protection against open-circuit faults. This means that open-circuit faults can remain undetected for an extended period of time, leading to potential secondary faults in the converter or in other drive components. According to the lack of converter self-diagnostic capabilities, an industry-based survey shows the current industry dissatisfaction with the reliability of power electronics monitoring methods [14].

Converters fault diagnosis is essential in electrical drives as well as in wind turbine applications, not only to avoid catastrophic consequences, but also to trigger remedial actions in a fault-tolerant system, and to adequately schedule maintenance operations. However, fault diagnostic techniques

are rarely integrated into the fault-tolerant systems proposed in the literature [49],[105], being often assumed that proper fault diagnosis can be performed, which is not always true and, in practice, invalidates the adoption of the fault-tolerant system.

Despite its importance, converters fault diagnosis in wind turbine applications has only recently been addressed in the literature. As far as the doubly fed induction generator (DFIG) is concerned, some diagnostic techniques as well as system reconfigurations were proposed for both open-circuit faults [106]-[111], and sensor faults [112]-[114]. Regarding open-circuit fault diagnosis in DFIG drives, a voltage-based approach was proposed to perform the fault detection in several fault-tolerant systems [106]-[108], achieving fast detection times thanks to FPGA-based implementation. Diagnostic methods based on the normalized average currents together with some enhancements in order to solve the problem of false alarms around DFIG synchronous speed operation were suggested in [109]-[111]. Regarding converter fault diagnosis in PMSG drives for wind turbine applications, there is little research in this field, which is one of the main contributions of this thesis.

4.1 Power Switch Open-Circuit Fault Diagnosis

Most adopted approaches for open-circuit faults are classified as signal-based, namely, current-[118]-[136] or voltage-based [137]-[143], using these quantities for diagnostic purposes. Current-based methods have been widely proposed since they are independent of the system parameters and they do not require additional sensors. On the other hand, voltage-based techniques, despite some advantages, such as fast detection and an inherent higher immunity to false alarms, are often excluded because they require additional hardware, sometimes with high performance requirements (voltage sensors and ADCs), therefore increasing the system cost and complexity. Different approaches have also been addressed, such as IGBT collector-emitter or gate voltage monitoring [13],[115], allowing predictive maintenance, or model-based schemes [116]-[117], but additional voltage measurements and high computational demand are some disadvantages of these proposals.

Reviewing the current-based proposals in the literature, the current Park's Vector Approach was proposed in [118] as a fault diagnostic tool for converter faults, requiring very complex pattern recognition algorithms which are not suitable for integration into a drive controller. However, many fault diagnostic methods rely on this first strategy. The Average Current Park's Vector Approach was introduced in [119], in which converter power switch faults are detected when the vector modulus is different from zero, and the faulty switch is localized by the vector phase. Further works based on the Park's Vector Approach were also published, using probabilistic and fuzzy-based techniques for the boundaries definition between the different patterns in [120]-[121], or including the derivative of the vector phase for the detection procedure [122].

The analysis of the current space vector was performed in [123] by the slope of the vector tra-

jectory and the vector instantaneous frequency. A modified slope method [124] was proposed as an extension of the previous one, concerning the fault diagnosis of two simultaneous faulty switches.

The major drawbacks of the previous methods are the load dependence and the sensitivity to transients, which result in low diagnostic effectiveness for low load levels and false alarms during transients. In an attempt to overcome these weaknesses, the normalized average currents were suggested and refined in [125]-[127] with the current fundamental component value being the first choice for normalization quantity. In [127], an extension of the normalized average currents was proposed using the currents average absolute values as normalization quantities. Furthermore, by the calculation of additional variables, the robustness of the fault diagnostic method was enhanced and the detection of multiples faults was achieved.

A diagnostic method based on the calculation of the errors of the normalized currents average absolute values was proposed in [128]-[130], where independence of the mechanical operating conditions and immunity to false alarms were demonstrated by choosing the Park's Vector modulus as normalization quantity. A method based on the calculation of the reference current errors average values was suggested in [131]-[132], performing a quick diagnosis by means of a simple algorithm.

A method combining a detection method based on the derivative of the current Park's Vector phase with a localization method based on the currents polarity was firstly proposed in [133]-[134] for fault diagnosis of a grid-connected converter in a PMSG drive for with turbine applications, and later it was also successfully applied to a variable speed motor drive in [135]. Thanks to the detection method, an excellent immunity to false alarms is achieved, which has been found to be crucial for converter diagnosis under generating mode [134].

Fault diagnosis in brushless dc motor drives has also been performed by using a simple current-based approach in [136].

Regarding voltage-based diagnostics, a direct comparison between the measured voltages and the reference values is employed in [137], where discretization, quantization and dead time errors have to be minimized through a calibration procedure, and a time-delay is introduced to prevent false alarms. An FPGA-based implementation of a voltage-based approach is proposed in [107] and detection times shorter than $10\mu s$ are reported, by using the error between the measured and the estimated pole voltages. However, several problems arise in its practical implementation. The switching pattern used for the voltage estimation is not available in a DSP PWM generation, and a time criterion is also used, whose tuning depends to a very high degree on the hardware performance. Thus, to accomplish the fault diagnostic, semiconductors and respective drivers' characteristics have to be taken into account, and voltage sensors and ADCs with a very high frequency bandwidth are required, drastically increasing their cost. Alternatively, a low-cost proposal based on an indirect voltage measurement is obtained by using high-speed photocouplers [138]-[139]. However, once again the direct comparison between the switching states and the photocouplers output requires well defined time-delays, which are dependent on the nature of the power con-

verter. Besides this, aging of the semiconductors - which leads to longer switching times - is not considered. All these issues have inspired some recent works [140]-[143]. In [140] the errors influence is attenuated, but voltage measurements are required, and the diagnostic is not achieved below a minimal load level. Despite avoiding voltage measurements, the technique proposed in [141] is highly dependent on the parameter estimation, which invalidates its practical implementation. A proposal that intends to solve both problems was firstly proposed in [142] and improved in [143]. These are voltage-based approaches – without voltage sensors – for closed-loop controlled PWM AC voltage source converters. They use the information contained in the reference voltages available from the control system, and the robustness against false alarms is improved by employing a voltage observer. It has been proven that the algorithm is insensitive to parameter errors.

In summary, current-based approaches have to carefully consider the issue of false alarms and load dependence for an effective and reliable diagnostic. On the other hand, the performance of voltage-based ones is mainly related to the use of extra hardware and the ability to accommodate the inherent errors.

Reviews and surveys can be found in the literature regarding the analysis and performance comparison of several fault diagnostic methods for power switches open-circuit faults in voltage source inverters[144]-[145].

Due to the high dynamic behavior of a wind conversion system and its variable speed operation when employing a PMSG drive, fault diagnostic methods for this application must have a high immunity against the issue of false alarms resulting from load and speed transients. Hence, taking into account the specific features of this application and that reliable diagnosis is vital in order to trigger remedial procedures in fault-tolerant systems, the diagnostic methods for open-circuit faults reported in the literature were not appropriate for integration into the controller of a fault-tolerant PMSG drive.

Accordingly, in this thesis six fault diagnostic algorithms capable of assuring a high diagnostic effectiveness and immunity to false alarms are developed and applied to both converters of a PMSG drive. It is worth noting that sometimes the algorithms need to be combined in order to obtain the desired performance. With the aim of using quantities already available from the main control system, and therefore avoiding the use of additional sensors, the converter phase currents and reference voltages are suitable choices exploited in next sections.

4.1.1 Current Park's Vector Phase

The Current Park's Vector Phase (CPVP) method [134] is proposed for fault detection; it is applied to the output currents of both power converters of the PMSG drive, differing only in the threshold value definition. This method is based on the current Park's Vector Approach, which concentrates the information contained in the three-phase currents in just one vector, and it uses the derivative of the vector phase as its basic principle. The Park's Vector components i_d and i_q are

calculated according to the following equations:

$$i_d = \sqrt{\frac{2}{3}} i_a - \frac{1}{\sqrt{6}} i_b - \frac{1}{\sqrt{6}} i_c \tag{4.1}$$

$$i_q = \frac{1}{\sqrt{2}} i_b - \frac{1}{\sqrt{2}} i_c \tag{4.2}$$

where i_a, i_b and i_c are the phase currents instantaneous values. The Park's vector phase angle θ is given by:

$$\theta = \tan^{-1}\left(\frac{i_q}{i_d}\right) \tag{4.3}$$

Under normal steady-state operation, the Park's Vector rotates with a frequency equal to the currents frequency and the vector magnitude is approximately constant. Hence, the known current Park's Vector representation is a circle.

During a load transient, the vector magnitude changes, whereas the vector phase is practically not affected. The vector phase keeps varying uniformly from -180º to 180º in each period, with the same frequency. Nevertheless, during a speed transient, the frequency of the generator current Park's Vector phase changes, following the generator speed.

On the other hand, as a consequence of an open-circuit fault, the vector phase does not vary uniformly during one period, presenting deformations that can be detected by the derivative of the absolute vector phase, since its absolute value suffers a sudden reduction, tending to zero. Therefore, the fault detection algorithm makes use of the derivative of the absolute vector phase to detect a fault and to prevent the misinterpretation of transients, through the generation of a reliable fault alarm signal. Additionally, in order to accomplish this goal under speed transients, the generator speed information will be necessary to define the detection threshold, which is also available from the main control system.

Figure 4.1 illustrates the detection method formulation and the necessary mathematical considerations to obtain a detection variable with a nearly constant value under normal steady-state operating conditions, D, and which decreases below a certain threshold value when a fault occurs. Preceding the derivative calculation, a modulus function is applied to the vector phase (Figure 4.1b), obtaining a signal which varies between 0º and 180º (Figure 4.1c). Thus, its derivative alternates between positive and negative values (Figure 4.1d), both with the same absolute value. Finally, a modulus function is also applied to the derivative output and the detection variable, d, is obtained (Figure 4.1e):

$$d = \left| \frac{d}{dt} |\theta| \right| \tag{4.4}$$

Low-pass filters (LPF) have to be implemented in order to attenuate the high-frequency noise

presented in the phase currents and the noise introduced by the derivative operator. Concerning the filter design, the value of the cutoff frequency has to be higher than the rated currents fundamental frequency. A good performance is obtained for a value between three and six times the grid/generator rated frequency. All implemented low-pass filters are first-order filters with a cutoff frequency of 300 Hz, which can be considered a reference value for wind turbine applications (low speed operation) where operating frequencies are generally not higher than 50/60 Hz.

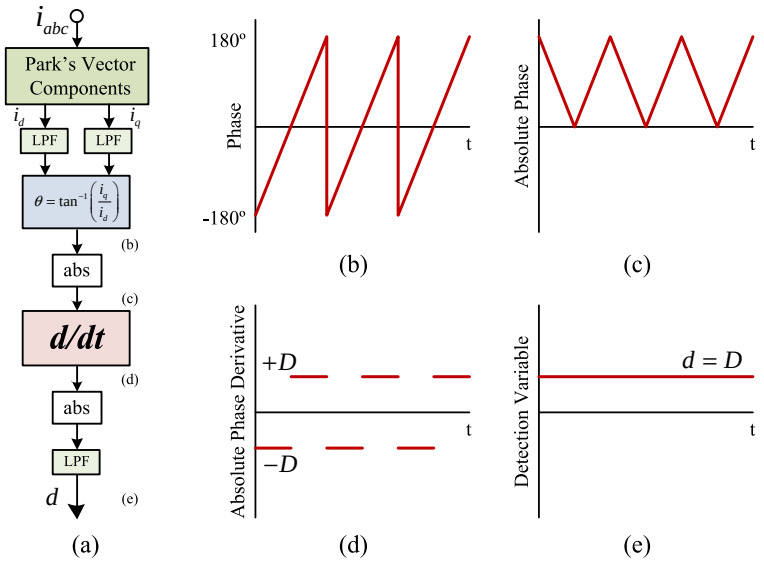

Figure 4.1: (a) Block diagram of the fault detection method; (b) Park's Vector phase; (c) Absolute Park's Vector phase; (d) Derivative of the absolute Park's Vector phase; (e) Detection variable under normal operating conditions.

As mentioned before, under normal steady-state operating conditions, the Park's Vector phase varies with a frequency equal to the currents frequency. Then, the detection variable will be around a constant value, D, proportional to the currents frequency, f, and expressed by:

$$D = 360 \times f \tag{4.5}$$

Therefore, once the grid frequency, f_{Grid}, is practically constant, the detection variable for the grid-side converter has an approximately constant value around D_{Grid}. On the other side, the generator speed is variable, and, as a result, its current frequency f_{PMSG} and, consequently, the detection variable for the generator-side converter are variable too. In the absence of any fault in both converters, the detection variables (d_{Grid} and d_{PMSG}) take values close to:

$$D_{Grid} = 360 \times f_{Grid},\ f_{Grid} = 50Hz \tag{4.6}$$

$$D_{PMSG} = 360 \times f_{PMSG},\ f_{PMSG} = \frac{n \times p}{60} Hz \tag{4.7}$$

where n is the generator mechanical speed, in rpm, and p is the generator number of pole pairs.

When an open-circuit fault occurs, the detection variable corresponding to the faulty converter does not remain close to D, it decreases pronouncedly due to the deformations presented in the vector phase. Thus, the threshold values that allow to perform the fault detection are defined as follows:

$$T_{dGrid} = k_{Grid} D_{Grid};\ T_{dPMSG} = k_{PMSG} D_{PMSG} \tag{4.8}$$

where k_{Grid} and k_{PMSG} correspond to percentage values equal to 0.3 and 0.4, respectively. These values were empirically established in order to accommodate high transients and to perform the fault detection in a wide range of operating conditions. When the detection variable reaches the threshold, the fault alarm is set to on and its state is held.

4.1.2 Current Polarity

The faulty power switches localization on the grid-side converter can be performed by using the Current Polarity (CP) method [134], which is based on the polarity of the grid phase currents. The proposed algorithm is illustrated in the block diagram of Figure 4.2, comprising the fault localization method together with the fault detection method (section 4.1.1). The currents polarity is obtained by determining, for each phase current, the percentages of the fundamental period for which they present positive and negative values. To achieve this goal, each current sample can be classified as non-negative, p_n, or non-positive, n_n, using the following relationships:

$$p_n = \begin{cases} 1,\ if\ i_n > -I_0 \\ 0,\ otherwise \end{cases},\ n_n = \begin{cases} 1,\ if\ i_n < I_0 \\ 0,\ otherwise \end{cases} \tag{4.9}$$

where n = *A, B, C* and I_0 is the threshold value for the current samples classification. Regarding the threshold value I_0, it is selected taking into account a low percentage of the grid rated current. Therefore, a value corresponding to 2.5% was empirically established.

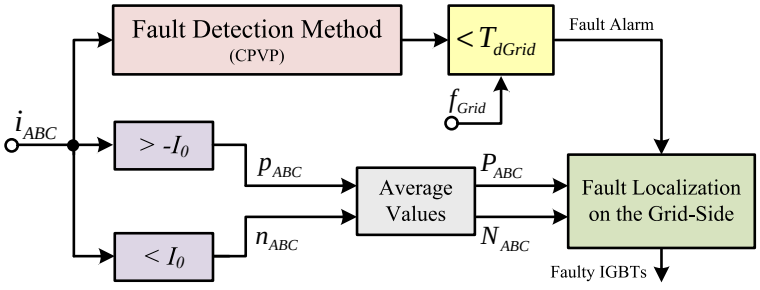

Figure 4.2: Fault diagnostic method for the grid-side converter, combining CPVP and CP methods.

Then, the average values of each p_n and n_n are calculated, resulting in six localization variables (P_n, N_n), one for each power switch. The variable P_n corresponds to the bottom IGBT of phase n,

whereas the variable N_n corresponds to the upper IGBT of phase n. Accordingly and considering the drive system scheme shown in Figure 2.1, the open-circuit faults can be identified using Table 4.1.

Table 4.1: Open-cicuit faults localization on the grid-side converter, using the CP method.

Faulty IGBT	P_A	P_B	P_C	N_A	N_B	N_C
I_1				$>T_{lGrid}$		
I_2	$>T_{lGrid}$					
I_3					$>T_{lGrid}$	
I_4		$>T_{lGrid}$				
I_5						$>T_{lGrid}$
I_6			$>T_{lGrid}$			

Under normal operating conditions, all the localization variables are close to 0.5 because the three-phase currents present a symmetrical sinusoidal waveform. On the other hand, under faulty operating conditions, the phase currents become null during part of the cycle or the entire cycle. In this case, the variables that indicate the faulty IGBTs will assume values close to 1. Therefore, the faulty switches are localized when the corresponding variables exceed the threshold T_{lGrid} established for the fault localization. This value was empirically set to 0.9.

With this method it is possible to identify all the 27 fault modes distinguishable through the grid-side converter phase currents.

4.1.3 Errors of the Normalized Currents Average Absolute Values Using the Park's Vector Modulus as Normalization Quantity

Open-circuit faults in the generator-side converter have a lower impact on the drive performance than faults in the grid-side converter. This fact is well evident in the affected generator phase current, which remains near zero only for a very short period of time as a consequence of a fault, because this converter operates as a rectifier and the current can flow through the diodes. Thus, fault localization is more difficult to perform and the method previously proposed (Current Polarity method) is not feasible in this context.

Therefore, an adaptation of the fault diagnostic technique proposed in [130] (Errors of the Normalized Currents Average Absolute Values - ENCAAV) is suggested [134], in order to achieve the localization of single IGBT open-circuit faults and single-phase open-circuit faults. The block diagram of the fault localization method for the generator-side converter is shown in Figure 4.3. As a first step, the normalized generator phase currents (i_{nN}) are obtained from the generator phase currents (i_n) by using the Park's Vector modulus $\left|\overline{i_s}\right|$:

$$i_{nN} = \frac{i_n}{\left|\overline{i_s}\right|} \tag{4.10}$$

where $n = a,\ b,\ c$. The Park's Vector modulus is defined as:

$$\left|\overline{i_s}\right| = \sqrt{i_d^2 + i_q^2} \tag{4.11}$$

where i_d and i_q components are obtained from the generator phase currents using equations (4.1) and (4.2).

The three diagnostic variables, e_n, are given by:

$$e_n = \xi - f_{PMSG} \int_0^{\frac{1}{f_{PMSG}}} |i_{nN}|\, dt \tag{4.12}$$

with ξ being a constant value approximately equal to 0.5198, corresponding to the average absolute value of the normalized generator phase currents under normal operating conditions. Thus, under normal operation, the variables e_n assume values near zero, whereas under faulty operating conditions, only the variable corresponding to the affected phase takes a positive value higher than the threshold value T_{lPMSG} independently of the generator operating conditions. The threshold value T_{lPMSG} was empirically set to 0.02. Finally, since the diagnostic variables just allow identifying the faulty phase, in order to complete the diagnosis, the normalized average values (I_{nN}) are used to identify the faulty switch and to distinguish a single IGBT open-circuit fault from a single phase open-circuit fault (Table 4.2).

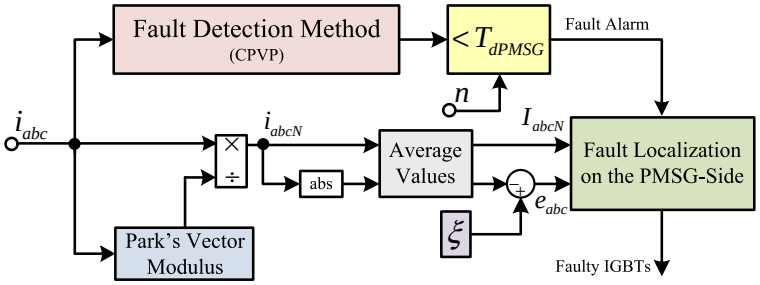

Figure 4.3: Fault diagnostic method for the PMSG-side converter, combining CPVP and ENCAAV-CPVM methods.

Table 4.2: Open-cicuit faults localization on the PMSG-side converter, using ENCAAV-CPVM method.

Faulty IGBTs	e_a	e_b	e_c	I_{aN}	I_{bN}	I_{cN}
R_1	$>T_{lPMSG}$			$<-T_{lPMSG}$		
R_2	$>T_{lPMSG}$			$> T_{lPMSG}$		
R_1, R_2	$>T_{lPMSG}$			*otherwise*		
R_3		$>T_{lPMSG}$			$<-T_{lPMSG}$	
R_4		$>T_{lPMSG}$			$> T_{lPMSG}$	
R_3, R_4		$>T_{lPMSG}$			*otherwise*	
R_5			$>T_{lPMSG}$			$<-T_{lPMSG}$
R_6			$>T_{lPMSG}$			$> T_{lPMSG}$
R_5, R_6			$>T_{lPMSG}$			*otherwise*

4.1.4 Errors of the Normalized Currents Average Absolute Values Using the Instantaneous Maximum Value of the Currents Absolute Values as Normalization Quantity

The instantaneous maximum value of the three-phase currents absolute values is proposed as a new normalization quantity [146], which can achieve a performance similar to the normalization based on the modulus of the Park's Vector (section 4.1.3) but with a lower computational effort.

Therefore, by assuming a perfectly balanced three-phase sinusoidal current system:

$$\begin{cases} i_a = I_m \cos(\omega t + \phi) \\ i_b = I_m \cos\left(\omega t - \frac{2\pi}{3} + \phi\right) \\ i_c = I_m \cos\left(\omega t + \frac{2\pi}{3} + \phi\right) \end{cases} \tag{4.13}$$

where I_m stands for the phase current amplitude, ω for the angular frequency, and ϕ for the initial phase angle; the instantaneous maximum value of the three-phase currents absolute values, under normal operating conditions, can be approximated by the following expression:

$$max\left\{|i_a|, |i_b|, |i_c|\right\} \approx I_m \left[\sqrt{\frac{3}{2}} + \left(1 - \sqrt{\frac{3}{2}}\right) |\cos(3\omega t + \phi)|\right] \tag{4.14}$$

which can be obtained by geometric analysis of Figure 4.4, in which equation (4.14) is plotted, elucidating that it corresponds to a good approximation of $max\left\{|i_a|, |i_b|, |i_c|\right\}$.

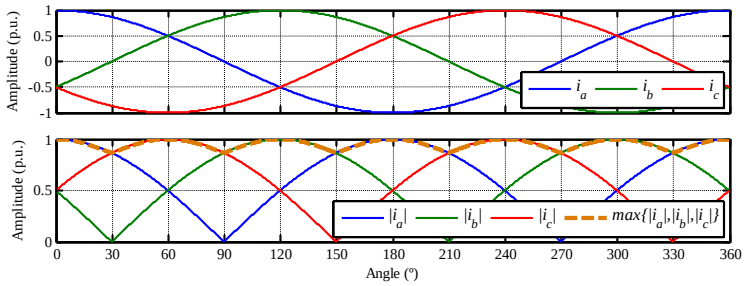

Figure 4.4: Waveforms of the phase currents ($i_a,\ i_b,\ i_c$), absolute phase currents ($|i_a|, |i_b|, |i_c|$), and instantaneous maximum of the absolute three-phase currents given by (4.14), under normal operating conditions.

The normalized phase currents are given by:

$$i_{nN} = \frac{i_n}{max\left\{|i_a|, |i_b|, |i_c|\right\}} \tag{4.15}$$

where $n = a,\ b,\ c$. Thus, the normalized phase currents always assume values within the range of ±1.

Regarding the localization of the faulty phase, the average absolute values of the normalized currents are introduced:

$$\langle |i_{nN}| \rangle = \frac{\omega}{2\pi} \int_0^{\frac{2\pi}{\omega}} |i_{nN}| \, dt \tag{4.16}$$

Under normal operating conditions, and once more assuming a perfectly balanced three-phase sinusoidal current system as described in (4.13) and Figure 4.4, the variables $\langle |i_{nN}| \rangle$ take values approximately equal to $\xi = 2/3 \approx 0.6667$. Therefore, the fault localization variables (l_n) can be defined as follows:

$$l_n = \xi - \langle |i_{nN}| \rangle \tag{4.17}$$

which present values near zero under normal conditions. As a consequence of an open-circuit fault, the localization variable corresponding to faulty phase increases, allowing the identification of a phase affected by a single power switch open-circuit fault or even by a single-phase open-circuit fault. A localization variable l_n only reaches ξ when an open-circuit fault leads to a null current (single-phase fault in an inverter stage).

The proposed diagnostic technique is depicted in the block diagram of Figure 4.5. However, in order to ensure a superior robustness against false alarms, the inclusion of the detection method proposed in section 4.1.1 might be considered. This is particular important for applying the technique to the PMSG-side converter. Accordingly, provided that robustness is ensured by the fault detection CPVP method (section 4.1.1), a low threshold value k_t equal to 0.03 can be defined for fault localization. Table 4.3 allow the technique to identify the phase affected by an open-circuit fault.

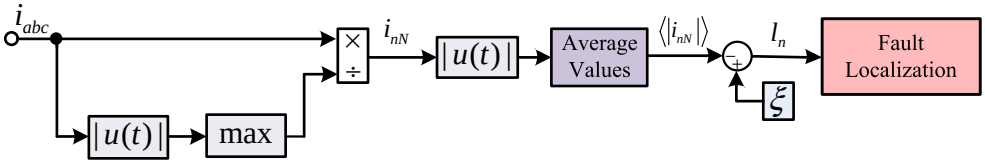

Figure 4.5: Block diagram of the ENCAAV-CMax method.

Table 4.3: Open-cicuit faults localization, using the ENCAAV-CMax method.

Faulty Phase	l_a	l_b	l_c
Phase *a*	$>k_t$	–	–
Phase *b*	–	$>k_t$	–
Phase *c*	–	–	$>k_t$

4.1.5 Average Values of the Normalized Reference Voltages and Average Values of the Normalized Voltage Errors

The main selling points of the proposed voltage-based approach [143] are: simplicity (less complex than the current-based approaches, without requiring extra hardware or a demanding tuning), robustness and effectiveness. It takes advantage of the information contained in the reference voltages available from the control system, and the optional inclusion of a voltage observer is considered with the aim of increasing the robustness against the misinterpretation of transients. Thus, in comparison with the previously proposed techniques in this thesis, in which a dedicated detection method (CPVP method) might be included in order to ensure robustness and effectiveness under the converter operation as a rectifier (PMSG-side converter), the technique proposed in this section allows fault diagnosis to be achieved effectively through a simpler algorithm by using different quantities to formulate the diagnostic variables - voltages are used instead of currents.

The proposed diagnostic technique is subdivided in two alternative versions: (1) the simplest one only requires the reference voltages and the dc link voltage, with the average values of the normalized reference voltages being used as diagnostic variables; (2) the more complex one uses an additional voltage observer, with the average values of the normalized voltage errors being used as diagnostic variables. The block diagram of Figure 4.6 depicts the proposed diagnostic techniques, where the second version is obtained by selecting the voltage observer block output as input of the diagnostic algorithm.

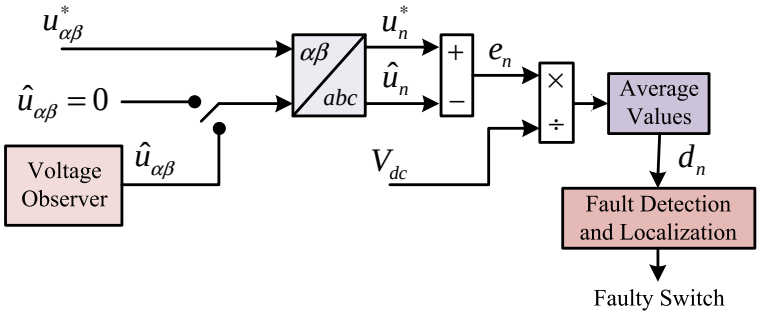

Figure 4.6: Block diagram of the voltage-based fault diagnostic techniques.

4.1.5.1 Average Values of the Normalized Reference Voltages

Firstly, the approach based on the average values of the normalized reference voltages is presented, which is obtained from the block diagram of Figure 4.6 by ignoring the voltage observer. Then, the required quantities for diagnostic purposes are only the reference voltages ($u^*_{\alpha\beta}$) and the dc-link voltage (V_{dc}), both easily obtained from the main control system. The reference voltages are transformed from the $\alpha\beta$ stationary reference frame ($u^*_{\alpha\beta}$) into the *abc* reference frame (u^*_n), and normalized by dividing them by V_{dc}. Therefore, by averaging the normalized reference voltages,

the diagnostic variables are given by:

$$d_n = \left\langle \frac{u_n^*}{V_{dc}} \right\rangle \tag{4.18}$$

where $n = a,\ b,\ c$. The reference voltages are directly available from the main control system when a voltage modulator (SVM, for instance) is applied, or they can be reconstructed from the switching pattern, when HCC or DTC are the employed control strategies (equation 2.28).

After the occurrence of a single open-circuit fault, the converter can no longer synthesize eight voltage space vectors, and it is not able to follow the imposed reference voltage. Under these conditions, the actual voltages differ from the reference ones, which is the basic principle of most voltage-based approaches proposed in the literature. Somewhat differently, the approach proposed in this section exploits the response of closed-loop systems to an actuator fault. As a consequence of a switch open-circuit fault, the control targets cannot be fulfilled, resulting in high errors between the input reference signal and the feedback signal (phase currents), which are reflected in the controller output signals (reference voltages), as an attempt to compensate the fault effects. Therefore, the reference voltages may contain the necessary information to perform the fault diagnosis.

By defining a fault detection threshold value k_d and according to the diagram of a typical voltage source converter shown in Figure 2.1, the signatures for fault detection and localization are shown in Table 4.4. Although all the diagnostic variables may exceed the threshold values ($k_d/-k_d$) as a consequence of an open-circuit fault, the faulty switch corresponds to the first verified condition in Table 4.4. The threshold value k_d is chosen to be equal to 0.05, based on the experimental results presented later on (section 4.3.3).

Table 4.4: Open-cicuit faults localization, using AVNRV and AVNVE methods.

Faulty Switches	d_a d_A	d_b d_B	d_c d_C
R_1/I_1	$> k_d$		
R_2/I_2	$< -k_d$		
R_3/I_3		$> k_d$	
R_4/I_4		$< -k_d$	
R_5/I_5			$> k_d$
R_6/I_6			$< -k_d$

4.1.5.2 Average Values of the Normalized Voltage Errors

The average values of the normalized voltage errors method is obtained by including the voltage observer in Figure 4.6. Since the noise introduced by the voltage observer is well accommodated

by averaging the normalized voltage errors, there is lack of need for filtering the voltage signals. Therefore, the diagnostic variables are given by:

$$d'_n = \left\langle \frac{u^*_n - \hat{u}_n}{V_{dc}} \right\rangle \tag{4.19}$$

where $\hat{u}_n$ stands for the estimated phase voltage (section 4.1.5.3).

The inclusion of a voltage observer is intended to improve the robustness against false alarms, since the information regarding transient conditions is also incorporated by the diagnostic technique. The inherent disadvantage is the complexity increase, but it is marginal whether a flux observer is used for control purposes (without extra voltage sensors), such as in DTC drives and direct RFOC IM drives.

When a state observer is employed, its parameter sensitivity must be taken into consideration. Concerning only diagnostic purposes, it is not justifiable to integrate either complex state observers or on-line parameter estimators. Thus, the fault diagnostic algorithm must be able to accommodate the introduced error, in order to simply need a rough knowledge of the system parameters, and, at the same time, to ensure an effective diagnostic.

The error $u^*_n - \hat{u}_n$ under normal operation is mainly related to the machine/grid parameters uncertainties [147] and power converter non-linearity (dead time, switching times, and voltage drops) [148], which assumes an alternating and symmetrical waveform with null average value, due to its dependence on the phase currents and rotor position. Under faulty operating conditions, the voltage estimation also does not endanger the correct diagnostic, since $\langle \hat{u}_n \rangle \approx 0$, and the fault signatures are the same as in Table 4.4. The threshold value k_d is chosen to be equal to 0.03, based on the experimental results presented later on (section 4.3.3).

4.1.5.3 Voltage Estimation

According to the formulation of the diagnostic variable based on the average values of the normalized voltage errors (section 4.1.5.2), estimation errors due to parameter sensitivity and measurement noise are eliminated. Thus, simple open-loop observers - without feedback correction - fulfill the diagnostic technique requirements. Moreover, an open-loop observer provides nearly instantaneous tracking capability [147], which is of paramount importance for increasing the technique robustness during transient conditions. In this thesis the diagnostic technique is applied to a PMSG drive with a back-to-back converter, then, voltage observers for both PMSG and grid are necessary.

Through the mathematical model of PMSG in the stationary reference frame, and measuring both stator current and mechanical speed, the stator flux is given by equation 2.32, the so-called current model open-loop flux observer, which avoids extra voltage sensors. Then, by neglecting the stator resistance, the stator voltage is obtained as follows:

$$\hat{u}_{s\alpha} = \frac{d}{dt}\hat{\psi}_{s\alpha};\ \hat{u}_{s\beta} = \frac{d}{dt}\hat{\psi}_{s\beta} \tag{4.20}$$

The previous simplification is performed because the algorithm has the ability to eliminate the introduced error, and not because of considering the stator resistance very small. In high performance DTC drives, where the mechanical speed is measured, a flux observer based on the current model is usually used for operation at low speeds or even at zero speed, because the voltage model achieves a low accuracy for such operating conditions. Thus, its use for diagnosing open-circuit faults does not represent an additional computational effort. On the other hand, in RFOC PMSG drives this estimator is not usually available.

Regarding a grid connected converter, in which the grid voltages are commonly measured, and neglecting the filter resistance, the converter voltages can be expressed as:

$$\hat{u}_{c\alpha} = u_{g\alpha} - L_f\frac{di_{g\alpha}}{dt};\ \hat{u}_{c\beta} = u_{g\beta} - L_f\frac{di_{g\beta}}{dt} \tag{4.21}$$

4.1.5.4 Theoretical Considerations

An open-circuit fault prevents the current flow through the affected power switch, and consequently sinusoidal waveforms cannot be shaped. Thus, current-based techniques appear as a straight forward approach for fault diagnosis. However, under low load levels and transient conditions, the phase currents assume low amplitudes and large variations, respectively, which makes difficult to accurately diagnose a fault trough a very simple algorithm. Alternatively, by considering the analysis of the reference voltages in a closed-loop drive, a small current error, resulting from a fault, is amplified by the current control loop, whereas transients are characterized by smaller variations of the reference voltages. This has motivated the development of the proposed techniques, in order to reduce both implementation and computational efforts.

Therefore, under normal operating conditions, by assuming a perfectly balanced three-phase sinusoidal reference voltage system:

$$u_n^* = \begin{cases} u_A^* = V_m^* \cos(\omega t) \\ u_B^* = V_m^* \cos\left(\omega t - \frac{2\pi}{3}\right) \\ u_C^* = V_m^* \cos\left(\omega t + \frac{2\pi}{3}\right) \end{cases} \tag{4.22}$$

where V_m^* is the reference voltages amplitude, the diagnostic variables, d_n and d'_n, assume null values, because $\langle u_n^* \rangle = 0$.

Taking as an example a fault in I_1 (upper switch of phase *A* - grid-side converter) under inverter operation, the current in phase *A* cannot become positive through IGBT I_1:

$$i_A = \begin{cases} 0, & 0 < \omega t \leq \pi \\ I_m \sin(\omega t + \phi), & \pi < \omega t \leq 2\pi \end{cases} \tag{4.23}$$

Then, the resulting error between the reference currents and the measured currents is fed to the controller, leading to an increased reference voltage for phase A as follows:

$$u_A^* = \begin{cases} u_f^* + V_m^* \cos(\omega t), & 0 < \omega t \leq \pi \\ V_m^* \cos(\omega t), & \pi < \omega t \leq 2\pi \end{cases} \tag{4.24}$$

if the converter operates as inverter, or as follows:

$$u_A^* = \begin{cases} V_m^* \cos(\omega t), & 0 < \omega t \leq \pi \\ u_f^* + V_m^* \cos(\omega t), & \pi < \omega t \leq 2\pi \end{cases} \tag{4.25}$$

if the converter operates as rectifier, being u_f^* the voltage compensation imposed by the closed-loop controller. Thus, in both operating modes, with $u_f^* > 0$, a fault in I_1 leads to a positive value of d_A, given by:

$$d_A = \frac{\omega}{\pi} \int_0^{\frac{\omega}{\pi}} \frac{u_f^*}{V_{dc}} dt \tag{4.26}$$

Moreover, since $u_A^* + u_B^* + u_C^* = 0$, for a fault in I_1, it can be deduced that $d_A = -2d_B = -2d_C$, which means that the diagnostic variable corresponding to the faulty phase assumes the highest absolute value. Consequently, the diagnostic variable of the faulty phase (d_A) is the first one to reach the threshold value d_n, allowing for the use of Table 4.4.

All the previous explanation can be extended to the remaining phases (I_3, I_5) as well as to the bottom switches (I_2, I_4, I_6). However, it is worth pointing out that for a fault in a bottom switch the reference voltage assumes negative values and, consequently, the diagnostic variable d_n corresponding to the faulty phase is negative.

Regarding the use of the average values of normalized voltage errors (d_n'), and considering the grid-side converter, the voltage can be estimated through equation (4.21), and for a fault in I1, the phase A estimated voltage is given as:

$$\hat{u}_{cA} = \hat{u}_{c\alpha} = u_{g\alpha} - L_f \frac{d}{dt} i_{g\alpha} \tag{4.27}$$

where $i_{g\alpha} = i_A$ (4.23), which leads to a null average value of the estimated voltage, $\langle \hat{u}_{cA} \rangle = 0$. Similar conclusion is drawn if the PMSG-side converter and the respective model are considered. Therefore, by using (4.19) the errors due to the system parameters are eliminated, and during steady-state $d_n \approx d_n^{'}$ for both normal and faulty operating conditions, because $\langle \hat{u}_n / V_{dc} \rangle \approx 0$. On the other hand, during transient conditions, as $\hat{u}_n$ varies according to the forced transient (tracking

capability of the voltage observer), $u_n^* - \hat{u}_n$ suffers variations with lower amplitude than u_n^* solely. Consequently, $d^{'}{}_n$ remains closer to zero than d_n, allowing to increase the diagnostic robustness against false alarms (misinterpretation of transients).

Finally, it is emphasized that the method is intended to operate in the linear modulation range (overmodulation is not considered). Therefore, the maximum value for the fault detection threshold value (k_d) can be obtained through a rough approximation of the minimum value assumed by the diagnostic variable d_A under faulty operating conditions (excluding SVM-based strategies), by considering a modulation index equal to one, and that a fault forces the reference phase voltage to the six-step operating mode:

$$d_A = \frac{\omega}{\pi} \int_0^{\frac{\omega}{\pi}} \frac{u_f^*}{V_{dc}} dt = \frac{1}{\pi} \left[\frac{4\pi}{9} - \frac{2}{\sqrt{3}} \right] \approx 0.077 \tag{4.28}$$

A comprehensive analysis of the fault detection threshold definition is provided in section 4.3.3, through experimental results under normal and faulty operating conditions with HCC, DTC, and SVM techniques.

4.2 Current Sensor Fault Diagnosis and Fault Tolerance

In PMSG drives with full-scale power converters, closed-loop control systems are mandatory in order to obtain variable speed operation and fulfill the grid requirements with a high performance. Consequently, an erroneous feedback due to a sensor failure reduces the system's performance, and it may lead to secondary faults in other components. The fault severity depends on the control system's sensitivity to the incorrect measurement. Then, in such a drive, an immediate sensor fault diagnosis is strongly recommended [149]. In particularly, for a current closed-loop controlled drive, the reliability of the data measured by the current sensors must be guaranteed before using it for control purposes.

In this context, the condition monitoring of the current sensors used in a PMSG drive for WECS should be integrated into the drive controller, not only to avoid catastrophic consequences, but also to trigger remedial procedures in a fault-tolerant system. However, current sensor fault diagnosis in PMSG drives for WECS has not been discussed in the literature yet.

Regarding the occurrence of sensor faults, in general, some research has been conducted. The effects of current measurement errors in motor drives, such as offset error and scaling error, were analyzed and compensated in [94]-[95] reducing the torque ripple introduced by such errors.

Some studies report on the fault detection and isolation of several sensor types, namely, speed, dc-link voltage and current sensors [150]-[152]. In [150] a sequence of offline tests is performed to detect a fault and the missing current information is obtained using a state observer. An adaptive observer is used to estimate the phase currents in [151], and the faulty sensor identification uses

a deterministic rule, which in practice takes a few electrical cycles. The extended Kalman filter is also applied to detect and isolate the faulty sensor in [152] as well as to achieve fault tolerance with respect to speed sensor failures in [153]-[154]. A dc-link voltage sensor monitoring technique using a combination of PI and predictive methods was proposed in [155], adding an extra protective function to the inverter of a wind turbine. A wavelet-based approach to abrupt sensor fault diagnosis was presented in [156]. The analysis of the current error vector locus in an FPGA implementation of hysteresis current control was proposed in [157] to diagnose current sensor faults. Fault detection by using parity space approach was addressed in [158], which is able to detect the instantaneous variation introduced by a sudden current or voltage sensor fault.

As far as the doubly fed induction generator (DFIG) for WECS is concerned, some diagnostic techniques, as well as system reconfigurations were proposed for sensor faults [112]-[114]. Luenberger current observers are used in [112] to provide residuals for fault detection and replacement signals for the reconfiguration. After the fault detection, the control is temporarily switched from closed loop into open-loop, and finally the fault is isolated using parity equations. However, the authors state that switching again to a closed-loop operation is a difficult task. A similar approach is presented in [113], using two Luenberger observers in parallel, for current sensor fault detection in a back-to-back converter applied to a DFIG. An FPGA-based grid-side converter with current sensor fault-tolerant control is reported in [114]. The current sensor fault detection is obtained by comparing the absolute value of the sum of the three measured currents with a non-normalized threshold, while the faulty sensor identification is achieved by using a predictive model.

In short, a review of the state of the art in the field of current sensor faults allows us to conclude that the most common approach for diagnosing them is based on state observers, generating residuals. Residuals result from a continuous comparison of the actual system outputs with the ones of a mathematical model. Luenberger observers and Kalman filters are state estimators widely used for reconstructing the system outputs. The dependence between the different measured quantities (analytical redundancy) is the basic principle of these model-based approaches, thus providing a virtual sensor to substitute the faulty one, without increasing the required number of sensors.

The aforementioned methods, classified as model- or observer-based, use system models and rely on the system's parameters. Consequently, they are typically complex and computationally demanding, which makes their real-time implementation difficult. It should be also noticed that the observers have to be properly tuned, which represents an additional implementation effort. Moreover, their performance depends highly on the accuracy of the parameters estimation and the detection times can be too long in order to avoid closed-loop instability.

4.2.1 Normalized Currents Average Absolute Values

Taking into account the literature review above, a simple and effective approach is proposed for the fault diagnosis of current sensor faults in PMSG drives for WECS, through which fault

tolerance can also be achieved by using a current sensor per phase and then taking advantage of the provided analytical redundancy. The considered faults are those that lead to a null sensor output (for example, sensor disconnection or supply failure). The proposed approach may be classified as signal-based, since it only requires the already measured phase currents. Therefore, due to its light computational burden, the algorithm is suitable for real-time implementation and may be applied to both power converters of a conventional back-to-back topology.

In order to endow a diagnostic technique based on the current measurements with insensitivity to load transients and independence from the load level, the phase currents should be normalized, since they are prone to suffer large variations. Now for current fault diagnosis, the instantaneous maximum value of the three-phase currents absolute values is proposed again as normalization quantity [146].

The proposed diagnostic technique is depicted in the block diagram of Figure 4.7. This algorithm permits to compensate the initial current sensor offsets, to detect a fault, and to locate the faulty current sensor by using only the three measured currents (i_{abc}). Additionally, it is possible to discriminate a sensor fault from an open-circuit fault and to identify the faulty phase in both cases. It must be noticed that fault localization is performed by means of the algorithm presented in section 4.1.4.

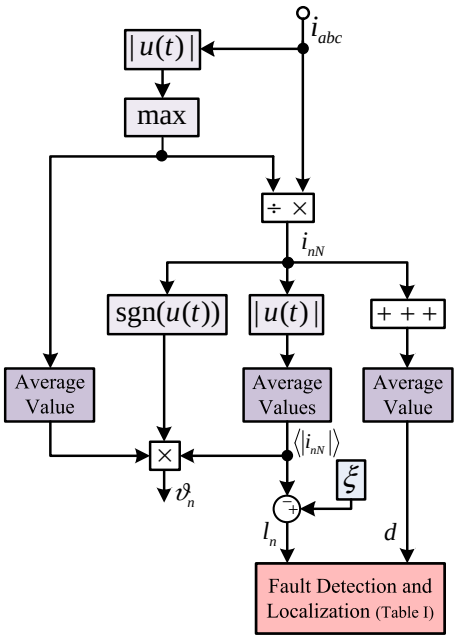

Figure 4.7: Block diagram of the fault diagnostic technique for current sensor faults.

The fault detection method verifies if the sum of the three currents is practically zero, which in a three-phase three-wire system should be always the case. Otherwise, a ground fault or a current sensor fault has occurred. In the case of a ground fault the differential protection forces the system to shutdown. On the other hand, a current sensor fault can remain undetected, degrading the

system performance and leading to secondary faults. The proposed detection variable results from the average absolute value of the sum of the normalized three-phase currents:

$$d = \frac{\omega}{2\pi} \int_0^{\frac{2\pi}{\omega}} |i_{aN} + i_{bN} + i_{cN}| \, dt \tag{4.29}$$

Ideally, under normal operating condition, $i_a + i_b + i_c = 0$, and then the detection variable (d) is equal to zero. When the considered current sensor faults occur the respective phase current seen by the control system becomes null. Considering that the fault occurs in phase a ($i_a = 0$), the detection variable value will be no longer null and it will depend on the values assumed by the remaining phase currents. By assuming that the remaining phase currents stay unchanged - which is the case for an open-loop control system - and analyzing Figure 4.8, the detection variable can be given by:

$$\frac{\omega}{2\pi} \int_0^{\frac{2\pi}{\omega}} |i_{bN} + i_{cN}| \, dt = \frac{2\omega}{\pi} \int_0^{\frac{\pi}{2\omega}} \frac{\cos(\omega t + \phi)}{\cos\left(\omega t - \frac{\pi}{3} + \phi\right)} dt \approx 0.8028 \tag{4.30}$$

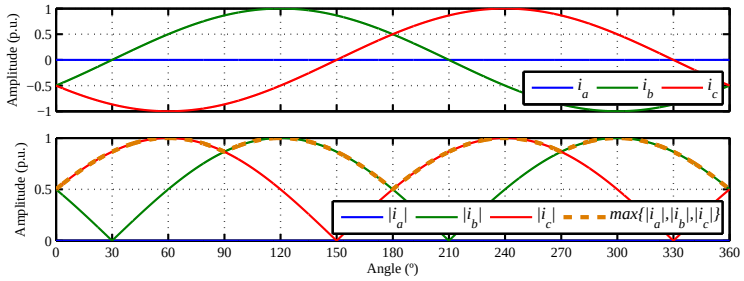

Figure 4.8: Waveforms of the phase currents ($i_a,\ i_b,\ i_c$), absolute phase currents ($|i_a|, |i_b|, |i_c|$), and instantaneous maximum of the absolute three-phase currents, when considering $i_a = 0$ and an open-loop control system.

However, as a consequence of the closed loop control system response, the remaining currents will change and the value of the detection variable will tend to exceed the value obtained in (4.30). For example, in a typical vector-controlled drive with space vector modulation (SVM), when the control system receives information that $i_a = 0$, it reacts in order to produce the same current space vector with the remaining phase currents only, which is possible if the phase displacement between i_b and i_c changes from 120º to 60º [97]. The post-fault currents ($i_b^{'},\ i_c^{'}$) can then be expressed as:

$$i_b' = I_m' \cos\left(\omega t - \frac{2\pi}{3} - \frac{\pi}{6} + \phi\right) \tag{4.31}$$

$$i_c' = I_m' \cos\left(\omega t + \frac{2\pi}{3} + \frac{\pi}{6} + \phi\right) \tag{4.32}$$

Accordingly, the current amplitude in the faulty phase ($i_a' = -i_b' - i_c'$) is $\sqrt{3}$ times higher than

in the other phases, and the value assumed by the detection variable can be calculated by analyzing Figure 4.9:

$$\frac{\omega}{2\pi}\int_0^{\frac{2\pi}{\omega}} \left|i'_{bN}+i'_{cN}\right| dt = \frac{2\omega}{\pi}\int_0^{\frac{\pi}{2\omega}} \frac{\sqrt{3}\cos\left(\omega t+\phi\right)}{\cos\left(\omega t-\frac{\pi}{6}+\phi\right)} dt \approx 1.1972 \tag{4.33}$$

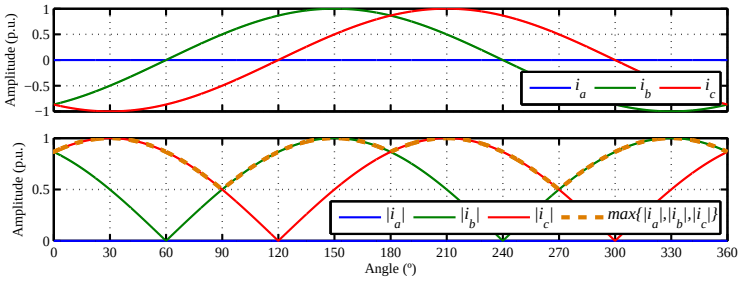

Figure 4.9: Waveforms of the phase currents ($i_a,\ i_b,\ i_c$), absolute phase currents ($|i_a|, |i_b|, |i_c|$), and instantaneous maximum of the absolute three-phase currents, when considering $i_a = 0$ and a closed-loop control system.

The compensation of the current sensor offsets is a common drive self-commissioning procedure, which is usually performed by calculating the average values of the three measured currents. However, taking advantage of the proposed diagnostic method and not forgetting the desirable minimal increase of the computational effort, the initial current sensor offsets can be calculated as:

$$\vartheta_n = sgn(i_{nN}) \left\langle \max\left\{|i_a|, |i_b|, |i_c|\right\}\right\rangle \left\langle |i_{nN}|\right\rangle \tag{4.34}$$

where $sgn(i_{nN})$ and $\left\langle \max\left\{|i_a|, |i_b|, |i_c|\right\}\right\rangle$ stand for the sign function of the normalized currents and the average value of the normalization quantity, respectively. Thus, before operating the drive, the offset values should be sampled, held and subtracted from the measured phase currents.

It is worth emphasizing that the whole algorithm (Figure 4.7) implies a reduced increase of the computational burden, since, comparing with the common offset compensation procedure, only the average values of two quantities and some simple mathematical operations are required.

To accomplish fault diagnosis of current sensor faults and power switch open-circuit faults, three threshold values can be defined, namely, k_d and k_s for current sensor fault detection and localization, and k_t for open-circuit fault identification:

$$D = \begin{cases} H\ if\ d \geq k_d \\ L\ if\ d < k_d \end{cases} \tag{4.35}$$

$$L_n = \begin{cases} S\ if\ l_n < d\ \&\ l_n \geq k_s \\ T\ if\ l_n \geq d\ \&\ l_n \geq k_t \end{cases} \tag{4.36}$$

Therefore, according to the previous relationships the fault diagnostic signatures presented in Table 4.5 allow the technique to identify the affected phase and to distinguish between current sensor and open-circuit faults. All the threshold values were established on the basis of the theoretical formulation presented in this section and on the extensive analysis of the diagnostic variables behavior, through simulation and experimental results. Thus, k_d must be lower than (4.30) as well as k_s and k_t must be lower than $\xi = 2/3$, and all of them should be higher than the highest values assumed by the respective diagnostic variables under normal operating conditions. Therefore, k_d, k_s and k_t values were selected to be equal to 0.4, 0.2 and 0.03, allowing the diagnostic technique to achieve a good tradeoff between robustness against false alarms and detection speed, together with a high effectiveness in a wide range of operating conditions. The experimental results presented in section 4.4 support their definition as universal threshold values.

Table 4.5: Diagnostic signatures for current sensor and open-circuit faults.

Fault		D	L_a	L_b	L_c
Type	Location				
Current Sensor	Phase *a*	H	S	–	–
	Phase *b*	H	–	S	–
	Phase *c*	H	–	–	S
Power Switch Open-Circuit	Phase *a*	L	T	–	–
	Phase *b*	L	–	T	–
	Phase *c*	L	–	–	T

4.2.2 Current Sensor Fault Tolerance

Measurement redundancy obtained with the third current sensor is vital in order to achieve fault tolerance. This way, the two healthy sensors together with the fault localization information allow the fault-tolerant algorithm to reconstruct properly the three-phase currents, which will be used by the drive control system. Figure 4.10 shows the block diagram of the fault tolerant strategy, which allows the control system to replace the erroneous measurement.

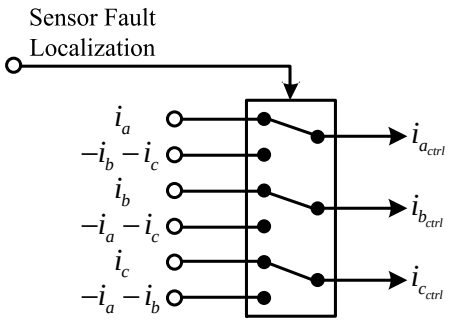

Figure 4.10: Block diagram of the current sensor fault tolerant technique.

4.3 Simulation and Experimental Results - Open-Circuit Fault Diagnosis

4.3.1 Current Park's Vector Phase, Current Polarity and Errors of the Normalized Currents Average Absolute Values Methods Using the Park's Vector Modulus as Normalization Quantity

Vector control was implemented for both converters, with the PMSG-side converter being controlled by the RFOC strategy with HCC and the grid-side converter being controlled by a VOC strategy with SVM. The parameters of the used machine are given in Table A.2 - Appendix A. For fault diagnosis in both converter sides, CPVP and CP methods (section 4.1.2) are applied to the grid-side converter, and CPVP and ENCAAV-CPVM methods (section 4.1.3) are applied to the PMSG-side converter. The value I_0 was chosen to be equal to 0.15 A, since the maximum rated grid current is considered equal to 6 A.

4.3.1.1 Simulation Results

Figure 4.11 and Figure 4.12 present the simulation results regarding the converters output currents together with the variables used to perform fault detection and localization, during load transients and fault occurrences in both converters, with an imposed reference speed of 900 rpm. These results are presented in order to show the behavior of the variables proposed for the diagnostic purpose.

Three load steps are introduced. At $t = 0.12\ s$ the load torque increases from 16% of the rated load torque to its rated value (T_L). Inversely, the load torque is reduced to 16% of its rated value at $t = 0.14\ s$, and finally, at $t = 0.2\ s$, it increases again to 50% of the rated load torque. Regarding the detection variables for both converters, d_{PMSG} and d_{Grid}, it is evident that during these transients they remain far from the established threshold values. So, the immunity to false alarms resulting from load variations is verified. Furthermore, it is important to notice that as a consequence of the load decreasing at $t = 0.14\ s$, the generator and grid phase currents become almost null. Consequently, if the diagnostic method was based only on the localization variables (e_n, I_{nN}, P_n, N_n), this would lead to the misinterpretation of this transient, proving that the fault detection method is crucial to obtain a reliable fault diagnosis.

With the aim to evaluate the diagnostic performance under faulty conditions, a load torque of 50% of the rated load torque is assumed, and four distinct faulty operating conditions are considered: a single IGBT open-circuit fault on the PMSG-side converter ($t = 0.227\ s$), a single-phase open-circuit on the PMSG-side converter ($t = 0.247\ s$), a single IGBT open-circuit fault on the grid-side converter ($t = 0.260\ s$), and a single-phase open-circuit on the grid-side converter ($t = 0.310\ s$). Firstly, Figures 4.11 and 4.12 show that the fault occurrences in one converter prac-

tically do not affect the variables on the other converter, which allows the implementation of two completely independent diagnostic methods.

Immediately after the first fault occurrence in the PMSG-side converter, the detection variable decreases below T_{dPMSG}. Meanwhile, the diagnostic variable e_a increases above T_{lPMSG} and the average value of the phase a normalized current takes a negative value, allowing for the localization of the faulty IGBT R_1. Fault detection and localization are achieved in times corresponding to 9% and 10% of the generator phase currents fundamental period, respectively. When the two IGBTs of the same phase are in open-circuit, d_{PMSG} also decreases below T_{dPMSG}, e_a increases even more and I_{aN} becomes null, corresponding to the signature of the generator phase a in open-circuit (Table 4.2). Regarding the faults in the grid-side converter, the results are presented in Figure 4.12. After the fault occurrence in IGBT I_1, the detection variable reaches T_{dGrid} in a time corresponding to 7% of the grid currents fundamental period, whereas N_A exceeds the fault localization threshold in 39% of the same period. The second fault in phase A provokes the increasing of P_A, which exceeds T_{lGrid}, identifying I_2 as a faulty switch.

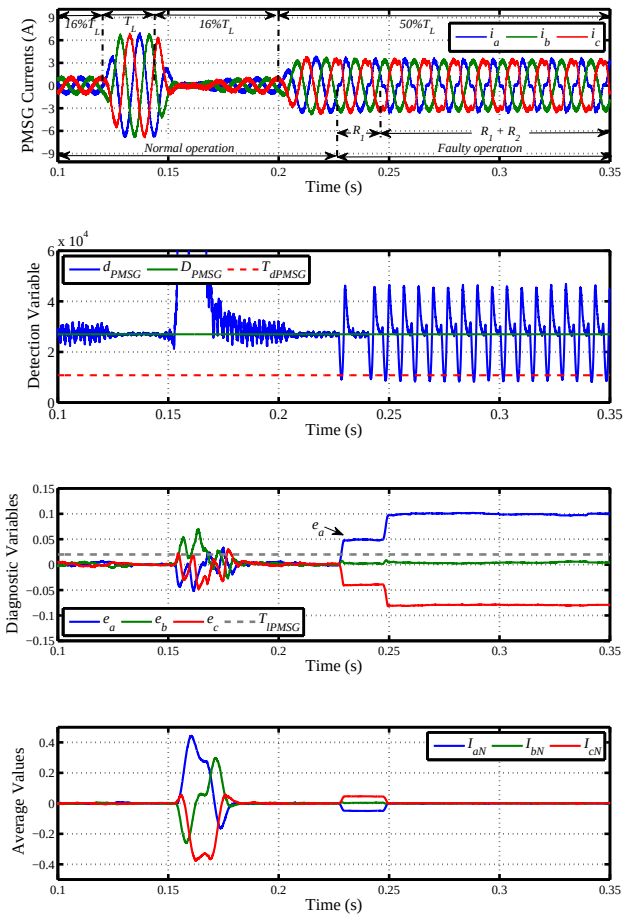

Figure 4.11: Simulation results regarding the time-domain waveforms of the generator phase currents, the detection variable and the localization variables for the generator-side converter.

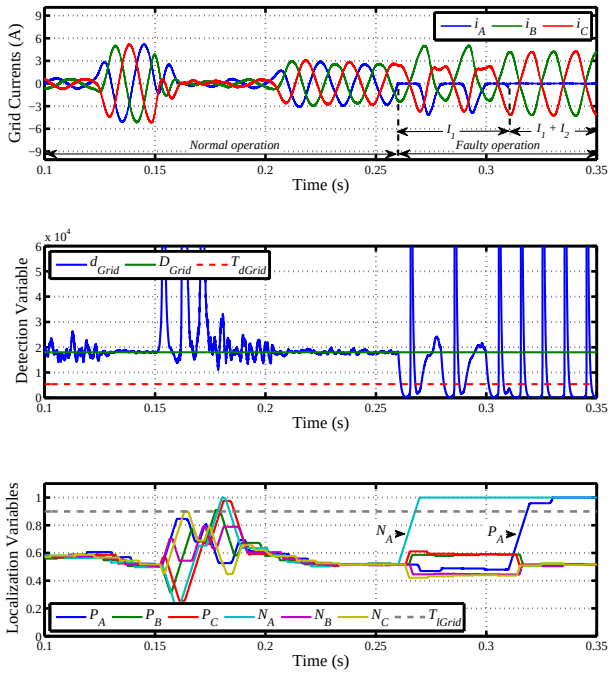

Figure 4.12: Simulation results regarding the time-domain waveforms of the generator phase currents, the detection variable and the localization variables for the grid-side converter.

4.3.1.2 Experimental Results

The experimental results were carried out at a grid phase-to-phase voltage of 120 V and a reference dc-link voltage of 250 V. The results presented in this section have two main goals. Firstly, they intend to demonstrate the diagnostic immunity to false alarms resulting from transients, and, secondly, to show the capabilities to diagnose single and multiple open-circuit faults.

Immunity to False Alarms - Figure 4.13 and Figure 4.14 present two distinct transient responses, to a load step and to a speed step, respectively. Knowing that the detection variables are responsible to ensure the robustness to transients, preventing their misinterpretation, the detection variables are the only ones analyzed here.

The load transient presented in Figure 4.13 corresponds to an instantaneous change, at $t = 0.17\ s$, from the rated load torque to a load level equivalent to 16% of its value, with an imposed reference speed of 900 rpm, similar to the one identified as the most severe regarding the diagnostic reliability in the simulation results. The transient response is clearly visible on the generator and grid phase currents, which decrease sharply. It can be seen that the detection variable of the generator-side converter decreases immediately, which is due to a slight reduction of the mechanical speed. Concerning also the detection variables, it is noticeable that, even after reaching a steady-state operation, d_{PMSG} and d_{GRID} deviate from their reference values, D_{PMSG} and D_{GRID}, as a consequence of the currents being almost null. Nevertheless, they remain far from the defined threshold values, which demonstrates that the detection method resists to harsh load variations

without generating false alarms.

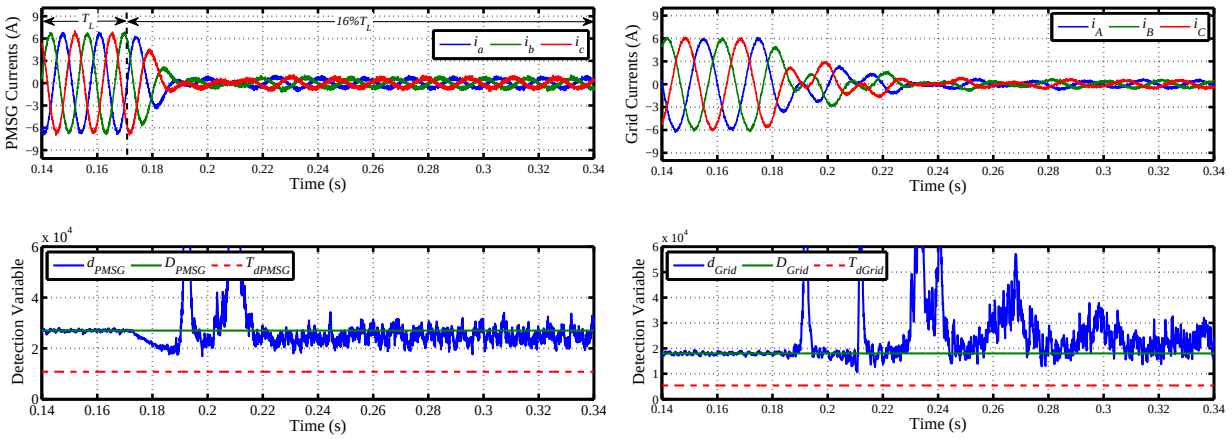

Figure 4.13: Experimental results regarding the time-domain waveforms of the generator phase currents, the detection variable for the generator-side converter, the grid phase currents and the detection variable for the grid-side converter, during a load transient.

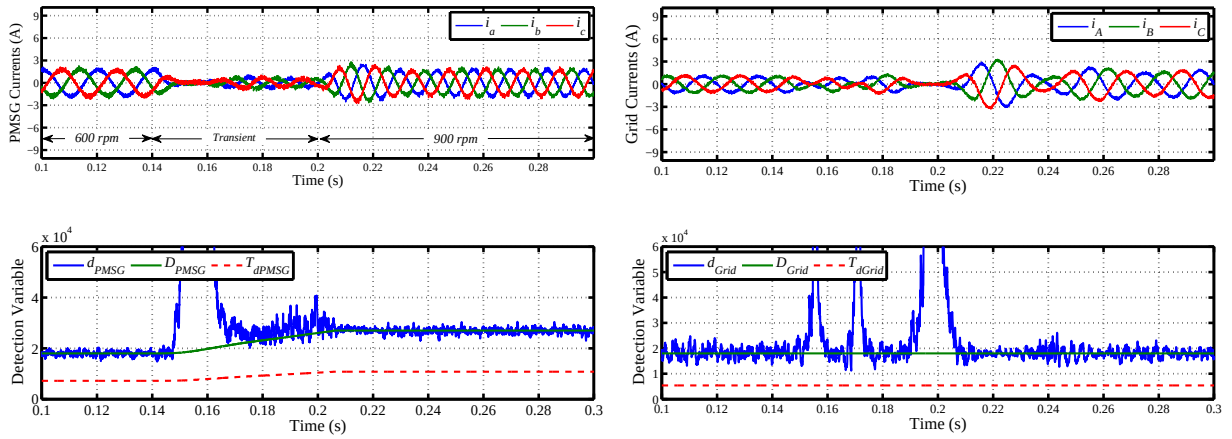

Figure 4.14: Experimental results regarding the time-domain waveforms of the generator phase currents, the detection variable for the generator-side converter, the grid phase currents and the detection variable for the grid-side converter, during a speed transient.

The results presented in Figure 4.14 show the detection variables behavior during a speed transient, as result of a speed step, at $t = 0.14\ s$, from 600 rpm to 900 rpm, with a constant load level of 33% of the rated torque. With regard to the grid-side converter, the behavior is quite similar to the one observed for the load transient, since the speed change also results in an abrupt variation of the power delivered to the grid. On the other hand, the detection variable of the PMSG-side converter increases, as a consequence of the rising currents frequency, and it follows the generator mechanical speed. However, once again, despite the PMSG phase currents approaching zero, d_{PMSG} does not approach T_{dPMSG}. Although complete immunity to false alarms is not guaranteed, it is demonstrated that the detection method, together with the considered thresholds, endows

the fault diagnostic with a remarkable robustness against the misinterpretation of speed and load transients.

Diagnostics Effectiveness - The experimental results presented in Figures 4.15 and 4.16 address the diagnostic method capabilities to diagnose multiple open-circuit faults in both converters, and their independence from the generator mechanical operating conditions. The fault diagnostic performance is analyzed under two distinct mechanical conditions: a reference speed of 600 rpm together with a load torque equal to 33% of the rated torque (Figures 4.15a and 4.16a), and a reference speed of 900 rpm together with a load level of 50% of the rated value (Figures 4.15b and 4.16b).

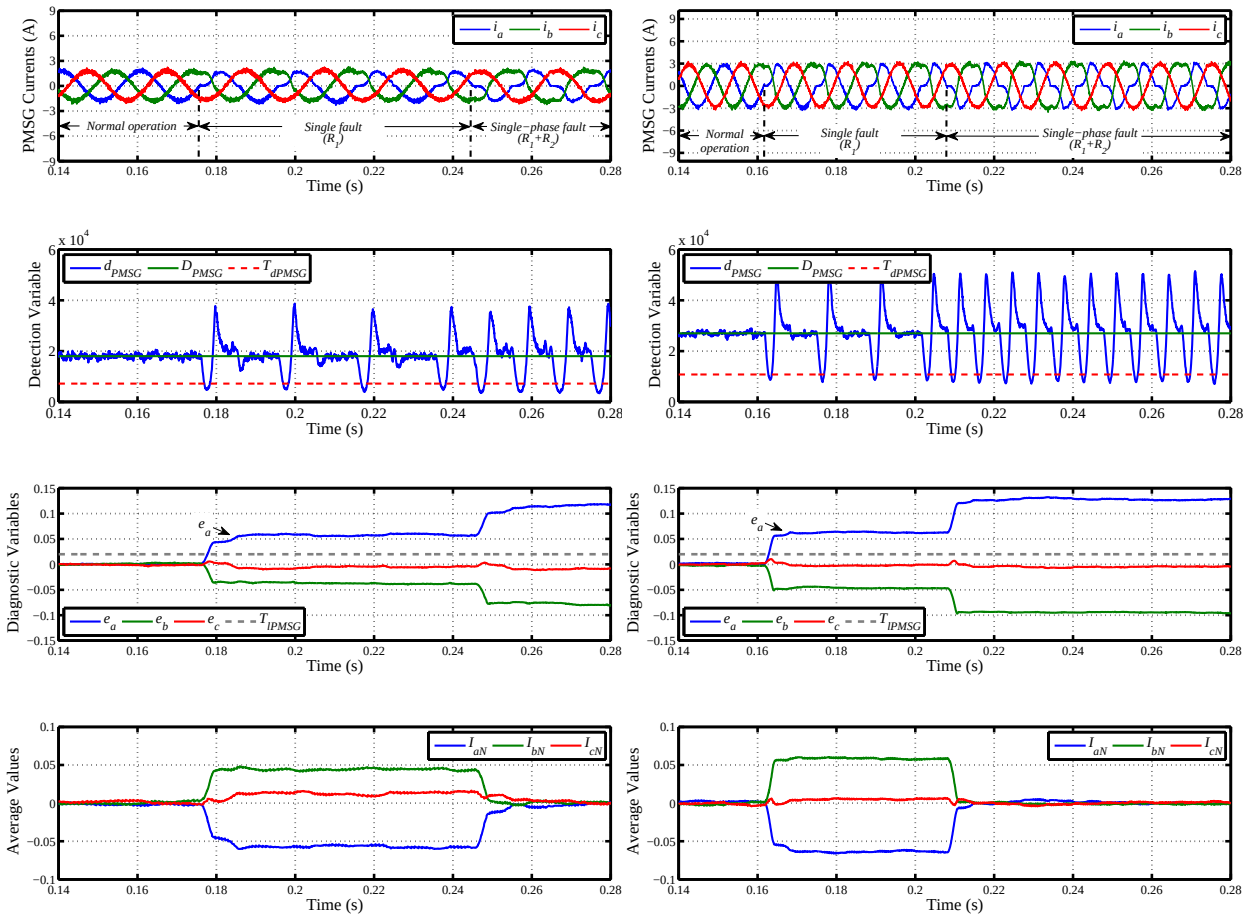

Figure 4.15: Experimental results regarding the time-domain waveforms of the PMSG phase currents, the detection variable and the localization variables for the PMSG-side converter: (a) under 600 rpm and 33% of the rated load torque; (b) under 900 rpm and 50% of the rated load torque.

Considering firstly open-circuit faults in the PMSG-side converter, Figure 4.15a presents the results under low speed and low load level, where a fault happens at $t = 0.176\ s$ and it is detected after 5% of the currents fundamental period. Through variables e_n, it is possible to identify the phase a as the faulty one when e_a exceeds T_{lPMSG}, which happens in a time corresponding to

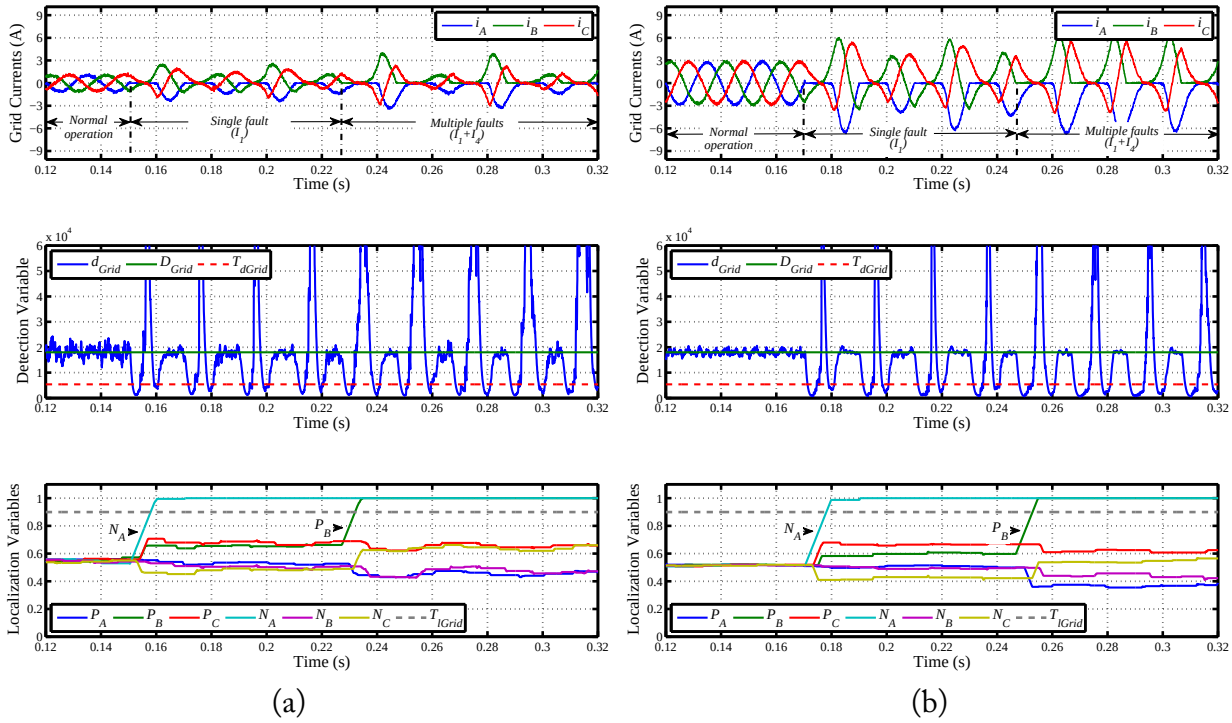

Figure 4.16: Experimental results regarding the time-domain waveforms of the PMSG phase currents, the detection variable and the localization variables for the grid-side converter: (a) under 600 rpm and 33% of the rated load torque; (b) under 900 rpm and 50% of the rated load torque.

10% of the currents fundamental period. In order to complete the diagnostic, the discrimination of the faulty IGBT R_1 is performed by I_{aN} that presents a negative value. At $t = 0.245\ s$ the gate command signal of R_2 is inhibited (Figure 4.15a). As a consequence, e_a increases even more, so the affected phase is successfully identified for a double fault in the same leg of the converter, as well as for a single fault. Meanwhile, I_{aN} becomes null, which characterizes a single-phase open-circuit fault. Comparing the results presented in Figure 4.15a with the ones in Figure 4.15b, it becomes clear that, in spite of the different mechanical operating conditions, the obtained fault diagnostic variables have a very similar behavior when the same faulty conditions are introduced. In Figure 4.15b the failure of R_1 happens at $t = 0.162\ s$, being detected and localized in 8% and 9% of the generator currents period. The same behavior is also verified when at $t = 0.208\ s$ the command signal of R_2 is removed.

Regarding the open-circuit faults in the grid-side converter, the results presented in Figure 4.16 allow to perform a similar analysis to the one already presented for the generator-side. In Figure 4.16a, under 600 rpm and 33% of the rated load torque, two open-circuit faults in the grid-side converter, at $t = 0.151\ s$ and $t = 0.227\ s$, are introduced, with the detection being performed in 5% of the grid currents period, when d_{Grid} reaches T_{dGrid}. When N_A and P_B exceed T_{lGrid}, the fault localization of I_1 and I_4 is accomplished in time intervals corresponding to 38% and 25% of grid-phase currents fundamental period, respectively. The same faulty conditions were also

introduced to obtain the results presented in Figure 4.16b, for a higher load level, which show an identical behavior of the fault diagnostic variables and equivalent detection and localization times.

Therefore, the comparison between Figure 4.16a and Figure 4.16b, as well as between Figure 4.15a and Figure 4.15b, supports the conclusion that the diagnostic capabilities of the proposed method are independent of the generator mechanical conditions.

The analyzed results show that an open-circuit fault can be detected in a time interval shorter than 10% of the currents fundamental period, independently of the affected converter. On the other hand, the localization time depends on the faulty converter, since the fault localization method for each one is distinct. Therefore, the fault localization for the PMSG-side converter can be achieved in a time of about 10% of the generator currents period, whereas for the grid-side converter it is accomplished in a time interval of about 40% of the grid currents period. The slower localization performance of the grid-side converter diagnostic method is justified due to its superior diagnostic capabilities, since it allows to identify 27 distinct faulty situations, instead of 9 allowed by the localization method for the PMSG-side. It is also possible that an open-circuit fault may occur but its effects in the currents might only be noticed in the next current half-cycle. In this case, beyond the inherent detection and localization time of each algorithm, a maximum delay time equivalent to 50% of the currents period is also introduced.

Finally, comparing Figure 4.15a with Figure 4.16a, it is visible that under normal operating conditions d_{PMSG} has oscillations with lower amplitude than d_{Grid}, and under faulty operating conditions d_{PMSG} decreases less. These observations justify the choice of a higher percentage value (k_{PMSG}) for the definition of T_{dPMSG}.

4.3.2 Errors of the Normalized Currents Average Absolute Values Using the Instantaneous Maximum Value of the Currents Absolute Values as Normalization Quantity

Vector control with SVM was implemented for both converters. The parameters of the used machine are given in Table A.1 - Appendix A. For fault diagnosis, the ENCAAV-CMax method (section 4.1.4) is applied to both converter sides of the PMSG drive.

4.3.2.1 Simulation Results

A load profile similar to the one imposed in section 4.3.1.1 is used for Figure 4.17 under normal operating conditions. Having achieved the steady-state at a speed of 900 rpm and a load level of 50% of the PMSG rated load torque, open-circuit faults are introduced at $t = 0.3\ s$ and $t = 0.35\ s$ in both converters. Figure 4.17a shows the PMSG phase currents and the respective diagnostic variables, where it can be seen that transients and faulty operating conditions are responsible for variations of the diagnostic variables. The faults are introduced in R_1 and R_2, leading to the increase

of l_a and allowing the technique to diagnose phase a as the faulty one. Despite the fact that the diagnostic variables assume the highest values under faulty operating conditions, their maximum absolute value under normal operating conditions is very close to the value of l_a as a consequence of a single switch open-circuit fault in R_1. Moreover, as a consequence of the load decreasing at $t = 0.16\ s$, the threshold value k_t of 0.03 is exceeded. All this indicates that the fault detection method in section 4.1.1 (CPVP method) must be also included for fault diagnosis in the PMSG-side converter. Accordingly, fault localization is only considered after fault detection, ensuring immunity to false alarms.

On the other hand, faults in the grid-side converter (Figure 4.17b) cause a higher increase o the diagnostic variables and the method of the errors of the normalized currents average absolute values can be applied without the addition of a dedicated fault detection method. The method ability to diagnose single switch and single-phase open-circuit faults is demonstrated in Figure 4.17b, as a result of faults in I_1 and I_2.

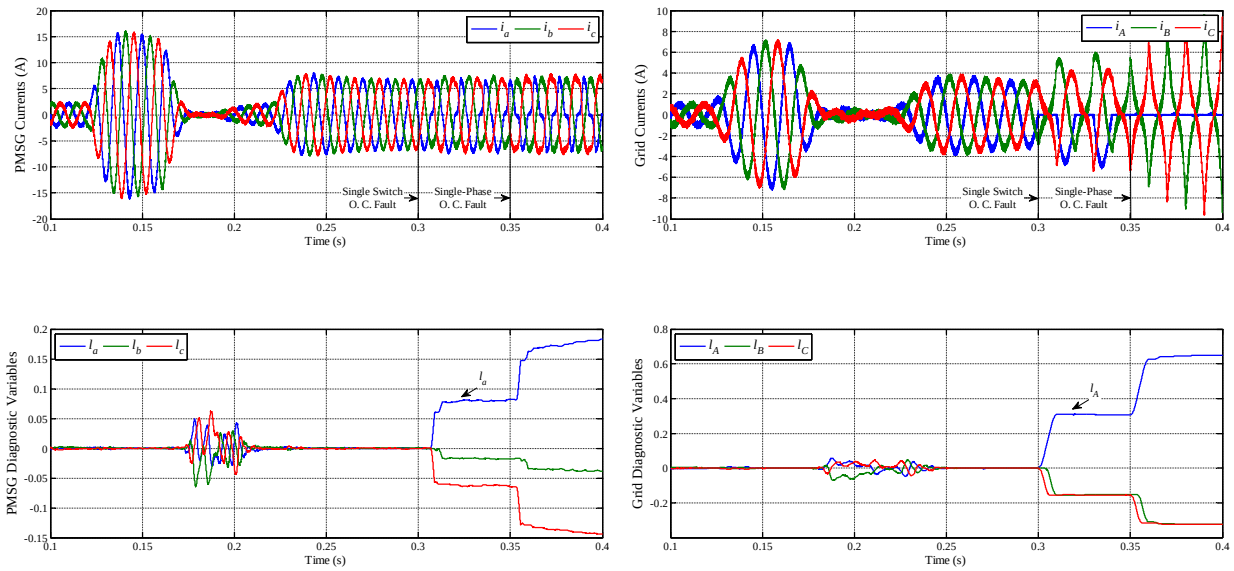

Figure 4.17: Simulation results regarding the time-domain waveforms of the phase currents and the diagnostic variables for: (a) the PMSG-side converter; (b) the grid-side converter.

4.3.2.2 Experimental Results

Taking into account that immunity to false alarms should be attributed by the detection method in section 4.3.1.1 (CPVP method), this is not analyzed in this section, only the technique effectiveness in the localization of the faulty phase is analyzed. For the experimental results, a reference speed of 600 rpm and load level of 50% of the PMSG rated torque are assumed.

Figure 4.18 presents the phase currents and the diagnostic variables for both PMSG- and grid-side converters in the presence of single power switch and single-phase open-circuit faults in the respective converter side. For both sides, after the first fault occurrence (single fault), the localization variable corresponding to the affected phase increases, increasing even more when a single-phase fault is introduced. The variable l_a in Figure 4.18a assumes lower values than l_A in Figure 4.18b because an open-circuit fault is less severe in the rectifier stage. It is worth noting that the phase current only becomes null for a single-phase open-circuit fault in the inverter stage (grid-side converter). In this case, the localization variable reaches the value of 0.66. Thus, the phase affected by an open-circuit fault can be identified by selecting k_t to be equal to 0.03.

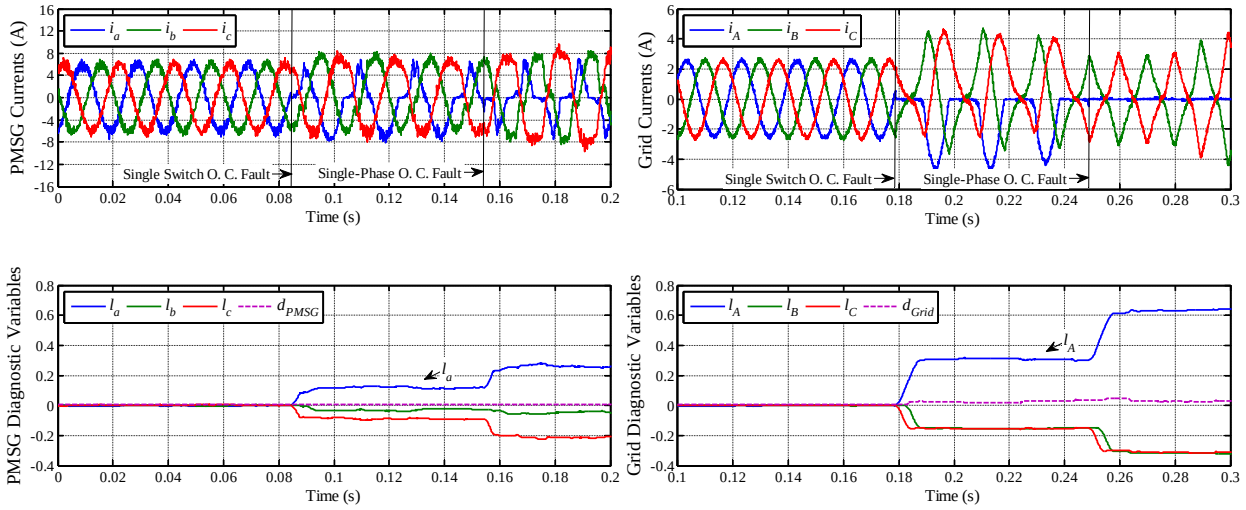

Figure 4.18: Experimental results regarding the time-domain waveforms of the phase currents and the diagnostic variables, under single switch and single-phase open-circuit faults in the: (a) PMSG-side converter; (b) grid-side converter.

4.3.3 Average Values of the Normalized Reference Voltages and Average Values of the Normalized Voltage Errors

The parameters of the used machine are given in Table A.1 - Appendix A. For the simulation results, vector control with HCC was implemented for both converters. Additionally, for the experimental results, RFOC strategy with SVM and conventional DTC were implemented for the PMSG-side converter. Open-circuit fault diagnosis is performed by means of AVNRV and AVNVE methods (section 4.1.5).

4.3.3.1 Simulation Results

The same load profile used for the simulation results of section 4.3.2.1 is shown in Figure 4.19. Open-circuit faults are introduced in both converters (IGBTs R_1 and I_1). Figure 4.19 elucidates that the values assumed by the diagnostic variables under normal and faulty operating conditions are well distinct, thereby adopting this diagnostic technique, the inclusion of a dedicated detection method is avoided, resulting in a simpler approach. It is shown that a fault in IGBT R_1 in the PMSG-side converter can be identified using d_a or d'_a. Identically, for the grid-side converter, d_A or d'_A permit to identify the IGBT I_1 as the faulty one. Additionally, it is noticed that diagnostic variables d'_n suffer variations with lower amplitude than variables d_n, which is a proof of superior robustness.

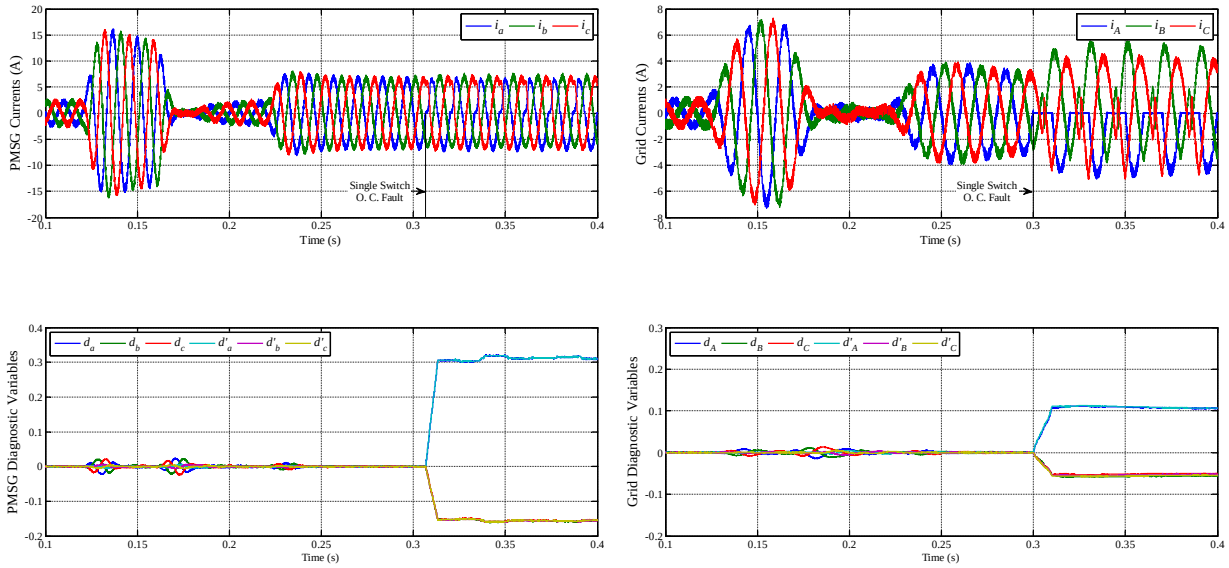

(a) (b)

Figure 4.19: Simulation results regarding the time-domain waveforms of the phase currents and the diagnostic variables for: (a) the PMSG-side converter; (b) the grid-side converter.

4.3.3.2 Experimental Results

The presented results aim to assess the applicability of the proposed AVNRV and AVNVE diagnostic techniques, when applied to voltage source converters with distinct control strategies and under different operating conditions. Accordingly, different control strategies were integrated into the digital control together with the diagnostic technique, namely RFOC with HCC, RFOC with SVM, conventional DTC and VOC with HCC were considered. It is worth noting that for HCC and DTC the reference voltages are reconstructed from the switching states, whereas for SVM the reference voltages are directly available from the control system. Such an extensive analysis

is valuable in order to clearly show the technique advantages and disadvantages (when compared to previously proposed approaches), and also necessary due to the use of reference values, whose generation differs according to the used control strategies.

A sampling frequency of 20 kHz is common for all the implemented control strategies, and the SVM was implemented through the slave DSP on the DS1103 (Texas Instruments TMS320F240) with a PWM frequency of 5 kHz.

The analysis and discussion of the experimental results is divided in three sections: (1) behavior under normal operating conditions, focusing the response to transients; (2) behavior under faulty operation, analyzing the dependence on the operating conditions and control strategies; and (3) definition of the required fault detection threshold, by using the results in the two previous sections.

Behavior Under Normal Operating Conditions - In order to evaluate the diagnostic method robustness and to define a fault detection threshold value, the maximum absolute value assumed by the diagnostic variables under normal operating conditions must be known. The largest values usually result from transient conditions - as a consequence of large variations of the analyzed quantities - which may be misinterpreted as a fault occurrence. Therefore, various harsh transients were analyzed, by imposing both load torque and reference speed variations (such as load steps from no-load conditions to the rated load torque and vice-versa, and speed variations between low speed values and the rated speed with high acceleration rates). The maximum values assumed by d_n and d'_n for the considered control strategies are shown in Figure 4.20. As could be expected, the higher values of d_n are shown for the control strategies with higher dynamic performance (DTC, HCC). When using d'_n, the maximum value of the diagnostic variable decreases significantly, which may permit to improve the technique robustness or detection speed, according to the threshold value definition.

For better illustration, the two proposed diagnostic variables together with the PMSM phase currents are shown in Figure 4.21a, regarding a load step from half load under motoring operation to half load under regenerative operation (at a reference speed of 600 rpm, with HCC). The effectiveness of including the voltage observer is clearly illustrated, since variables d'_n suffer smaller variations than variables d_n (Figure 4.21a). Moreover, it can be seen that the errors in the voltage estimation (due to parameters mismatch, power switches voltage drop, switching times, dead time, discretization and quantization errors) have no impact on the diagnostic variables d'_n, remaining close to zero under normal operating conditions. Similar conclusions can be drawn from Figure 4.21b, regarding a speed transient from 1500 rpm to 600 rpm with a high deceleration rate of approximately $628\ rad/s^2$.

Behavior under Faulty Operating Conditions - To investigate the dependence on the mechanical operating conditions of the proposed technique, five load levels (no-load, ±20% and ±50% of the rated load torque) and three reference speed values (600 rpm, 1200 rpm, 1750 rpm) were considered.

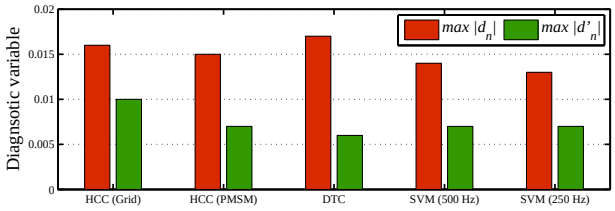

Figure 4.20: Experimental results regarding the maximum absolute values assumed by the two proposed diagnostic variables (d_n, d'_n) under normal operating conditions, as a consequence of load and speed transients.

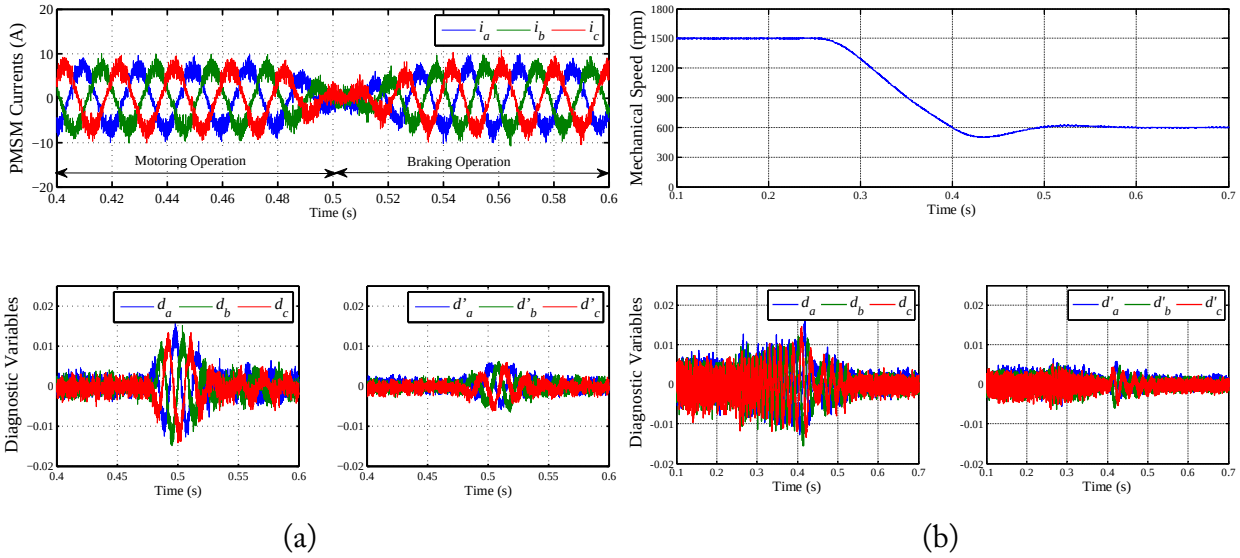

Figure 4.21: Experimental results regarding transients under normal operating conditions (RFOC with HCC): (a) load transient at 600 rpm; (b) speed transient at 50% of the PMSG rated torque.

The results concerning an open-circuit fault in the upper switch of phase a (R_1) are summarized in Figure 4.22, in which only the steady state value of the diagnostic variable corresponding to the faulty phase is presented ($d_a \approx d'_a$).

Figure 4.22a shows that d_a is practically load independent for HCC and DTC strategies. Nevertheless, it presents considerable distinct values depending on the converter operating mode (inverter or rectifier operation), with d_a assuming higher values when the converter operates as a rectifier. This can be explained by means of Figure 4.23, by considering an open-circuit fault in R_1 of the machine-side converter when employing RFOC with HCC. As a consequence of the fault, the phase currents cannot follow their reference signals and the resulting current error is fed to the controller, leading to an increase of the reference voltage as an attempt to compensate the disturbance. Then, the average value of the reference phase voltage becomes non-null, allowing the algorithm to detect the fault. When the fault occurs during the rectifier operation (Figure 4.23b), the voltage reference has a wider range of freedom to try to compensate the fault effect, which leads

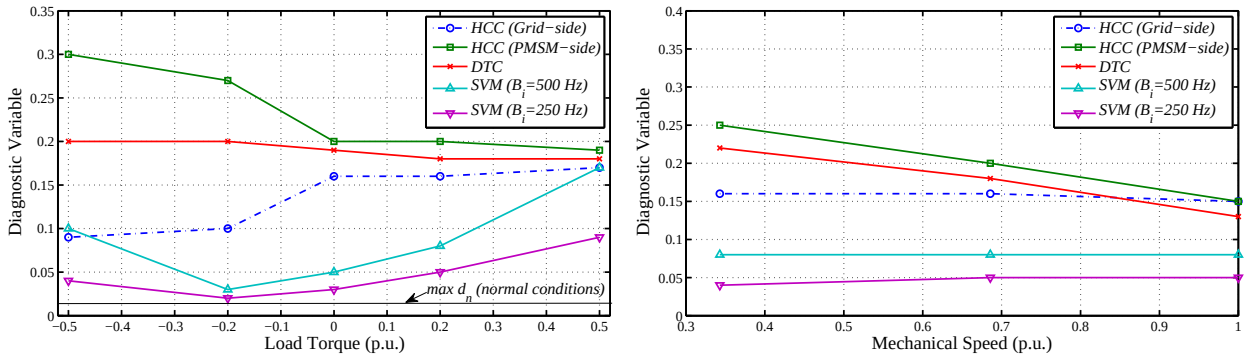

(a) (b)

Figure 4.22: Experimental results regarding the steady state value of the diagnostic variable corresponding to the faulty switch R_1 for: (a) five load levels, at a constant reference speed of 1200 rpm; (b) three speed levels, at a constant load equivalent to 20% of the PMSM rated torque.

to a higher value of d_a. It is worth noting that during rectifier operation, the fault impact in the currents is reduced (Figure 4.23b), becoming the fault diagnosis through a current-based approach difficult and requiring more complex algorithms as those analyzed in sections 4.1.1-4.1.4. However, the reference voltages are highly affected, allowing the proposed method to diagnose effectively an open-circuit fault during both inverter and rectifier operating modes.

Additionally, Figure 4.23 verifies that under both normal and faulty steady-state operating conditions d_n (average values of the normalized reference voltages) and d'_n (average values of the normalized voltage errors) assume similar values. Thus, the technique effectiveness is not affected by including the voltage observer as explained in section 4.1.5.3.

Concerning the RFOC strategy with SVM, the behavior of d_a is clearly load dependent (Figure 4.22a), since its value increase with the load. Contrary to what is verified for HCC and DTC, the highest values of d_n are assumed during faulty operating conditions as inverter. Moreover, it is shown in Figure 4.22a that the diagnostic variables are affected by the current control loop bandwidth (B_i), by considering two bandwidth values: 500 Hz and 250 Hz. All these events are justified by the generation process of the reference voltages when an SVM modulator is employed, which are generated through PI controllers with the current errors as their inputs. Consequently, the higher the current error and the control loop bandwidth, the higher the increase of the reference voltage and the value of d_a. Thus, the behavior is clearly distinct from HCC and DTC strategies, where the current error always yields high amplitude reference voltages.

Despite this, Figure 4.22a shows that the faulty operating conditions can be distinguished from transients, because the lowest value of d_a under faulty operating conditions is higher than the largest absolute value of d_n under normal operating conditions. However, by considering the use of the average values of the normalized reference voltages (d_n) when SVM with B_i=250 Hz is employed, a

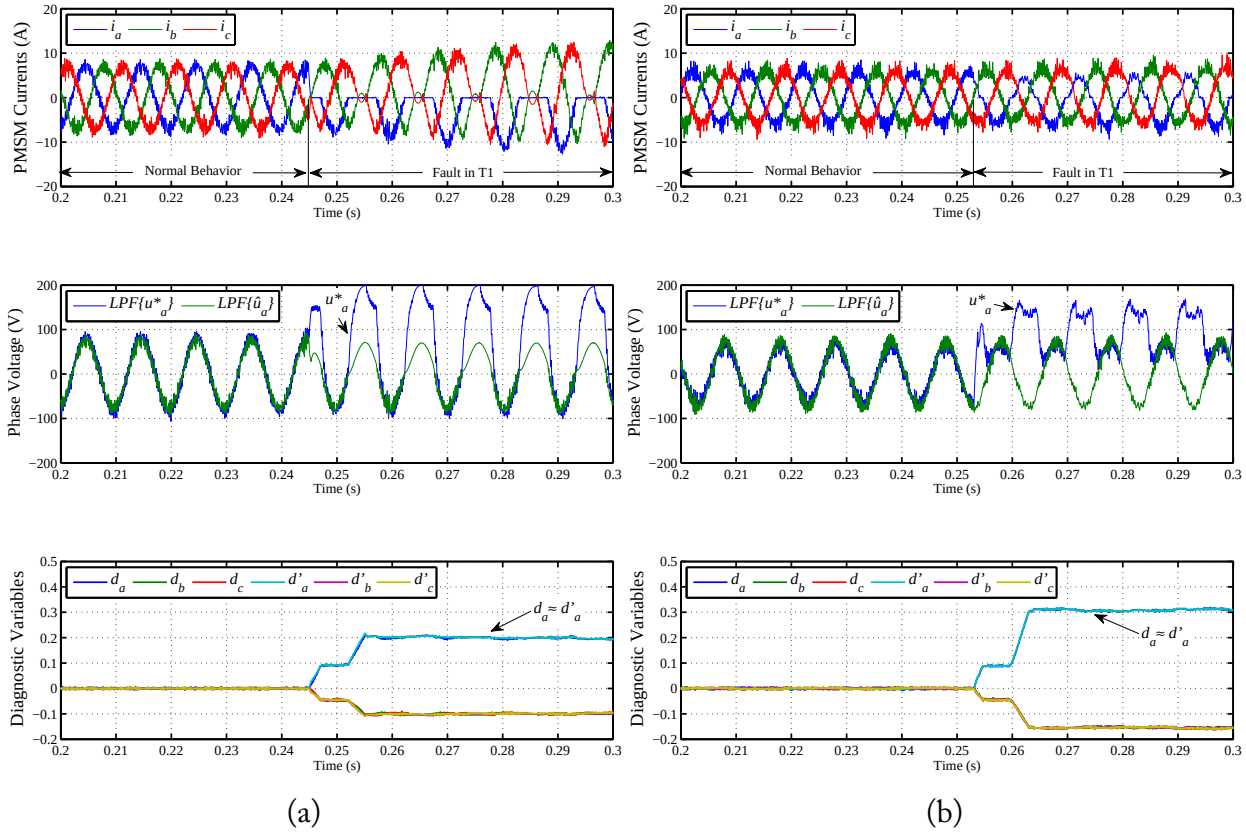

Figure 4.23: Experimental results regarding the PMSM phase currents, reference and estimated voltages (filtered for illustration purposes only) and diagnostic variables, for an open-circuit fault in switch R_1 of the PMSM-side converter under: (a) inverter operation ; (b) rectifier operation.

comfortable safety margin for the definition of the fault detection threshold is not available. In such conditions, it is advisable to use d'_n as diagnostic variables, because they assume lower values under normal operating conditions. But if the control bandwidth is forced to be even lower (for example, due to switching frequency limitations), the desired effectiveness may not be achieved for low load levels, because faults cannot be distinguished from transients and they may remain undetected. Thus, it is concluded that the proposed diagnostic should be only adopted for SVM-based strategies if high current control loop bandwidth is guaranteed (which means that a low current error results in a considerable increase of the reference voltage). A reference value of 500 Hz should be considered as minimum bandwidth of the current control loop, in order to ensure the diagnostic effectiveness over a wide operating range. Otherwise, previously proposed current-based diagnostic techniques must be preferred, which are well suited to counteract the load dependence of the phase currents through more complex algorithms.

Regarding the speed dependence of the proposed diagnostic method, Figure 4.22b shows that the method is independent of the speed when applied to SVM-based strategies, which means that u_f^* assumes a constant value for a given load level. On the other hand, for HCC and DTC applied to

the PMSM-side converter, the diagnostic variable value decreases with the speed increase, because $u_f^*+V_m^*\cos(\omega t)$ in (4.24) remains practically constant, then the increase of V_m^* leads to the reduction of u_f^*, which is more evident with the speed variation due to the high impact on the modulation index. In spite of this, when the modulation index becomes close to the unity, the diagnostic variable remains far from the values assumed under normal operating conditions, permitting to perform the fault diagnosis.

Finally, a similar behavior of the diagnostic technique is observed when it is applied to the grid-side converter (VOC with HCC). The visible differences between the grid- and PMSM-sides in Figure 4.22 (both with HCC) are due to the high and approximately constant modulation index presented by the grid-side converter. Thus, it can be inferred that the diagnostic technique is also suitable for integration with other control strategies applied to the grid-side converter, such as DPC and VOC with SVM.

Fault Detection Threshold Definition - By taking advantage of the previous detailed analysis of the diagnostic variables behavior, the definition of the fault detection threshold value k_d becomes straightforward. It has to be defined between the maximum absolute value of the considered diagnostic variables (d_n or d'_n) under normal operating conditions ($max|d_n|$ or $max|d'_n|$) in Figure 4.20 and the absolute minimum value of the variable corresponding to the faulty phase under faulty operating conditions (Figure 4.22a), which is usually empirically accomplished according to a trade-off between detection speed and robustness against false alarms. However, in order to evaluate the robustness attributed by a given threshold value, a Robustness Factor (RF) can be defined:

$$RF = 1 - \frac{max|d_n|}{k_d} \tag{4.37}$$

Therefore, two case scenarios can be analyzed: (1) d'_n are chosen as diagnostic variables; or (2) d_n are the ones chosen as diagnostic variables. In the first scenario, which is intended to be applied to SVM-based strategies with B_i≥500 Hz, the maximum possible value of k_d is given by the minimum value of d'_n in Figure 4.22 for SVM with B_i=500Hz. Then, k_d can be chosen to be equal to 0.03 when d'_n are used, with the aim to attribute the highest robustness to the minimum bandwidth condition. Consequently, since $max|d'_n|$ is equal to 0.01, the obtained RF is equal to 0.67. An equivalent RF is obtained by using variables d_n with k_d equal to 0.05 (case in which $max|d_n| = 0.017$), representing a good choice according to Figure 4.22. In conclusion, 0.05 and 0.03 can be considered universal threshold values for d_n and d'_n diagnostic variables, respectively. Additionally, it is worth noting that by adopting d'_n with k_d equal to 0.05, an increased robustness against false alarms can be achieved for the other control strategies. Taking DTC as an example, an RF equal to 0.99 is obtained.

4.4 Simulation and Experimental Results - Current Sensor Fault Diagnosis and Fault Tolerance

Vector control (RFOC/VOC) with SVM was implemented for both converters. The parameters of the used machine are given in Table A.1 - Appendix A.

The misinterpretation of harsh transients and the low accuracy at low load levels are usually the main drawbacks of current-based approaches for faults diagnosis. Thus, the behavior of the proposed diagnostic variables during transients and under the presence of faulty conditions must be distinct, allowing the definition of threshold values that guarantee robustness against false alarms as well as independence of the load level. Accordingly, in order to validate the merits of the proposed diagnostic technique, simulation and experimental results regarding abrupt load variations and fault occurrences under different load levels are presented next. At the end, the performance of the fault-tolerant control is also evaluated.

4.4.1 Normalized Currents Average Absolute Values

4.4.1.1 Simulation Results

The same load profile used for the simulation results of section 4.3.2.1 is shown in Figure 4.24. Current sensor faults are introduced in both converters. Figure 4.24 demonstrates that the maximum absolute values assumed by the diagnostic variables under normal operating conditions, as a consequence of a load transient, are much lower than the values presented by them under faulty operating conditions. Thus, a threshold value can be defined to perform a reliable fault diagnosis. In Figure 4.24a, d_{PMSG} and l_a are able to diagnose a current sensor fault in phase a of the PMSG-side converter, while, in Figure 4.24b, a fault in phase A of the grid-side converter is identified through d_{Grid} and l_A.

4.4.1.2 Experimental Results

All the experimental results were carried out at a reference mechanical speed of 600 rpm. Current sensor faults are introduced by setting the sensor output to zero via software.

Normal Operating Conditions - A load step from the generator rated load torque to 16% of the rated torque is shown in Figure 4.25. The variation is introduced at $t = 0.2\ s$, leading to a drastic reduction of both PMSG and grid phase currents. As a consequence of the higher current ripple obtained for the lower load level, the oscillation of the diagnostic variables becomes larger. Nevertheless, they remain near zero and far from the values expected for a current sensor fault (1.19 and 0.66 for d and l_n, respectively). According to Figure 4.25 the highest values assumed by PMSG diagnostic variables d and l_n are 0.064 and 0.047, respectively. Therefore, in order to tolerate high

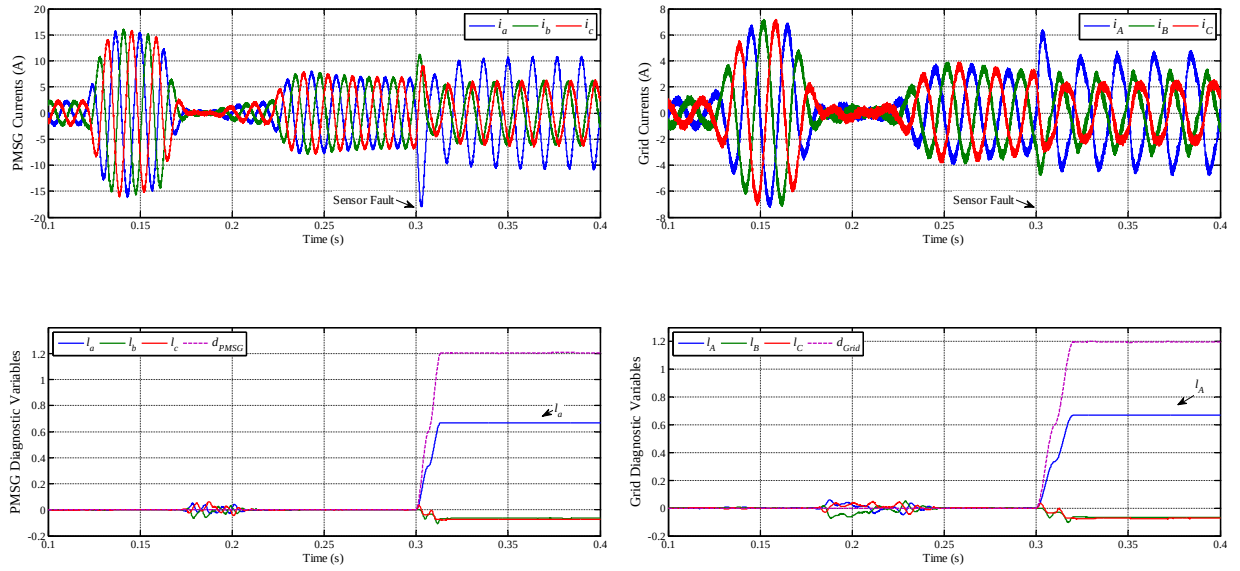

Figure 4.24: Simulation results regarding the time-domain waveforms of the phase currents and the diagnostic variables for: (a) the PMSG-side converter; (b) the grid-side converter.

ripple and noise levels without leading to the generation of false fault alarms, k_d and k_s values can be selected to be equal to 0.4 and 0.2.

Current Sensor Faults - The effects of a current sensor fault in the phase currents as well as the diagnostic variables behavior are shown in Figures 4.26 and 4.27, for both converter sides under two distinct load levels: 20% and 50% of the generator rated torque.

In Figure 4.26a at $t = 0.147\ s$ the current sensor output of the generator phase a is forced to zero. Consequently phase a current is seen as null by the control system, which leads to a phase displacement of 60º between i_b and i_c and the increase of i_a amplitude by a factor of $\sqrt{3}$. Under these conditions, the system efficiency is reduced and both converter and generator are subject to a higher thermal stress, while the electromagnetic torque presents oscillations at twice of the currents fundamental frequency. The detection variable d_{PMSG} and the localization variable l_a increase and tend to 1.1972 and 0.6667, respectively. Therefore, the identification of the faulty sensor is accomplished when both thresholds values k_d and k_s are exceed, which takes a time period equivalent to approximately 25% of the currents fundamental period.

Results for the same fault condition and different load levels are intended to verify that the diagnostic variables behavior is independent of the load level, which becomes clear by comparing Figure 4.26a with Figure 4.26b. It can be seen in Figure 4.26b that with a low load torque equivalent to 20% of generator rated torque and consequently low current amplitude, an effective and accurate diagnostic is also performed.

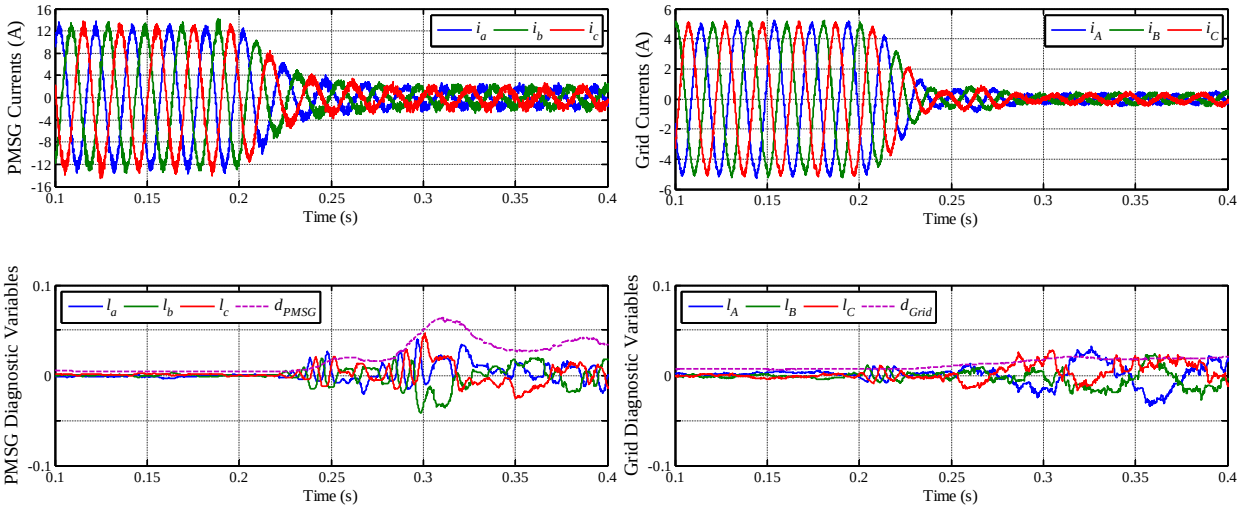

Figure 4.25: Experimental results regarding the time-domain waveforms of the generator phase currents, the diagnostic variables for the generator-side converter, the grid phase currents and the diagnostic variables for the grid-side converter, during a load transient.

When applied to the current measurements of the grid-side converter the diagnostic technique has a similar performance (Figure 4.27), since the impact of a current sensor fault in grid phase currents is identical to the observed for the generator currents.

In Figure 4.27 the fault is introduced in the current sensor of phase *A*, which is successfully identified through d_{Grid} and l_A in time periods corresponding to 40% and 33% of the currents fundamental period. Once more, the diagnostic shows to be load independent and a good accuracy is achieved for low current amplitudes.

Current Sensor Fault-Tolerant System - To achieve a fault-tolerant system, the fault information obtained through the diagnostic technique should allow the control system to trigger suitable remedial procedures. Therefore, as opposed to Figure 4.26 and Figure 4.27, in Figure 4.28 after the diagnostic variables reach the threshold values, the faulty sensor is immediately replaced, by taking advantage of the analytical redundancy given by the use of the three current sensors. Therefore, it can be observed that $i_a = -i_b - i_c$. Since the faulty sensor identification can be accomplished in a time period approximately equal to 40% of the currents fundamental period, a fast recovery of stable closed-loop operation is achieved and the perturbation introduced by the fault occurrence is completely overcome within two fundamental periods.

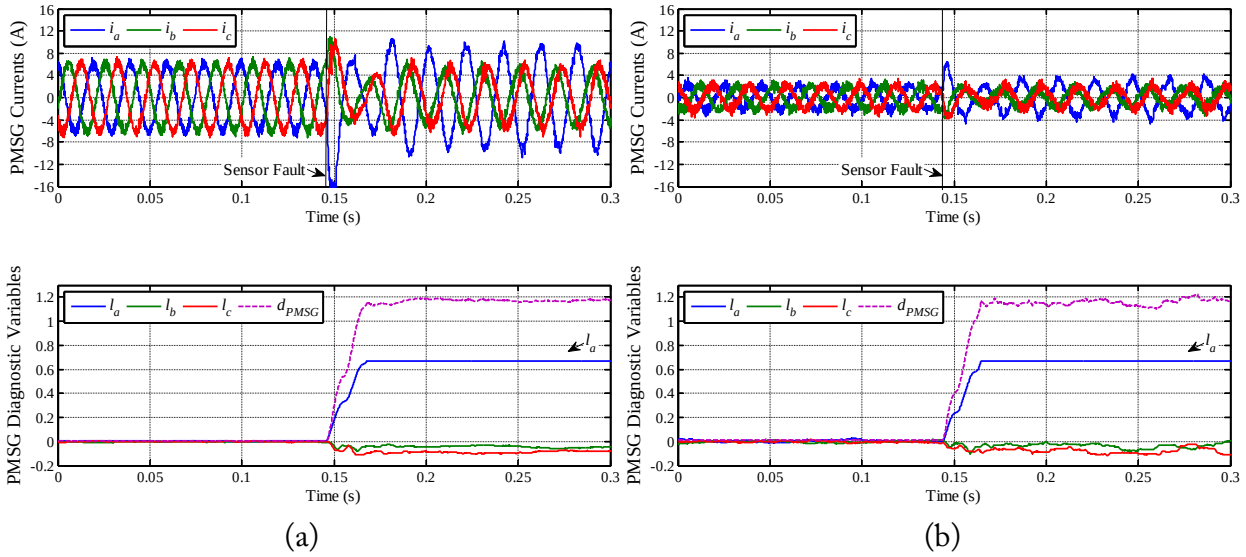

Figure 4.26: Experimental results regarding the time-domain waveforms of the PMSG phase currents and the diagnostic variables for the PMSG-side converter: (a) under 50% of the rated load torque; (b) under 20% of the rated load torque.

4.5 Detection Times and Performance Comparison of the Open-Circuit Fault Diagnostic Methods

Regarding open-circuit fault diagnosis, six algorithms have been proposed for power converter self-diagnostic in this thesis. Therefore, an experimental-based assessment of the six algorithms is included through the analysis of key features such as detection speed, localization capabilities, implementation effort, computational burden and tuning effort. The results obtained allow to compare their performances and they are a valuable contribution for assessing the applicability of the diagnostic techniques to a specific drive system.

To recapitulate, the proposed fault diagnostic methods are the following ones: current Park's Vector phase (CPVP); current polarity (CP); errors of the normalized currents average absolute values using the Park's Vector modulus as normalization quantity (ENCAAV-CPVM); errors of the normalized currents average absolute values using the instantaneous maximum value of the currents absolute values as normalization quantity (ENCAAV-CMax); average values of the normalized reference voltages (AVNRV); and average values of the normalized voltage errors (AVNVE).

Firstly, the detection speed is analyzed by using Figure 4.29 and Table 4.6, taking into account the previously proposed threshold values. Figure 4.29 shows that the detection speed depends on the instant of the phase current period in which the fault occurs, which is common to both current-based and voltage-based diagnostic techniques. The noticeable increase of the detection times when the fault angle becomes close to 180º (Figure 4.29a), and subsequent higher detection times, is due to the fact that a fault in the upper switch R_1 or I_1 is always considered, which means that the

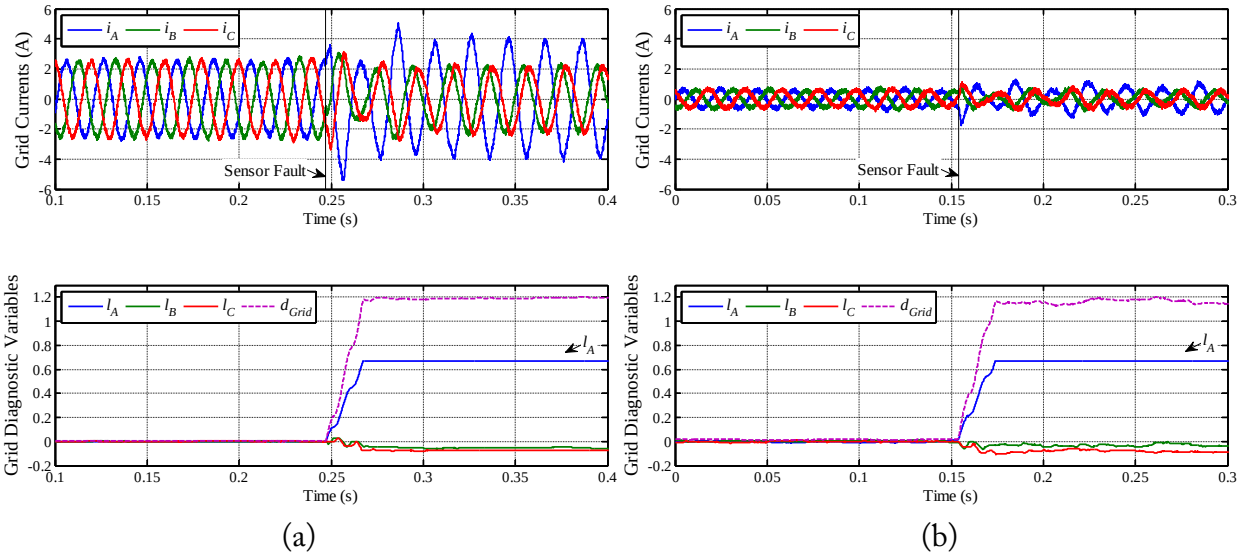

Figure 4.27: Experimental results regarding the time-domain waveforms of the grid phase currents and the diagnostic variables for the grid-side converter: (a) under 50% of the rated load torque; (b) under 20% of the rated load torque.

current in the faulty phase is affected during the positive half-cycle (0-180º) only. Figure 4.29 demonstrates that the proposed techniques are well suited for triggering remedial procedures in fault-tolerant systems, since detection times are always below one fundamental period of the phase currents. Furthermore, a clear distinct pattern is found for the detection times, depending on the converter operation mode (Figure 4.29), because the phase current waveforms are less affected when the converter operates as a rectifier. Accordingly, the CP method cannot be employed, and the remaining current-based approaches present a considerable increase of the detection times during this operation mode (PMSG-side converter). On the other hand, voltage-based approaches show a similar behavior for both operation modes, thus, being better suited for the PMSG-side converter. Table 4.6 also summarizes the detection speed results, showing the minimum, maximum and average detection times achieved by each technique.

Concerning a fault in IGBT I_1 of the grid-side converter (Figure 4.29a), the slowest detection is accomplished by the CP method, while the fastest is achieved by the AVNVE method. All the others show an identical performance, so, their comparison should be based on further parameters such as the ones in Table 4.7. For the PMSG-side converter, considering a fault in IGBT R_1, Figure 4.29b and Table4.6 show that AVNVE method is also the fastest one, whereas current-based approaches (CPVP, ENCAAV-CPVM, ENCAAV-CMax) present higher and identical detection times.

The localization capabilities of the proposed methods are quantified by the number of fault signatures that each one is able to distinguish. The CPVP method is intended to detect a fault only. The CP method distinguishes 27 fault signatures, but it cannot be applied to the PMSG-

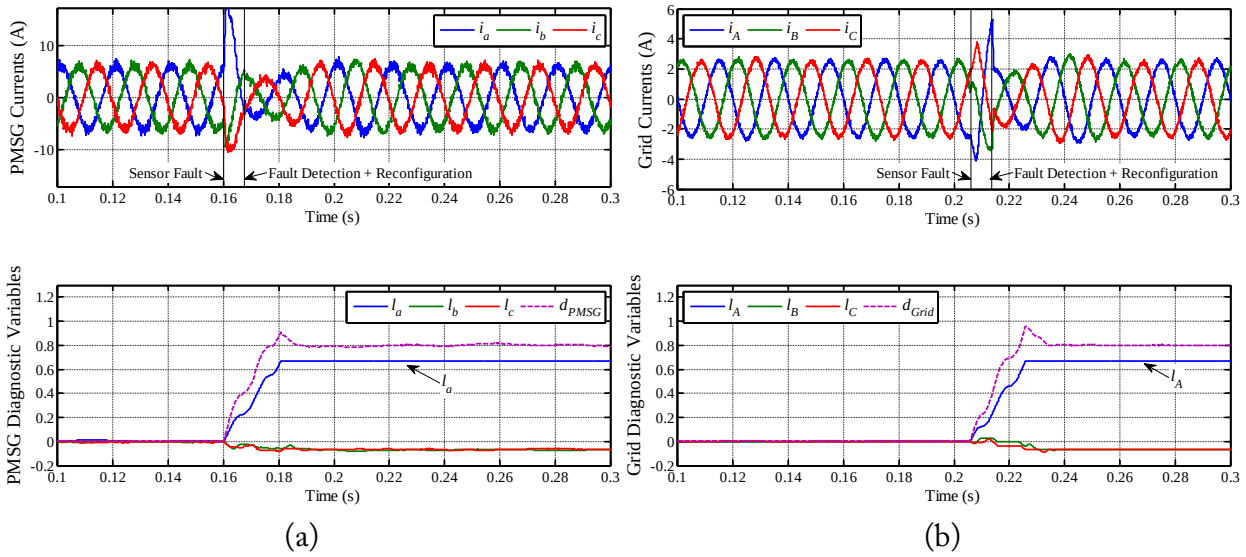

Figure 4.28: Experimental results regarding the time-domain waveforms of the phase currents and the diagnostic variables under 50% of the rated load torque for : (a) the PMSG-side converter; (b) the grid-side converter.

Table 4.6: Fault diagnostic methods detection speed (% of the current period).

		CPVP	CP	ENCAAV CPVM	ENCAAV CMax	AVNRV	AVNVE
Inverter Operation (Grid-side)	Min	4	49	5	6	10	5
	Max	64	98	62	64	60	56
	Avg	26	83	27	27	29	20
Rectifier Operation (PMSG-side)	Min	5	-	7	8	8	5
	Max	89	-	85	88	59	55
	Avg	44	-	45	47	28	20

side converter. All the other localization methods are suitable for the PMSG-side converter, and their localization capabilities are shown in Table 4.7. The ENCAAV-CPVM method is able to discriminate single switch and single phase open-circuit faults (9 fault signatures). A simplified version of the ENCAAV-CPVM method (SENCAAV-CPVM) is also considered here, where the normalized average values are not used. The SENCAAV-CPVM provides only information about the faulty converter leg (3 fault signatures), similarly to the ENCAAV-CMax, making the comparison between this two methods possible. Finally, AVNRV and AVNVE methods are able to discriminate single switch open-circuit faults (6 fault signatures).

The effort required to implement an algorithm is related to the number of mathematical, logic and other operations involved, as well as the complexity of the decision-making process. A good way to quantify this is through the size of the programming code, which is shown in Table 4.7.

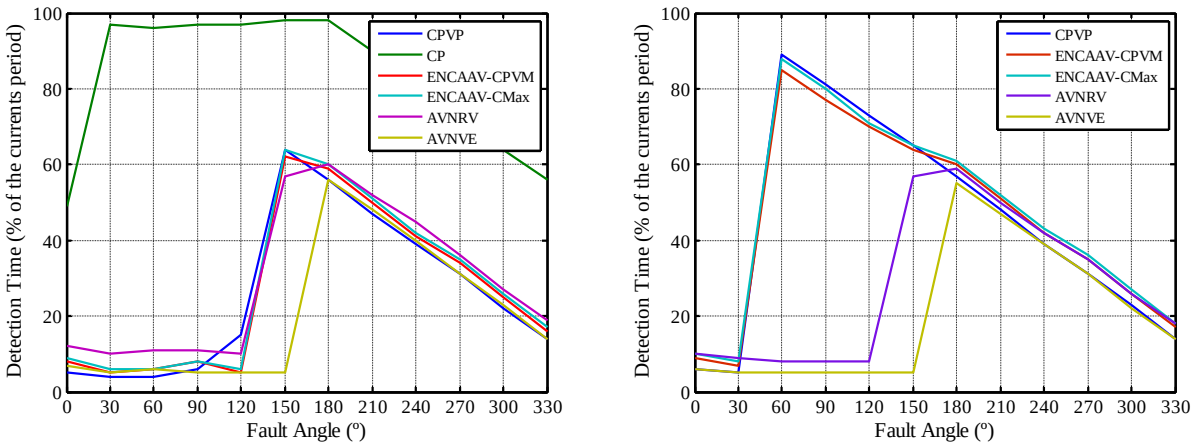

Figure 4.29: Experimental results regarding the detection times of an open-circuit fault in: (a) IGBT I_1 of the grid-side converter; (b) IGBT R_1 of the PMSG-side converter.

Table 4.7: Fault diagnostic methods key features evaluation.

	CPVP	**CP**	**ENCAAV CPVM**	**SENCAAV CPVM**	**ENCAAV CMax**	**AVNRV**	**AVNVE**
Localization Capabilities (Fault Signatures)	1	27	9	3	3	6	6
Implementation Effort (File Size in kB)	37	41	52	47	36	38	63
Computational Burden (Execution Time in µs)	1.1	3.2	3.5	1.9	1.7	2.0	4.3
Tuning Effort (Parameters Number)	2	2	1	1	1	1	1

Therefore, the less complex codes, with similar sizes, are CPVP, ENCAAV-CMax and AVNRV methods. Also taking into account the localization capabilities, the AVNRV method might be considered the simplest one. The AVNVE method turns out to be the more complex method, as a consequence of the voltage observer inclusion.

The computational requirements of a given algorithm depend on how complex and demanding is the implemented programming code. One way to quantify this is to measure the computational burden taken by the controller to perform all the algorithm calculations. Following the procedure described in [159], the average execution times taken by each algorithm in the dSPACE DS1103 controller are presented in Table 4.7. Reflecting the implementation effort, CPVP, ENCAAV-CMax and AVNRV methods together with SENCAAV methods have the lowest execution times. Once again, due to the voltage observer inclusion, AVNVE method is the most computationally demanding.

The tuning effort is related to the number of parameters that have to be tuned in order to achieve

the desired performance tradeoff, and the complexity of their tuning procedure. The required parameters are the threshold values for fault detection, and the cutoff frequency of the low-pass filters in the case of the CPVP method. The complexity of the parameters tuning procedure can be considered similar, since they are all established empirically by analyzing the diagnostic variables behavior. Additionally, some methods require the knowledge of some rated values of the system, such as current and frequency, which are easily obtained from the machine or converter name plate.

4.6 Summary

All the proposed diagnostic methods fulfill the requirements for their integration into a drive controller and real-time implementation, namely, lack of need for extra hardware, simple implementation and low computational requirements. Furthermore, their effectiveness and accuracy is independent of the operating conditions, they are robust to transients, such as load and speed variations, and fault diagnosis is accomplished in a relatively short period of time. Thus, these methods have the required features to be accepted by the industry and to be integrated into a fault-tolerant drive.

In summary, with respect to open-circuit faults, the proposed current-based approaches are endowed with a remarkable robustness against false alarms thanks to the inclusion of the dedicated detection algorithm based on the derivative of the absolute current Park's Vector phase (CPVP method). If the information about the faulty phase is sufficient, the method of the errors of the normalized currents average absolute values using the instantaneous maximum value of the currents absolute values as normalization quantity (ENCAAV-CMax) excels at simplicity and low computational effort. On the other hand, if the exact localization of the faulty switch is required through a very simple algorithm, the proposed voltage-based approaches might be optimum choices. However, these techniques are especially suitable for drives with high dynamic performance, such as those incorporated with DTC and HCC strategies, and when employed together with SVM a high current control loop bandwidth must guaranteed.

Provided that a current sensor per phase is available, which is quite common in industrial drives, tolerance to current sensor faults with a fast recovery of stable closed-loop operation was demonstrated to be successfully accomplished by means of a low demanding current-based algorithm.

Chapter 5

Alternative Converter Topologies and Control Strategies for Post-Fault Operation

A fault-tolerant converter is intended to maintain its operation after an internal fault occurrence until a maintenance operation can be scheduled, with an acceptable performance and without endangering the overall system. Considering open-circuit faults, generally, hardware reconfiguration for circuit topology rearrangement is compulsory as well as software reconfiguration for an effective control of the obtained power converter.

The design of a fault-tolerant drive is of prime importance, and it has to take into account the tradeoff between post-fault performance and cost increase. Naturally, to achieve the same performance under normal operation and under post-fault operation a more expensive solution is required, which typically includes redundant components to directly replace the faulty components. Such approach is justified for applications in which the safety of people is involve, for instance, airplanes and nuclear plants [105]. Alternatively, allowing the drive to operate in a degraded mode and within a limited operating range, more cost-effective and non-redundant solutions can be adopted. In such non-redundant fault-tolerant converters, a converter topology different from the one used under normal operation is used under post-fault operation, seeking to minimize the overall cost increase. This reconfiguration is usually accomplished by means of additional low cost switches, such as relays or TRIACs. In addition to the hardware reconfiguration, control strategies and their reference values might need to be redefined. Therefore, taking into account that non-redundant fault-tolerant converters are economically attractive and that they demand new and optimized control strategies, they are the main focus of this thesis.

Different converter topologies have been adopted in the literature to endow a two-level voltage source converter with fault-tolerant capabilities. Firstly, considering the redundant fault-tolerant converters, a redundant leg can be connected to all the converter phases through TRIACs [107], [160]-[162], permitting the replacement of the faulty leg and keeping the same converter topology and respective control strategy. An extra leg connected to the machine neutral point is another

alternative topology [163]-[165], where the healthy phase currents increase by a factor of $\sqrt{3}$ and the extra leg should be designed with a current rating three times as high as the standard converter to achieve the normal rated conditions.

With respect to the non-redundant fault-tolerant converters, the four-switch three-phase converter (FSTPC) has been addressed in various studies, by connecting the midpoint of the dc bus to the converter phases [111], [166]-[168] or to the machine neutral point [97], [169]-[171]. As a consequence of the reduced number of switches, in comparison with the conventional six-switch voltage source converter, these topologies have a reduced output voltage capability, for instance, the maximum output voltage is halved by connecting the midpoint of the dc bus to a converter phase. Furthermore, the phase currents increase by a factor of $\sqrt{3}$ when the midpoint of the dc bus and the neutral point are connected. Such issues lead to the need for oversizing the drive components or derating the system under post-fault operation.

Regarding the control of the aforementioned converters, vector control strategies are widely used, and their performance has been optimized through various distinct PWM techniques, with goals such as torque ripple minimization [172], current distortion reduction [173]-[174] and dc-link imbalance compensation [168], [175]-[178]. On the other hand, direct control techniques have been less applied in fault-tolerant converters, and few studies have been reported on fault-tolerant converters with DTC [169], [179]-[182]. DPC with fault-tolerant capabilities was proposed in [183] by employing a FSTPC.

In a back-to-back converter, the phases of both sides (grid/machine) can also be connected to each other through TRIACs [184]-[187]. Therefore, under post-fault operation one leg is shared and the converter is usually called a five-leg converter, requiring switches with power rating four times higher to reach the rated conditions.

Concerning a fault-tolerant PMSG dive for WECS, a three-switch three-phase rectifier (TSTPR) was proposed for post-fault operation of the generator-side converter in order to avoid extra hardware [183], [188]-[189], both DTC and vector control strategies were considered.

Alternatively to the two-level converter, multilevel converters can offer a wide range of fault-tolerant options, due to the inherent redundancies and modularity of such topologies. Modular structures such as cascade H-bridge and flying capacitor converters are very attractive and fault tolerance is usually straightforward to achieve through the bypass of the faulty module [190]. In the case of the neutral-point-clamped converter, extra hardware is usually required [191]-[192], and similar solutions to the ones adopted for the two-level converter are also employed [193]. Some contributions towards fault tolerant operation of multilevel converters can be found in [194]-[197]. However, further research on this subject is mandatory in order to effectively increase the reliability of multilevel converters [198].

Modular power converters, with cascade H-bridge modules, for direct-drive wind turbines were addressed in [199]-[200] with the aim of achieving fault tolerance. Modular converters, with two-

level back-to-back converters, are a common option for high power wind turbines [20],[201], whose modularity can be exploited to increase reliability. Therefore, post-fault operation is possible by isolating the faulty module and reducing the maximum output power.

In this work, four converter topologies and respective control strategies are proposed as alternatives for post-fault operation of a PMSG drive. For post-fault operation of the PMSG-side converter, a three-switch three-phase rectifier (TSTPR) is addressed, whereas three distinct topologies are analyzed for the grid-side converter: a four-switch three-phase converter with a phase connected to dc-bus midpoint (FSTPC-PCM); a four-switch three-phase converter with the transformer neutral point connected to dc-bus midpoint (FSTPC-NCM); and a five-leg converter (FLC) with the shared-leg connected to a phase of the generator and to the grid transformer neutral point.

5.1 Three-Switch Three-Phase Rectifier for the PMSG-Side Converter

On the generator-side converter there is no need for hardware reconfiguration, because an alternative path for the current is available through the diodes, hence, additional hardware is avoidable. The fault isolation consists of the inhibition of the control signals of the three upper or bottom power switches (Figure 5.1), depending on whether an upper or a bottom IGBT is faulty, respectively. Although the fault isolation allows the generator to achieve a balanced operation (concerning the phase currents), the semi-controlled rectification leads to an increased distortion of the phase currents and oscillation of the generator electromagnetic torque. Accordingly, to guarantee continuous operation of the PMSG drive, the reduction of the torque oscillation is the main goal of the control strategies proposed in this section.

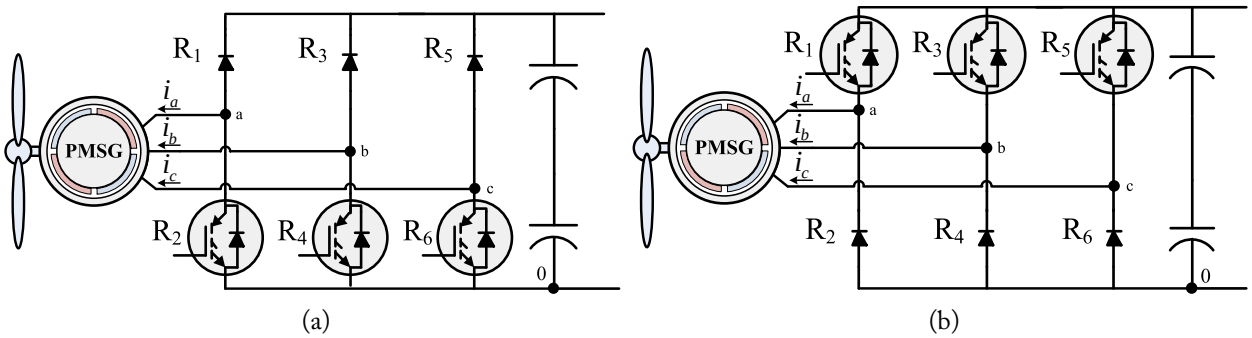

Figure 5.1: Three-switch three-phase rectifier for post-fault operation of the PMSG-Side converter, considering an open-circuit fault in: (a) one of the upper switches (R_1, R_3, R_5); (b) one of the bottom switches (R_2, R_4, R_6).

When controlling a TSTPR, there are parts of the complex plane where a reduced number of converter voltage vectors are available [202]-[205], because the TSTPR works partially as a non-

controlled rectifier. Consequently, the current control in one or two phases might be impossible, depending on the currents polarity, which implies that sinusoidal currents cannot be shaped. Taking as an example the case in which all upper IGBTs are in open-circuit (Figure 5.1a), for the generator phase currents assuming positive values they must flow through the bottom diodes (freewheeling diodes R_2, R_4 and R_6). Thus, during the period of time in which a phase current is positive, the phase current flow is independent of the respective IGBT switching state as well as the phase-to-zero voltages:

$$u_{n0} = \begin{cases} V_{dc}S_n, & if\ i_n < 0 \\ 0, & if\ i_n > 0 \end{cases},\ n = a,\ b,\ c \tag{5.1}$$

Firstly, it is not taken into consideration the case in which $i_n = 0$, and the phase voltages are expressed as follows:

$$\begin{cases} u_{an} = \frac{1}{3}V_{dc}(2S_an_a - S_bn_b - S_cn_c) \\ u_{an} = \frac{1}{3}V_{dc}(2S_bn_b - S_an_a - S_cn_c) \\ u_{an} = \frac{1}{3}V_{dc}(2S_cn_c - S_an_a - S_bn_b) \end{cases} \tag{5.2}$$

where n_n defines if the current in phase n is negative ($n_n = 1$) or positive ($n_n = 0$):

$$n_n = \frac{1 - sgn(i_n)}{2} \tag{5.3}$$

and the sign function is given by:

$$sgn(i_n) = \begin{cases} 1, & if\ i_n > 0 \\ -1, & if\ i_n < 0 \end{cases},\ n = a,\ b,\ c \tag{5.4}$$

Lastly, the space voltage vectors in $\alpha\beta$ axes are deduced as:

$$\begin{cases} u_{c\alpha} = \frac{1}{3}V_{dc}(2S_an_a - S_bn_b - S_cn_c) \\ u_{c\beta} = \frac{1}{\sqrt{3}}V_{dc}(S_bn_b - S_cn_c) \end{cases} \tag{5.5}$$

It becomes clear that the converter space voltage vectors depend on the switching states as well as on the phase currents polarity. Since $i_a + i_b + i_c = 0$ implies that the three currents never assume negative values simultaneously, the available voltage vectors are limited to four, when two of the phase currents are negative, or to two, if only one is negative. According to the sector definition in Figure 2.7, the available voltage vectors are summarized in Tables 5.1 and 5.2.

Moreover, if a phase current becomes null and the respective phase voltage is positive, it remains null till the phase voltage becomes negative and the bottom diode forward biased. During this time period the voltage in that phase is equal to the back electromotive force, and the converter generates

Table 5.1: Voltage space vectors of the TSTPR with bottom switches.

Stator Voltage Sector	I	II	III	IV	V	VI
Two Negative Phase Currents	V_0	V_0	V_0	V_0	V_0	V_0
	V_1	V_1	V_3	V_3	V_1	V_1
	V_2	V_2	V_4	V_4	V_5	V_5
	V_3	V_3	V_5	V_5	V_6	V_6
One Negative Phase Current	V_0	V_0	V_0	V_0	V_0	V_0
	V_1	V_3	V_3	V_5	V_5	V_1

Table 5.2: Voltage space vectors of the TSTPR with upper switches.

Stator Voltage Sector	I	II	III	IV	V	VI
Two Positive Phase Currents	V_1	V_2	V_2	V_4	V_4	V_1
	V_2	V_3	V_3	V_5	V_5	V_2
	V_6	V_4	V_4	V_6	V_6	V_6
	V_7	V_7	V_7	V_7	V_7	V_7
One Positive Phase Current	V_7	V_7	V_7	V_7	V_7	V_7
	V_2	V_2	V_4	V_4	V_6	V_6

a non-defined and floating voltage vector. Hence, it can be concluded that the minimum current distortion should be achieved with current and voltage in phase opposition (unity power factor), reducing to a minimum time period with null current and increasing the current conduction through the diodes. If the phase displacement between current and voltage space vectors becomes different from 180º, the area of the complex plane with reduced number of voltage vectors increase, degrading the phase current waveforms. A detailed analysis of the phase currents in a half-controlled converter is presented in [206], showing their dependence on the power factor.

5.1.1 RFOC with HCC

Through the mathematical model of a surface-mounted PMSG (SPMSG) in the synchronous reference frame, and neglecting R_s, the stator voltage space vector (u_s) is given by:

$$u_s = R_s i_s + j\omega_s \psi_s \approx j\omega_s \psi_s \tag{5.6}$$

To neglect the stator resistance (Rs) is generally valid for high power machines as well as for low power machines operating in the high speed range.

Typically, in vector control strategies for SPMSGs, i_{sd} is set to zero to maximize the torque per ampere ratio, as illustrated in Figure 5.2a. Consequently, the displacement between i_s and ψ_s is load dependent, being reduced with the load increase (δ increases). Thus, such control strategy applied to a TSTPR leads to a higher current distortion as the load increases (longer time periods with null current), consequently, the torque ripple also increases.

To achieve minimized current distortion given by a constant displacement between i_s and u_s

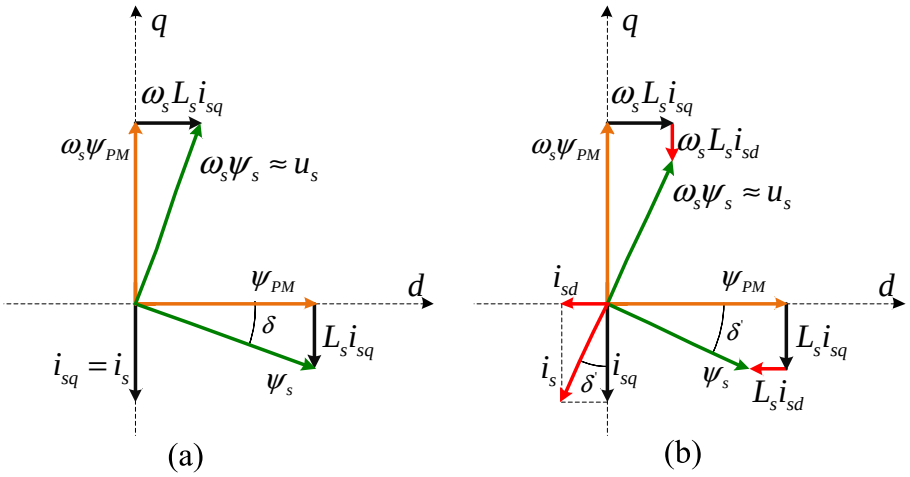

Figure 5.2: Vector control phasor diagram: (a) $i_{sd}^* = 0$; (b) i_{sd}^* controlled to minimize the torque ripple when using a TSTPR.

equal to 180º (equivalent to i_s lagging ψ_s by 90º, neglecting R_s) (Figure 5.2b), the angle between the stator current space vector (i_s) and its q-axis component must be equal to angle between the stator and rotor flux space vectors (δ'), verifying that:

$$\tan \delta' = \frac{|\psi_{sq}|}{|\psi_{sd}|} = \frac{|i_{sd}|}{|i_{sq}|} = \frac{|i_{sq}|}{\frac{\psi_{PM}}{L_s} - |i_{sd}|} \tag{5.7}$$

By solving the quadratic equation resulting from (5.7):

$$-|i_{sd}|^2 + \frac{\psi_{PM}}{L_s}|i_{sd}| - |i_{sq}|^2 = 0 \tag{5.8}$$

in order to $|i_{sd}|$, the absolute value of the d-axis stator currents is given as function of i_{sq} by:

$$|i_{sd}| = \frac{1}{2}\left[\frac{\psi_{PM}}{L_s} - \sqrt{\left(\frac{\psi_{PM}}{L_s}\right)^2 - 4\left(i_{sq}\right)^2}\right] \tag{5.9}$$

with real solution for $|i_{sq}| \leq \psi_{PM}/(2L_s)$. As a consequence of i_{sd} being different from zero, i_{sq} must be limited in accordance with:

$$i_{sd}^2 + i_{sq}^2 \leq I_s^2 = I_{sq}^2, \; I_{sq} = \frac{2}{3}\frac{T_n}{p\psi_{PM}} \tag{5.10}$$

to avoid exceeding the machine rated current I_s (considered equivalent to the current generated at the rated torque (T_n) with $i_{sd} = 0$: I_{sq}). Then, by substituting (5.9) in (5.10), the new maximum value of the stator current component responsible for the developed torque is obtained:

$$I'_{sq} = \frac{L_s}{\psi_{PM}} I_{sq} \sqrt{\left(\frac{\psi_{PM}}{L_s}\right)^2 - \left(I_{sq}\right)^2} = 0 \tag{5.11}$$

Accordingly, for an operation with i_{sd} equal to (5.9), a torque reduction factor can be defined by I'_{sq}/I_{sq}.

With the aim to minimize the torque ripple, the d-axis stator current component can be generated in feedforward manner, by imposing the following reference value:

$$i^*_{sd} = -\frac{1}{2}\left[\frac{\psi_{PM}}{L_s} - \sqrt{\left(\frac{\psi_{PM}}{L_s}\right)^2 - 4\left(i^*_{sq}\right)^2}\right], \; |i^*_{sq}| \leq I'_{sq} \tag{5.12}$$

where i^*_{sq} stands for reference q-axis current generated by the speed controller (Figure 5.3). By using the reference value instead of the actual one of the q-axis current, an additional coordinate transformation is avoided as well as an additional low-pass filter to attenuate the noise presented in the measured currents. It should be pointed out that i_{sd} is always intended to be negative, for generator operation with positive speed and negative i_{sq} as well as with negative speed and positive i_{sq}.

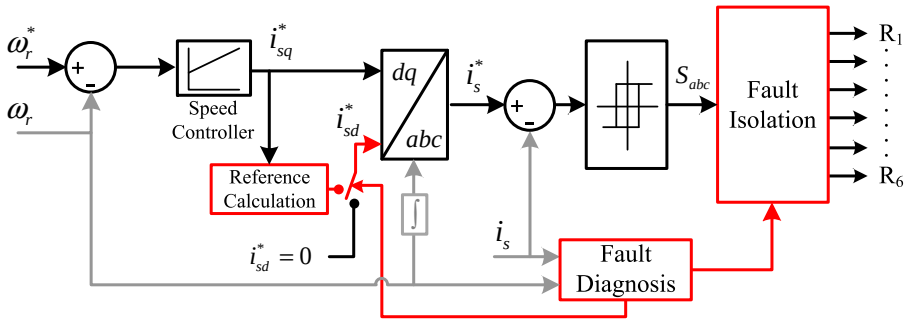

Figure 5.3: Block diagram of the fault-tolerant RFOC strategy with HCC for the PMSG-side converter.

The block diagram of the proposed RFOC strategy with fault-tolerant capabilities is depicted in Figure 5.3, where the fault diagnostic technique triggers the fault isolation and the control of i_{sd} by imposing (5.12) as reference value. The simple feedforward control of i_{sd} for reducing the torque ripple will work properly whether the error of the machine parameter estimation is negligible. In the case of a rough parameter estimation, it is recommended to select a higher value for ψ_{PM}/L_s, avoiding an excessive increase of the stator current. It is worth noting that neglecting R_s in a low power machine operating at low speed has a similar contribution.

As an example, the machine parameters of Table A.1 - Appendix A are used to illustrate the impact of the proposed compensation method in the PMSG stator current; $|i_{sq}|$, $|i_{sd}|$ (5.9), and $|i_s|$ are shown in Figure 5.4 as function of the electromagnetic torque together with experimental results for three distinct load levels (25%, 50% and 75% of the rated torque), using I_{sq} and T_n as base quantities. Figure 5.4 shows that i_{sq} increases linearly with the torque, whereas i_{sd} increases quadratically. The rated current is achieved for a torque equivalent to 83% of T_n, and at 89% of T_n the maximum real solution of $|i_{sd}|$ is reached (which is fixed for higher torque levels, meaning that further compensation of the torque ripple is not performed)

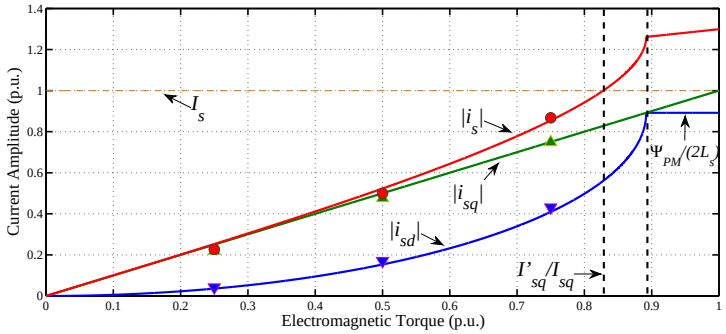

Figure 5.4: Stator current as function of the electromagnetic torque for the proposed torque ripple minimization strategy: theoretical values (lines) and experimental results for 25%, 50% and 75% of the PMSG rated torque (markers).

5.1.2 RFOC with SVM

Despite the extremely simplicity of HCC, the variable switching frequency is a major drawback, which is overcome in the RFOC strategy by introducing SVM (section 2.2.1.2). Accordingly, a suitable voltage modulator (SVM) is proposed, by revising the symmetric PWM switching pattern for the SSTPC in Table 2.2.

In the SVM block for the SSTPC, the switching time for the null vector (t_0) is equally divided by $V_0(000)$ and $V_7(111)$. However, only one null vector can be synthesized by the TSTPR, as can be seen in Tables 5.1 and 5.2. Thus, only one null vector should be used to ensure that it is always synthesized. Accordingly, the vectors sequence and respective switching times should be modified to synthesize a voltage vector as close as possible to the reference voltage and to reduce the number of commutations. This can be accomplished if the PWM period starts and ends with the available null vector, which is applied during the whole time period t_0. The resultant vectors sequence and timing plan are presented in Tables 5.3 and 5.4 for the two case scenarios of a TSTPR with bottom switches and a TSTPR with upper switches, respectively. Naturally, the correct sequence is chosen with basis on the fault diagnosis information.

Table 5.3: SVM voltage vectors sequence for the TSTPR with bottom switches.

Sector	Voltage Vector Sequence	Voltage Vector Timing
I	$V_0 \rightarrow V_1 \rightarrow V_2 \rightarrow V_1 \rightarrow V_0$	$t_0 \rightarrow t_x \rightarrow 2t_y \rightarrow t_x \rightarrow t_0$
II	$V_0 \rightarrow V_3 \rightarrow V_2 \rightarrow V_3 \rightarrow V_0$	$t_0 \rightarrow t_y \rightarrow 2t_x \rightarrow t_y \rightarrow t_0$
III	$V_0 \rightarrow V_3 \rightarrow V_4 \rightarrow V_3 \rightarrow V_0$	$t_0 \rightarrow t_x \rightarrow 2t_y \rightarrow t_x \rightarrow t_0$
IV	$V_0 \rightarrow V_5 \rightarrow V_4 \rightarrow V_5 \rightarrow V_0$	$t_0 \rightarrow t_y \rightarrow 2t_x \rightarrow t_y \rightarrow t_0$
V	$V_0 \rightarrow V_5 \rightarrow V_6 \rightarrow V_5 \rightarrow V_0$	$t_0 \rightarrow t_x \rightarrow 2t_y \rightarrow t_x \rightarrow t_0$
VI	$V_0 \rightarrow V_1 \rightarrow V_6 \rightarrow V_1 \rightarrow V_0$	$t_0 \rightarrow t_y \rightarrow 2t_x \rightarrow t_y \rightarrow t_0$

Table 5.4: SVM voltage vectors sequence for the TSTPR with upper switches.

Sector	Voltage Vector Sequence	Voltage Vector Timing
I	$V_7 \rightarrow V_2 \rightarrow V_1 \rightarrow V_2 \rightarrow V_7$	$t_0 \rightarrow t_y \rightarrow 2t_x \rightarrow t_y \rightarrow t_0$
II	$V_7 \rightarrow V_2 \rightarrow V_3 \rightarrow V_2 \rightarrow V_7$	$t_0 \rightarrow t_x \rightarrow 2t_y \rightarrow t_x \rightarrow t_0$
III	$V_7 \rightarrow V_4 \rightarrow V_3 \rightarrow V_4 \rightarrow V_7$	$t_0 \rightarrow t_y \rightarrow 2t_x \rightarrow t_y \rightarrow t_0$
IV	$V_7 \rightarrow V_4 \rightarrow V_5 \rightarrow V_4 \rightarrow V_7$	$t_0 \rightarrow t_x \rightarrow 2t_y \rightarrow t_x \rightarrow t_0$
V	$V_7 \rightarrow V_6 \rightarrow V_5 \rightarrow V_6 \rightarrow V_7$	$t_0 \rightarrow t_y \rightarrow 2t_x \rightarrow t_y \rightarrow t_0$
VI	$V_7 \rightarrow V_6 \rightarrow V_1 \rightarrow V_6 \rightarrow V_7$	$t_0 \rightarrow t_x \rightarrow 2t_y \rightarrow t_x \rightarrow t_0$

The block diagram of the proposed fault-tolerant RFOC strategy with SVM is depicted in Figure 5.5, using the TSTPR under post-fault operation. Reduced oscillation of the electromagnetic torque under post-fault operation is achieved combining the modified modulator (SVM) with the control of i^*_{sd} proposed in the previous section (section 5.1.1).

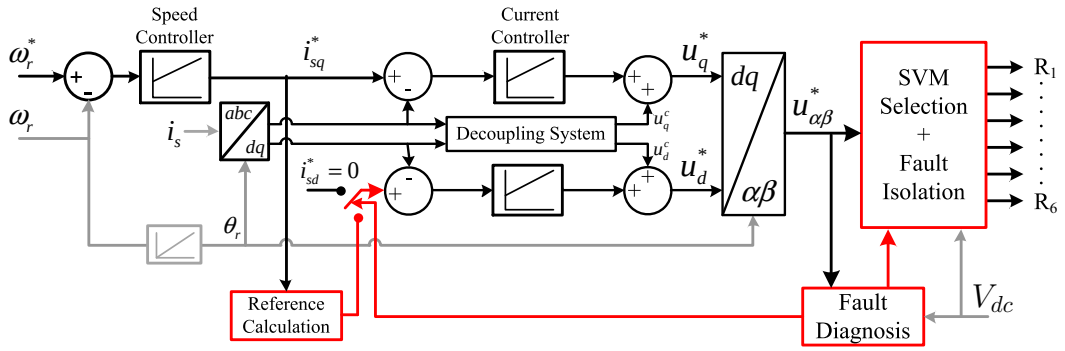

Figure 5.5: Block diagram of the fault-tolerant RFOC strategy with SVM for the PMSG-side converter.

5.1.3 Conventional DTC

The block diagram of the fault-tolerant DTC strategy proposed is shown in Figure 5.6. Under normal operation the conventional DTC is implemented to control the generator speed (ω_r), imposing a fixed reference flux (ψ^*_s). The current model based flux estimator (2.32) is adopted to avoid additional voltage sensors, because in a semi-controlled rectifier the switching states information is insufficient to reconstruct the machine terminal voltages. After a fault occurrence, the fault diagnosis indicates which three switches must be isolated, either the upper (R_1, R_3, R_5) or the bottom ones (R_2, R_4, R_6), and, accordingly, an optimized switching table is selected.

With a DTC strategy, the limited performance of a TSTPR results in a reduced capability to control the stator flux. However, the ability to keep a reduced torque oscillation makes DTC quite interesting for controlling a TSTPR for generator applications.

Firstly, taking as an example the TSTPR with bottom switches (all the upper IGBTs are in

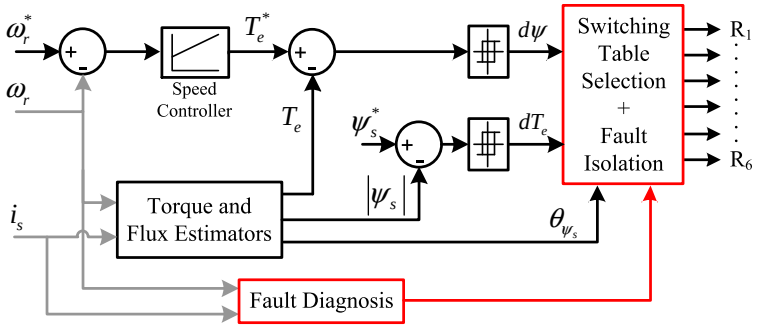

Figure 5.6: Bolck diagram of the fault-tolerant DTC strategy for the PMSG-side converter.

open-circuit) (Figure 5.1a), it is worth noting that for the generator phase currents to assume positive values they must flow through the bottom diodes (freewheeling diodes R_2, R_4 and R_6), which is possible while the respective phase voltage presents the lowest terminal voltage (during 120º) or the phase current is forced by the other two phases. In a similar way, with the bottom IGBTs in open-circuit, the phase currents are forced to flow through the upper diodes when the respective phase voltage presents the highest terminal voltage. Thus, during 120º, each phase of the TSTPR behaves similarly to a non-controlled three-phase rectifier, whose operation is summarized in Table 5.5. The phase voltages in Table 5.5 are presented as a function of the stator flux vector position, by neglecting the stator resistance and then considering that the flux vector always lags the voltage vector by 90º.

Table 5.5: Non-controlled three-phase rectifier operation.

		I	II	III	IV	V	VI
Phase Voltages	Lowest	u_{cn}	u_{an}	u_{an}	u_{bn}	u_{bn}	u_{cn}
	Highest	u_{bn}	u_{bn}	u_{cn}	u_{cn}	u_{an}	u_{an}
Diodes in conduction		R6 R3	R2 R3	R2 R5	R4 R5	R4 R1	R6 R1

Consequently, while the freewheeling diodes of the IGBTs in operation are forward biased, the respective IGBT should be turned off, since it does not influence the current flow and then useless commutations are avoided. For example, considering the TSTPR with the upper switches turned off, in sector I diode R_6 is forced to conduct because u_{cn} is the lowest phase voltage, then in order to keep the IGBT R_6 turned off, the state of S_c should be equal to 1. On the other hand, for the TSTPR with the bottom switches turned off, the IGBTs in operation are disabled by forcing to 0 the switching state of the respective phase. Therefore, based on the switching table of the conventional DTC (Table 2.3) and the operation of the non-controlled rectifier (Table 5.5), the switching tables for the DTC of the two possible TSTPR can be obtained as highlighted in Tables 5.6 and 5.7.

A further modification of the switching pattern is introduced to guarantee that an effective

torque control is always possible and to reduce its oscillating nature, which is accomplished by applying always a null vector in order to decrease the torque. This is achieved by connecting the three phases to the negative dc rail (Table 5.6) or to the positive dc rail (Table 5.7).

Table 5.6: DTC switching table for a TSTPR with bottom switches.

$d\psi$	dTe	Sector					
		I	II	III	IV	V	VI
+	+	V_7 (111)	V_2 (110)	V_7 (111)	V_4 (011)	V_7 (111)	V_6 (101)
	-	V_5 (001)	V_1 (100)	V_1 (100)	V_3 (010)	V_3 (010)	V_5 (001)
-	+	V_4 (011)	V_7 (111)	V_6 (101)	V_7 (111)	V_2 (110)	V_7 (111)
	-	V_5 (001)	V_1 (100)	V_1 (100)	V_3 (010)	V_3 (010)	V_5 (001)

Table 5.7: DTC switching table for a TSTPR with upper switches.

$d\psi$	dTe	Sector					
		I	II	III	IV	V	VI
+	+	V_1 (100)	V_0 (000)	V_3 (010)	V_0 (000)	V_5 (001)	V_0 (000)
	-	V_6 (101)	V_6 (101)	V_2 (110)	V_2 (110)	V_4 (011)	V_4 (011)
-	+	V_0 (000)	V_5 (001)	V_0 (000)	V_1 (100)	V_0 (000)	V_3 (010)
	-	V_6 (101)	V_6 (101)	V_2 (110)	V_2 (110)	V_4 (011)	V_4 (011)

For a better understanding of the switching tables proposed for an implementation with low effort of DTC for a TSTPR (Tables 5.6 and 5.7), an equivalent table with the actually applied voltage vectors as a consequence of the imposed switching pattern is shown in Table 5.8, permitting a straightforward comparison with the switching table of the conventional DTC (Table 2.3). Therefore, it can be noticed that the torque control is always performed correctly (with the decrease in T_e being always achieved by applying a null vector), whereas the flux control is not possible in part of each sector, in which only a non-null vector and a null vector can be synthesized by the TSTPR due to the dependence on the phase currents polarity. Indeed, the limitations of this topology become evident when both flux and torque are intended to increase since the stator flux cannot be increased in part of three sectors. As a consequence, when the flux vector reaches the next sector, its amplitude is intended to increase, and the limitation on the simultaneous flux decrease and torque increase is not expected to influence the control performance, because this action is not selected. For instance, with the upper IGBTs in open-circuit, if the stator flux vector is located in sector I and the phase a current is negative the converter has capability to synthesize four vectors (V_0, V_1, V_2, V_3), when i_a assumes positive values the available vectors are reduced to two (V_0, V_3), because

diodes R_2 and R_6 conduct (equivalent to $S_a = 0$ and $S_c = 0$) and then the conduction state of R_4 is the only one controllable through S_b. Thus, in sector I, with $i_a > 0$, the only available vector to increase torque leads the flux to decrease (V_3). Consequently, at the beginning of sector II, the stator flux is intended to increase and the impossibility of performing the action $-d\psi/+dT_e$ while $i_c > 0$ is not noticed. Moreover, the phase current i_a becomes null for a short period of time while neither R_1 nor R_2 can conduct, as a consequence the respective phase voltage (u_{an}) floats, leading to undefined output voltage vectors as shown in Figure 5.7a. For these reasons, a circular trajectory cannot be followed by the stator flux vector, as shown in Figure 5.7b.

Table 5.8: Equivalent DTC switching table with the actual vectors applied by the TSTPR by using Tables 5.6 and 5.7.

$d\psi$	dTe	Open IGBTs	Sector					
			I	II	III	IV	V	VI
+	+	R1 R3 R5	V_2 (i_a<0) / V_3 (i_a>0)	V_3	V_4 (i_b<0) / V_5 (i_b>0)	V_5	V_6 (i_c<0) / V_1 (i_c>0)	V_1
		R2 R4 R6	V_2	V_3 (i_c>0) / V_4 (i_c<0)	V_4	V_5 (i_a>0) / V_6 (i_a<0)	V_6	V_1 (i_b>0) / V_2 (i_b<0)
	-		V_0 V_7	V_0 V_7	V_0 V_7	V_0 V_7	V_0 V_7	V_0 V_7
-	+	R1 R3 R5	V_3	V_3 (i_c>0) / V_4 (i_c<0)	V_5	V_5 (i_a>0) / V_6 (i_a<0)	V_1	V_1 (i_b>0) / V_2 (i_b<0)
		R2 R4 R6	V_2 (i_a<0) / V_3 (i_a>0)	V_4	V_4 (i_b<0) / V_5 (i_b>0)	V_6	V_6 (i_c<0) / V_1 (i_c>0)	V_2
	-		V_0 V_7	V_0 V_7	V_0 V_7	V_0 V_7	V_0 V_7	V_0 V_7

5.1.4 DTC with SVM

In the previous section (section 5.1.3), the conventional DTC is proposed as an optimum choice for torque ripple minimization in a TSTPR. However, the variable switching frequency remains an inherent drawback of the table-based DTC. Taking this into consideration, DTC with SVM is also proposed for an optimized control of the TSTPR. Accordingly, the suitable voltage modulator (SVM) proposed in section 5.1.2 is implemented together with the DTC strategy with SVM (section 2.2.2.2).

The block diagram of the proposed control strategy is depicted in Figure 5.8. The torque and flux controllers generate the reference voltages, which under post-fault operation are synthesized by the modified voltage modulator (SVM) for a TSTPR.

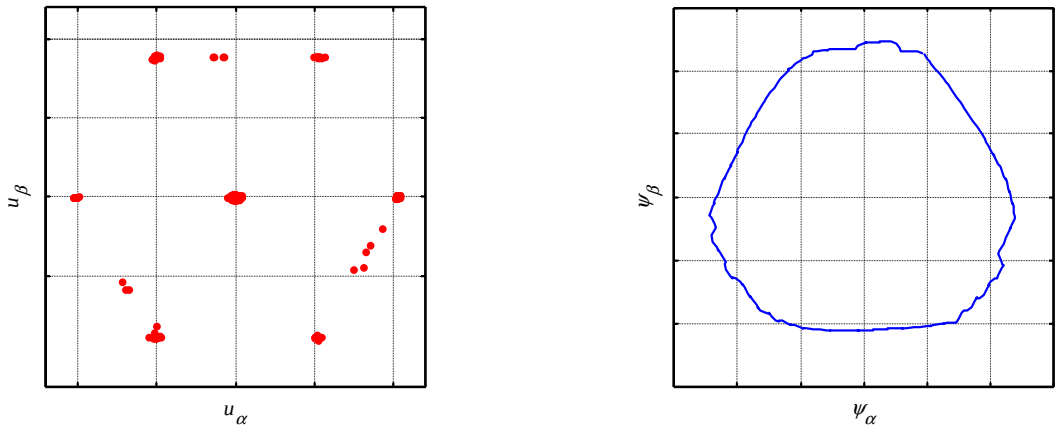

(a) (b)

Figure 5.7: Experimental results regarding the TSTPR operation with the upper IGBTs in open-circuit by using the proposed DTC strategy: (a) generator terminal voltage; (b) generator stator flux.

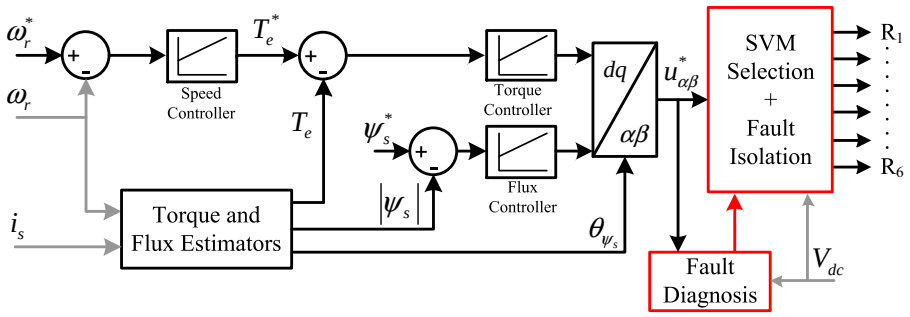

Figure 5.8: Bolck diagram of the fault-tolerant DTC strategy with SVM for the PMSG-side converter.

5.1.5 Simulation Results

The simulation results in Figure 5.9 were obtained at a reference dc link voltage of 250 V, a reference speed of 600 rpm, and a load torque equivalent to 50% of the PMSG rated torque. The PMSG parameters are given in Table A.1 - Appendix A. The PMSG-side converter operates as a TSTPR with bottom switches, which is the adopted topology after a fault occurrence in one of the upper IGBTs.

Figure 5.9 shows the PMSG phase currents for the four control strategies proposed. It can be observed that a balanced three-phase current system is provided, but, independently of the chosen control strategy, sinusoidal phase currents are not achieved. The RFOC strategy with HCC is able to shape the closest phase current to a sinusoidal waveform (Figure 5.9a), as a result of the independent control of each phase together with the control of i_{sd} proposed in section 5.1.1. Similar phase current waveforms with increased distortion are obtained by the RFOC strategy with SVM (Figure 5.9b). A less effective compensation of the current distortion through the control of i_{sd}^* when employing SVM can be justified by the generation of a lower value of i_{sq}^* by the speed con-

troller, leading to a lower absolute value of i_{sd}^{*} (equation (5.12)). Conventional DTC and DTC with SVM seem to generate more distorted current waveforms, and similar to each other (Figures 5.9c and 5.9d). However, reduced torque oscillation can be obtained by DTC-based strategies as verified in the next section by means of experimental results.

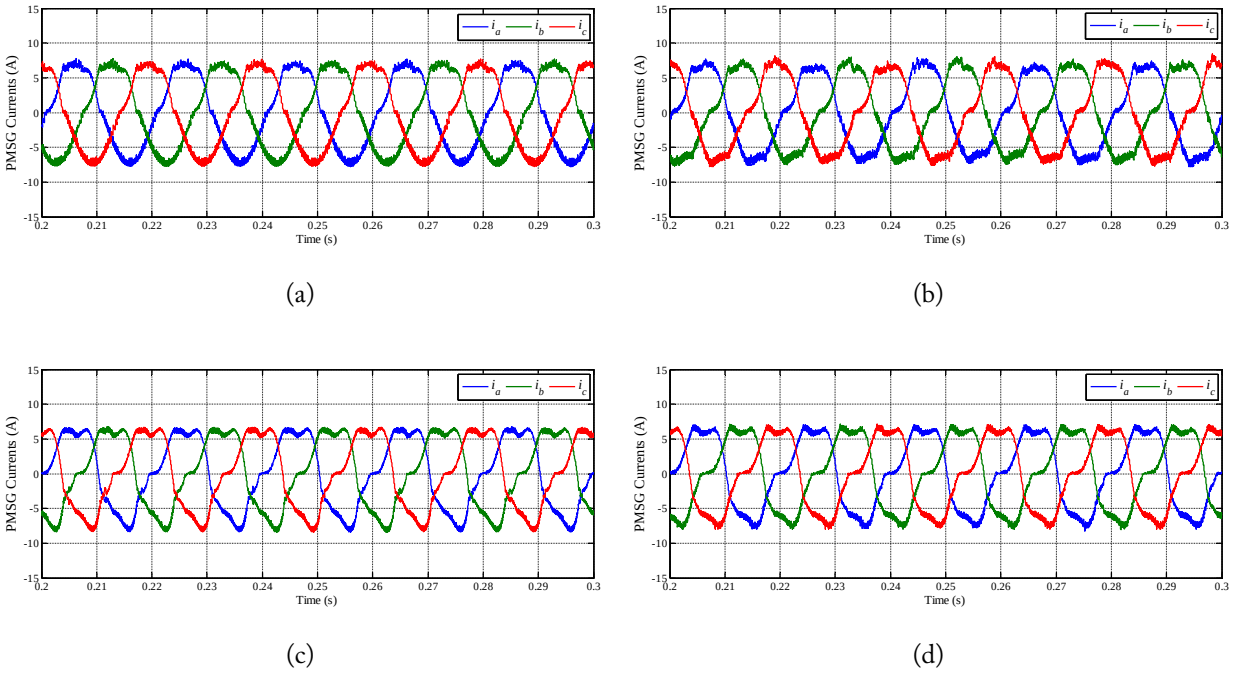

Figure 5.9: Simulation results regarding the time-domain waveforms of the PMSG phase currents with the PMSG-side converter under post-fault operation, operating as a TSTPR with bottom switches: (a) RFOC strategy with HCC; (b) RFOC strategy with SVM; (c) Conventional DTC strategy; (d) DTC strategy with SVM.

5.1.6 Experimental Results

The same operating conditions of the previous section were imposed for the experimental results shown in Figure 5.10. Hence, in good agreement with the simulation results, phase currents close to the sinusoidal waveform are shaped by the RFOC strategy with HCC and electromagnetic torque with reduced oscillation is generated (Figure 5.10a). On the other hand, RFOC strategy with SVM exhibits the lowest performance, which mainly results from the deficient compensation of i_{sd} in order to reduced the torque oscillation as previously explained. Such issue is a consequence of the generation of i_{sd}^{*} in feedforward manner, in other words in open-loop without error compensation. Therefore, DTC-based control strategies appear to be the optimum choice, since torque oscillations are compensated in closed-loop. Figures 5.10c and 5.10d elucidate that DTC allows the PMSG to be controlled by a TSTPR with reduced torque ripple at the expense of a limited control of the stator flux, leading to non-sinusoidal phase currents.

Table 5.9 clarifies the qualitative analysis above, with RFOC with HCC and conventional DTC presenting the lowest current THD values and torque TWO values, and RFOC with SVM showing the poorest performance. Despite an increased current distortion, DTC with SVM demonstrates a fairly satisfactory performance regarding the torque oscillation, together with operation at constant switching frequency.

Table 5.9: PMSG current THD values and electromagnetic torque TWO values.

Control Strategy	PMSG Current THD	Torque TWO
RFOC HCC	11.8 %	10.7 %
RFOC SVM	20.0 %	18.6 %
Conventional DTC	11.8 %	7.8 %
DTC SVM	18.3 %	10.9 %

Finally, the efficiency measurements in Figure 5.11 show that SVM-based techniques present higher efficiency values for the considered operating conditions, with DTC with SVM assuming the highest efficiency. Comparing Figure 5.11 with Figure 2.19, it can be concluded that the TSTPR has a higher efficiency than the SSTPC, which largely results from the lower switching losses of the TSTPR. However, for high load levels (load torque higher than 75%) the SSTPC is expected to provide improved efficiency due to the higher PMSG rms currents forced by TSTPR (exceeding the PMSG rated current).

Therefore, although the PMSG should operate in a narrower torque range when controlled by a TSTPR in order not to exceed its rated current, a fairly acceptable performance is provided by the TSTPR together with the proposed strategies, being viable options for post-fault operation of an SSTPC PMSG-side converter.

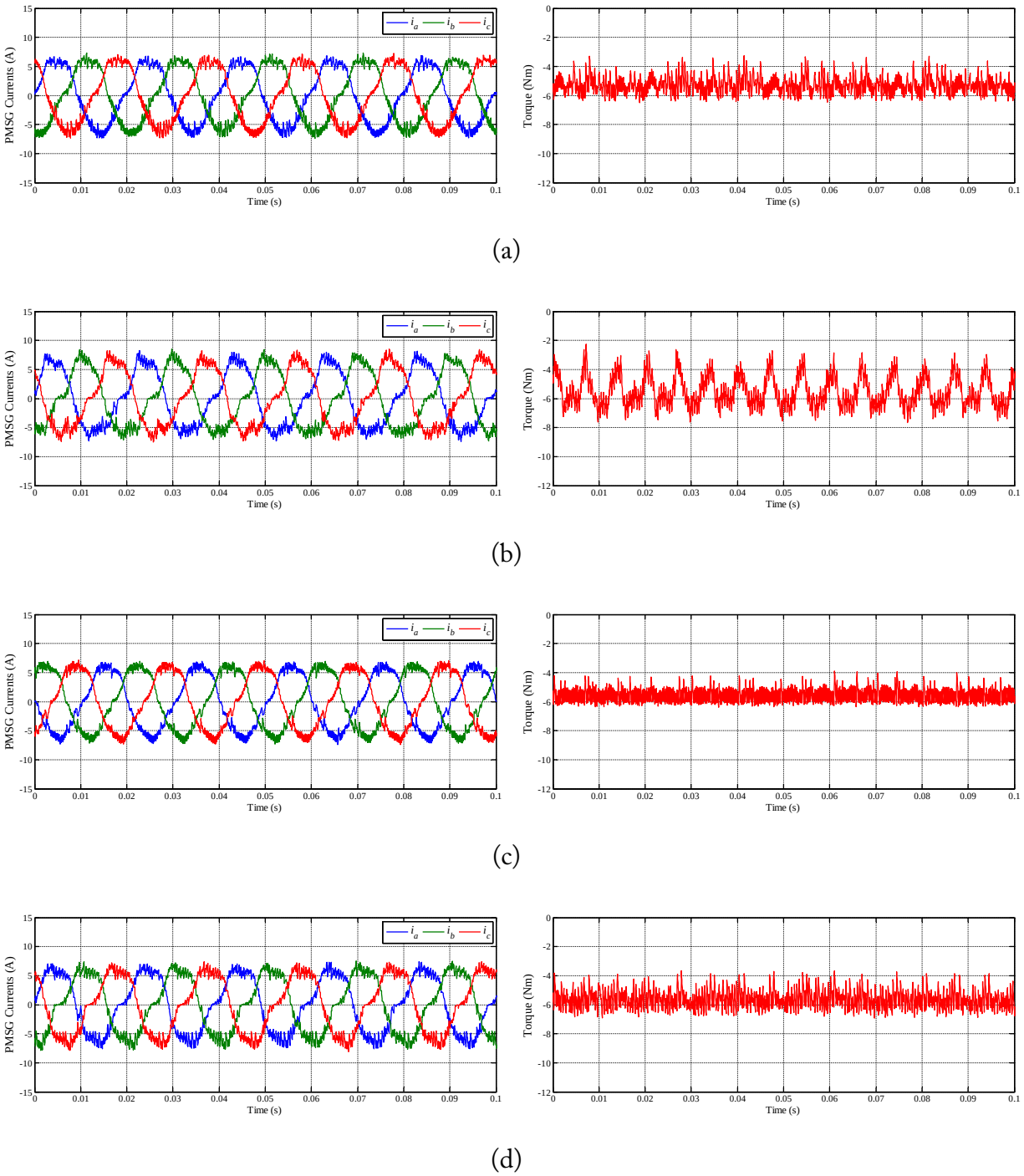

Figure 5.10: Experimental results regarding the time-domain waveforms of the PMSG phase currents and estimated electromagnetic torque with the PMSG-side converter under post-fault operation, operating as a TSTPR with bottom switches: (a) RFOC strategy with HCC; (b) RFOC strategy with SVM; (c) Conventional DTC strategy; (d) DTC strategy with SVM.

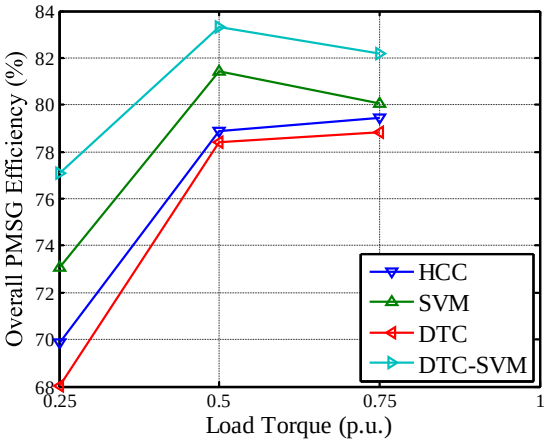

Figure 5.11: Experimental results regarding the overall efficiency of the PMSG-side system (PMSG + Converter) at a reference speed of 1200 rpm and three distinct load levels (25%, 50% and 75% of the PMSG rated torque).

5.2 Four-Switch Three-Phase Converter with a Phase Connected to DC Bus Midpoint for the Grid-Side Converter

On the grid-side converter (inverter stage), reconfiguration of the circuit topology is a mandatory action after the occurrence of an open-circuit fault, because there is no path through the affected phase for the current flowing in both directions. One possible solution for post-fault operation is the four-switch three-phase converter (FSTPC) with a phase connected to the dc-bus midpoint in Figure 5.12b, which requires three additional TRIACs (Triodes for Alternating Current) that remain open under normal operating conditions (Figure 5.12a). Therefore, the detection of an open-circuit fault is followed by the isolation of the faulty phase (inhibition of its control signals), then, the connection of that phase to the dc bus midpoint through the respective TRIAC (hardware reconfiguration), and software reconfiguration, selecting a suitable control strategy and imposing a dc bus reference voltage twice as high. This considerable increase of the dc-link voltage is the main drawback of the FSTPC, forced by the reduced voltage capability of the converter and by the constant grid voltage. As a consequence, the voltage rating of all the drive components has to be doubled.

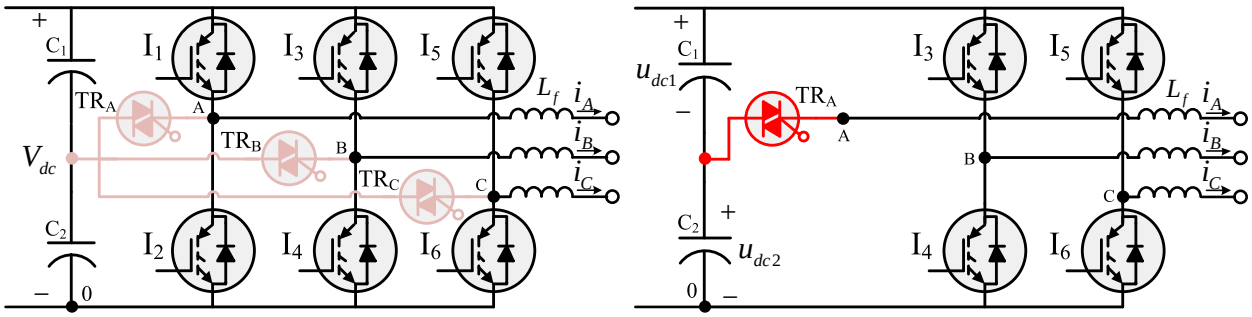

Figure 5.12: Fault-tolerant grid-side converter: (a) six-switch three-phase converter for normal operation; (b) four-switch three-phase converter with a phase connected to the dc-bus midpoint (FSTPC-PCM) for post-fault operation, considering an open-circuit fault in phase A (I_1 or I_2).

By connecting a given phase to the dc bus midpoint its phase-to-zero voltage is fixed to half of the dc bus voltage, whereas in the remaining phases their voltages depend on the states of the respective switches.

For instance, considering that phase A is connected to the dc bus midpoint:

$$u_{A0} = V_{dc}/2;\ u_{B0} = V_{dc}S_B;\ u_{C0} = V_{dc}S_C \tag{5.13}$$

where V_{dc} represents the dc bus voltage and S_A, S_B and S_C are the switching states (ON: 1, OFF: 0) of the upper IGBTs (I_1, I_3, I_5) of phases A, B and C, respectively. Therefore, by substituting (5.13) in (2.25) and (2.25) in (2.24), the following voltage vectors in $\alpha\beta$ axes can be deduced:

$$u_{c\alpha} = \frac{1}{3}V_{dc}\left(1 - S_B - S_C\right);\ u_{c\beta} = \frac{1}{\sqrt{3}}V_{dc}\left(S_B - S_C\right) \tag{5.14}$$

In a similar way, the FSTPC voltage vectors can be obtained for the case in which phase B is connected to the dc link midpoint:

$$u_{c\alpha} = \frac{1}{3}V_{dc}\left(2S_A - \frac{1}{2} - S_C\right);\ u_{c\beta} = \frac{1}{\sqrt{3}}V_{dc}\left(\frac{1}{2} - S_C\right) \tag{5.15}$$

as well as for the case where phase C is connected to the dc link midpoint:

$$u_{c\alpha} = \frac{1}{3}V_{dc}\left(2S_A - S_B - \frac{1}{2}\right);\ u_{c\beta} = \frac{1}{\sqrt{3}}V_{dc}\left(S_B - \frac{1}{2}\right) \tag{5.16}$$

Since there are four possible switching states, the four available voltage vectors are presented in Table 5.10 and depicted in Figure 5.13 for all case scenarios of post-fault operation.

It is important to emphasize that the maximum output voltage is halved, by replacing the SSTPC by the FSTPC. Consequently, the dc bus voltage must assume a value twice as high, in order to ensure that both capacitors of the dc link bank have a voltage higher than the maximum value of the grid phase-to-phase voltages.

Having analyzed the FSTPC operation, the necessary modifications to the control strategies presented in section 2.3 for the SSTPC are analyzed next for the FSTPC with a phase connected to the dc-bus midpoint.

Table 5.10: Voltage space vectors synthesized by the four-switch three-phase converter.

Faulty Phase	$V_1(00)$		$V_2(10)$		$V_3(11)$		$V_4(01)$	
	$u_{1\alpha}$	$u_{1\beta}$	$u_{2\alpha}$	$u_{2\beta}$	$u_{3\alpha}$	$u_{3\beta}$	$u_{4\alpha}$	$u_{4\beta}$
A	$\frac{V_{dc}}{3}$	0	0	$\frac{V_{dc}}{\sqrt{3}}$	$-\frac{V_{dc}}{3}$	0	0	$\frac{-V_{dc}}{\sqrt{3}}$
B	$-\frac{V_{dc}}{6}$	$\frac{V_{dc}}{2\sqrt{3}}$	$\frac{V_{dc}}{2}$	$\frac{V_{dc}}{2\sqrt{3}}$	$\frac{V_{dc}}{6}$	$\frac{-V_{dc}}{2\sqrt{3}}$	$-\frac{V_{dc}}{2}$	$\frac{-V_{dc}}{2\sqrt{3}}$
C	$-\frac{V_{dc}}{6}$	$\frac{-V_{dc}}{2\sqrt{3}}$	$\frac{V_{dc}}{2}$	$\frac{-V_{dc}}{2\sqrt{3}}$	$\frac{V_{dc}}{6}$	$\frac{V_{dc}}{2\sqrt{3}}$	$-\frac{V_{dc}}{2}$	$\frac{V_{dc}}{2\sqrt{3}}$

5.2.1 VOC with HCC

The simplest fault-tolerant control of the grid-side converter is achieved by employing the VOC strategy with HCC, whose block diagram is shown in Figure 5.14. In this case, the isolation of the faulty and the new reference dc-link voltage are the only required actions. Further control modifications are not required, since the direct control of the phase currents can be performed by controlling the two healthy phases without changing their reference currents. Accordingly, and

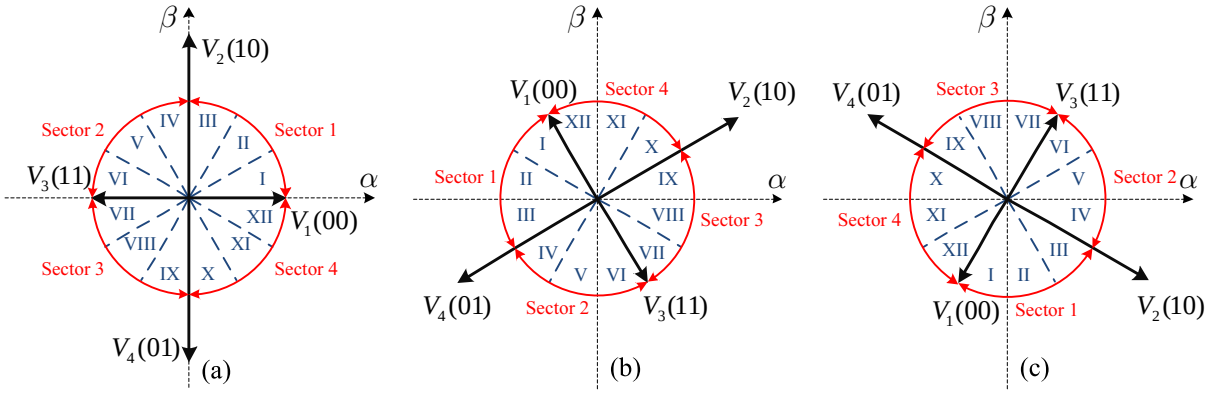

Figure 5.13: Voltage vectors of the FSTPC for the three possible connections to the dc bus midpoint: (a) Phase A; (b) Phase B; (c) Phase C.

taking as an example a fault in phase A, phase A current is imposed by the currents in phases B and C: $i_A = -i_B - i_C$.

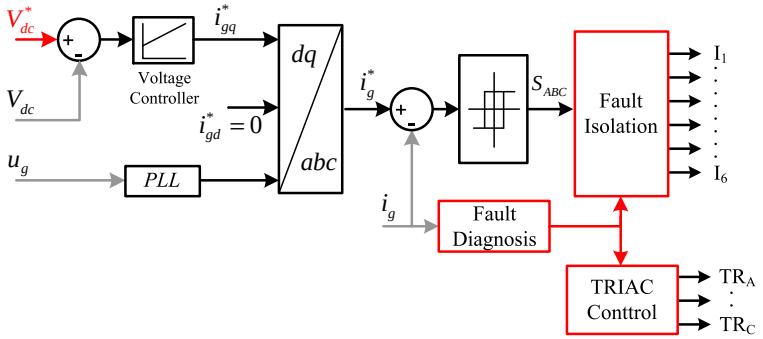

Figure 5.14: Block diagram of the fault-tolerant VOC strategy with HCC for the grid-side converter.

5.2.2 VOC with SVM

Seeking constant switching, the VOC strategy with SVM is also proposed for the FSTPC (Figure 5.15). As opposed to the eight voltage vectors synthesized by the SSTPC, the FSTPC is able to synthesize four active vectors and none null vector. Accordingly, it is compulsory to redesign the voltage modulator proposed in section 2.2.1.2.

In order to synthesize the reference voltage vector (V_c^*), the two converter voltage vectors adjacent to the reference voltage vector need to be applied during suitable time periods within each T_s (t_x, t_y), during the remaining time period a null vector should be applied (t_0). Since there is no available null vector, two vectors with opposite direction and the same magnitude can be applied for the same amount of time $(t_0/2)$ to synthesize an average null vector. Therefore, always choosing the small vectors (V_1 and V_3) for this task, and taking as an example the reference vector in sector I, the following relationship should be verified:

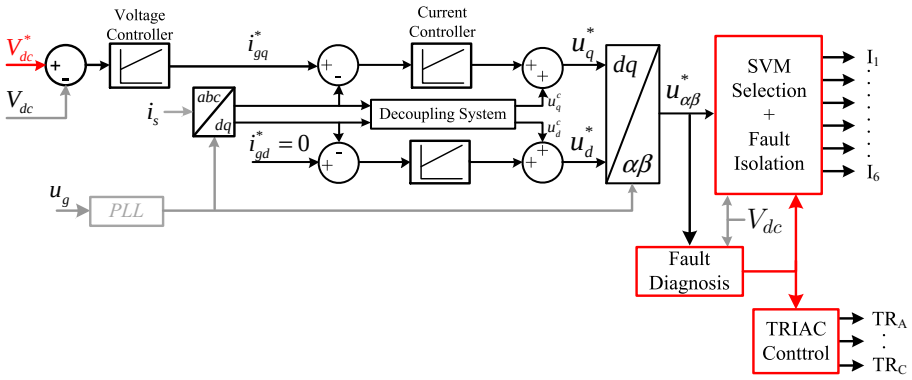

Figure 5.15: Block diagram of the fault-tolerant VOC strategy with SVM for the grid-side converter.

$$T_s V_c^* = (t_x + t_0/2)V_1 + t_y V_2 + (t_0/2)V_3 \tag{5.17}$$

and the switching times are calculate as follows:

$$\begin{cases} t_x = |V_c^*|\, T_s \cos(\alpha) \,/\, |V_1| = \dfrac{3\,|V_c^*|}{V_{dc}} T_s \cos(\alpha) \\ t_y = |V_c^*|\, T_s \sin(\alpha) \,/\, |V_2| = \dfrac{\sqrt{3}\,|V_c^*|}{V_{dc}} T_s \sin(\alpha) \\ t_0 = T_s - t_x - t_y \end{cases} \tag{5.18}$$

The relationships above are valid for all the four sectors defined in Figure 5.13 (sectors 1 to 4).

The voltage vectors sequence and respective timing plan are shown in Table 5.11 for the case scenarios in which phase A or phase C is the faulty one. When phase B is the faulty one, in accordance with the sector definition in Figure 5.13, the correct voltage vector sequence is obtained by replacing V_2 with V_4 and V_4 with V_2 in Table 5.11.

The maximum amplitude of the reference voltage vector is $V_{dc}/(2\sqrt{3})$, which means that the voltage capability of the FSTPC is halved in comparison to the SSTPC.

Table 5.11: SVM voltage vectors sequence and timing plan for the FSTPC.

Sector	Voltage Vector Sequence	Voltage Vector Timing
1	$V_1 \rightarrow V_2 \rightarrow V_3 \rightarrow V_2 \rightarrow V_1$	$t_x + t_0/2 \rightarrow t_y \rightarrow t_0 \rightarrow t_y \rightarrow t_x + t_0/2$
2	$V_3 \rightarrow V_2 \rightarrow V_1 \rightarrow V_2 \rightarrow V_3$	$t_y + t_0/2 \rightarrow t_x \rightarrow t_0 \rightarrow t_x \rightarrow t_y + t_0/2$
3	$V_3 \rightarrow V_4 \rightarrow V_1 \rightarrow V_4 \rightarrow V_3$	$t_x + t_0/2 \rightarrow t_y \rightarrow t_0 \rightarrow t_y \rightarrow t_x + t_0/2$
4	$V_1 \rightarrow V_4 \rightarrow V_3 \rightarrow V_4 \rightarrow V_1$	$t_y + t_0/2 \rightarrow t_x \rightarrow t_0 \rightarrow t_x \rightarrow t_y + t_0/2$

5.2.3 VOC with Vector-based HCC

With the aim to overcome some disadvantages of the conventional HCC but retaining its main advantages, a fault-tolerant VOC strategy with vector-based HCC is also proposed, whose block diagram is depicted in Figure 5.16. In [207], it was verified that such control strategy allows the converter to operate at an average switching frequency lower than the conventional HCC.

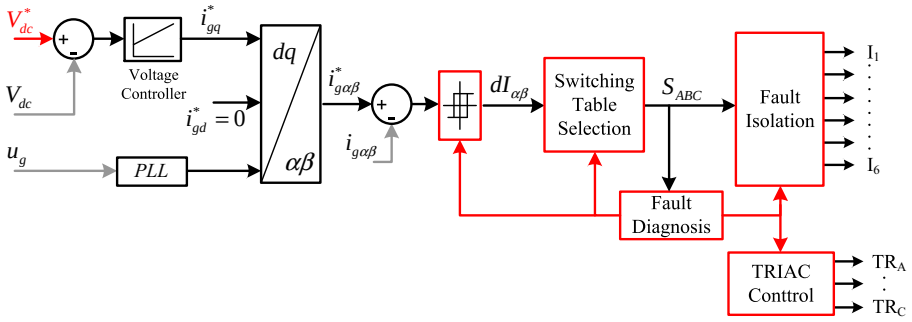

Figure 5.16: Block diagram of the fault-tolerant VOC strategy with vector-based HCC for the grid-side converter.

Therefore, considering the three possible hardware reconfigurations for post-fault operation and substituting respective voltage vectors (Table 5.10) in equations (2.41) and (2.42), three switching tables are formulated (Tables 5.12, 5.13 and 5.14) by adopting two-level hysteresis comparators with outputs dI_α and dI_β, which decide if the $\alpha\beta$-components of the grid current are intended to decrease (0) or increase (1).

Table 5.12: Switching table for the FSTPC with phase A connected to the dc link midpoint.

		dI_β	
		0	1
dI_α	0	V_3 (11)	V_2 (10)
	1	V_4 (01)	V_1 (00)

Table 5.13: Switching table for the FSTPC with phase B connected to the dc link midpoint.

		dI_β	
		0	1
dI_α	0	V_4 (01)	V_1 (00)
	1	V_3 (11)	V_2 (10)

Table 5.14: Switching table for the FSTPC with phase C connected to the dc link midpoint.

		dI_β	
		0	1
dI_α	0	V_1 (00)	V_4 (01)
	1	V_2 (10)	V_3 (11)

5.2.4 DPC

The block diagram of the fault-tolerant DPC strategy proposed for the grid-side converter is shown in Figure 5.17, for which new switching tables are needed to ensure post-fault operation.

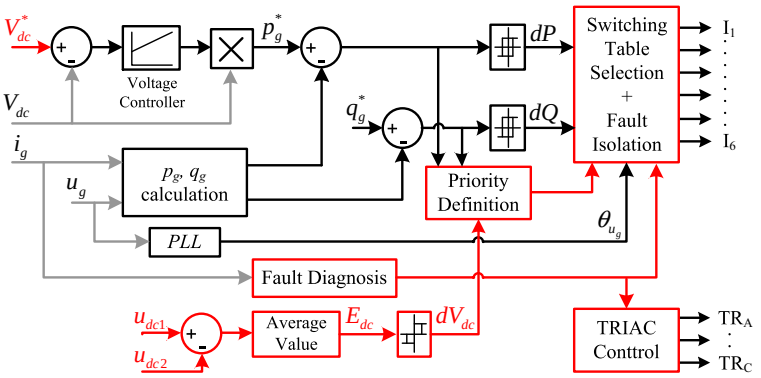

Figure 5.17: Block diagram of the fault-tolerant DCP strategy for the grid-side converter.

Since the switching table is intended to choose which converter voltage space vector leads, in a more effective way, to the desired variation in the instantaneous powers, a comprehensive analysis of the power derivatives forced by each converter voltage vector allows us to define the most appropriate switching table. Taking as an example the case in which phase A is the one connected to the dc bus midpoint and substituting each voltage vector that the FSTPC can synthesize (Table 5.10) in equations (2.51) and (2.52), the instantaneous active and reactive power variations caused by the application of each voltage vector over a period of the grid voltage are shown in Figure 5.18. Regarding the two remaining cases, the differences are due to the angular displacement of the voltage vectors with respect to the case of phase A (Figure 5.13).

Let us start by dividing the complex plane into four sectors (as illustrated in Figure 5.13):

$$(1-s)\frac{\pi}{2} \leq \theta(s) - \theta_n < s\frac{\pi}{2},\ s = 1,\ ...,\ 4 \tag{5.19}$$

where s stands for the sector number, $\theta(s)$ for the angles covered by sector s, and θ_n for the angular position of V_1, depending on which phase ($n = A,\ B,\ C$) is connected to the dc bus midpoint ($\theta_A = 0,\ \theta_B = 2\pi/3,\ \theta_C = 4\pi/3$).

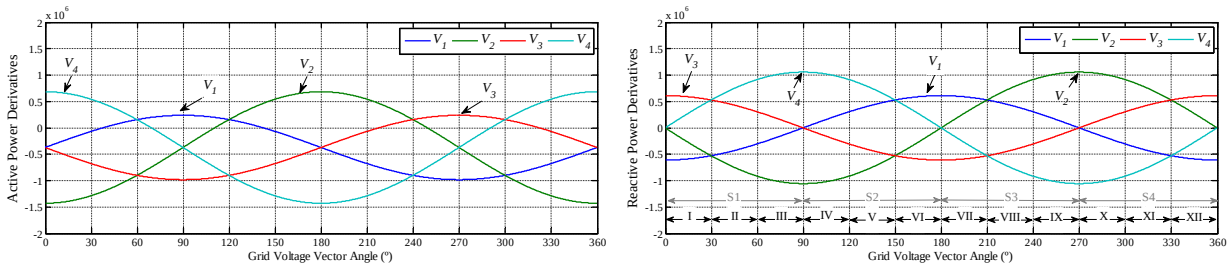

Figure 5.18: Instantaneous active and reactive power derivatives imposed by the FSTPC, for the case in which phase A is connected to the dc bus midpoint.

In Figure 5.18, it can be seen that over all sector 1 V_1 and V_2 have the capability to reduce the reactive power, whereas V_3 and V_4 increase it. On the other hand, due to the negative dc component visible in the active power derivatives, V_2 and V_3 are able to decrease the active power over all sector 1 but V_1 and V_4 only increase p_g for a considerable portion of the sector. Thus, at the beginning of sector 1, where only V_4 permits the increase of p_g , it is not possible to satisfy simultaneously an increase in p_g and a decrease in q_g $(+dP/-dQ)$. Identically, at the end of sector 1, where only V_1 permits the increase of p_g , it is not possible to increase at the same time both p_g and q_g $(+dP/+dQ)$. Despite this, by assigning priority to the control of q_g, a simple switching table can be obtained (Table 5.15), at the cost of a poor control of the active power at the sector extremities.

Table 5.15: DCP switching table 1.

dP	dQ	Sector			
		1	2	3	4
+	+	V_4	V_1	V_2	V_3
	-	V_1	V_2	V_3	V_4
-	+	V_3	V_4	V_1	V_2
	-	V_2	V_3	V_4	V_1

To improve the DPC performance, the complex plane can be divided into twelve sectors (Figure 5.13):

$$(1-s)\frac{\pi}{6} \leq \theta(s) - \theta_n < s\frac{\pi}{6},\ s = I,\ ...,\ XII \tag{5.20}$$

As mentioned before, there is no voltage vector that leads to $dp_g/dt > 0$ and $dq_g/dt < 0$ in sector I (first third of sector 1). By analyzing the power derivatives in this sector: V_4 forces p_g to increase and q_g to increase with the smallest derivative; whereas by applying V_1, p_g decreases with the smallest derivative and q_g decreases. Therefore, both V_1 and V_4 may be used to keep the power errors as small as possible in sector I, because the opposite effect to the desired action $(+dP/-dQ)$

is the minimum. The first suggested in Table 5.15 is a particular case where priority is given to the control of q_g by choosing V_1 that always decreases q_g during sector I. However, such an option leads to an increase in the active power error, while the reactive power error is kept small. To mitigate this limitation, the priority can be assigned according to the absolute values of the power errors:

$$Priority = \begin{cases} P, & if \ \ |p_g^* - p_g| > |q_g^* - q_g| \\ Q, & otherwise \end{cases} \tag{5.21}$$

Thus, if the absolute value of the active power error is larger than the absolute value of the reactive power error, the priority is assigned to the control of p_g and, for instance, V_4 is selected to increase p_g and decrease q_g ($+dP/-dQ$) in sector I, in spite of leading to a slight increase of q_g. Similar cases are found in sectors IV, VII and X where there is no vector that leads to $dp_g/dt > 0$ and $dq_g/dt < 0$ over practically all the sector as well as in sectors III, VI, IX and XII regarding $dp_g/dt > 0$ and $dq_g/dt > 0$.

A further improvement can also be introduced when dP is intended to be negative in sector I, VI, VII and XII, taking advantage of redundant states. Once again, taking sector I as an example (Figure 5.18), there are two voltage vectors that allow us to fulfill $+dP/-dQ$, namely, V_1 and V_2. However, the absolute values of the power derivatives imposed by them are well distinct: V_1 causes the largest negative derivative of the reactive power, whereas the largest variation of the active power is achieved by applying V_2. Therefore, the largest power error should be opposed by the voltage vector that causes the largest power variation, which can be achieved by using the priority definition (5.21).

Generalizing the previous considerations for the twelve sectors, an enhanced switching table is formulated (Table 5.16), by also using the absolute values of the power errors in order to define to which power the control priority should be given. Table 5.16 is intended to reduce power oscillations and as a consequence the grid current harmonic distortion.

Finally, it is pointed out that the switching tables shown in Tables 5.15 and 5.16 are only valid for the cases in which phases A and C are connected to the dc bus midpoint. On the other hand, according to Table 5.10 and Figure 5.13, for the case of phase B, with the aim of keeping the sectors increase in the counterclockwise direction, sector 1 is defined as the one between V_1 and V_4 instead of being between V_1 and V_2. Therefore, the DPC switching tables for the case in which phase B is connected to the dc bus midpoint are easily obtained by exchanging V_2 and V_4 one with the other in Tables 5.15 and 5.16.

5.2.4.1 Control of the Capacitor Voltage Offset

So far in this section, the dc link has been considered ideal, assuming the two capacitor voltages (u_{dc1}, u_{dc2}) as constants and equals. Nevertheless, as a consequence of the fundamental current flow through the capacitors, the capacitor voltages oscillation and deviation are inherent issues of

Table 5.16: DCP switching table 2.

dP	*dQ*	Priority (if dV_{dc}=0)	Sector											
			I	II	III	IV	V	VI	VII	VIII	IX	X	XI	XII
+	+	*P*	V_4	V_4	V_1	V_1	V_1	V_2	V_2	V_2	V_3	V_3	V_3	V_4
		Q			V_4			V_1			V_2			V_3
	-	*P*	V_4	V_1	V_1	V_1	V_2	V_2	V_2	V_3	V_3	V_3	V_4	V_4
		Q	V_1			V_2			V_3			V_4		
-	+	*P*	V_3	V_3	V_3	V_4	V_4	V_4	V_1	V_1	V_1	V_2	V_2	V_2
		Q						V_1						V_3
	-	*P*	V_2	V_2	V_2	V_3	V_3	V_3	V_4	V_4	V_4	V_1	V_1	V_1
		Q	V_1						V_3					

an FSTPC. Concerning the voltage oscillation, a proper design of the capacitors can provide an acceptable performance, even because its degradation may be tolerated during post-fault operation, which is usually maintained for a short period of time. On the other hand, the capacitor voltage deviation may force the converter to shutdown, due to a transient state or an unbalanced current distribution through the two capacitors (as a consequence of capacitor impedances being somewhat different). Thus, it is worth controlling the capacitors voltage offset in real-time, by including an additional voltage sensor to monitor the voltage drift and changing the switching pattern to eliminate it.

Accordingly, the following procedure is proposed for voltage equalization. The average value of the error between the capacitor voltages is first calculated:

$$E_{dc} = f \int_0^{1/f} (u_{dc1} - u_{dc2})\, dt = f \int_0^{1/f} (V_{dc} - 2u_{dc2})\, dt \tag{5.22}$$

If E_{dc} exceeds a given range ($\Delta V_{dc}/2$), the priority assignment to the control of active and reactive powers (5.21) is disabled, and then the priority is assigned to annul E_{dc}. The decision process employs a three-level hysteresis comparator with output dV_{dc}:

$$dV_{dc} = \begin{cases} +V_{dc2}, & if\ E_{dc} > \Delta V_{dc}/2 \\ -V_{dc2}, & if\ E_{dc} < -\Delta V_{dc}/2 \\ 0, & otherwise \end{cases} \tag{5.23}$$

where ΔV_{dc} stands for the hysteresis controller bandwidth. Hence, when the average value of u_{dc2} exceeds the average value of u_{dc1} by $\Delta V_{dc}/2$, u_{dc2} is intended to decrease ($-V_{dc2}$) and consequently, u_{dc1} is intended to increase, keeping V_{dc} constant. Such action can be performed by forcing the discharge of the capacitor C_2, which is commonly accomplished in series-connected capacitors through additional switches and resistors [208]. Nevertheless, the voltage space vector $V_1(00)$ allows the FSTPC to only discharge C_2, without requiring extra hardware [175], whereas applying

$V_3(11)$ only discharges C_1. Therefore, the proposed approach is based on increasing the average utilization of V_1 and decreasing the average utilization of V_3 over a fundamental period to force u_{dc2} to decrease ($-V_{dc2}$) and u_{dc1} to increase. Naturally, the opposite action leads to decrease u_{dc1} and to increase u_{dc2} ($+V_{dc2}$). Table 5.17 shows the necessary modifications to DPC Table 2 (Table 5.16) in order to integrate the control of the capacitor voltage offset. For the case of $dV_{dc} = 0$, Table 5.16 remains unchanged.

Table 5.17: Modifications to DCP switching table 2 to control the capacitor voltage offset.

dP	*dQ*	dV_{dc}	Sector			
			III	IV	VII	XII
+	+	$+V_{dc2}$	V_4			V_3
		$-V_{dc2}$	V_1			V_4
	-	$+V_{dc2}$		V_2	V_3	
		$-V_{dc2}$		V_1	V_2	
-	+	$+V_{dc2}$				V_3
		$-V_{dc2}$				V_2
	-	$+V_{dc2}$			V_3	
		$-V_{dc2}$			V_4	

5.2.5 Simulation Results

A load level equivalent to 51% of the PMSG rated mechanical power is assumed for the simulation results in Figure 5.19, with a reference dc link voltage of 500 V being imposed, which corresponds to twice the value of reference dc link voltage under normal operating conditions (250 V). Figure 5.19 shows that the four control strategies proposed for the FSTPC with one phase (phase A) connected to the dc bus midpoint permit to reach a balanced and sinusoidal three-phase current system and approximately unit power factor. In comparison to grid-side converter operation with an SSTPC (Figure 2.17), it becomes clear the increase of the current ripple in Figure 5.19.

5.2.6 Experimental Results

The experimental results of Figure 5.20 and Table 5.18 were obtained under the same operating conditions of the simulation results in Figure 5.19. Through the analysis of the phase currents and active and reactive powers becomes evident the distinct performances of the four control strategies. The best performances regarding current harmonic distortion and power oscillation are shown by VOC with HCC and DPC strategies, due to the direct control of current and power, respectively. High current and power ripple is present by VOC with SVM and VOC with vector-based HCC strategies. In the case of the VOC with SVM, the increased current harmonic distortion can be

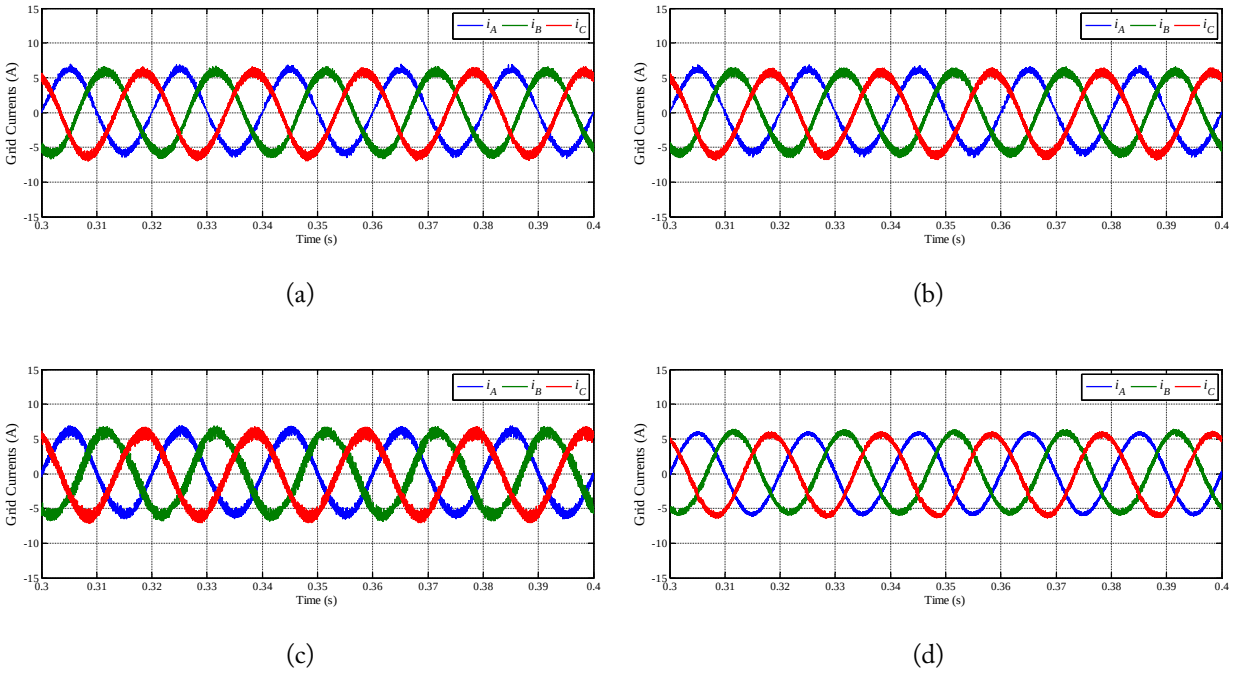

Figure 5.19: Simulation results regarding the time-domain waveforms of the grid phase currents with the grid-side converter under post-fault operation, operating as an FSTPC-PCM: (a) VOC strategy with HCC; (b) VOC strategy with SVM; (c) VOC strategy with vector-based HCC; (d) DPC strategy with switching table 2.

attributed to the indirect current control, whose performance is limited by the current control bandwidth and also by the capability of the voltage modulator to generate the reference voltage vector, which is negatively affected by the voltage oscillation of dc link midpoint. In the case of the VOC with vector-based HCC, the high current ripple can be justified by a considerable reduction of the average switching frequency in comparison to the VOC with HCC, which might be attenuated by narrowing the hysteresis band.

Regarding the overall efficiency of the grid-side system when employing a FSTPC-PCM (Figure 5.21), it is lower than when using the SSTPC (Figure 2.21) due to the great increase of the dc link voltage, contributing to the increase of the switching losses and filter core losses.

Comparing the performance of FSTPC-PCM with the SSTPC (section 2.5.2) for the grid-side converter, it is verified that a lower but acceptable performance is provided by the FSTPC-PCM when controlled by the proposed strategies. Thus, this converter topology and respective control strategies are viable options for post-fault operation of the grid-side converter of a PMSG drive.

Additional results are presented concerning the DPC strategy for the FSTPC-PCM. Figure 5.22 and Table 5.19 allow the performance comparison of the two switching tables proposed for the DPC of a grid-connected FSTPC. Both tables are able to control the dc link voltage as well as to keep a power factor practically equal to one. In Figure 5.22 Table 1 (Table 5.15) is replaced by Table 2 (Table 5.16) at $t = 0.43\ s$, showing that Table 2 leads to more sinusoidal waveforms

Table 5.18: Grid current THD values and active power TWO values for the FSTPC-PCM.

Control Strategy	Grid Current THD	Active Power TWO
VOC HCC	3.7 %	14.0 %
VOC SVM	6.2 %	16.5 %
VOC VHCC	6.8 %	22.4 %
DPC	4.6 %	12.9 %

of the phase currents and less oscillating instantaneous powers. By analyzing Table 5.19, it can be confirmed that an effective reduction of the active instantaneous power TWO value is achieved with Table 2 and consequently the grid currents THD is also reduced. Thus, according to the theoretical formulation in section 5.2.4, the Switching Table 2 proves to be a quite good choice to implement a DPC strategy for an FSTPC with a better performance than Table 1.

Table 5.19: Evaluation parameters of the proposed DPC switching tables.

	DPC Table 1	DPC Table 2
Grid Currents THD_{eq}	5.04 %	3.85 %
Grid Power Factor	0.985	0.978
Active Power TWO	8.93 %	7.19 %

Figure 5.23 shows the effectiveness of the proposed strategy to control the offset between the average capacitor voltages. Initially, DPC Table 2 is applied without monitoring the two dc bus voltage capacitors, by forcing dV_{dc} to 0, and the offset E_{dc} assumes a value of approximately 8 V, with u_{dc1} being the highest voltage. At $t = 0.065\ s$ the control of the capacitor voltages deviation is enabled, with ΔV_{dc} equal to 1% of V_{dc} (3 V), allowing the offset to tend to zero. Consequently, while the modified switching table (Table 5.17) is used, the phase current distortion increases because the control of the capacitor voltages is achieved at the expense of a less optimized control of the instantaneous powers. After E_{dc} becomes within the bandwith ΔV_{dc}, the grid currents become practically sinusoidal, similarly to the results in Figure 5.22. Concerning the total dc bus voltage (V_{dc}), Figure 5.23 also shows that V_{dc} is always kept practically constant.

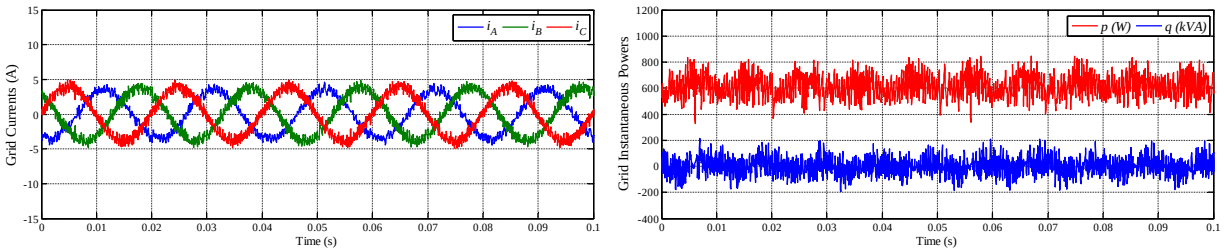

(a)

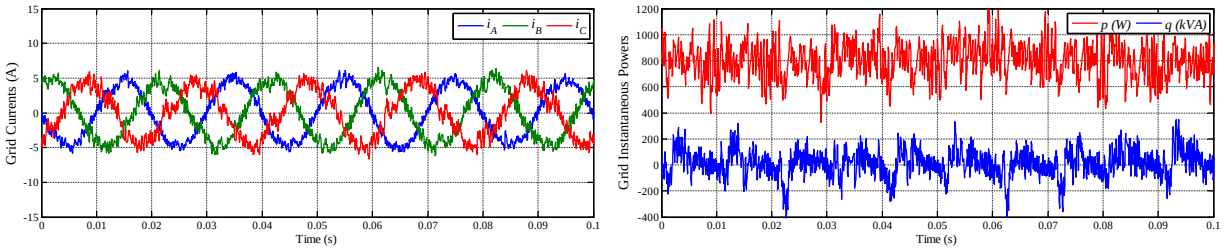

(b)

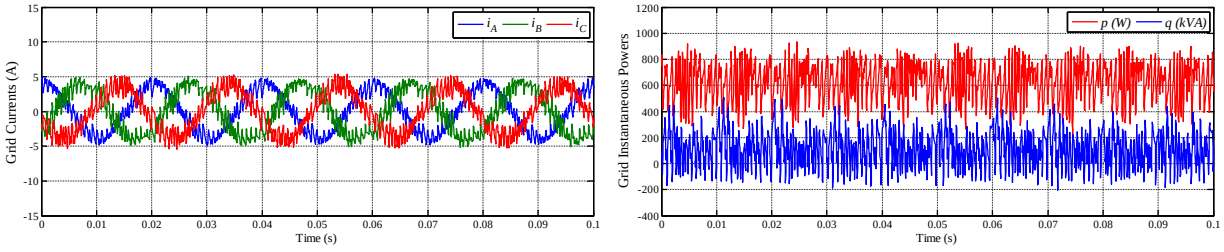

(c)

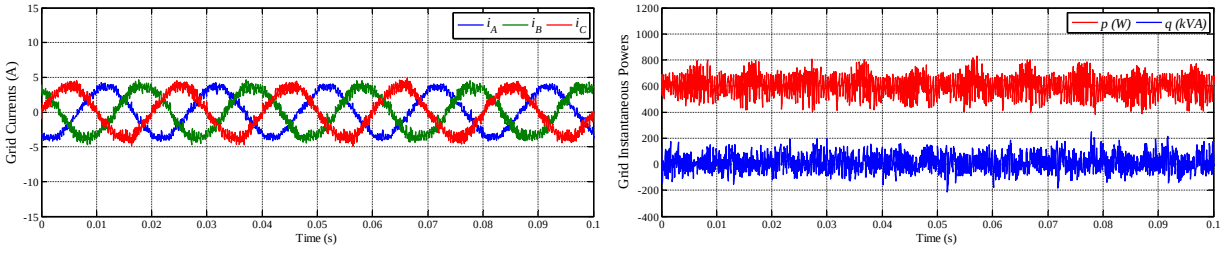

(d)

Figure 5.20: Experimental results regarding the time-domain waveforms of the grid phase currents and the instataneous active and reactive powers with the grid-side converter under post-fault operation, operating as an FSTPC-PCM: (a) VOC strategy with HCC; (b) VOC strategy with SVM; (c) VOC strategy with vector-based HCC; (d) DPC strategy with switching table 2.

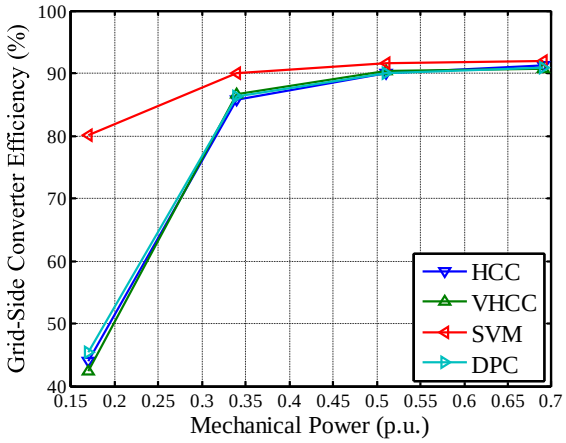

Figure 5.21: Experimental results regarding the overall efficiency of the grid-side system (converter + output filter) for four distinct load levels (17%, 34%, 51% and 69% of the PMSG rated mechanical power).

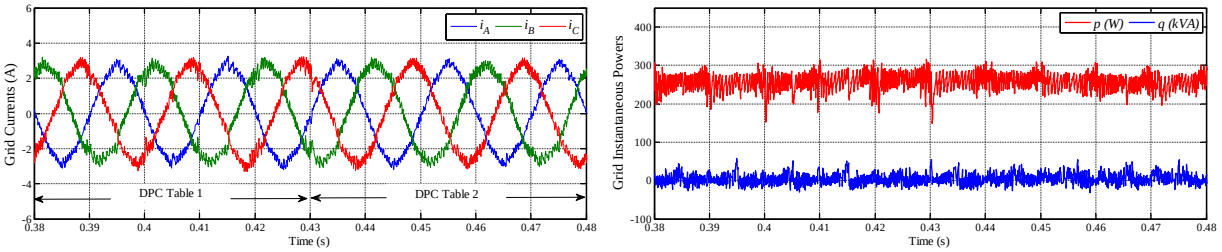

Figure 5.22: Experimental results regarding the two proposed DPC switching tables.

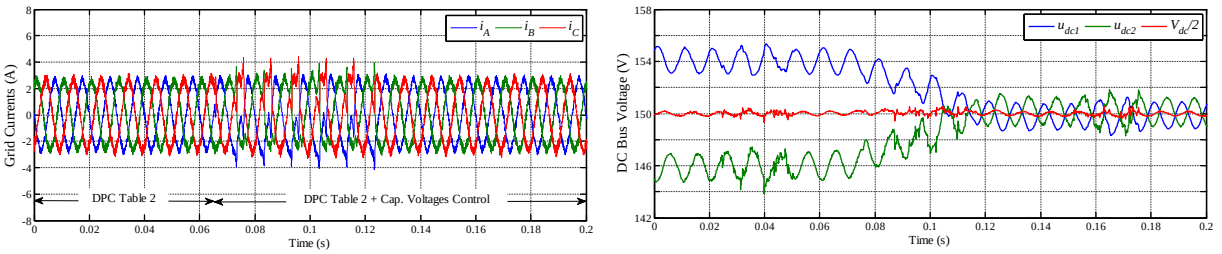

Figure 5.23: Experimental results regarding the control of the capacitor voltages deviation.

5.3 Four-Switch Three-Phase Converter with the Transformer Neutral Point Connected to DC Bus Midpoint for the Grid-Side Converter

As opposed to the fault-tolerant control for the FSTPC with a phase connected to the dc-bus midpoint (FSTPC-PCM) (section 5.2), the FSTPC with the transformer neutral point connected to dc-bus midpoint (FSTPC-NCM) in Figure 5.24 requires to trigger one TRIAC only. Moreover, a lower increase of the dc-link voltage is required, which might lead to a more cost-effective solution.

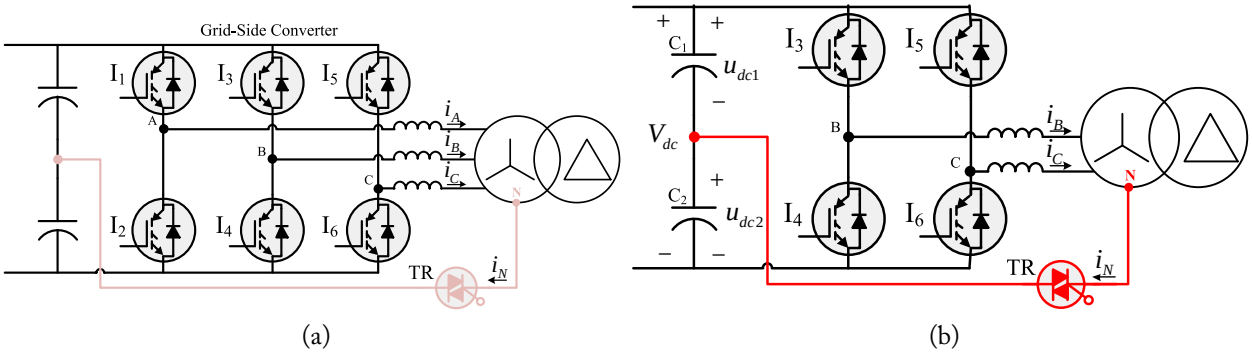

Figure 5.24: Fault-tolerant grid-side converter: (a) six-switch three-phase converter for normal operation; (b) four-switch three-phase converter with the transformer neutral point connected to dc-bus midpoint (FSTPC-NCM) for post-fault operation, considering an open-circuit fault in phase A (I_1 or I_2).

The detection of the faulty phase is followed by its isolation (inhibition of its control signals). Then, the connection of the transformer neutral point to the dc bus midpoint through the TRIAC (hardware reconfiguration) takes place, and finally, the software reconfiguration, by imposing proper reference values and control strategy.

Similarly to the previous section, four control strategies are considered: VOC strategy with HCC, VOC strategy with vector-based HCC, VOC strategy with SVM, and DPC strategy. The block diagrams of all the considered strategies are shown in Figure 5.25. Nevertheless, the VOC strategy with HCC is the only one that demands a fault-tolerant algorithm different from the one applied to the FSTPC-PCM, being here analyzed together with the FSTPC-NCM.

Analyzing the FSTPC-NCM in Figure 5.24b, it can be inferred that both capacitors of the dc-link must assume a voltage value higher than the peak phase-to-neutral voltage (V_{ph}) at the converter output (transformer windings connected in wye), allowing the current control. Thus, the dc bus voltage for the FSTPC-NCM (V'_{dc}) should be higher than $2V_{ph}$, which, compared with the standard six-switch three-phase converter (where $V_{dc} > \sqrt{3}V_{ph}$), results in an increase of approximately 15% [170]: $V'_{dc}/V_{dc} = 2/\sqrt{3} \approx 1.15$.

On the other hand, the usable maximum output voltage can be analytically deduced through the voltage space vectors synthesized by the converter (2.24). For the case in which phase A is

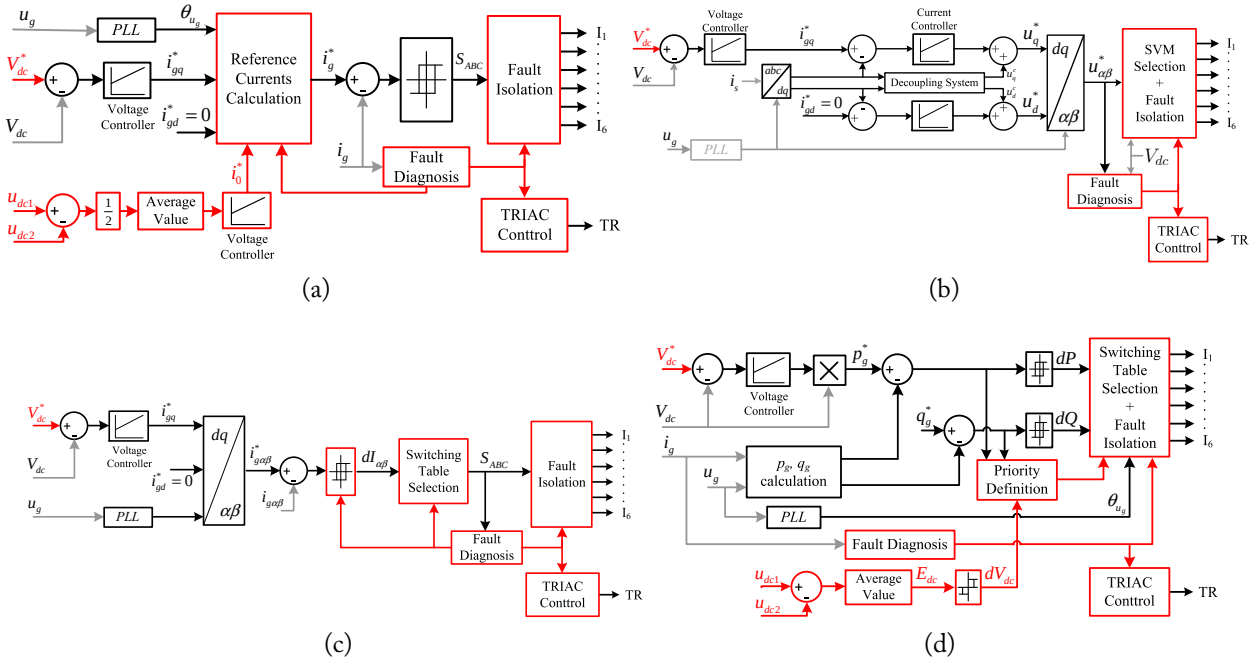

Figure 5.25: Bolck diagrams of the fault-tolerant control strategies for the grid-side converter with the FSTPC-NCM: (a) VOC strategy with HCC; (b) VOC strategy with SVM; (c) VOC strategy with vector-based HCC; (d) DPC strategy.

isolated ($i_A = 0$), the phase-to-neutral voltages can be expressed by:

$$u_{AN} = V_{ph}\sin(\omega t);\ u_{BN} = V_{dc}\left(S_B - \frac{1}{2}\right);\ u_{CN} = V_{dc}\left(S_C - \frac{1}{2}\right) \tag{5.24}$$

Therefore, by substituting (5.24) in (2.24), the following voltage vectors in $\alpha\beta$ axes can be deduced:

$$u_{c\alpha} = \frac{1}{3}V_{dc}\left(1 - S_B - S_C\right) + \frac{2}{3}V_{ph}\sin(\omega t);\ u_{c\beta} = \frac{1}{\sqrt{3}}V_{dc}\left(S_B - S_C\right) \tag{5.25}$$

and presented in Table 5.20 for the available switching states. Since the voltage space vectors do not only depend on the converter switching states (Figure 5.26b), to guarantee that $u_{1\alpha}$ (α-axis component of V_1) always assumes positive values as well as $u_{3\alpha}$ (α-axis component of V_3) assumes negative values, the following relationship must be verified:

$$V'_{dc} > 2V_{ph} \tag{5.26}$$

where V'_{dc} stands for the post-fault dc-link voltage. Therefore, to achieve the same maximum voltage than for an SSTPC, $r = V_{dc}/\sqrt{3}$ (with r being the radius of the inner circle in Figure 5.26a), a minimum DC-link voltage equal to $2V_{ph}$ is required, elucidating the initial assumption.

Additionally, taking into consideration the non-ideal DC bus, the capacitor voltages oscillation and deviation are inherent issues of an FSTPC, as a consequence of the fundamental current flow

Table 5.20: Voltage space vectors of the FSTPC-NCM with ideal dc link.

	$u_{c\alpha}$	$u_{c\beta}$
$V_1(00)$	$\frac{V_{dc}}{3}+\frac{2}{3}V_{ph}\sin(\omega t)$	0
$V_2(10)$	$\frac{2}{3}V_{ph}\sin(\omega t)$	$\frac{V_{dc}}{\sqrt{3}}$
$V_3(11)$	$-\frac{V_{dc}}{3}+\frac{2}{3}V_{ph}\sin(\omega t)$	0
$V_4(01)$	$\frac{2}{3}V_{ph}\sin(\omega t)$	$-\frac{V_{dc}}{\sqrt{3}}$

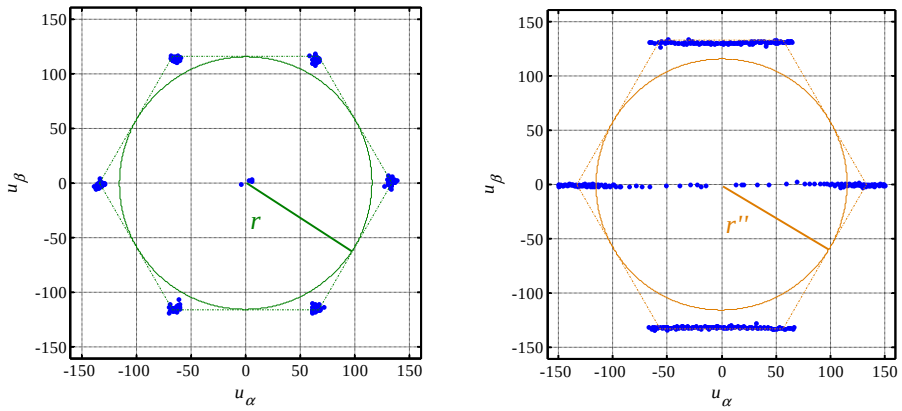

Figure 5.26: Measured grid-side converter voltages in $\alpha\beta$-axes ($V_{ph} = 100$ V): (a) Normal operation with $V_{dc} = 200$ V; (b) Post-fault operation with $V_{dc} = 230$ V, after a fault in phase A of the grid-side converter.

through the capacitors, which leads u_{dc1} and u_{dc2} (voltages of capacitors C_1 and C_2 (Figure 5.24b), respectively) to be different from $V_{dc}/2$. Accordingly, by considering that $V_{dc} = u_{dc1} + u_{dc2}$ assumes a constant value, the deviation of each capacitor voltage is defined as:

$$\Delta u_{dc} = \frac{u_{dc1} - u_{dc2}}{2} \tag{5.27}$$

and, consequently, the capacitor voltages are given by:

$$u_{dc1} = \frac{V_{dc}}{2} + \Delta u_{dc};\ u_{dc2} = \frac{V_{dc}}{2} - \Delta u_{dc} \tag{5.28}$$

Then, by expressing u_{BN} and u_{CN} as function of u_{dc1} and u_{dc2}:

$$u_{BN} = u_{dc1}S_B + u_{dc2}\left(S_B - 1\right);\ u_{CN} = u_{dc1}S_C + u_{dc2}\left(S_C - 1\right) \tag{5.29}$$

the space voltage vectors can be recalculated by using (2.24), allowing to verify that $u_{c\beta}$ remains

unchanged (as given by (5.25)), whereas $u_{c\alpha}$ is given by:

$$u_{c\alpha} = \frac{1}{3}V_{dc}\left(1 - S_B - S_C\right) - \frac{2\triangle u_{dc}}{3} + \frac{2}{3}V_{ph}\sin(\omega t) \tag{5.30}$$

Consequently, Table 5.21 is obtained and the following relationship must be verified:

$$V''_{dc} - \triangle u_{dc,max} > 2V_{ph} \tag{5.31}$$

where V''_{dc} stands for the post-fault DC-link voltage when considering a non-ideal DC bus, and $\triangle u_{dc,max}$ stands for the maximum absolute value of $\triangle u_{dc}$ over a fundamental period of the grid currents. Thus, the minimum dc link voltage that ensures the converter controllability is given by $V''_{dc} = 2V_{ph} + \triangle u_{dc,max}$, and the resulting increase of V_{dc} is given by $V''_{dc}/V_{dc} = 2/\sqrt{3} + \triangle u_{dc,max}/\left(\sqrt{3}V_{ph}\right)$.

Figure 5.26 is presented as an example, where the dc link is 15% increased for post-fault operation. It can be noticed that $V_{dc} = 200$ V would be the minimum DC-link voltage in order to satisfy (5.26) and to ensure post-fault operation, but V_{dc} has to be higher as a consequence of both the voltage drop in the output filter and the capacitor voltage oscillation (5.31). Therefore, by considering the need for approximately extra 10 V in the DC-link voltage for compensating the voltage drop and $\triangle u_{dc,max} = 20$ V, the same maximum output voltage is obtained under both normal and post fault operation if V_{dc} is increased to 230 V under post-fault operation, and, consequently, the inner circles of Figure 5.26a and Figure 5.26b have equal radius ($r = r''$). Thus, in comparison with the minimum DC-link voltage required for normal operation ($\approx$ 183 V), an increase of approximately 25% of V_{dc} is mandatory. Finally, it is worth pointing out that this increase depends on the DC-link capacitor bank design, namely, its rated capacitance (section 6.2.1).

Table 5.21: Voltage space vectors of the FSTPC-NCM with non-ideal dc link.

	$u_{c\alpha}$	$u_{c\beta}$
$V_1(00)$	$\frac{V_{dc} - 2\Delta u_{dc}}{3} + \frac{2}{3}V_{ph}\sin(\omega t)$	0
$V_2(10)$	$\frac{2}{3}V_{ph}\sin(\omega t) - \frac{2\Delta u_{dc}}{3}$	$\frac{V_{dc}}{\sqrt{3}}$
$V_3(11)$	$-\frac{V_{dc} + 2\Delta u_{dc}}{3} + \frac{2}{3}V_{ph}\sin(\omega t)$	0
$V_4(01)$	$\frac{2}{3}V_{ph}\sin(\omega t) - \frac{2\Delta u_{dc}}{3}$	$-\frac{V_{dc}}{\sqrt{3}}$

5.3.1 VOC with HCC

Regarding the current control under post-fault operation with the VOC strategy with HCC (Figure 5.25a), the imposed reference currents are intended to generate a magnetomotive force

equal to that obtained under normal operation (with a balanced three-phase sinusoidal current system). Therefore, the produced magnetic flux as well as the induced electromotive force can remain unchanged. Taking as an example a fault occurrence in phase A, the phase A current becomes null after the fault isolation, and the same current space vector $\left(i_g = i'_B e^{j2\pi/3} + i'_C e^{j4\pi/3}\right)$ is achieved if:

$$\begin{cases} i'_B = \sqrt{3} I_m \cos\left(\omega t - \frac{2\pi}{3} - \frac{\pi}{6} + \phi\right) \\ i'_C = \sqrt{3} I_m \cos\left(\omega t + \frac{2\pi}{3} + \frac{\pi}{6} + \phi\right) \end{cases} \tag{5.32}$$

where I_m is the currents amplitude under normal operating conditions, ω is the currents angular frequency and ϕ is the initial phase angle. Thus, the phase currents increase by a factor of $\sqrt{3}$ and their displacement changes from 120º to 60º. Consequently, the neutral current amplitude is three times as high as the phase currents amplitude under normal operation:

$$i_N = i_B + i_C = 3 I_m \cos\left(\omega t + \pi + \phi\right) \tag{5.33}$$

Therefore, to meet the grid connection requirements under post-fault operation, for the three distinct case scenarios of phases A, B and C affected by an open-circuit fault, the reference phase currents $(i_A^*,\ i_B^*,\ i_C^*)$ are respectively given by:

$$\begin{cases} i_B^* = \sqrt{3}\left[-i_{gd}^* \cos\left(\theta_{u_g} + \frac{\pi}{6}\right) + i_{gq}^* \sin\left(\theta_{u_g} + \frac{\pi}{6}\right)\right] \\ i_C^* = \sqrt{3}\left[-i_{gd}^* \cos\left(\theta_{u_g} - \frac{\pi}{6}\right) + i_{gq}^* \sin\left(\theta_{u_g} - \frac{\pi}{6}\right)\right] \end{cases} \tag{5.34}$$

$$\begin{cases} i_A^* = \sqrt{3}\left[i_{gd}^* \cos\left(\theta_{u_g} + \frac{\pi}{6}\right) - i_{gq}^* \sin\left(\theta_{u_g} + \frac{\pi}{6}\right)\right] \\ i_C^* = \sqrt{3}\left[-i_{gd}^* \sin\left(\theta_{u_g}\right) - i_{gq}^* \cos\left(\theta_{u_g}\right)\right] \end{cases} \tag{5.35}$$

$$\begin{cases} i_A^* = \sqrt{3}\left[i_{gd}^* \cos\left(\theta_{u_g} - \frac{\pi}{6}\right) - i_{gq}^* \sin\left(\theta_{u_g} - \frac{\pi}{6}\right)\right] \\ i_B^* = \sqrt{3}\left[i_{gd}^* \sin\left(\theta_{u_g}\right) + i_{gq}^* \cos\left(\theta_{u_g}\right)\right] \end{cases} \tag{5.36}$$

where θ_{u_g} is the angular position of the grid voltage vector, and $i_{gd}^*,\ i_{gq}^*$ are the reference currents in the synchronous reference frame (outputs of the reactive power and dc-link voltage controllers, respectively).

5.3.1.1 Capacitor Voltage Balancing

The capacitor voltage deviation may force increased stress, due to an unbalanced current distribution through the two capacitors. Thus, the control of the capacitors voltage offset is crucial. This goal can be accomplished under hysteresis current control, by monitoring the voltage drift (through an additional voltage sensor) and by adding a dc offset (i_0^*) to the two reference currents (i_n^*) given in (5.34)-(5.36), according to the error between the capacitor average voltages. Therefore,

the switching states for each phase n are obtained as follows:

$$S_n = \begin{cases} 1 & \text{if } i_n^* + i_0^* > i_n + B_{hcc}/2 \\ 0 & \text{if } i_n^* + i_0^* < i_n - B_{hcc}/2 \end{cases} \tag{5.37}$$

A positive value of i_0^* leads to the increased utilization of the switching state (11) and consequent discharge of the capacitor C_1, whereas a negative value of i_0^* implies the increased utilization of the switching state (00), discharging C_2. So, the center point voltage can be controlled by controlling the value of i_0^*, which can be generated through an additional control loop with the average value of the error between the capacitor voltages as input of a proportional-integral controller (Figure 5.25a):

$$\langle \Delta u_{dc} \rangle = f \int_0^{1/f} \left(\frac{u_{dc1} - u_{dc2}}{2} \right) dt = f \int_0^{1/f} \left(\frac{V_{dc}}{2} - u_{dc2} \right) dt \tag{5.38}$$

where f stands for the grid fundamental frequency in Hz.

The neutral current flowing through the dc-link capacitors (for example, $i_N = i_B^* + i_C^* + 2i_0^*$) allows to control the capacitor voltage deviation according to:

$$\left\langle \frac{d}{dt} \Delta u_{dc} \right\rangle = -\frac{\langle i_N \rangle}{2C} = -\frac{i_0}{C} \tag{5.39}$$

where C stands for the capacitance of each DC-link capacitor ($C = C_1 = C_2$).

The voltage control loop is depicted in Figure 5.27, where the controller and DC-link transfer functions are given by:

$$C(s) = K_P + \frac{1}{T_I s};\ G(s) = \frac{1}{Cs} \tag{5.40}$$

In order to ensure stability of the closed-loop control system in Figure 5.27, the PI controller parameters (K_P, T_I) can be tuned by choosing a phase margin equal to 60º, for a given crossover frequency f_c. The resultant controller parameters are then the following ones:

$$T_I = \frac{2}{C\left(2\pi f_c\right)^2};\ K_P = \frac{\sqrt{3}}{T_I 2\pi f_c} \tag{5.41}$$

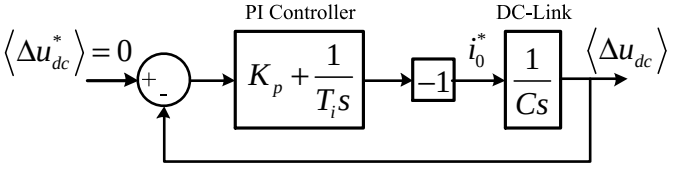

Figure 5.27: Capacitor voltage deviation control loop.

Regarding the choice of the crossover frequency, f_c should be lower than the grid frequency

and also lower than the crossover frequency of the total dc-link voltage (V_{dc}) controller. This way the tuning of the two voltage controllers in Figure 5.25a can be performed independently. The experimental results in section 5.3.3 were obtained with $f_c = 2$ Hz.

Additionally, to avoid the injection of a high dc component into the transformer phase currents, the controller output should be limited to low values. The amplitude of i_0^* is here limited to $B_{hcc}/2$. It is worth noting that under steady-state the dc component present in the phase currents (i_0) is null, due to the action of the PI controller. It should be pointed out that the proposed approach is similar to the one proposed for a Vienna rectifier in [209]-[210]. However, the control of an FSTPC has no degree of freedom to control the center point voltage without adversely affecting its output currents.

5.3.2 Simulation Results

In Figure 5.28 are presented the simulation results of the FSTPC-NCM with phase A isolated, for a load level equivalent to 51% of the PMSG rated mechanical power. The reference dc link voltage is increase 16% in comparison to the normal operating conditions with the SSTPC as grid-side converter, assuming a value of 290 V. The phase and neutral currents for the four control strategies considered are shown in Figure 5.28, demonstrating that all the control strategies are able to generate two phase currents (i_B, i_C) approximately sinusoidal and displaced by 60º, and that the neutral current is given by the sum of i_B and i_C with an amplitude $\sqrt{3}$ times higher. In comparison to the simulation results with the SSTPC in Figure 2.17, it is clear the increase of the phase currents amplitude when using the FSTPC-NCM.

5.3.3 Experimental Results

The operating conditions of the previous simulations results were replicated for the experimental results in Figure 5.29, thus, the FSTPC-NCM intends to keep a constant dc link voltage equal to 290 V and null instantaneous reactive power. Figure 5.29 and Table 5.22 show that the best performances regarding current harmonic distortion and power oscillation are shown by VOC with HCC and DPC strategies, similarly to the results obtained for the FSTPC-PCM (section 5.2.6). Once again, such superior performance can be attributed to the direct control of current or power, with high capability to track the respective references. In spite of presenting increased current and power ripple, an acceptable performance can be provided by VOC with vector-based HCC. The worst performance is given by VOC with SVM, characterized by highly oscillating active and reactive powers (Figure 5.29b and Table 5.22). Such issue might be attenuated by increasing the bandwidth of the current control loop, which was verified by means of simulation results and is illustrated by the low distorted phase currents in Figure 5.28.

Regarding the overall efficiency of the grid-side system when employing a FSTPC-NCM (Fig-

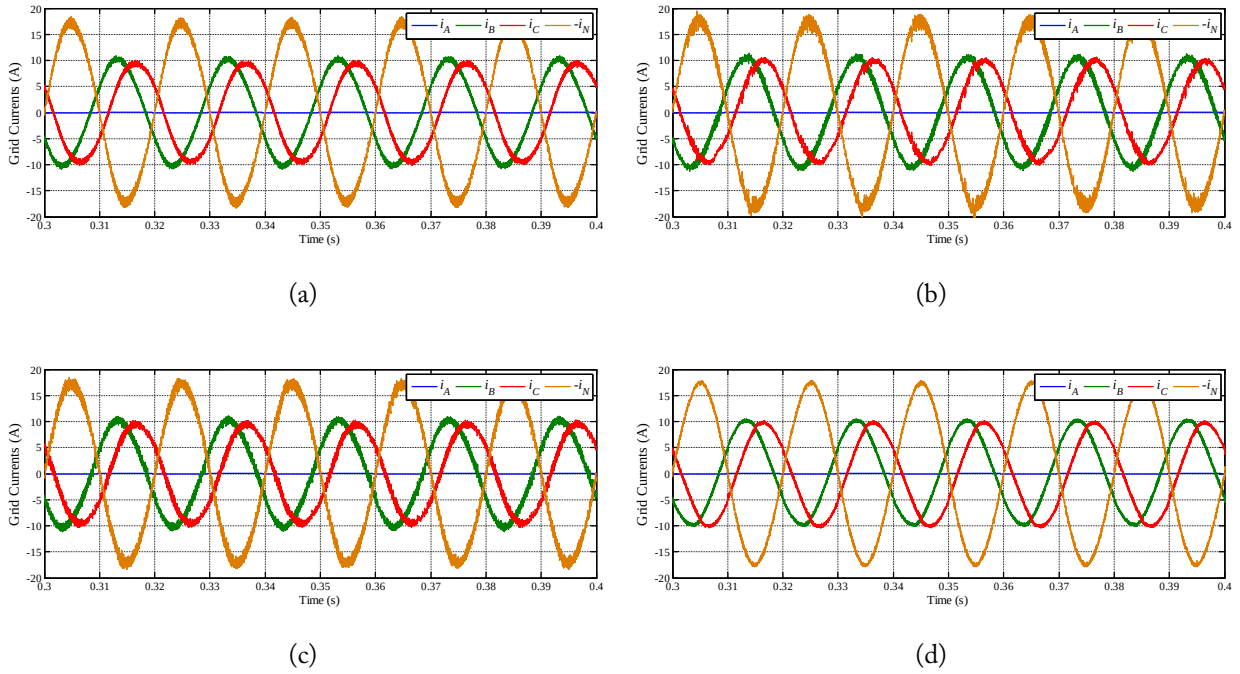

Figure 5.28: Simulation results regarding the time-domain waveforms of the grid phase currents with the grid-side converter under post-fault operation, operating as an FSTPC-NCM: (a) VOC strategy with HCC; (b) VOC strategy with SVM; (c) VOC strategy with vector-based HCC; (d) DPC strategy with switching table 2.

ure 5.30), it is lower than when using the SSTPC (Figure 2.21) due to the increase of both dc link voltage and grid phase currents, increasing the converter and filter losses. Results at 69% of the PMSG rated mechanical power are not presented because the rated grid currents are exceed for load levels above 58% of the PMSG rated mechanical power. Therefore, comparing the efficiency measurements of the FSTPC-NCM (Figure 5.30) with the ones of the FSTPC-PCM (Figure 5.21), with the exception of the VOC with SVM, the FSTPC-NCM tends to present higher efficiency for low load levels, since the predominant switching losses are reduced due to the lower dc link voltage, whereas the FSTPC-PCM shows higher efficiency values for high load levels.

Taking all this into account, it is concluded that an acceptable post-fault performance can be achieved by the FSTPC-NCM when controlled by the proposed strategies. Moreover, it might be an excellent choice when a fault-tolerant drive is intended only to keep its operation in a limited range.

Table 5.22: Grid current THD values and active power TWO values for the FSTPC-NCM.

Control Strategy	Grid Current THD	Active Power TWO
VOC HCC	2.0 %	9.9 %
VOC SVM	5.5 %	26.2 %
VOC VHCC	5.1 %	16.2 %
DPC	3.9 %	9.1 %

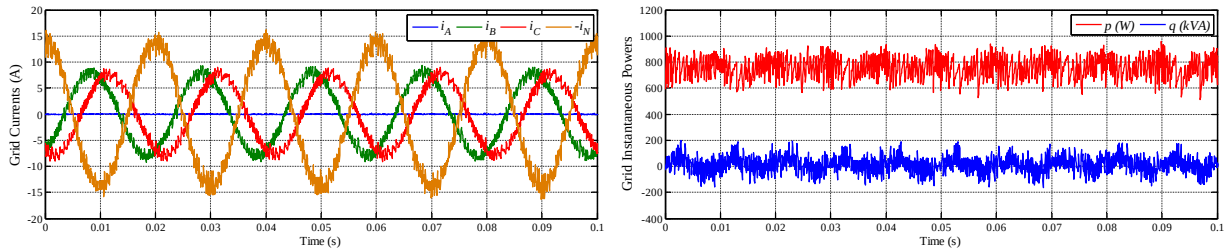

(a)

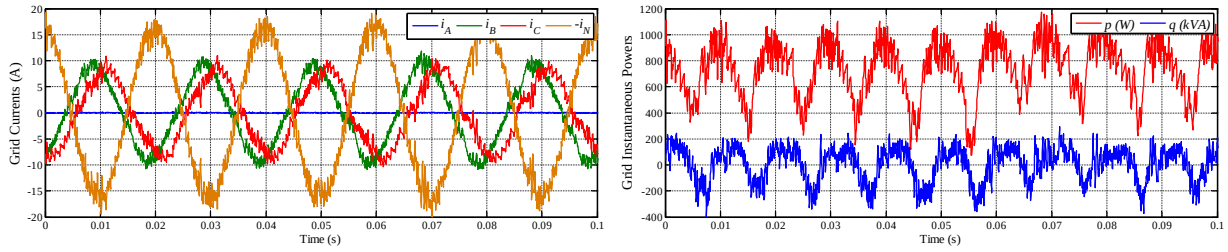

(b)

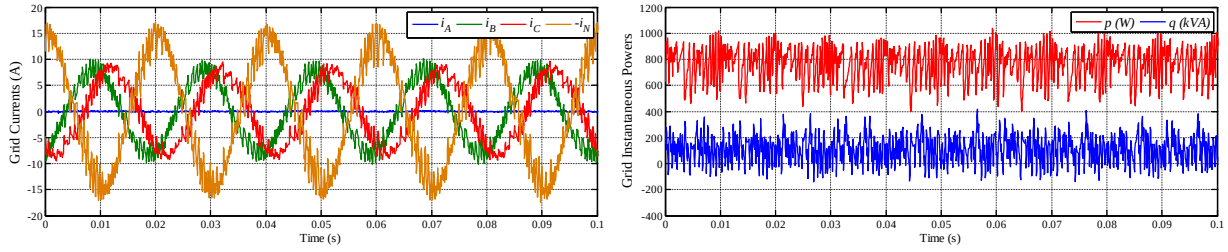

(c)

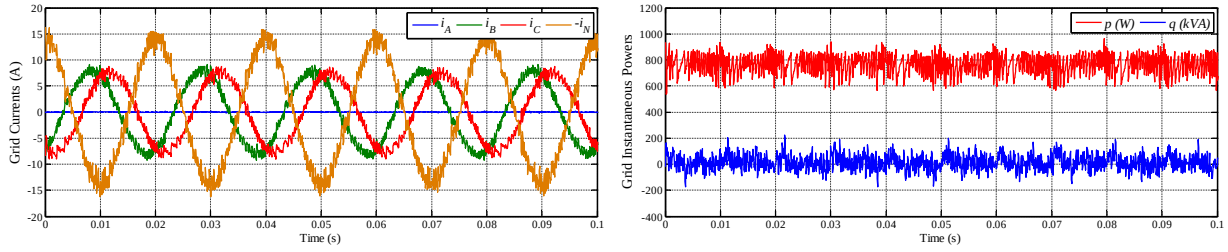

(d)

Figure 5.29: Experimental results regarding the time-domain waveforms of the grid phase currents and the instataneous active and reactive powers with the grid-side converter under post-fault operation, operating as an FSTPC-NCM: (a) VOC strategy with HCC; (b) VOC strategy with SVM; (c) VOC strategy with vector-based HCC; (d) DPC strategy with switching table 2.

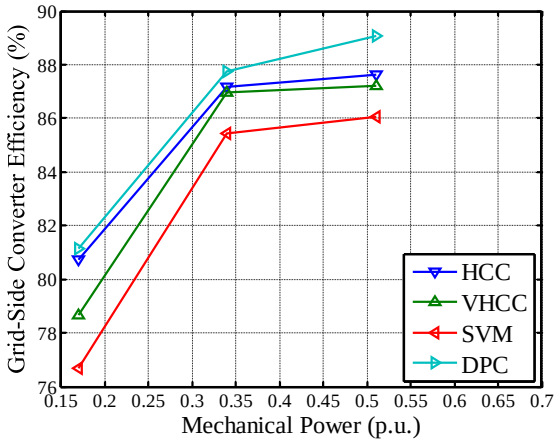

Figure 5.30: Experimental results regarding the overall efficiency of the grid-side system (converter + output filter) for three distinct load levels (17%, 34% and 51% of the PMSG rated mechanical power).

5.4 Five-Leg Converter with a Shared-Leg Connected to the Transformer Neutral Point

In this section a five-leg converter with the shared-leg connected to a phase of the generator and to the transformer neutral point is proposed as an alternative topology for post-fault operation of the grid-side converter (Figure 5.31). Such topology allows the drive to operate in a limited operating range without oversizing the ratings of any component, thus, overcoming the issue of a bulky capacitor bank with high current and voltage ratings.

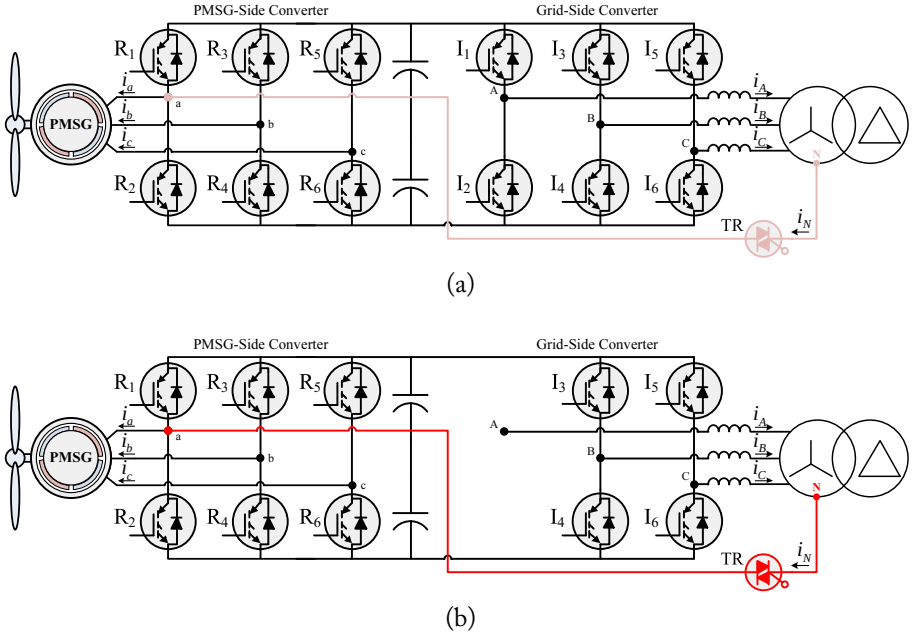

Figure 5.31: Fault-tolerant grid-side converter: (a) six-switch three-phase converter for normal operation; (b) five-leg converter (FLC) with the shared-leg connected to phase a of the generator and to the transformer neutral point for post-fault operation, considering an open-circuit fault in phase A (I_1 or I_2).

After a fault occurrence in the grid-side converter, the converter is intended to operate as a five-leg converter with the shared-leg connected to the transformer neutral point and to a generator phase. Taking as an example a fault in phase A (Figure 5.31b), after fault detection and isolation ($i_A = 0$), the grid (at the filter terminals) and machine voltages during post-fault operation are given by:

$$\begin{cases} u_{AN} = V_{ph}\sin(\omega t) \\ u_{BN} = V_{dc}\,(S_B - S_a) \\ u_{CN} = V_{dc}\,(S_C - S_a) \end{cases} \tag{5.42}$$

$$\begin{cases} u_{an} = \frac{1}{3}V_{dc}\left(2S_a - S_b - S_c\right) \\ u_{bn} = \frac{1}{3}V_{dc}\left(2S_b - S_a - S_c\right) \\ u_{cn} = \frac{1}{3}V_{dc}\left(2S_c - S_a - S_b\right) \end{cases} \tag{5.43}$$

where S_a corresponds to the switching state common to both converter-sides.

The converter voltage capability depends on the machine ($V_{s,ph}$) and grid ($V_{g,ph}$) rated voltages, then, the linear modulation range can be defined as follows:

$$\sqrt{3}V_{s,ph} + V_{g,ph} < V_{dc} \tag{5.44}$$

Therefore, by considering that both assume equal phase-to-neutral values ($V_{s,ph} = V_{g,ph}$), when compared with the SSTPC, the converter voltage capability is reduced by approximately 37 %, which means that the same output voltage can be obtained with an increase of 58% of the dc-link voltage. In comparison to the five-leg converter with the shared-leg connected to the grid and machine phases that requires an increase of 100% of the dc-link voltage, the proposed topology has an improved voltage capability.

The grid-side currents (i_A, i_B, i_N) under post-fault operation can be expressed by equations (5.32) and (5.33), leading to the generation of a magnetomotive force equal to that obtained under normal operation with a balanced three-phase sinusoidal current system. Thus, the phase currents amplitude increase by a factor of $\sqrt{3}$, while the neutral current amplitude is three times as high as the phase currents amplitude under normal operating conditions. Consequently, since the current in the shared leg is equal to the sum of the phase a PMSG current (i_a) with the neutral current (i_N), the shared leg has to be designed with a rated current four times as high as the remaining converter legs, if the rated operating conditions are intended to be reached under post-fault operation.

Regarding the control strategies for the FLC, it was verified that conventional DTC and DPC as well as vector-based HCC are not suitable strategies, since for unsynchronized operation of the PMSG and grid sides (at different frequencies), it might be impossible to synthesize two voltage vectors that satisfy the actions required by the two sides. Therefore, seeking a reduced implementation effort, HCC and sinusoidal-PWM (S-PWM) are proposed for controlling the FLC.

5.4.1 HCC

Adopting hysteresis current control (HCC) of the PMSG and grid currents, under post-fault operation, the reference phase currents are calculated as under normal operation for the PMSG-side converter, whereas the reference currents for the grid-side converter have to be recalculated. Accordingly, for the case in which phase A has been isolated, the reference phase currents for the grid-side converter are given by equation (5.34) and the reference neutral current by:

$$i_N^* = i_B^* + i_C^* \tag{5.45}$$

In a similar way, the reference currents are obtained for the case in which phase B has been isolated by equation (5.35) and:

$$i_N^* = i_A^* + i_C^* \tag{5.46}$$

as well as for the case in which phase C has been isolated by equation (5.36) and:

$$i_N^* = i_A^* + i_B^* \tag{5.47}$$

Therefore, the HCC allows the control strategy to be implemented in a simple way [185] by attributing priority to the control of the current with the highest error (assuming that the hysteresis controllers bandwidths have identical values, otherwise the relative error should be used instead). The block diagram of the proposed control strategy is shown in Figure 5.32. The main drawback of this simple approach is the variable switching frequency, which encourage the development of a PWM strategy with constant switching frequency in the next section.

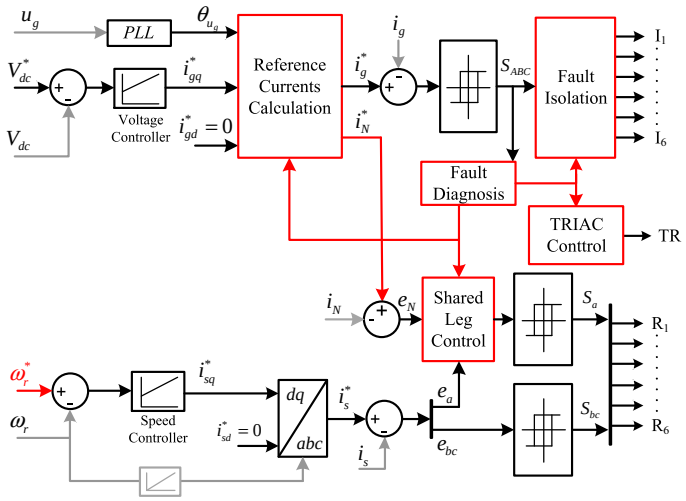

Figure 5.32: Block diagram of the fault-tolerant control strategy for the five-leg converter with HCC.

5.4.2 S-PWM

The block diagram of the proposed control strategy with sinusoidal-PWM (S-PWM) is shown in Figure 5.33. In the implementation of the S-PWM technique, the reference voltages are usually generated through PI controllers in the dq synchronous reference frame, and afterwards transformed for the abc stationary reference frame (Figure 5.33). Thus, if under normal operation the reference grid voltages are denoted as u_{ga}^*, u_{gb}^*, u_{gc}^* and the reference PMSG voltages as

u^*_{sa}, u^*_{sb}, u^*_{sc}, under post-fault operation only the reference voltages for the PMSG-side converter need to be recalculated, being respectively given for the three possible case scenarios of faults in phase A, B and C as follows:

$$u^{**}_{sa} = 0;\ u^{**}_{sb} = u^*_{sb} - u^*_{sa};\ u^{**}_{sc} = u^*_{sc} - u^*_{sa} \tag{5.48}$$

$$u^{**}_{sa} = u^*_{sa} - u^*_{sb};\ u^{**}_{sb} = 0;\ u^{**}_{sc} = u^*_{sc} - u^*_{sb} \tag{5.49}$$

$$u^{**}_{sa} = u^*_{sa} - u^*_{sc};\ u^{**}_{sb} = u^*_{sb} - u^*_{sc};\ u^{**}_{sc} = 0 \tag{5.50}$$

where u^{**}_{ga}, u^{**}_{gb}, u^{**}_{gc} stand for the post-fault reference PMSG voltages. Finally, the switching pattern is generated by comparing the reference voltages with a high frequency triangular carrier.

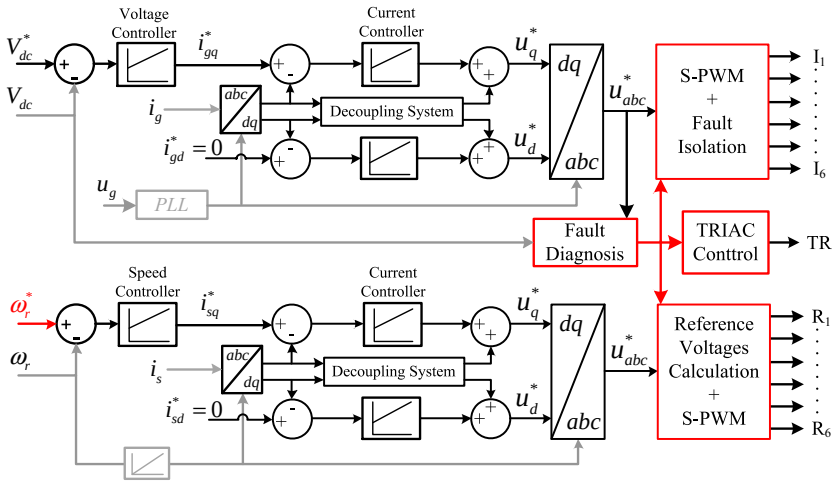

Figure 5.33: Block diagram of the fault-tolerant control strategy for the five-leg converter with S-PWM.

5.4.3 Simulation Results

The simulation of the FLC was performed at a reference dc link voltage of 200 V, a reference speed of 600 rpm, and a load torque equivalent to 50% of the PMSG rated torque. The obtained results are presented in Figure 5.34 regarding the time-domain waveforms of the grid phase currents and the PMSG phase currents. For the grid-side, a current system similar to the one with the FSTPC-NCM is obtained, while for the PMSG-side, a balanced and sinusoidal three-phase current system is obtained, similar to the normal operating conditions. Both HCC (Figure 5.34a) and S-PWM (Figure 5.34b) strategies are able to reach the imposed control targets with satisfactory performace: (1) speed control; (2) dc-link voltage control; and (3) unity power factor at the grid connection point (transformer-side with delta connection).

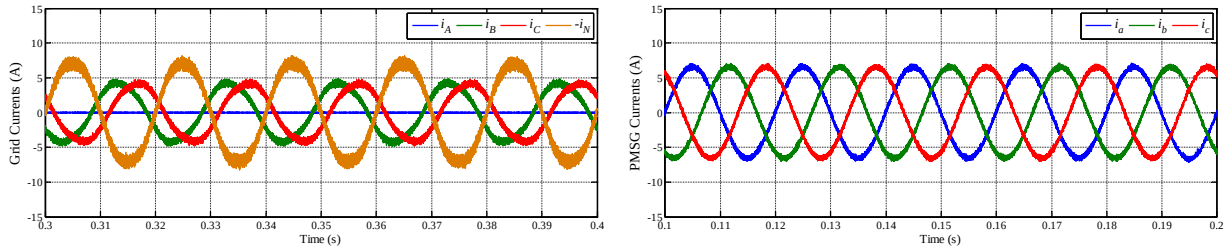

(a)

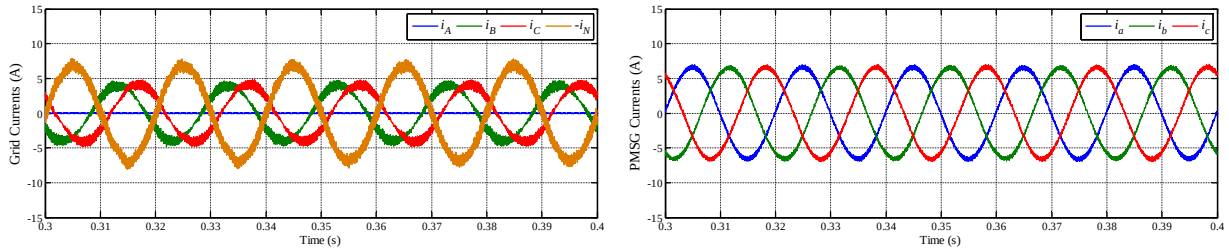

(b)

Figure 5.34: Simulation results regarding the time-domain waveforms of the grid phase currents and the PMSG phase currents with the grid-side converter under post-fault operation, operating as an FLC: (a) HCC; (b) S-PWM.

5.4.4 Experimental Results

A reference dc link voltage of 200 V, a reference speed of 600 rpm, and a load torque equivalent to 50% of the PMSG rated torque (17% of the PMSG rated mechanical power) are also imposed for the experimental results in Figure 5.35 and Table 5.23. Analyzing these results, it is concluded that superior performance regarding current harmonic distortion and power oscillation is provided by S-PWM. Moreover, they are in good agreement with the simulations results.

Table 5.23: Grid current THD values and active power TWO values for the FLC.

Control Strategy	PMSG Current THD	Grid Current THD	Active Power TWO
HCC	3.2 %	10.5 %	43.1 %
S-PWM	2.8 %	6.8 %	27.2 %

5.5 Summary

In this chapter, four converter topologies and respective control strategies have been proposed as alternatives for post-fault operation of the two power converters of a PMSG drive.

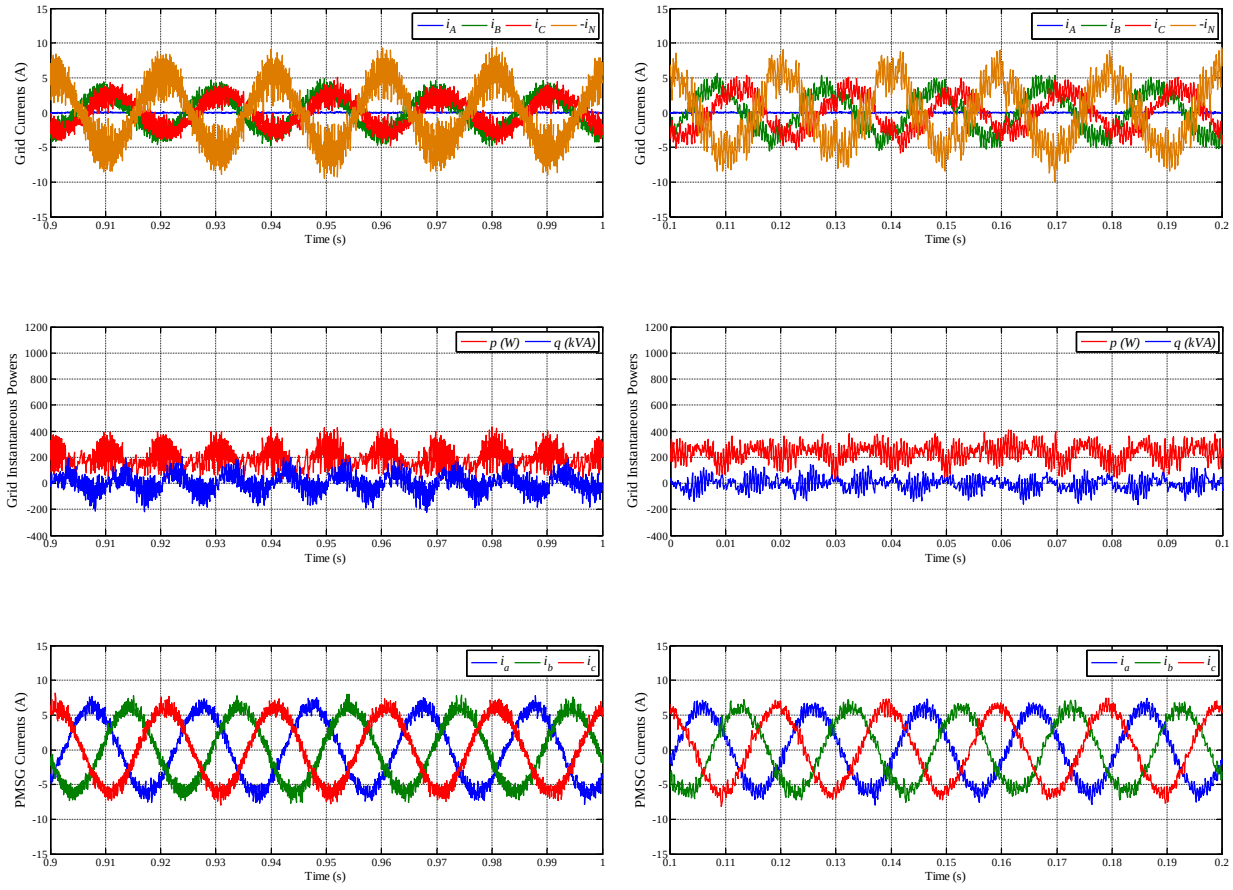

(a) (b)

Figure 5.35: Experimental results regarding the time-domain waveforms of the grid phase currents, the instataneous active and reactive powers, and the PMSG phase currents with the grid-side converter under post-fault operation, operating as an FLC: (a) HCC; (b) S-PWM.

A three-switch three-phase rectifier (TSTPR) is addressed for post-fault operation of the PMSG-side converter, without requiring extra hardware. Among the four control strategies proposed with the aim to minimize the torque oscillation, DTC-based strategies appear to be excellent choices, since they are able to compensate the torque oscillation in closed-loop.

Three distinct topologies are analyzed for post-fault operation of the grid-side converter: a four-switch three-phase converter with a phase connected to dc-bus midpoint (FSTPC-PCM); a four-switch three-phase converter with the transformer neutral point connected to dc-bus midpoint (FSTPC-NCM); and a five-leg converter (FLC) with the shared-leg connected to a phase of the generator and to the grid transformer neutral point. The choice of a given converter topology depends on the desired tradeoff between post-fault performance and cost increase. Thus, the FSTPC-NCM and the FLC might be the most cost-effective solutions when considering the drive derating for post-fault operation, since there is lack of need for a great increase of the dc link voltage due to their higher voltage capability in comparison to the FSTPC-PCM. Moreover, to perform

the hardware reconfiguration the FSTPC-NCM and the FLC require one TRIAC only, instead of the three TRIACs required by the FSTPC-PCM. Both vector control and direct control have shown to be viable options for controlling the FSTPC-PCM and the FSTPC-NCM. For the FLC, vector control with HCC and S-PWM has been proposed and validated.

Additionally, it was verified that the information provided by the fault diagnostic methods assumes paramount important, since post-fault operation relies on the knowledge of the faulty switch or faulty phase to select a proper control strategy.

Chapter 6

Fault-Tolerant Converters for PMSG Drives: Design Considerations, Control System and Real-Time Response

Reliable and fast fault diagnosis and proper post-fault control are major issues in order to achieve fault tolerance, both addressed in previous chapters (chapters 4 and 5). Moreover, the converter design, the integration of the overall control system into the drive controller, and the drive real-time response to a fault must be considered, which are the concerns of this chapter regarding three distinct fault-tolerant converter topologies.

Taking into account that a correct design of the converter components is mandatory to ensure safe post-fault operation and not to reduce the drive lifetime, two options might be taken: oversizing of the drive components and/or drive derating. As a consequence, different tradeoffs between operating limits and cost increase may be achieved. For instance, the topologies with connection to the dc bus midpoint (FSTPC-PCM and FSTPC-PCM) require a careful design of the capacitors, which is usually ignored.

For real-time implementation and operation, the control system of a fault-tolerant drive has to include: control strategies for normal operation; fault diagnostic algorithms; procedures for transition between normal control and post-fault control; and control strategies for post-fault operation. Thus, it is worth analyzing the interplay between all the steps that take place after a fault occurrence by means of experimental results.

Although all the proposed diagnostic techniques and control strategies for post-fault operation have shown to be viable options, only some of them are chosen to exemplify the real-time response of three distinct fault-tolerant PMSG drives. These three converter topologies are considered to be the most interesting ones, resulting from the combination of the alternative topologies studied in chapter 5.

6.1 Fault-Tolerant Converter Topology I

The first proposed fault-tolerant converter for the PMSG drive results from the combination of the TSTPR (section 5.1) with the FSTPC-PCM (section 5.2), as illustrated in Figure 6.1. Therefore, the extra components (TRIACs) as well as the oversizing of the standard ones (IGBTs and capacitor bank) are only related to the post-fault operation of the grid-side converter, because, in this case, the dc bus voltage doubles and a grid phase current flows through the capacitors.

The remaining modifications to the drive system under normal operating conditions are software related: fault isolation, hardware reconfiguration and control reconfiguration. Such tasks can be successfully performed by integrating into the drive controller the fault diagnostic techniques proposed in chapter 4 and the control strategies proposed in sections 5.1 and 5.2.

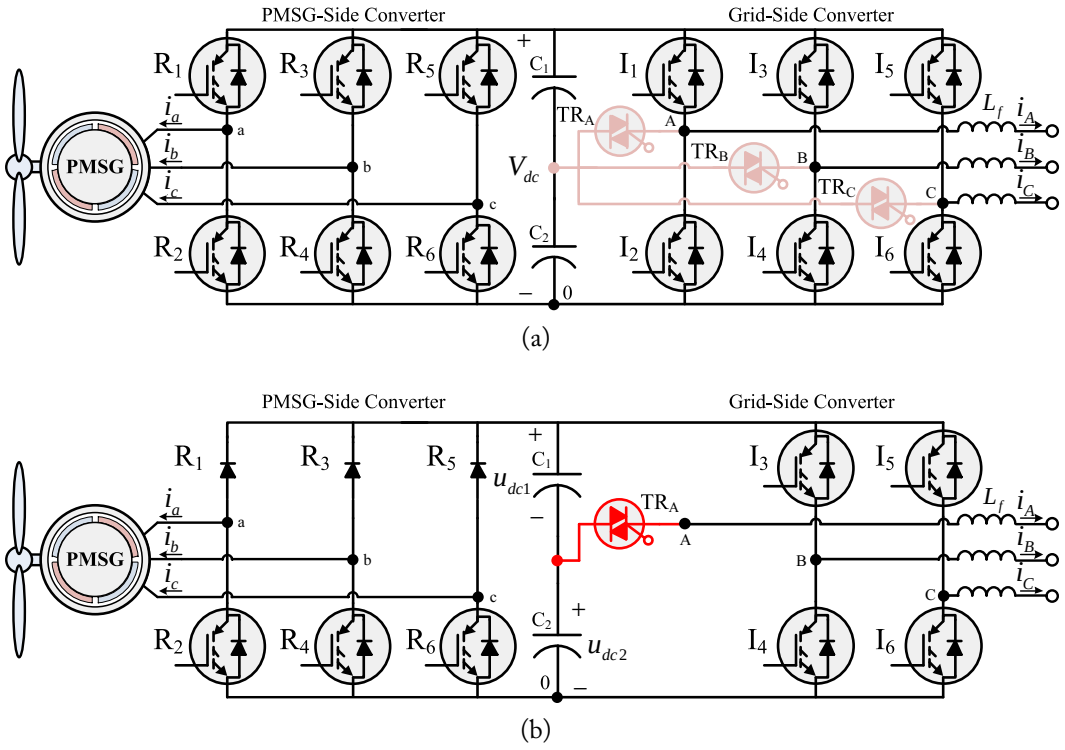

Figure 6.1: Fault-tolerant PMSG drive I: (a) under normal operating conditions; (b) after fault occurrences in power switches R_1 and I_1.

6.1.1 Design Considerations

Compared with the standard SSTPC, the fault-tolerant converter in Figure 6.1 requires power switches (IGBTs) and a capacitor bank with doubled voltage rating, whereas the TRIACs must have half of the IGBTs' voltage rating and equal current rating.

The load of the two dc link capacitors is increased by half of the rated current of the grid-side converter, with a fixed fundamental frequency (50 Hz), accordingly, and following the design

guidelines of [211], the maximum current stress on the capacitors ($I_{C,rms}$) can be given by:

$$I_{C,rms} = \sqrt{\left(\frac{I_{PMSG,rms}}{\sqrt{2}k_{PWM,PMSG}}\right)^2 + \left(\frac{I_{Grid,rms}}{2k_{PWM,Grid}}\right)^2 + \left(\frac{I_{Grid,rms}}{2k_{50Hz}}\right)^2} \tag{6.1}$$

For the sake of simplicity, the generator and grid rated rms currents can be considered to have equal values $\left(I_{PMSG,rms} = I_{Grid,rms} = I_{rated}/\sqrt{2}\right)$as well as the PWM frequencies of both converters, leading to:

$$I_{C,rms} = \frac{I_{rated}}{\sqrt{2}}\sqrt{\frac{3}{4k_{PWM}^2} + \frac{1}{4k_{50Hz}^2}} \tag{6.2}$$

where the constant values k_{PWM} and k_{50Hz} result from the frequency dependence of the capacitors equivalent series resistance (R_{ESR}). With the R_{ESR} at 100 Hz ($R_{ESR,100Hz}$) being usually the reference value, k_{PWM} and k_{50Hz} are given by: $k_{PWM} = \sqrt{R_{ESR,100Hz}/R_{ESR,PWM}}$; $k_{50Hz} = \sqrt{R_{ESR,100Hz}/R_{ESR,50Hz}}$

Taking as an example the use of electrolytic capacitors and PWM frequencies between 1 kHz and 10 kHz, an increase of the capacitors maximum current between 30% and 40% should be expected. It is worth noting that for high power levels metallized film capacitors are the best option, because they offer a cost-effective solution for high current ratings together with long lifetime. As last remark, it is pointed out that the required oversizing of the capacitors current rating allows their lifetime to be extended, since under normal operating conditions (standard SSTPC) they operate below the maximum temperature. This may also result in a valuable contribution for increasing the drive reliability, because capacitors are great contributors to power converter failures.

Finally, the necessary rated capacitance to limit the voltage oscillation as a consequence of the low frequency current can be easily estimated [167]:

$$C = \frac{I_{rated}}{2\omega\Delta u_{dc,max}} \tag{6.3}$$

where $\Delta u_{dc,max}$ stands for the maximum permissible voltage oscillation of each capacitor, which should be chosen to meet the desired converter performance. The minimum allowable capacitance can be obtained with $\Delta u_{dc,max} = V_{dc}/2 - \sqrt{3U_g}$, which guaranties the converter controllability, but may lead to a poor performance.

Therefore, the topology proposed in this section is more cost-effective for wind turbine applications than those which have been already proposed in the literature for fault-tolerant back-to-back topologies. On the one hand, three TRIACs are necessary instead of the six used in a back-to-back topology with two FSTPC [167], avoiding the connection of a machine phase to the dc bus midpoint. Thus, the fundamental component of the machine phase currents does not circulate in the dc bus, which can reach quite low frequencies and makes the capacitor bank design difficult. In addition to this, without increasing the dc bus voltage for post-fault operation of the PMSG-

side converter, the switching losses do not increase as well as the stress on the generator winding insulation. On the other hand, only the IGBTs voltage rating has to double, whereas for a five-leg converter both current and voltage ratings have to double leading to a fourfold power rating [184], which is expected to imply a higher cost increase than the dc link oversizing in the proposed topology. Moreover, contrary to the five-leg converter, the proposed system is capable of handling simultaneous faults in both converter sides.

Taking into account the converter design considerations in this section, after a fault in grid-side converter, the FSTPC-PCM is able to allow the PMSG drive to operate at its rated operating conditions. On the other hand, using the TSTPR for post-fault operation of the PMSG-side, according to the theoretical and experimental analysis of the PMSG rms current for the proposed vector control (Figure 5.4) and direct control strategies, the maximum torque should be limited to 83% and 90% of the PMSG rated torque, respectively, in order not to exceed the PMSG rated current (Appendix A - Table A.1).

6.1.2 Control System

A reliable and effective fault diagnosis is crucial in a fault-tolerant system to trigger the remedial procedures. Accordingly, the detection method in section 4.1.1 (CPVP method) and the localization method in section 4.1.3 (ENCAAV-CPVM method) are adopted for both converter sides of the fault-tolerant PMSG drive I. Taking into account the goals of the fault-tolerant drive under analysis, the algorithm applied to the grid-side converter has to identify the faulty phase only, hence, SENCAAV-CPVM method is able to provide the necessary information. But for the PMSG-side converter it is relevant to exactly localize the faulty switch, using the ENCAAV-CPVM method.

Fault diagnosis is immediately followed by fault isolation, which differs depending on the faulty converter side. In the PMSG-side converter, the fault is isolated by inhibiting the control signals of the three upper or bottom power switches, depending on whether an upper or a bottom IGBT is faulty, respectively. In the grid-side converter, the fault is isolated by inhibiting the control signals of the faulty phase.

Hardware reconfiguration is only considered for the grid-side converter by turning on the TRIAC corresponding to the faulty. This task only can be performed after guaranteeing that both switches of the faulty phase are turned off. Otherwise, the connection of the phase to the dc link midpoint might lead to short-circuit one of the capacitors. Therefore, a time delay of one sampling period between fault isolation and hardware reconfiguration must be included. Together with the hardware reconfiguration, the control reconfiguration is also triggered, selecting a suitable control strategy for the FSTC-PCM and imposing a dc bus reference voltage twice as high.

Control reconfiguration is immediately triggered after fault detection in the PMSG-side converter, by choosing a proper control strategy.

The execution time of all the described tasks is mainly related to the fault detection time and

the turn on time of the TRIAC in the case of the grid-side converter.

As an example, DTC strategy (section 5.1.3) and DPC strategy (section 5.2.4) are chosen to illustrate the real-time response of the fault-tolerant PMSG drive I in the next section.

6.1.3 Real-Time Response

The experimental setup used to validate the fully-integrated fault-tolerant converter I is depicted in Figure 6.2, including an additionally TRIAC. All the experimental results were carried out at a grid phase-to-phase voltage of 75 V, a reference speed of 720 rpm and a load torque equivalent to 50% of the generator rated torque. A reference dc link voltage of 150 V is imposed under normal operating conditions as well as under a fault in the PMSG-side converter, whereas it is increased to 300 V after a fault occurrence in the grid-side converter.

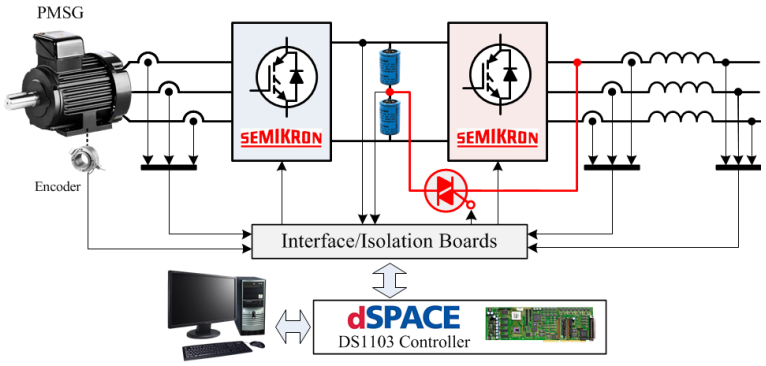

Figure 6.2: Diagram of the experimental setup: fault-tolerant PMSG drive I.

6.1.3.1 Real-Time Response to a Fault in the Grid-Side Converter

All the required steps to guarantee proper post-fault operation of the grid-side converter are well visible in Figure 6.3a, by imposing a delay time of 100 ms between each one. At $t = 0.05\ s$, a fault is introduced in IGBT I_1, as a consequence the instantaneous active power presents a pulsating behavior and the dc bus cannot be kept constant, while the instantaneous reactive power oscillation also increases drastically. This behavior is obviously undesired by the converter that is exposed to additional stress, as well as by the grid, concerning issues such as power quality and voltage stability.

The converter phase A is identified as faulty by the diagnostic method and then isolated at $t = 0.15\ s$, by removing the gate command signals of phase A (I_1 and I_2). This way the path for the current flow in phase A is extinguished and the converter loses the control of the dc bus voltage. Finally, at $t = 0.25\ s$ hardware and software reconfigurations are performed simultaneously, which means that the TRIAC of phase A is turned on, the reference dc bus voltage is doubled, and the

switching table, as well as the sector definition, is chosen according to the hardware reconfiguration. Therefore, the grid phase currents become sinusoidal when the dc bus voltage exceeds the double of the phase-to-phase voltage peak value (212 V), which occurs at $t = 0.325\ s$, and the reactive power becomes null. Then, the active power and the dc bus voltage tend together to the steady-state.

By removing the delay time, Figure 6.3b shows the actual response of the fault-tolerant grid-side converter to a fault. The fault occurrence is detected and localized in 1.2 ms, corresponding to 6% of the grid phase currents fundamental period. Immediately after the fault detection, the required remedial procedures (fault isolation, hardware and software reconfigurations) are accomplished, allowing a fast recovery. It can be seen that the grid instantaneous powers only present undesired oscillations during a short period of time after the fault occurrence, then the active power becomes negative to increase the dc bus voltage and the steady-state is reached at $t = 0.3\ s$. Therefore, V_{dc} is kept constant and equal to the reference value, and unit power factor, instantaneous powers with low oscillation and sinusoidal currents with low THD are provided by the implemented DPC strategy of the FSTPC-PCM.

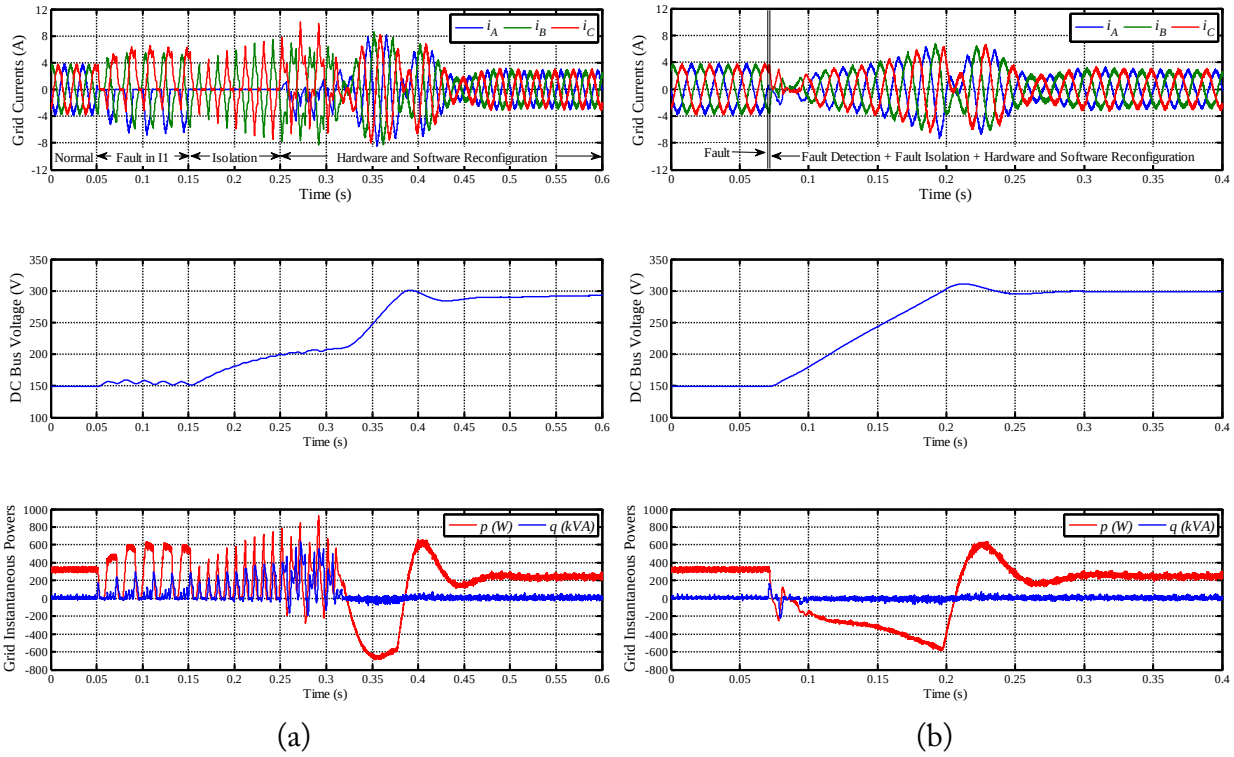

Figure 6.3: Experimental results regarding the fault-tolerant drive I response to an open-circuit in the grid-side converter: (a) with a delay time of 100 ms between each step (for illustration purposes only); (b) actual real-time response.

6.1.3.2 Real-Time Response to a Fault in the PMSG-Side Converter

In Figure 6.4a, a delay time of 200 ms is imposed to observe the step-by-step behavior of the fault-tolerant drive after a fault occurrence in IGBT R_1 of the PMSG-side converter. The fault is introduced at $t = 0.1\ s$, leading to a pulsating electromagnetic torque, with a high pulsating component at the generator currents fundamental frequency (60 Hz), and an oscillating amplitude of the stator flux. Although the converter operation and the speed control remain possible for the considered operating conditions, it is worth noting that for higher load levels the torque pulsating behavior might increase and force the system to shutdown if remedial actions are not quickly adopted. The fault isolation is executed at $t = 0.3\ s$ in order to allow a balanced operation, by removing the gate command signal of the upper IGBTs, that leads to a marked reduction of both torque and flux oscillation. Finally, at $t = 0.5\ s$ the conventional DTC switching table is replaced by Table 5.6, permitting a slight reduction of the torque and flux oscillation as well as the elimination of useless commutations of the IGBTs in operation. In comparison with the faulty operation, the topology used for post fault operation allows the generator to operate with lower torque and flux oscillation.

For the results in Figure 6.4b the delay time was removed to evaluate the response of the integrated fault diagnostic technique. Figure 6.4b shows that the fault detection triggers fault isolation and software reconfiguration 1 ms after the fault occurrence, preventing the torque pulsating behavior. Therefore, a smooth torque is developed under post-fault operation, whereas the stator flux control is limited by the reduced number of available voltage vectors. Despite this, taking into account that additional hardware is avoided by using the TSTPR, a fairly satisfactory performance is achieved by the fault-tolerant generator-side converter, allowing it to reach the rated operating conditions whether the currents rms values can exceed their rated value in approximately 10%..

6.2 Fault-Tolerant Converter Topology II

The second fault-tolerant converter proposed for the PMSG drive results from the combination of the TSTPR (section 5.1) with the FSTPC-NCM (section 5.3), as illustrated in Figure 6.5.

In comparison to the fault-tolerant PMSG drive I (section 6.1), the topology proposed in this section for post-fault operation of the grid-side converter has a higher voltage capability, requiring a lower increase of the DC-link voltage as well as fewer extra components (only one TRIAC). Thus, allowing the minimization of the hardware requirements and leading to a lower increase of the system cost.

The fault-tolerant control system of the PMSG drive includes a suitable fault diagnostic technique for each converter side (chapter 4) and one of the control strategies proposed in sections 5.1 and 5.3 for post-fault operation of each converter side.

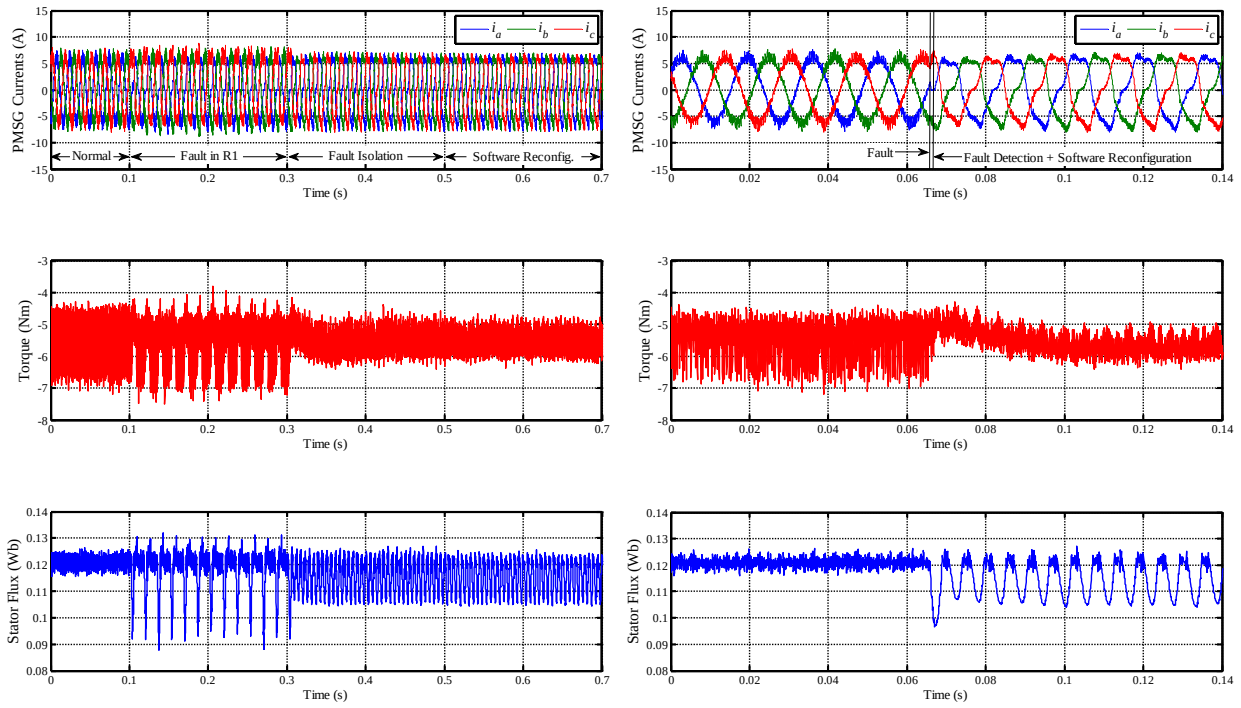

(a) (b)

Figure 6.4: Experimental results regarding the fault-tolerant drive I response to an open-circuit in the PMSG-side converter: (a) with a delay time of 200 ms between each step (for illustration purposes only); (b) actual real-time response.

6.2.1 Design Considerations

Due to the use of the FSTPC-NCM, the fault-tolerant converter in Figure 6.5 requires power switches (IGBTs) and a capacitor bank with a voltage rating increased by a minimum of 15% (section 5.3) in comparison with the standard SSTPC, whereas the TRIAC must have half of the IGBTs' voltage rating. To avoid oversizing the current ratings for the IGBTs and transformer, the maximum output power must be limited to 58% of the drive rated power $\left(1/\sqrt{3} \approx 0.58\right)$. Consequently, both TRIAC and neutral wire are sized for a current rating 73% higher than the converter phases.

The load of the two dc link capacitors is increased by 87% of the rated current of the grid-side converter $\left(\sqrt{3}/2 \approx 0.87\right)$, with a fixed fundamental frequency (50 Hz), accordingly, and following the same design considerations of the section 6.1.1, the maximum current stress on the capacitors can be given by:

$$I_{C,rms} = \frac{I_{rated}}{\sqrt{2}} \sqrt{\frac{3}{4k_{PWM}^2} + \frac{3}{4k_{50Hz}^2}} \tag{6.4}$$

Taking as an example the use of electrolytic capacitors and PWM frequencies between 1 kHz

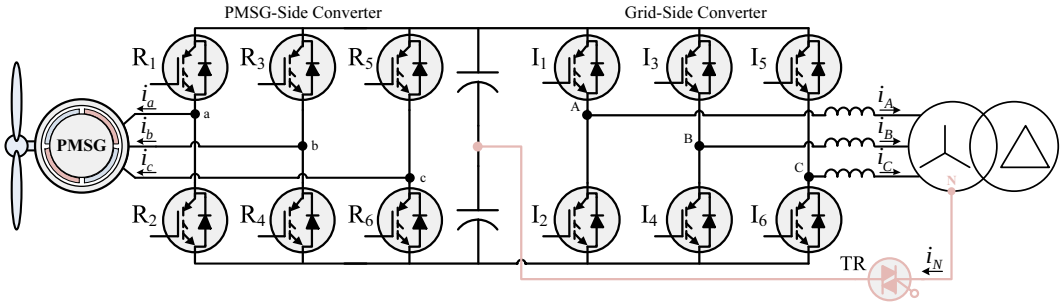

(a)

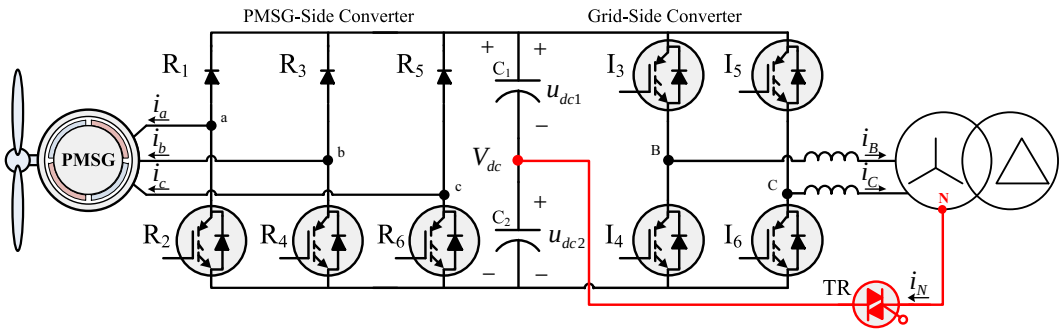

(b)

Figure 6.5: Fault-tolerant PMSG drive II: (a) under normal operating conditions; (b) after fault occurrences in power switches R_1 and I_1.

and 10 kHz, an increase of the capacitors maximum current between 80% and 100% should be expected.

The required rated capacitance of each capacitor to limit the maximum voltage oscillation ($\Delta u_{dc,max}$) as a consequence of the low frequency current can be given by:

$$C = \frac{\sqrt{3} I_{rated}}{2\omega \Delta u_{dc,max}} \tag{6.5}$$

The requirement of a transformer in the proposed fault-tolerant drive can be seen as a disadvantage, because it may not be available and its inclusion would not be a cost-effective solution in order to achieve fault-tolerance. However, it is worth noting that the transformer is usually included at the converter output in high-power wind turbines with low-voltage two-level voltage source converters [19].

6.2.2 Control System

For open-circuit fault diagnosis, the same methods adopted in section 6.1 are here adopted for the fault-tolerant PMSG drive II (CPVP method and ENCAAV-CPVM method). In comparison with the fault-tolerant PMSG drive I (section 6.1), the main distinctive task when adopting topology II is related to the hardware reconfiguration (FSTPC-NCM), which is always accomplished

by connecting the transformer neutral point to the dc bus midpoint independently of the faulty phase. Finally, the control system is reconfigured by means of the control strategies in sections 5.1 and 5.3. In the next section RFOC with HCC (section 5.1.1) and VOC with HCC (section 5.3.1) are taken as examples for the control of the TSTPR and FSTPC-NCM, respectively.

6.2.3 Real-Time Response

The experimental setup used to validate the fault-tolerant converter II is depicted in Figure 6.6, comprising additionally a three-phase core-type transformer and a TRIAC. The experiments were carried out at a grid phase-to-neutral voltage amplitude of 100 V (transformer-side with wye connection), a reference speed of 900 rpm and a load torque equivalent to 75% of the generator rated torque. A reference dc link voltage of 200 V is imposed under normal operating conditions as well as under a fault in the PMSG-side converter, whereas it is increased to 230 V after a fault occurrence in the grid-side converter.

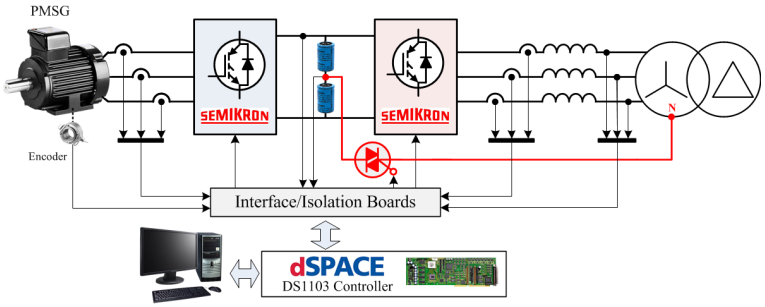

Figure 6.6: Diagram of the experimental setup: fault-tolerant PMSG drive II.

6.2.3.1 Real-Time Response to a Fault in the Grid-Side Converter

Figure 6.7 shows the system response to a fault in the IGBT I_1 of the grid-side converter at $t = 0.11\ s$. Before the fault occurrence, the SSTPC topology provides a balanced three-phase current system as well as constant and balanced capacitor voltages. After the fault detection, which is performed in 1.75 ms (9% of the fundamental period), the remedial procedures are triggered, by turning off the phase A gate command signals, turning on the TRIAC, imposing new reference currents and increasing in 15% the reference dc link voltage. As can be seen in Figure 6.7, during post-fault operation the converter phase currents become $\sqrt{3}$ times higher than during normal operation, while the neutral current is $\sqrt{3}$ times higher than the phase current. The capacitor voltages (u_{dc1}, u_{dc2}) oscillates at the grid frequency (50 Hz), as a consequence of the current flow through the dc bus midpoint, but the average error between u_{dc1} and u_{dc2} is approximately null,

thanks to the control of the capacitor voltages performed by introducing an offset in the reference currents (section 5.3.1.1).

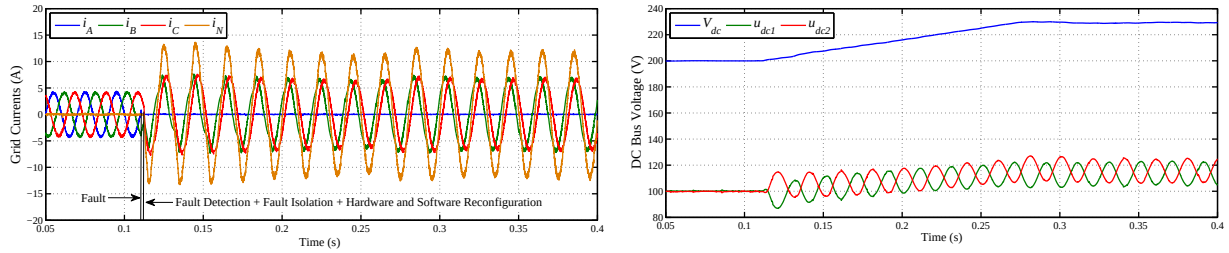

Figure 6.7: Experimental results regarding the fault-tolerant drive II response to a fault in phase A of the grid-side converter.

6.2.3.2 Real-Time Response to a Fault in the PMSG-Side Converter

Figure 6.8 shows the electromagnetic torque behavior as a result of a fault occurrence, with an imposed delay time of 100 ms between each step of the fault-tolerant control for illustration purposes only. The fault (introduced at $t = 0.16s$) yields a pulsating electromagnetic torque, with a high pulsating component at the generator currents fundamental frequency. The fault isolation consists in removing the gate command signal of the upper IGBTs ($t = 0.26s$), resulting in the converter operation as a TSTPR. Despite balanced phase currents, they are highly distorted (Figures 6.9a and 6.9b) and remain generating oscillating electromagnetic torque. Finally, the software compensation is considered, controlling i_{sd} with the aim to minimize both current distortion and torque ripple, which is effectively accomplished and well illustrated by Figures 6.8 and 6.9, confirming that the proposed control strategy permits a marked reduction of the electromagnetic torque ripple.

By removing the time delay in Figure 6.8, the actual real-time response of the fault-tolerant PMSG drive II to a fault in the PMSG-side converter is illustrated in Figure 6.10, demonstrating that stable post-fault operation with reduced torque oscillation can be reached quickly even when the detection time becomes close to one fundamental period of the phase currents.

6.3 Fault-Tolerant Converter Topology III

The third proposed fault-tolerant converter for the PMSG drive combines the TSTPR (section 5.1) for post-fault operation of the PMSG-side converter with the FLC with the shared-leg connected to a phase of the generator and to the transformer neutral point (section 5.4) for post-fault operation of the grid-side converter, as illustrated in Figure 6.11. As a consequence, simultaneous faults in both PMSG- and grid-side cannot be tolerated.

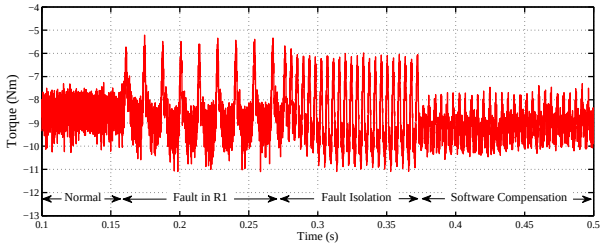

Figure 6.8: Experimental results regarding the generator electromagnetic torque response to a fault in the PMSG-side converter with a delay time of 100 ms between each step of the fault-tolerant control (topology II), for illustration purposes only.

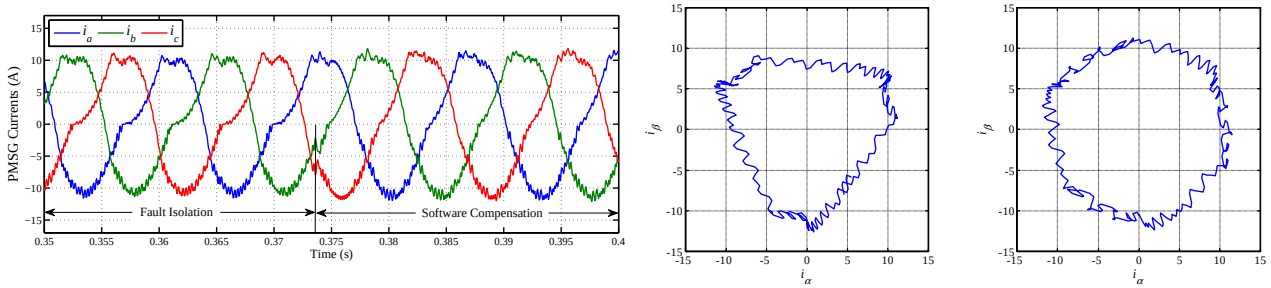

Figure 6.9: Experimental results regarding the phase currents in the time-domain and in the stationary reference frame, during : (a) fault isolalion and software compensation; (b) fault isolalion ($i_{sd} = 0$); (c) software compensation by controlling i_{sd} (5.12).

The topology III aims to minimize hardware requirements and, consequently, the cost increase. Therefore, voltage and current ratings of the dc-link capacitor are intended to remain unchanged, which consists in the main drawback of converter topologies with reduced number of power switches in the previous sections. This topology requires only three relays and one TRIAC, for fault isolation and converter topology reconfiguration in the grid-side converter, respectively. The FLC allows the drive to operate in a limited operating range without oversizing the ratings of any component, thus, overcoming the issue of a bulky capacitor bank with high ratings. Moreover, neither extra hardware nor system oversizing are required for post-fault operation of the PMSG-side converter as a TSTPR.

6.3.1 Design Considerations

The analysis of the five-leg converter in section 5.4 allows to conclude that operation at full power under post-fault operation requires oversizing of voltage and current ratings of the power switches, dc-link capacitors, output filter and transformer, which does not lead to a cost-effective solution. However, by considering the system derating, a quite cost-effective solution may be achieved, turning out to be more advantageous than the ones that have been already proposed in

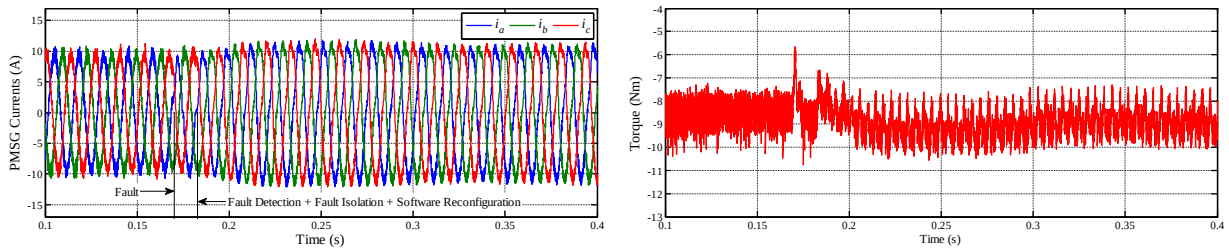

Figure 6.10: Experimental results regarding the fault-tolerant drive II response to an open-circuit in the PMSG-side converter.

the literature because the operation is possible with no increase of the dc-link voltage. The increase of V_{dc} is usually forced by the lower voltage capability of the alternative converter topologies for post-fault operation, and by the constant grid voltage. It is worth noting that in inverter-fed motor drives with fault-tolerant capabilities the maximum motor speed can be reduced in order to avoid increasing the voltage ratings and allowing its operation in a narrower range.

First of all, to avoid the oversizing of the current ratings in the grid-side due to the increase of the phase currents amplitude by a factor of $\sqrt{3}$, the maximum output power has to be limited to 58% of the rated power. This condition is automatically fulfilled when the dc-link voltage is intended to remain unchanged, which is possible by limiting the maximum speed to 42 % of the rated speed $\left(1 - 1/\sqrt{3} \approx 0.42\right)$, since $V_{s,ph}$ is proportional to the generator speed, then, complying with the condition in (5.44).

The rated current of the shared-leg ($I_{shared,p.u.}$) can be defined as a function of the maximum speed under post-fault operation ($\omega_{max,p.u}$) and the maximum torque at the maximum speed ($T_{max,p.u}$):

$$I_{shared,p.u.} = T_{max,p.u}\left(3\omega_{max,p.u} + 1\right) \tag{6.6}$$

Therefore, there is lack of need for increasing the current rating of the shared leg if the maximum torque is limited as a function of the speed, as given by:

$$T_{max,p.u} = \frac{1}{3\omega_{max,p.u} + 1} \tag{6.7}$$

which results in the operating area B depicted in Figure 6.12. On the other hand, if the generator should be able to develop the rated torque over all the post-fault speed range (operating area C in Figure 6.12), the rated current of the shared-leg has to be increased approximately 127 % $\left(4 - \sqrt{3} \approx 2.27\right)$. It should be noted that the previous considerations take into account an ideal system with an efficiency of 100%, thus, in a practical implementation the operating range may be slightly extended by simply taking into consideration the maximum generator and converter effi-

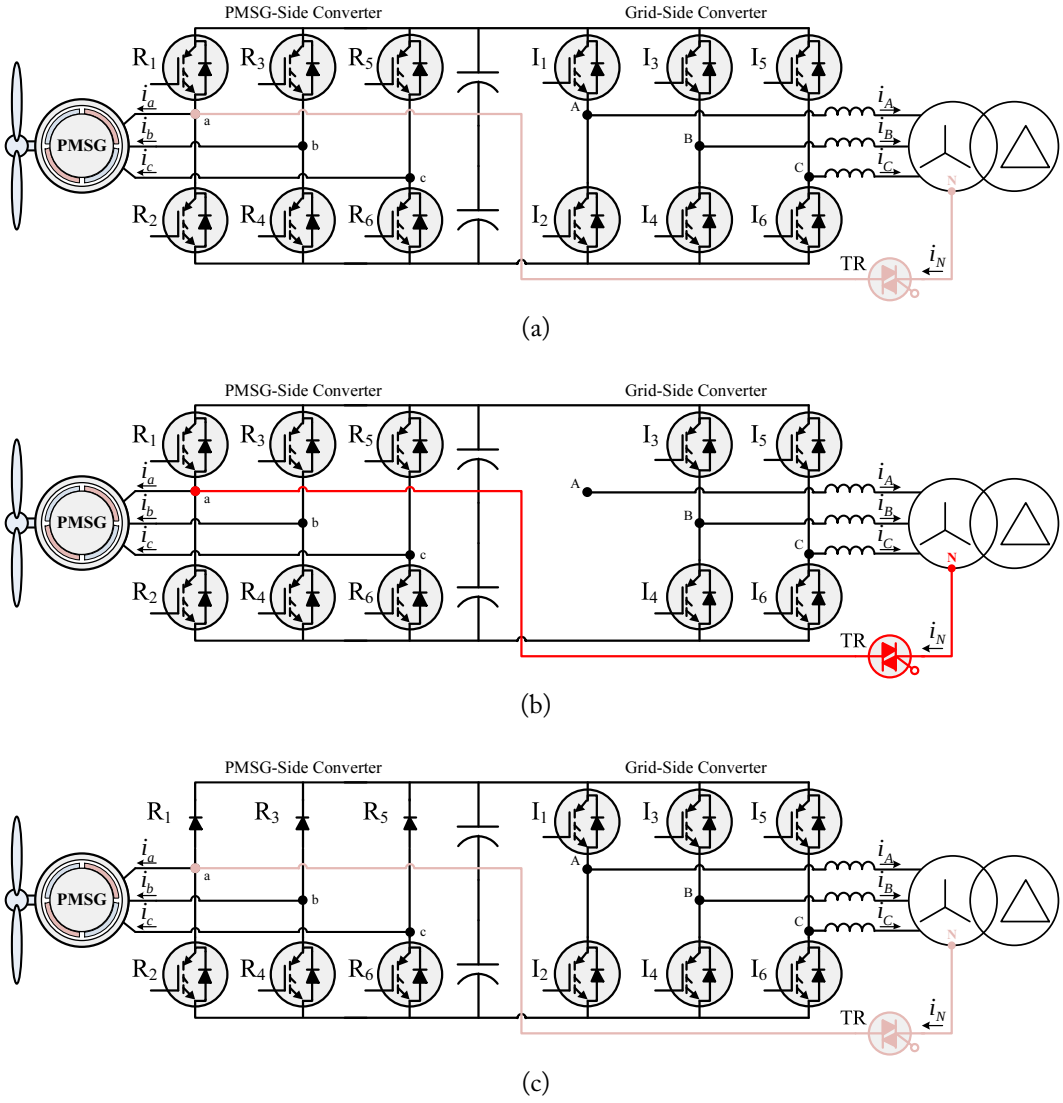

Figure 6.11: Fault-tolerant converter topologies: (a) under normal operating conditions (two SSTC); (b) after a fault occurrence in I_1 or I_2 (FLC); (c) after a fault occurrence in R_1, R_3 or R_5 (TSTPR and SSTC).

ciencies (η_{PMSG}, η_{conv}) in the considered operating range. This leads to a revised expression for the rated current of the shared-leg:

$$I_{shared,p.u.} = T_{max,p.u}\eta_{PMSG}\left(\eta_{conv}3\omega_{max,p.u} + 1\right) \tag{6.8}$$

6.3.2 Control System

To monitor both PMSG- and grid-side converters, the voltage-based approach proposed in section 4.1.5.1 (AVNRV method) is integrated into the drive control system, allowing a reliable diagnostic with low computational demand and no extra hardware. Moreover, two control strategies are required for post-fault operation, DTC with SVM for the TSTPR (section 5.1.4) and HCC

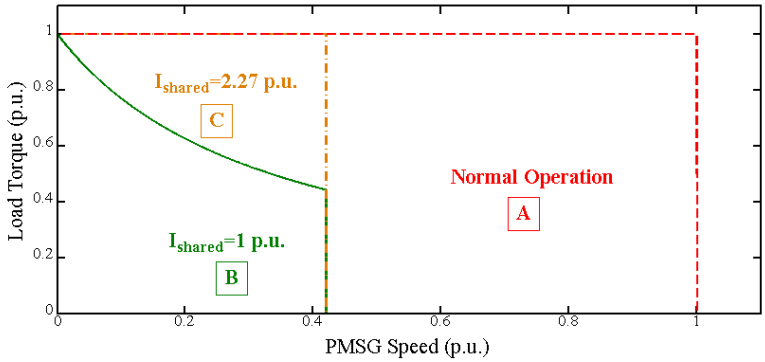

Figure 6.12: Operating limits of the fault-tolerant PMSG drive III defined by three operation areas: A) normal operation; B) post-fault operation with no oversizing of the shared-leg; C) post-fault operation with oversizing of the shared-leg to allow operation at the rated torque over the all speed range of area B.

for the FLC (section 5.4.1) are the selected ones.

Regarding post-fault operation of the PMSG-side converter, the same procedures considered in sections 6.1 and 6.2 are necessary for operation as a TSTPR (fault diagnosis, fault isolation, and control reconfiguration). For the FLC, after diagnosing the faulty phase, this is isolated by inhibiting its gate control signals and also by opening the respective relay, hence, completely isolating the faulty converter phase from the grid. Then, the TRIAC is turned on and a new control strategy and a proper reference speed need to be selected, according to section 5.4 and Figure 6.12.

6.3.3 Real-Time Response

The experimental setup of the fault-tolerant PMSG drive III is depicted in Figure 6.13, comprising additionally a three-phase core-type transformer, a relay, and a TRIAC. The experiments were carried out at a grid phase-to-phase rms voltage of 110 V (transformer-side with wye connection) and a reference dc link voltage of 200 V, allowing the generator to reach a maximum speed of 1500 rpm under normal operating conditions.

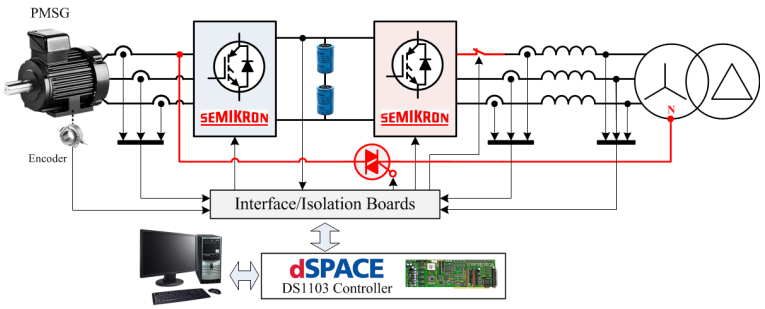

Figure 6.13: Diagram of the experimental setup: fault-tolerant PMSG drive III.

6.3.3.1 Real-Time Response to a Fault in the Grid-Side Converter

In order to ensure the drive operation after a fault occurrence in grid-side converter, fault diagnosis must be correctly performed, then, triggering fault isolation (inhibition of the gate pulses and isolation of the faulty phase), hardware reconfiguration (rearrangement of the topology by turning on the TRIAC), and software reconfiguration (switching to post-fault control without exceeding the operating limits). As a consequence of the reduced voltage capability of the five-leg converter and according to the system design (section 6.3.1), to increase the dc-link voltage or to decrease the generator speed are the two available options if the PMSG operates at a speed higher than 42% of the rated speed when the fault occurs. In this paper, the presented results only consider the speed limitation (Figure 6.14a) because it turns out to be the most cost-effective option for a fault-tolerant drive. Therefore, under post-fault operation the maximum admissible reference speed is considered to be equal to 600 rpm (0.4×1500 rpm).

Figure 6.14a shows that the fault detection is accomplished in approximately 6 ms (30% of the fundamental current period), identifying the switch I_1 as the faulty one, and then the remedial procedures are triggered. It can be seen that the TRIAC allows the converter topology to be reconfigured almost instantaneously, but the used relay has a release time of 30 ms, only after which phase A is isolated and its current becomes completely null. Such behavior is acceptable in response to an open-circuit fault, allowing the adoption of low cost relays for isolating the faulty phase. Meanwhile, the reference speed is automatically changed from 1500 rpm to the maximum admissible reference speed of 600 rpm, and the drive is able to keep operating in the limited range defined in Figure 6.12.

6.3.3.2 Real-Time Response to a Fault in the PMSG-Side Converter

In the PMSG-side converter, hardware reconfiguration is not required, thus, the fault detection of switch R_1 (Figure 6.14b) is, immediately, followed by the inhibition of the gate command signals of all the upper switches and by the control strategy reconfiguration. Therefore, operation with high torque ripple as a consequence of an open-circuit fault is automatically avoided by the fault-tolerant control system. Figure 6.14b shows that the generator speed can be controlled under post-fault operation as well as a smooth electromagnetic torque can be developed. Consequently, operation with low vibration and noise levels is possible by controlling a TSTPR with DTC-SVM.

6.4 Summary

In this chapter three fault-tolerant converter topologies have been proposed for PMSG drives for wind turbine applications, which are considered to be interesting options from both performance and economic points of view.

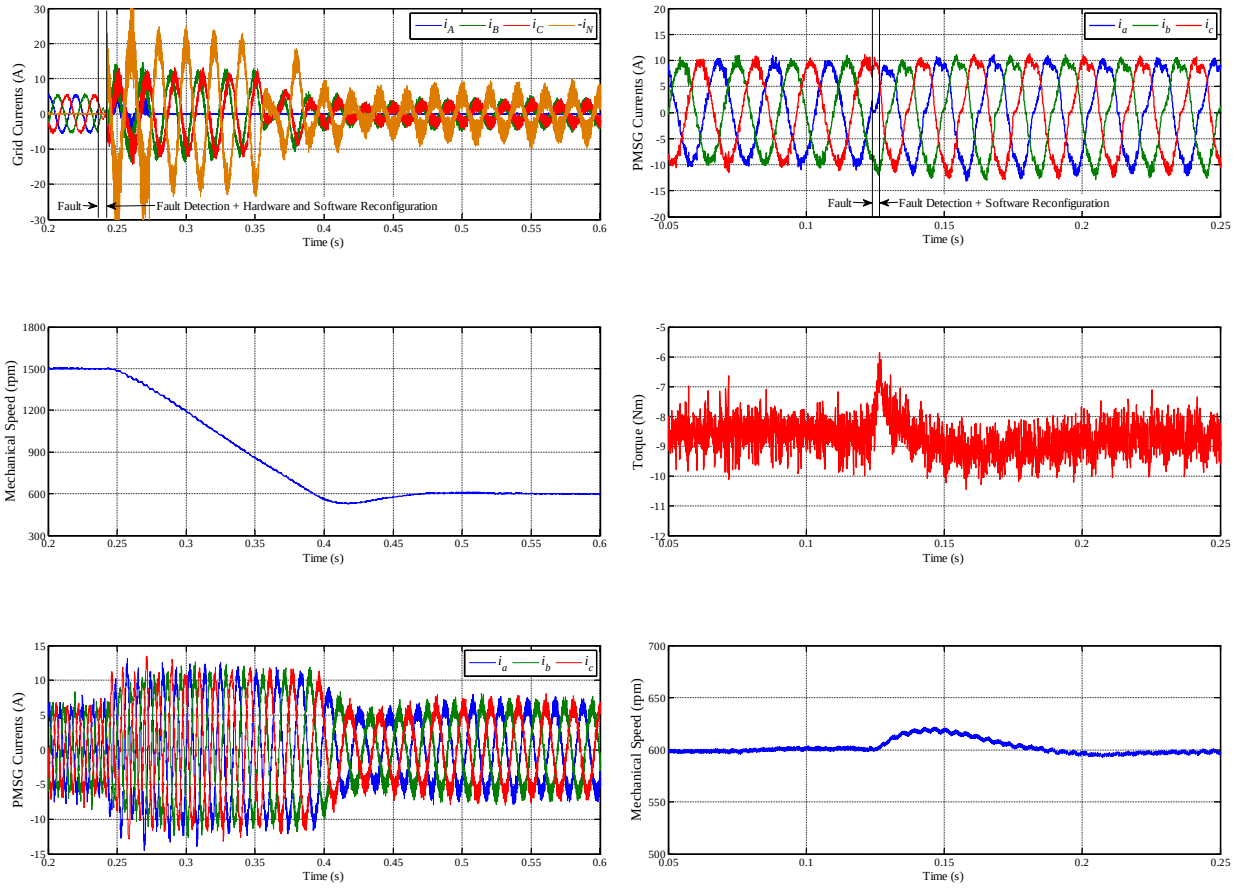

(a) (b)

Figure 6.14: Experimental results regarding the fault-tolerant drive III response to an open-circuit fault: (a) in phase A of the grid-side converter (IGBT I_1), at a reference dc-link voltage of 200 V and 50% of the PMSG rated torque; (b) in IGBT R_1 of the PMSG-side converter, at a reference speed of 600 rpm and 75% of the PMSG rated torque..

The design considerations in this chapter permit to decide which of the proposed topologies better fit into practical applications by clarifying their operating limits and the hardware requirements associated to the drive cost increase. Table 6.1 reveals the hardware requirements of the proposed fault-tolerant converter topologies for PMSG drives together with three other topologies previously proposed in the literature that are suitable for PMSG drives, comparing them with the standard SSTPC. The criterion of choice used in Table 6.1 intends to minimize the hardware requirements increase, hence, the system derating (if possible) is considered preferable for post-fault operation.

In short, the proposed topologies are characterized by a minimum number of extra components, and topologies II and III are able to reduce the cost increase significantly by limiting the drive operating range. Thus, they can be considered more cost-effective than the ones previously proposed [107], [167], [185]. With respect to the main drawbacks of proposed topologies, topology I re-

quires to double the voltage rating of all the drive components and topology II leads to a significant increase of the dc link capacitors current rating.

All the considered fully-integrated fault-tolerant converters have shown a quite good real-time response, allowing the PMSG drive to achieve stable post-fault operation in a short period of time.

Table 6.1: Comparison of fault-tolerant converter topologies.

			Redudant Leg	4 Leg	5 Leg	Topology I	Topology II	Topology III
TRIACs			6	6	3	3	1	1
IGBTs	Extra		2	-	-	-	-	-
	Rating Increase	*V*	-	100%	100%	100%	≥15%	-
		I	-	-	-	-	-	-
Capacitors	Rating Increase	*V*	-	100%	100%	100%	≥15%	-
		I	-	$I_{Grid} + I_{PMSG}$	-	I_{Grid}	$\sqrt{3}\ I_{Grid}$	-
System Derating Factor			-	-	50%	-	58%	19%
Mutiple Faults			-	✓	-	✓	✓	-

Chapter 7

Conclusions and Future Work

7.1 Conclusions

This thesis has presented an investigation on fault-tolerant PMSG drives, concerning open-circuit faults and current sensor faults. To start with, normal and faulty operation of the PMSG drive were studied, and then fault diagnostic methods and control strategies for post-fault operation were developed separately. To finish with, control strategies for normal operation, fault diagnostic algorithms and control strategies for post-fault operation were integrated into the drive controller, leading to three distinct solutions in order to reach fault-tolerance and continuous operation.

Under normal operating conditions four control strategies were considered for each converter side of the PMSG drive. For the PMSG-side converter, RFOC with HCC, RFOC with SVM, conventional DTC and DTC with SVM were considered, while VOC with HCC, VOC with SVM, VOC with vector-based HCC and DPC were considered for the grid-side converter. The obtained results verify that SVM-based strategies tend to present a better performance under steady-state operation, minimizing the ripple of the controlled quantities and enhancing efficiency. However, they are outperformed by variable switching frequency strategies in simplicity of implementation and tuning, robustness to the variation of the system parameters, and dynamic response.

The faulty operation analysis has shown that typical converter protections are not triggered by open-circuit faults and current sensor faults, which might endanger the whole system and cause secondary faults. An open-circuit fault has different impacts on the drive behavior, depending on the affected converter side as well as on the employed control strategy, with a fault in grid-side converter (inverter stage) being the most severe one. Although current-based techniques appear as straightforward approaches, an open-circuit fault in the PMSG-side converter might be difficult to diagnose, due its small impact on the phase currents. Concerning post-fault operation, the lack of path for the current flow as a consequence of an open-circuit fault in the grid-side converter indicates that there is need for hardware reconfiguration. On the other hand, for an open-circuit fault in the PMSG-side converter, control reconfiguration may provide an acceptable performance

under post-fault operation.

In relation to a current sensor fault, it has similar repercussions in both converter sides independently of the control strategy, but HCC does not tolerate this fault condition, leading to the converter shut-down due to over-current. Provided that there is a current sensor per phase, a simple software reconfiguration permits proper operation after the occurrence of a current sensor fault.

The proposed diagnostic methods fulfill the requirements for their integration into a drive controller and real-time implementation, namely, lack of need for extra hardware, simple implementation and low computational requirements. Furthermore, their effectiveness and accuracy is independent of the operating conditions, they are robust to transients, such as load and speed variations, and fault diagnosis is accomplished in relatively short period of time.

With respect to open-circuit faults, the proposed current-based approaches are endowed with a remarkable robustness against false alarms thanks to the inclusion of the dedicated detection algorithm based on the derivative of the absolute current Park's Vector phase (CPVP method). If the information about the faulty phase is sufficient, the method of the errors of the normalized currents average absolute values using the instantaneous maximum value of the currents absolute values as normalization quantity (ENCAAV-CMax) excels at simplicity and low computational effort. On the other hand, if the exact localization of the faulty switch is required through a very simple algorithm, the proposed voltage-based approaches might be optimum choices.

Four converter topologies and respective control strategies have been addressed as alternatives for post-fault operation of the two power converters of a PMSG drive. A three-switch three-phase rectifier (TSTPR) is proposed for post-fault operation of the PMSG-side converter, without requiring extra hardware. Among the four control strategies proposed with the aim to minimize the torque oscillation, DTC-based strategies appear to be excellent choices, since they are able to compensate the torque oscillation in closed-loop.

Three distinct topologies are analyzed for post-fault operation of the grid-side converter. The FSTPC-NCM and the FLC might be the most cost-effective solutions when considering the drive derating for post-fault operation, since there is lack of need for a great increase of the dc link voltage due to their higher voltage capability in comparison to the FSTPC-PCM. Moreover, to perform the hardware reconfiguration the FSTPC-NCM and the FLC require one TRIAC only, instead of the three TRIACs required by the FSTPC-PCM. Both vector control and direct control have shown to be viable options for controlling the FSTPC-PCM and the FSTPC-NCM. For the FLC, vector control with HCC and S-PWM has been proposed, with S-PWM outperforming HCC.

Finally, three fault-tolerant converter topologies have been proposed for PMSG drives for wind turbine applications, defining their operating limits and the hardware requirements associated to the drive cost increase. The proposed topologies are characterized by a minimum number of extra components, and topologies II and III are able to reduce the cost increase significantly by adopting the FSTPC-NCM and the FLC and limiting the drive operating range. Thus, they can be consid-

ered more cost-effective than the ones previously proposed. With respect to the main drawbacks of proposed topologies, topology I requires to double the voltage rating of all the drive components and topology II leads to a significant increase of the dc link capacitors current rating. The three considered fully-integrated fault-tolerant converters have shown a quite good real-time response, allowing the PMSG drive to achieve stable post-fault operation in a short period of time.

7.2 Future Work

In the sequence of the presented work, some suggestions for future research are pointed out. First of all, the application of the proposed fault-tolerant PMSG drives in a wind turbine prototype would allow their full validation. A more exhaustive analysis of the considered converter topologies would be also useful, for instance, by means of thermal and acoustic experiments. A detailed thermal analysis would help to validate the component design, namely, the design of the capacitors for the FCTPC-PCM and FCTPC-NCM. On the other hand, acoustic analysis is a relevant topic for wind turbine applications.

Furthermore, the integration of more advanced and complete condition monitoring techniques by taking into consideration all the drive components that are prone to fail (generator, capacitors, inductances, feedback sensors) is an interesting research field that will be welcomed by the industry.

Focusing wind turbine applications and fault-tolerant converters, more complex converter topologies and control systems will be important research topics, for instance, multilevel converters and predictive control with increased fault-tolerant capabilities and control flexibility.

Bibliography

[1] *The European Wind Initiative - Wind Power Research and Development to 2020*. Available: http://www.ewea.org/fileadmin/files/library/publications/reports/EWI_2013.pdf

[2] Z. Chen, J. M. Guerrero and F. Blaabjerg, "A review of the state of the art of power electronics for wind turbines", *IEEE Transactions on Power Electronics*, vol. 24, no. 8, pp. 1859-1875, Aug. 2009.

[3] *Siemens D6 platform - 6.0 MW direct drive wind turbine - The new standard for offshore*. Available: http://www.energy.siemens.com/hq/pool/hq/power-generation/renewables/wind-power/Siemens_D6_Platform_6.0-MW.pdf. Accessed Sept. 2013.

[4] *GE 4.1 MW - 113 offshore wind turbine brochure*. Available: http://www.ge-energy.com/content/multimedia/_files/downloads/GE%20Offshore%20Wind%204.1-113.pdf. Accessed Sept. 2013.

[5] *Alstom wind power solutions*. Available: http://www.alstom.com/Global/Power/Resources/Documents/Brochures/wind-power-solutions.pdf. Accessed Sept. 2013.

[6] *Gamesa 5.0 MW brochure*. Available: http://www.gamesacorp.com/recursos/doc/productos-servicios/aerogeneradores/catalogo-offshore-eng.pdf. Accessed Sept. 2013.

[7] *Vestas offshore V14-8.0 MW brochure*. Available: http://nozebra.ipapercms.dk/Vestas/Communication/Productbrochure/OffshoreProductBrochure/OffshoreProductBrochure/. Accessed Sept. 2013.

[8] F. Spinato, P. J. Tavner, G. J. W. Bussel and E. Koutoulakos, "Reliability of wind turbine subassemblies", *IET Renewable Power Generation*, vol. 3, no. 4, pp. 387-401, Dec. 2009.

[9] J. Ribrant and L. M. Bertling, "Survey of failures in wind power systems with focus on swedish wind power plants during 1997–2005", *IEEE Transactions on Energy Conversion*, vol. 22, no. 1, pp. 167-173, Mar. 2007.

[10] B. K. Bose, "Power electronics and motor drives recent progress and perspective", *IEEE Transactions on Industrial Electronics*, vol. 56, no. 2, pp.581-588, February 2009.

[11] J. Holtz, "Power Electronics-A Continuing Challenge", *IEEE Industrial Electronics Magazine*, vol. 5, no. 2, pp. 6-15, June 2011.

[12] K. Fischer, T. Stalin, H. Ramberg, T. Thiringer, J. Wenske and R. Karlsson, "Investigation of converter failure in wind turbines", *Elforsk report*, Nov. 2012. Available: http://www.elforsk.se/Global/Vindforsk/Rapporter%20VFIII/12_58_report_ConFail.pdf. Accessed Sept. 2013.

[13] S. Yang, D. Xiang, A. Bryant, P. Mawby, L. Ran and P. Tavner, "Condition monitoring for device reliability in power electronic converters: a review", *IEEE Transactions on Power Electronics*, vol. 25, no. 11, pp. 2734-2752, Nov. 2010.

[14] S. Yang, A. Bryant, P. Mawby, D. Xiang, L. Ran and P. Tavner, "An industry-based survey of reliability in power electronic converters", *IEEE Transactions on Industry Applications*, vol. 47, no. 3, pp. 1441-1451, May/Jun. 2011.

[15] H. Li, Z. Chen, "Overview of different wind generator systems and their comparisons", *Renewable Power Generation, IET* , vol. 2, no. 2, pp.123-138, June 2008.

[16] M. Liserre, R. Cardenas, M. Molinas and J. Rodriguez, "Overview of multi-MW wind turbines and wind parks", *IEEE Transactions on Industrial Electronics*, vol. 58, no. 4, pp. 1081-1095, April 2011.

[17] Bimal K. Bose, "The past, present, and future of power electronics", *IEEE Industrial Electronics Magazine*, pp. 7-11, 2009

[18] H. Polinder, Van Der Pijl , F.F.A., G.-J. de Vilder and P. Tavner, "Comparison of direct-drive and geared generator concepts for wind turbines", *IEEE Transactions on Energy Conversion*, vol. 21, no. 3, pp.725-733, Sept. 2006.

[19] F. Blaabjerg, M. Liserre and Ke Ma, "Power electronics converters for wind turbine systems", *IEEE Transactions on Industry Applications*, vol. 48, no. 2, pp. 708-719, March-April 2012.

[20] R. Jones and P. Waite, "Optimised power converter for multi-MW direct drive permanent magnet wind turbines", *14th European Conference on Power Electronics and Applications*, 10 pp., Aug./Sept. 2011.

[21] B. Andresen and J. Birk, "A high power density converter system for the Gamesa G10x 4.5 MW wind turbine", *European Conference on Power Electronics and Applications*, 8 pp., Sept. 2007.

[22] J. Rodriguez, S. Bernet, W. Bin, J. O. Pontt, and S. Kouro, "Multilevel voltage-source-converter topologies for industrial medium-voltage drives", *IEEE Transactions on Industrial Electronics,* vol. 54, no .6, pp. 2930-2945, Dec. 2007.

[23] E. P. Wiechmann, P. Aqueveque, R. Burgos and J. Rodriguez, "On the Efficiency of Voltage Source and Current Source Inverters for High-Power Drives", *IEEE Transactions on Industrial Electronics*, vol. 55, no. 4, pp. 1771-1782, April 2008.

[24] F. Blaschke, "A new method for the structural decoupling of A.C. induction machines", IFAC *Conference Record*, Duesseldorf, Germany, 15 pp., October 1971.

[25] F. Blaschke, "The principle of field-orientation as applied to the transvector closed-loop control system for rotating-field machines", *Siemens Rev.*, vol. 34, no. 1, pp. 217–220, 1972.

[26] I. Takahashi and T. Noguchi, "A new quick-response and high-efficiency control strategy of an induction motor", *IEEE Transactions on Industry Applications*, vol. 22, no. 5, pp. 820–827, Sep./Oct. 1986.

[27] M. Depenbrock, "Direct self-control (DSC) of inverter-fed induction machine", *IEEE Transaction on Power Electronics*, vol. PE-3, No. 4, pp. 420-429, October 1988.

[28] G. S. Buja and M. P. Kazmierkowski, "Direct torque control of PWM inverter-fed AC motors - a survey", *IEEE Transactions on Industrial Electronics*, vol. 51, no. 4, pp. 1973-1980, Aug. 2004.

[29] Y. Zhang, J. Zhu, W. Xu, and Y. Guo, "A simple method to reduce torque ripple in direct torque-controlled permanent-magnet synchronous motor by using vectors with variable amplitude and angle", *IEEE Transactions on Industrial Electronics*, vol. 58, no. 7, pp. 2848-2859, July 2011.

[30] D. Casadei, F. Profumo, G. Serra and A. Tani, "FOC and DTC: two viable schemes for induction motors torque control", *IEEE Transactions on Power Electronics* , vol.17, no. 5, pp. 779-787, Sep 2002.

[31] J. R. Rodriguez, L. W. Dixon, J. R. Espinoza, J. Pontt and P. Lezana, "PWM regenerative rectifiers: state of the art", *IEEE Transactions on Industrial Electronics*, vol.52, no. 1, pp. 5-22, Feb. 2005.

[32] T. Noguchi, H. Tomiki, S. Kondo and I. Takahashi, "Direct power control of PWM converter without power-source voltage sensors", *IEEE Transactions on Industry Applications*, vol. 34, no. 3, pp. 473-479, May/June 1998.

[33] J. Alonso-Martinez, J. Eloy-Garcia, D. Santos-Martin and S. Arnalte, "A new variable frequency optimal direct power control algorithm", *IEEE Transactions on Industrial Electronics*, vol. 60, no. 4, pp. 1442-1451, April 2013.

[34] M. Malinowski, M. P. Kazmierkowski and A. M. Trzynadlowski, "A comparative study of control techniques for PWM rectifiers in AC adjustable speed drives", *IEEE Transactions on Power Electronics*, Vol. 18, no. 6, November, 2003.

[35] N. Freire, J. O. Estima and A. J. M. Cardoso, "A comparative analysis of PMSG drives based on vector control and direct control techniques for wind turbine applications", *Electrical Review*, Vol. 88, No. 1a, pp. 184 - 187, January 2012.

[36] M. P. Kazmierkowski, L. G. Franquelo, J. Rodriguez, M. A. Perez and J. I. Leon, "High-performance motor drives," *IEEE Industrial Electronics Magazine*, vol. 5, no. 3, pp. 6-26, Sept. 2011.

[37] P. Cortés, M. P. Kazmierkowski, Ralph M. Kennel, Daniel E. Quevedo and José Rodríguez, "Predictive control in power electronics and drives," *IEEE Transactions on Industrial Electronics*, vol. 55, no. 12, pp. 4312-4324, December 2008.

[38] T. Geyer, "A comparison of control and modulation schemes for medium-voltage drives: emerging predictive control concepts versus PWM-based schemes," *IEEE Transactions on Industry Applications*, vol. 47, no. 3, pp. 1380-1389, May/June 2011.

[39] J. Holtz, "Pulsewidth modulation-a survey", *IEEE Transactions on Industrial Electronics*, vol. 39, no. 5, pp. 410-420, October 1992.

[40] E. R. C. da Silva, E. C. dos Santos and C. B. Jacobina, "Pulsewidth modulation strategies", *IEEE Industrial Electronics Magazine*, vol. 5, no. 2, pp. 37-45, June 2011.

[41] M. Depenbrock, "Pulse width control of a 3-phase inverter with non-sinusoidal phase voltages", *IEEE Int. Semiconductor Power Converter Conf.*, pp. 399–403, 1977.

[42] A. Busse and J. Holtz, "A digital space vector modulator for the control of a three-phase power converter", *VDE-Conf. Microelektronic in Inverters and Electrical Drives*, Darmstadt, pp. 189–195, 1982.

[43] M. Kazmierkowski and L. Malesani, "Current control techniques for three-phase voltage-source PWM converters: a survey", *IEEE Transactions on Industrial Electronics*, vol. 45, no. 5, pp. 691-703, October 1998.

[44] A. M. Hava, R. Kerkman, and T. A. Lipo, "A high-performance generalized discontinuous PWM algorithm", *IEEE Transactions on Industry Applications,* vol. 34, pp. 1059–1071, Sept./Oct. 1998.

[45] A. M. Hava, R. J. Kerkman and T. A. Lipo, "Simple analytical and graphical methods for carrier-based PWM-VSI drives", *IEEE Transactions on Power Electronics*, vol. 14, no. 1, pp. 49-61, January 1999.

[46] C. B. Jacobina, A. M. N. Lima, E. R. C. da Silva, R. N. C. Alves, and P. F. Seixas, "Digital scalar pulse-width modulation: a simple approach to introduce non-sinusoidal modulating waveforms", *IEEE Transactions on Power Electronics*, vol. 16, pp. 351–359, May 2001.

[47] K. Zhou and D. Wang, "Relationship between space-vector modulation and three-phase carrier-based PWM: a comprehensive analysis", *IEEE Transactions on Industrial Electronics*, vol. 49, no. 1, pp. 186-196, February 2002.

[48] N. Urasaki, T. Senjyu and K. Uezato, "Relationship of parallel model and series model for permanent magnet synchronous motors taking iron loss into account", *IEEE Transactions on Energy Conversion*, vol. 19, no. 2, pp. 265-270, June 2004.

[49] J. O. Estima "Development and analysis of permanent magnet synchronous motor drives with fully integrated inverter fault-tolerant capabilities", PhD Thesis, *University of Coimbra, Faculty of Sciences and Technology,* 2012.

[50] M. Kazmierkovski, R. Krishnan and F. Blaabjerg, *Control in Power Electronics: Selected Problems*, Academic Press 2002, ISBN 0-12-402772-5.

[51] G. Abad, J. López, M. Rodríguez, L. Marroyo and G. Iwanski, *Doubly Fed Induction Machine: Modeling and Control for Wind Energy Generation*, Wiley-IEEE Press, December 2011, ISBN: 978-0-470-76865-5.

[52] P. Vas, *Sensorless Vector and Direct Torque Control*, Oxford University Press, 1998, ISBN 0-19-856465-1.

[53] M. H. Rashid, *Power Electronics Handbook,* Academic Press 2001, ISBN 0-12-581650-2.

[54] S. Buso, L. Malesani and P. Mattavelli, "Comparison of current control techniques for active filter applications" , *IEEE Transactions on Industrial Electronics* , vol. 45, no. 5, pp. 722-729, Oct. 1998.

[55] K. M. Rahman, M.R. Khan, M. A. Choudhury and M. A. Rahman, "Variable-band hysteresis current controllers for PWM voltage-source inverters", *IEEE Transactions on Power Electronics*, vol. 12, no. 6, pp. 964-970, Nov 1997.

[56] D. G. Holmes, R. Davoodnezhad and B. P. McGrath, "An Improved Three-Phase Variable-Band Hysteresis Current Regulator", *IEEE Transactions on Power Electronics*, vol. 28, no. 1, pp. 441-450, Jan. 2013.

[57] J. Holtz, J. Quan, J. Pontt, J. Rodriguez, P. Newman and H. Miranda, "Design of fast and robust current regulators for high-power drives based on complex state variables", *IEEE Transactions on Industry Applications*, vol. 40, no. 5, pp. 1388-1397, Sept./Oct. 2004.

[58] R. C. Panda, *Introduction to PID Controllers – Theory, Tuning and Aplication to Frontier Areas*, InTech 2012, ISBN 978-953-307-927-1.

[59] K. J. Aström and T. Hägglund, *PID Controllers: Theory, Design, and Tuning*, ISA 1995, ISBN 10-1556175167.

[60] H. W. Van der Broeck, H. C. Skudelny and G. V. Stanke, "Analysis and realization of a pulsewidth modulator based on voltage space vectors", *IEEE Transactions on Industry Applications* , vol. 24, no. 1, pp. 142-150, Jan./Feb. 1988.

[61] B. K. Bose, *Modern power electronics and AC drives*, Prentice-Hall 2001, ISBN 978-0130167439.

[62] L. Tang, L. Zhong, M. F. Rahman and Y. Hu, "A novel direct torque controlled interior permanent magnet synchronous machine drive with low ripple in flux and torque and fixed switching frequency", *IEEE Transactions on Power Electronics*, vol. 19, no. 2, pp. 346-354, March 2004.

[63] D. Świerczyński, "Direct torque control with space vector modulation (DTC-SVM) of inverter-fed permanent magnet synchronous motor drive", PhD Thesis, *Warsaw University of Technology*, 2005.

[64] Y. Zhang, J. Zhu, W. Xu, and Y. Guo, "A simple method to reduce torque ripple in direct torque-controlled permanent-magnet synchronous motor by using vectors with variable amplitude and angle", *IEEE Transactions on Industrial Electronics*, vol. 58, no. 7, pp. 2848-2859, July 2011

[65] Y. Xue, X. Xu, T. G. Habetler and D. M. Divan, "A low cost stator flux oriented voltage source variable speed drive", *IEEE Industry Applications Society Annual Meeting*, vol. 1, pp. 410-415, Oct. 1990.

[66] L. Shin Yen and H. C. Jian "A new approach to direct torque control of induction motor drives for constant inverter switching frequency and torque ripple reduction", *IEEE Transactions Energy Conversion*, vol. 16, no. 3, pp. 220-227, Sep. 2001.

[67] A. Timbus, M. Liserre, R. Teodorescu, P. Rodriguez and F. Blaabjerg, "Evaluation of current controllers for distributed power generation systems", *IEEE Transactions on Power Electronics*, vol. 24, no. 3, pp. 654-664, March 2009.

[68] A. G. Yepes, "Digital resonant current controllers for voltage source converters", PhD Thesis, *Vigo University of Technology,* 2011.

[69] M. P. Kazmierkowski and W. Sulkowski, "A novel vector control scheme for transistor PWM inverter-fed induction motor drive", *IEEE Transactions on Industrial Electronics*, vol. 38, no. 1, pp. 41-47, Feb 1991.

[70] M. P. Kazmierkowski, M. A. Dzieniakowski and W. Sulkowski, "Novel space vector based current controllers for PWM-inverters", *IEEE Transactions on Power Electronics*, vol. 6, no. 1, pp. 158-166, Jan. 1991.

[71] M. Mohseni, S. M. Islam and M. A. S. Masoum, "Enhanced hysteresis-based current regulators in vector control of DFIG wind turbines", *IEEE Transactions on Power Electronics*, vol. 26, no. 1, pp. 223-234, Jan. 2011.

[72] A. Bouafia, J. P. Gaubert and F. Krim, "Analysis and design of new switching table for direct power control of three-phase PWM rectifier", *Power Electronics and Motion Control Conference*, pp. 703-709, September 2008.

[73] J. Hu and Z. Q. Zhu, "Investigation on switching patterns of direct power control strategies for grid-connected DC–AC converters based on power variation rates", *IEEE Transactions on Power Electronics*, vol. 14, no. 4, pp. 3582-3598, Dec. 2011.

[74] J. A. Martínez, J. E. G. Carrasco and S. Arnaltes, "Table-based direct power control: a critical review for microgrid applications", *IEEE Transactions on Power Electronics*, vol. 25, no. 12, pp. 2949-2961, December 2010.

[75] A. Sato and T. Noguchi, "Voltage-source PWM rectifier–inverter based on direct power control and its operation characteristics", *IEEE Transactions on Power Electronics*, vol. 26, no. 5, pp. 1559-1567, May. 2011.

[76] M. Malinowski, M. P. Kazmierkowski, S. Hansen, F. Blaabjerg and G. D. Marques, "Virtual-flux-based direct power control of three-phase PWM rectifiers", *IEEE Transactions on Industry Appl*ications, vol. 37, no. 4, pp. 1019-1027, July/Aug. 2001.

[77] Zhi Dawei, Xu Lie and B.W. Williams, "Improved Direct Power Control of Grid-Connected DC/AC Converters", *IEEE Transactions on Power Electronics*, vol. 24, no. 5, pp. 1280-1292, May 2009.

[78] A. Bouafia, J. P Gaubert and F. Krim, "Predictive direct power control of three-phase pulsewidth modulation (PWM) rectifier using space-vector modulation (SVM)", *IEEE Transactions on Power Electronics* , vol. 25, no. 1, pp. 228-236, Jan. 2010.

[79] A. Patrycjusz , "Predictive control of three phase AC/DC converters", PhD Thesis, *Warsaw University of Technology*, 2009.

[80] "IEEE Recommended Practices and Requirements for Harmonic Control in Electrical Power Systems", *IEEE Std 519-1992* , 1993.

[81] D. Kastha and B. K. Bose, "Investigation of fault modes of voltage-fed inverter system for induction motor drive", *IEEE Transactions on Industry Applications*, vol. 30, no. 4, pp. 1028–1038, Jul./Aug. 1994.

[82] N. Bianchi, S. Bolognani and M. Zigliotto, "Analysis of PM synchronous motor drive failures during flux weakening operation", *27th Annual IEEE Power Electronics Specialists Conference*, vol. 2, pp. 1542-1548, June 1996.

[83] B. A. Welchko, T. M. Jahns and S. Hiti, "IPM synchronous machine drive response to a single-phase open circuit fault", *IEEE Transactions on Power Electronics*, vol. 17, no. 5, pp. 764-771, Sept. 2002.

[84] A. Gaeta, G. Scelba and A. Consoli, "Modeling and Control of Three-Phase PMSMs Under Open-Phase Fault", *IEEE Transactions on Industry Applications*, vol. 49, no. 1, pp. 74-83, Jan./Feb. 2013.

[85] T. Sun, S. H. Lee and J. P. Hong, "Faults analysis and simulation for interior permanent magnet synchronous motor using Simulink@MATLAB", *International Conference on Electrical Machines and Systems*, pp. 900-905, 8-11 Oct. 2007.

[86] K. H. Kim, D. U. Choi, B. G. Gu and I. S. Jung, "Fault model and performance evaluation of an inverter-fed permanent magnet synchronous motor under winding shorted turn and inverter switch open", *IET Electric Power Applications*, vol. 4, no. 4, pp. 214-225, April 2010.

[87] J. O. Estima and A. J. M. Cardoso, "Performance evaluation of permanent magnet synchronous motor drives under inverter fault conditions", *XVIII International Conference on Electrical Machines*, Vilamoura, Portugal, CD-ROM, 6 pp., September 2008.

[88] J. O. Estima and A. J. M. Cardoso, "Performance evaluation of DTC-SVM permanent magnet synchronous motor drives under inverter fault conditions", *IEEE Industrial Electronics Conference*, pp. 1228-1233, November 2009.

[89] J. O. Estima and A. J. M. Cardoso, "Impact of inverter faults in the overall performance of permanent magnet synchronous motor drives", *IEEE International Electric Machines and Drives Conference*, pp. 1319-1325, May 2009.

[90] J. O. Estima and A. J. M. Cardoso, "The occurrence of faults in permanent magnet synchronous motor drives and its effects on the power supply quality", *International Conference on Renewable Energies and Power Quality*, 6 pp., March 2008.

[91] S. M. A. Cruz and M. Ferreira, "Comparison between back-to-back and matrix converter drives under faulty conditions", *European Conference on Power Electronics and Applications*, 10 pp., September, 2009.

[92] J. O. Estima, J. L. J. Fernandes and A. J. M. Cardoso, "Faulty operation analysis of permanent magnet synchronous generator drives for wind turbine applications", *IET International Conference on Power Electronics*, *Machines and Drives*, 6 pp., Apr. 2010.

[93] N. Freire, J. O. Estima and A. J. M. Cardoso, "Comparison of distinct modulation techniques applied to PMSG drives for wind turbine applications under faulty operating conditions", *International Conference on Clean Electrical Power*, 6 pp., June 2011.

[94] D. W. Chung and S. K. Sul, "Analysis and compensation of current measurement error in vector-controlled AC motor drives", *IEEE Transactions on Industry Applications*, vol. 34, no. 2, pp. 340-345, March/April 1998.

[95] H. S. Jung, S. H. Hwang, J. M. Kim, C. U. Kim and C. Choi, "Diminution of current measurement error for vector controlled AC motor drives", *IEEE Transactions on Industry Applications*, vol. 42, no. 5, pp. 1249-1256, Sept./Oct. 2006.

[96] N. Freire, "Fault analysis and diagnosis in permanent magnet synchronous generator drives for wind turbine applications" (in Portuguese), MSc Thesis, *University of Coimbra*, July 2010.

[97] T. H. Liu, J. R. Fu and T. A. Lipo, "A strategy for improving reliability of field-oriented controlled induction motor drives", *IEEE Transactions on Industry Applications*, vol. 29, no. 5, pp. 910-918, Sept./Oct. 1993.

[98] P. Tavner; L. Ran; J. Penman and H. Sedding, *Condition monitoring of rotating electrical machines* , IET 2008, ISBN 9780863417412.

[99] B. Lu, Y. Li, X. Wu and Z. Yang, "A review of recent advances in wind turbine condition monitoring and fault diagnosis", *IEEE Power Electronics and Machines in Wind Applications*, pp. 1-7, Jun. 2009.

[100] Z. Daneshi-Far, G. A. Capolino and H. Henao, "Review of failures and condition monitoring in wind turbine generators", *International Conference on Electrical Machines*, pp.6, Sept. 2010.

[101] Z. Zijun, A.Verma and A. Kusiak, "Fault analysis and condition monitoring of the wind turbine gearbox", *IEEE Transactions on Energy Conversion*, vol. 27, no .2, pp. 526-535, June 2012.

[102] Y. Wenxian, P. J. Tavner, C. J. Crabtree and M. Wilkinson, "Cost-effective condition monitoring for wind turbines", *IEEE Transactions on Industrial Electronics*, vol. 57, no. 1, pp. 263-271, Jan. 2010.

[103] S. J. Watson, B. J. Xiang, Yang Wenxian, P. J. Tavner and C. J. Crabtree, "Condition monitoring of the power output of wind turbine generators using wavelets", *IEEE Transactions on Energy Conversion*, vol. 25, no. 3, pp. 715-721, Sep. 2010.

[104] W. Yang, P. J. Tavner and M. R. Wilkinson, "Condition monitoring and fault diagnosis of a wind turbine synchronous generator drive train", *IET Renewable Power Generation*, vol. 3, no. 1, pp. 1-11, Mar. 2009.

[105] H. Noura, D. Theilliol, J. C. Ponsart and A. Chamseddine, *Fault-tolerant Control Systems, Design and Practical Applications*, Springer 2009, ISBN 978-1-84882-652-6.

[106] A. Gaillard, S. Karimi, P. Poure, S. Saadate and E. Gholipour, "A fault tolerant converter topology for wind energy conversion system with doubly fed induction generator", *European Conference on Power Electronics and Applications*, pp. 1-6, Sep. 2007.

[107] S. Karimi, A. Gaillard, P. Poure and S. Saadate, "FPGA-based real-time power converter failure diagnosis for wind energy conversion systems", *IEEE Transactions on Industrial Electronics*, vol. 55, no. 12, pp. 4299-4308, Dec. 2008.

[108] A. Gaillard, P. Poure and S. Saadate, "Reconfigurable control and converter topology for wind energy conversion systems with switch failure fault tolerance capability", *IEEE Energy Conversion Congress and Exposition*, pp. 390-397, Sept. 2009.

[109] W. Sae-Kok and D. M. Grant, "Open switch fault diagnosis for a doubly-fed induction generator", 7*th International Conference on Power Electronics and Drive Systems*, pp. 131-138, Nov. 2007.

[110] P. Duan, K. Xie, L. Zhang and X. Rong, "Open switch fault diagnosis and system reconfiguration of doubly-fed wind power converter used in a microgrid", *IEEE Transactions on Power Electronics*, vol. 26, no. 3, pp. 816-821, Mar. 2011.

[111] W. S. Kok, D. M. Grant and B. W. Williams, "System reconfiguration under open-switch faults in a doubly fed induction machine", *IET Renewable Power Generation*, vol. 4, no. 5, pp. 458-470, Sep. 2010.

[112] K. Rothenhagen and F. W. Fuchs, "Doubly fed induction generator model-based sensor fault detection and control loop reconfiguration", *IEEE Transactions on Industrial Electronics*, vol. 56, no. 10, pp. 4229-4238, Oct. 2009.

[113] K. Rothenhagen and F. W. Fuchs, "Current sensor fault detection, isolation, and reconfiguration for doubly fed induction generators", *IEEE Transactions on Industrial Electronics*, vol. 56, no. 10, pp. 4239-4245, Oct. 2009.

[114] S. Karimi, A. Gaillard, P. Poure and S. Saadate, "Current sensor fault-tolerant control for WECS with DFIG", *IEEE Transactions on Industrial Electronics*, vol. 56, no. 11, pp. 4660-4670, Nov. 2009.

[115] M. A. R. Blanco, A. C. Sánchez, D. Theilliol, L. G. V. Valdés, P. S. Terán, L. H. González and J. A. Alquicira, "A failure-detection strategy for IGBT based on gate-voltage behavior applied to a motor drive system", *IEEE Transactions on Industrial Electronics*, vol. 58, no. 5, pp. 1625-1633, May 2011.

[116] D. U. Campos-Delgado and D. R. Espinoza-Trejo, "An observer-based diagnosis scheme for single and simultaneous open-switch faults in induction motor drives", *IEEE Transactions on Industrial Electronics*, vol. 58, no. 2, pp. 671-679, Feb. 2011.

[117] C. Kral and K. Kafka, "Power electronics monitoring for a controlled voltage source inverter drive with induction machines", *IEEE 31st Annual Power Electronics Specialists Conference*, vol. 1, pp. 213-217, 2000.

[118] A. M. S Mendes, A. J. M. Cardoso and E. S. Saraiva, "Voltage source inverter fault diagnosis in variable speed AC drives, by Park's vector approach", *Seventh International Conference on Power Electronics and Variable Speed Drives*, No. 456, pp. 538-543, 1998.

[119] A. M. S. Mendes and A. J. M. Cardoso, "Voltage source inverter fault diagnosis in variable speed ac drives, by the average current Park's vector approach", *IEEE International Electric Machines and Drives Conference*, pp. 704-706, May 1999.

[120] D. Diallo, M. E. H. Benbouzid, D. Hamad and X. Pierre, "Fault detection and diagnosis in an induction machine drive: a pattern recognition approach based on concordia stator mean current vector", *IEEE Transactions on Energy Conversion*, vol. 20, no. 3, pp. 512-519, Sept. 2005.

[121] F. Zidani, D. Diallo and M. Benbouzid and R. Nait-Said, "A fuzzy-based approach for the diagnosis of fault modes in a voltage-fed PWM inverter induction motor drive", *IEEE Transactions on Industrial Electronics*, vol. 55, no. 2, pp. 586-593, Feb., 2008.

[122] J. A. A. Caseiro, A. M. S. Mendes and A. J. M. Cardoso, "Fault diagnosis on a PWM rectifier AC drive system with fault tolerance using the average current Park's Vector Approach", *IEEE Electric Machines and Drives Conference*, pp. 695-701, 2009.

[123] R. Peuget, S. Courtine and J. P. Rognon, "Fault detection and isolation on a PWM inverter by knowledge-based model," *IEEE Transactions on Industry Applications*, vol. 34, no. 6, pp. 1318–1326, Nov./Dec. 1998.

[124] M. Trabelsi, M. Boussak and M. Gossa, "Multiple IGBTs open circuit faults diagnosis in voltage source inverter fed induction motor using modified slope method", *XIX International Conference on Electrical Machines*, 6 pp., Sept. 2010.

[125] S. Abramik, W. Sleszynski, J. Nieznanski and H. Piquet, "A diagnostic method for on-line fault detection and localization in VSI-fed AC drives", *European Conference on Power Electronics and Applications*, 8 pp., Sept. 2003.

[126] K. Rothenhagen and F. W. Fuchs, "Performance of diagnosis methods for IGBT open circuit faults in three phase voltage source inverters for AC variable speed drives," *Annual Power Electronics Specialists Conference*, 10 pp., 2005.

[127] W. Sleszynski, J. Nieznanski and A. Cichowski, "Open-transistor fault diagnostics in voltage-source inverters by analyzing the load currents", *IEEE Transactions on Industrial Electronics*, vol. 56, pp. 4681-4688, Nov. 2009.

[128] J. O. Estima and A. J. M. Cardoso, "A novel diagnostic method for single power switch open-circuit faults in voltage-fed PWM motor drives", *International Symposium on Power Electronics, Electrical Drives, Automation and Motion*, 6 pp., June, 2010.

[129] J. O. Estima and A. J. M. Cardoso, "A new approach for real-time multiple open-circuit fault diagnosis in voltage source inverters", *IEEE Energy Conversion Congress and Exposition*, pp. 4328-4335, September 2010.

[130] J. O. Estima and A. J. M. Cardoso, "A new approach for real-time multiple open-circuit fault diagnosis in voltage source inverters", *IEEE Transactions on Industry Applications*, vol. 47, no. 6, 8 pp., Nov./Dec. 2011.

[131] J. O. Estima and A. J. M. Cardoso, "Single power switch open-circuit fault diagnosis in voltage-fed PWM motor drives by the reference current errors", *8th IEEE International*

Symposium on Diagnostics for Electrical Machines, Power Electronics and Drives, pp. 364-371, 5-8 Sept. 2011.

[132] J. O. Estima and A. J. M. Cardoso, "A new algorithm for real-time multiple open-circuit fault diagnosis in voltage-fed PWM motor drives by the reference current errors", *IEEE Transactions on Industrial Electronics,* vol. 60, no. 8, pp. 3496-3505, Aug. 2013.

[133] N. M. A. Freire, J. O. Estima and A. J. M. Cardoso, "Converters fault diagnosis in PMSG drives for wind turbine applications", *36th Annual Conference of the IEEE Industrial Electronics Society*, pp. 403-408, Nov. 2010.

[134] N. M. A. Freire, J. O. Estima and A. J. M. Cardoso, "Open-circuit fault diagnosis in PMSG drives for wind turbine applications", *IEEE Transactions on Industrial Electronics*, vol. 60, no. 9, pp. 3957-3967, Sept. 2013.

[135] N. M. A. Freire, J. O. Estima and A. J. M. Cardoso, "Multiple open-circuit fault diagnosis in voltage-fed PWM motor drives using the current Park's Vector phase and the currents polarity", *8th IEEE International Symposium on Diagnostics for Electrical Machines, Power Electronics and Drives,* 8 pp., Sep. 2011.

[136] B.-G. Park, K.-J. Lee, R.-Y. Kim, T.-S. Kim, J.-S. Ryu and D.-S. Hyun, "Simple fault diagnosis based on operating characteristic of brushless direct-current motor drives," *IEEE Transactions on Industrial Electronics*, vol. 58, no. 5, pp. 1586–1593, May 2011.

[137] R. Ribeiro, C. Jacobina, E. da Silva and A. Lima, "Fault detection of open-switch damage in voltage-fed PWM motor drive systems," *IEEE Transaction on Power Electronics*, vol. 18, no. 2, pp. 587–593, March 2003.

[138] Q.-T. An, L.-Z. Sun and T. M. Jahns, "Low-cost diagnostic method for open-switch faults in inverters", *Electronics Letters*, vol. 46, no. 14, pp. 1021-1022, July 2010.

[139] Q.-T. An, L.-Z. Sun, K. Zhao and L. Sun, "Switching function model-based fast-diagnostic method of open-switch faults in inverters without sensors", *IEEE Transactions on Power Electronics*, vol. 26, no. 1, pp. 119-126, Jan. 2011.

[140] C. Choi and W. Lee, "Design and evaluation of voltage measurement-based sectoral diagnosis method for inverter open switch faults of permanent magnet synchronous motor drives", *IET Electric Power Applications*, vol. 6, no. 8, pp. 526-532, Sept. 2012.

[141] S.-M. Jung, J.-S. Park; H.-W. Kim; K.-Y. Cho and M.-J. Youn, "An MRAS-based diagnosis of open-circuit fault in PWM voltage-source inverters for PM synchronous motor drive systems", *IEEE Transactions on Power Electronics*, vol. 28, no. 5, pp. 2514-2526, May 2013.

[142] N. M. A. Freire, J. O. Estima and A. J. M. Cardoso, "A voltage-based approach for open-circuit fault diagnosis in voltage-fed SVM motor drives without extra hardware", *XX International Conference on Electrical Machines*, pp. 2378-2383, Sept. 2012.

[143] N. Freire, J. O. Estima and A. J. M. Cardoso, "A voltage-based approach without extra hardware for open-circuit fault diagnosis in closed-loop PWM AC regenerative drives", *IEEE Transactions on Industrial Electronics*, Early Access 2013.

[144] B. Lu and S. K. Sharma, "A literature review of IGBT fault diagnostic and protection methods for power inverters", *IEEE Transactions on Industry Applications*, vol. 45, no. 5, pp. 1770-1777, Sep./Oct. 2009.

[145] J. O. Estima, N. M. A. Freire and A. J. M. Cardoso, "Recent advances in fault diagnosis by Park's Vector Approach", *IEEE Workshop on Electrical Machines Design*, *Control and Diagnosis*, 10 pp., March 2013.

[146] N. Freire, J. O. Estima and A. J. M. Cardoso, "A New Approach for Current Sensor Fault Diagnosis in PMSG Drives for Wind Energy Conversion Systems", *IEEE Transactions on Industry Applications*, Early Access 2013.

[147] P. L. Jansen and R. D. Lorenz, "A physically insightful approach to the design and accuracy assessment of flux observers for field oriented induction machine drives ", *IEEE Transactions on Industry Applications*, vol. 30, no. 1, pp. 101-110, Jan./Feb. 1994.

[148] H. S. Kim; H. T. Moon and M. J. Youn, "On-line dead-time compensation method using disturbance observer", *IEEE Transactions on Power Electronics*, vol. 18, no. 6, pp. 1336- 1345, Nov. 2003.

[149] G. Betta and A. Pietrosanto, "Instrument fault detection and isolation: state of the art and new research trends", *IEEE Transactions on Instrumentation and Measurement*, vol. 49, no. 1, pp. 100-107, Feb. 2000.

[150] Y. Jeong, S. Sul, S. E. Schulz and N. R. Patel, "Fault detection and fault-tolerant control of interior permanent-magnet motor drive system for electric vehicle", *IEEE Transactions on Industry Applications*, vol. 41, no. 1, pp. 46-51, Jan./Feb. 2005.

[151] T. A. Najafabadi, F. R. Salmasi and P. J. Maralani, "Detection and isolation of speed-, dc-link voltage-, and current-sensor faults based on an adaptive observer in induction-motor drives", *IEEE Transactions on Industrial Electronics*, vol. 58, no. 5, pp. 1662-1672, May 2011.

[152] G. H. B. Foo, X. Zhang and B. M. Vilathgamuwa, "A novel speed, DC-link voltage and current sensor fault detection and isolation in IPM synchronous motor drives using an extended

Kalman filter", *IEEE Transactions on Industrial Electronics*, vol. 60, no. 8, pp. 3485-3495, Aug. 2013.

[153] A. Akrad, M. Hilairet and D. Diallo, "Design of a fault-tolerant controller based on observers for a PMSM drive", *IEEE Transactions on Industrial Electronics*, vol. 58, no. 4, pp. 1416-1427, April 2011.

[154] B. Tabbache, M. Benbouzid, A. Kheloui and J. M. Bourgeot, "Virtual-sensor-based maximum likelihood voting approach for fault-tolerant control of electric vehicle powertrains", *IEEE Transactions on Vehicular Technology*, vol. 62, no. 3, pp. 1075-1083, March 2013.

[155] Z. Wang and L. Chang, "A DC voltage monitoring and control method for three-phase grid-connected wind turbine inverters", *IEEE Transactions on Power Electronics*, vol. 23, no. 3, pp. 1118-1125, May 2008.

[156] J. Q. Zhang and Y. Yan, "A wavelet-based approach to abrupt fault detection and diagnosis of sensors", *IEEE Transactions on Instrumentation and Measurement*, vol. 50, no. 5, pp. 1389-1396, Oct. 2001.

[157] H. Berriri, M. W. Naouar, I. S.-Belkhodja and E. Monmasson, "Field programmable gate array-based fault-tolerant hysteresis current control for AC machine drives", *IET Electric Power Applications,* vol. 6, no. 3, pp. 181-189, Mar. 2012.

[158] H. Berriri, M. W. Naouar and I. S.-Belkhodja, "Easy and fast sensor fault detection and isolation algorithm for electrical drives", *IEEE Transactions on Power Electronics*,vol. 27, no. 2, pp. 490-499, Feb. 2012.

[159] dSPACE FAQ 23, *Measuring Execution Times of Block and Subsystems*, 4 pp., dSPACE GmbH, Paderborne, Germany, 2011.

[160] R. L. A. Ribeiro, C. B. Jacobina, E. R. C. Silva and A. M. N. Lima, "Fault-tolerant voltage-fed PWM inverter AC motor drive systems", *IEEE Transactions on Industrial Electronics*, vol. 51, no. 2, pp. 439- 446, April 2004.

[161] R. R. Errabelli and P. Mutschler, "Fault-tolerant voltage source inverter for permanent magnet drives", *IEEE Transactions on Power Electronics*, vol. 27, no. 2, pp. 500-508, Feb. 2012.

[162] M. Shahbazi, P. Poure, S. Saadate and M.R. Zolghadri, "FPGA-based fast detection with reduced sensor count for a fault-tolerant three-phase converter", *IEEE Transactions on Industrial Informatics*, vol. 9, no. 3, pp.1343-1350, Aug. 2013.

[163] S. Bolognani, M. Zordan and M. Zigliotto, "Experimental fault-tolerant control of a PMSM drive", *IEEE Transactions on Industrial Electronics*, vol. 47, no. 5, pp. 1134-1141, Oct. 2000.

[164] O. Wallmark, L. Harnefors and O. Carlson, "Control algorithms for a fault-tolerant PMSM drive", *IEEE Transactions on Industrial Electronics*, vol. 54, no. 4, pp. 1973-1980, Aug. 2007.

[165] N. Bianchi, S. Bolognani, M. Zigliotto and M. Zordan, "Innovative remedial strategies for inverter faults in IPM synchronous motor drives", *IEEE Transactions on Energy Conversion*, vol. 18, no. 2, pp. 306- 314, June 2003.

[166] V. D. Broeck, W. Heinz, V. Wyk and D. Jacobus, "A comparative investigation of a three-phase induction machine drive with a component minimized voltage-fed inverter under different control options", *IEEE Transactions on Industry Applications*, vol. IA-20, no. 2, pp. 309-320, March 1984.

[167] G. T. Kim and T. A. Lipo, "VSI-PWM rectifier/inverter system with a reduced switch count", *IEEE Transactions on Industry Applications*, vol. 32, no .6, pp. 1331-1337, Nov./Dec. 1996.

[168] M. B. R. Correa, C. B. Jacobina, E. R. C. Silva and A. M. N. Lima, "A general PWM strategy for four-switch three-phase inverters", *IEEE Transactions on Power Electronics*, vol. 21, no. 6, pp. 1618-1627, Nov. 2006.

[169] A. M. S. Mendes and A. J. M. Cardoso, "Fault-tolerant operating strategies applied to three-phase induction-motor drives", *IEEE Transactions on Industrial Electronics*, vol. 53, no. 6, pp. 1807-1817, December 2006.

[170] B. A. Welchko, T. A. Lipo, T. M. Jahns and S. E. Schulz, "Fault tolerant three-phase AC motor drive topologies: a comparison of features, cost, and limitations", *IEEE Transactions on Power Electronics*, vol. 19, no. 4, pp. 1108-1116, July 2004.

[171] B. R. Correa, C. B. Jacobina, E. R. C. Silva and A. M. N. Lima, "An induction motor drive system with improved fault tolerance", *IEEE Transactions on Industry Applications*, vol. 37, no. 3, pp. 873-879, May/Jun 2001.

[172] F. Blaabjerg, S. Freysson, H. H. Hansen and S. Hansen, "A new optimized space-vector modulation strategy for a component-minimized voltage source inverter", *IEEE Transactions on Power Electronics*, vol. 12, no. 4, pp. 704-714, Jul. 1997.

[173] Q. T. An, L. Sun, K. Zhao and T. M. Jahns, "Scalar PWM algorithms for four-switch three-phase inverters", *Electronics Letters* , vol. 46, no. 13, pp. 900-902, June 2010.

[174] J. Kim, J. Hong, and K. Nam, "A current distortion compensation scheme for four-switch inverters", *IEEE Transactions on Power Electronics*, vol. 24, no. 4, pp. 1032-1040, Apr. 2009.

[175] R. Wang, J. Zhao and Y. Liu, "Comprehensive investigation of four-switch three-phase voltage source inverter based on double fourier integral analysis", *IEEE Transactions on Power Electronics*, vol. 26, no. 10, pp. 2774-2787, Oct. 2011.

[176] F. Blaabjerg, D. O. Neacsu and J. K. Pedersen, "Adaptative SVM to compensate DC-link voltage ripple for four-switch three-phase voltage-source inverter", *IEEE Transactions on Power Electronics*, vol. 14, no. 4, pp. 1032-1040, Jul. 1999.

[177] G. A. Covic and G. L. Peters, "DC link imbalance compensation in four-switch inverter AC motor drives", *Electronics Letters*, vol. 33, no. 13, pp. 1101-1102, Jun. 1997.

[178] S. Dasgupta, S.N. Mohan, S.K. Sahoo and S.K. Panda, "Application of four-switch-based three-phase grid-connected inverter to connect renewable energy source to a generalized unbalanced microgrid system", *IEEE Transactions on Industrial Electronics*, vol. 60, no. 3, pp. 1204-1215, March 2013.

[179] M. Azab and A. L. Orille, "Novel flux and torque control of induction motor drive using four switch three phase inverter", *IEEE Annual Conference of the IEEE Industrial Electronics Society*, vol. 2, pp. 1268–1273, 2001.

[180] K. D. Hoang, Z. Q. Zhu and M. P. Foster, "Influence and compensation of inverter voltage drop in direct torque-controlled four-switch three-phase PM brushless AC drives", *IEEE Transactions on Power Electronics*, vol. 26, no. 8, pp. 2343-2357, Jul. 1997.

[181] S. B. Ozturk, W. C. Alexander and H. A. Toliyat, "Direct torque control of four-switch brushless DC motor with non-sinusoidal back EMF", *IEEE Transactions on Power Electronics*, vol. 25, no. 2, pp. 263-271, February 2010.

[182] B. El Badsi, B. Bouzidi and A. Masmoudi, "DTC scheme for a four-switch inverter-fed induction motor emulating the six-switch inverter operation", *IEEE Transactions on Power Electronics*, vol. 28, no. 7, pp. 3528-3538, July 2013.

[183] N. M. A. Freire and A. J. M. Cardoso, "A fault-tolerant direct controlled PMSG drive for wind energy conversion systems", *IEEE Transactions on Industrial Electronics*, vol. 61, no. 2, pp. 821-834, Feb. 2014.

[184] C. B. Jacobina, R. A. Ribeiro, A. M. N. Lima and E. R. C. da Silva, "Fault-tolerant reversible AC motor drive system", *IEEE Transactions on Industry Applications*, vol. 39, no. 4, pp. 1077-1084, Jul./Aug. 2003.

[185] C. B. Jacobina, I. S. de Freitas, E. R. C. Silva, A. M. N. Lima and R. L. A. Ribeiro, "Reduced switch count DC-link AC–AC five-leg converter", *IEEE Transactions on Power Electronics*, vol. 21, no. 5, pp. 1301-1310, Sep. 2006.

[186] A. Bouscayrol, B. Francois, P. Delarue and J. Niiranen, "Control implementation of a five-leg AC–AC converter to supply a three-phase induction machine", *IEEE Transactions on Power Electronics*, vol. 20, no. 1, pp. 107-115, Jan. 2005.

[187] M. Shahbazi, P. Poure, S. Saadate and M.R. Zolghadri, "FPGA-based reconfigurable control for fault-tolerant back-to-back converter without redundancy", *IEEE Transactions on Industrial Electronics*, vol. 60, no. 8, pp. 3360-3371, Aug. 2013.

[188] N. M. A. Freire and A. J. M. Cardoso, "A fault-tolerant PMSG drive for wind turbine applications with minimal increase of the hardware requirements", *IEEE Applied Power Electronics Conference and Exposition* (APEC), pp. 2836-2843, March 2013.

[189] N. M. A. Freire and A. J. M. Cardoso, "A fault-tolerant PMSG drive for wind turbine applications with minimal increase of the hardware requirements", *IEEE Transactions on Industry Applications*, (Early Access) 2013.

[190] P. Lezana and G. Ortiz, "Extended operation of cascade multicell converters under fault condition," *IEEE Trans. Ind. Electron.*, vol. 56, no. 7, pp. 2697–2703, Jul. 2009.

[191] S. Ceballos, J. Pou, E. Robles, J. Zaragoza and J.L. Martín, "Performance evaluation of fault-tolerant neutral-point-clamped converters", *IEEE Transactions on Industrial Electronics*, vol. 57, no. 8, pp. 2709-2718, Aug. 2010.

[192] S. Ceballos, J. Pou, J. Zaragoza, J. L. Martin, E. Robles, I. Gabiola and P. Ibanez, "Efficient modulation technique for a four-leg fault-tolerant neutral-point-clamped inverter", *IEEE Transactions on Industrial Electronics*, vol. 55, no. 3, pp. 1067-1074, March 2008.

[193] E. Silva, W. Lima, A. Oliveira, C. Jacobina, and H. Razik, "Detection and compensation of switch faults in a three level inverter", *37th IEEE Power Electron. Spec. Conf.* 2006.

[194] C. Turpin, P. Baudesson, F. Richardeau, F. Forest and T. Meynard, "Fault management of multicell converters", *IEEE Transactions on Industrial Electronics*, vol. 49, pp. 988–997, Oct. 2002.

[195] P. Hammond, "Enhancing the reliability of modular medium-voltage drives", *IEEE Transactions on Industrial Electronics*, vol. 49, pp. 948–954, Oct. 2002.

[196] F. Richardeau, P. Baudesson and T. A. Meynard, "Failures-tolerance and remedial strategies of a PWM multicell inverter", *IEEE Transactions on Power Electronics*, vol. 17, pp. 905–912, Nov. 2002.

[197] C. Turpin, F. Forest, F. Richardeau, T. Meynard and A. Lacarnoy, "Switching faults and safe control of a ARCP multicell flying capacitor inverter", *IEEE Transactions on Industrial Electronics*, vol. 18, pp. 1158–1167, Sep. 2003.

[198] M. Malinowski, K. Gopakumar, J. Rodriguez and M.A. Pérez, "A survey on cascaded multilevel inverters" , *IEEE Transactions on Industrial Electronics*, vol. 57, no. 7, pp. 2197-2206, July 2010.

[199] M. A. Parker, N. Chong and L. Ran, "Fault-tolerant control for a modular generator–converter scheme for direct-drive wind turbines", *IEEE Transactions on Industrial Electronics*, vol. 58, no. 1, pp. 305-315, Jan. 2011.

[200] M. A. Parker, L. Ran and S. J. Finney, "Distributed control of a fault tolerant modular multilevel inverter for direct-drive wind turbine grid interfacing", *IEEE Transactions on Industrial Electronics* , vol. 60, no. 2, pp. 509-522, Feb. 2013

[201] J. Birk and B. Andresen, "Parallel-connected converters for optimizing efficiency, reliability and grid harmonics in a wind turbine", *European Conference on Power Electronics and Applications*, 7 pp., Sept. 2007.

[202] C. H. Treviso and V. J. Farias, J. B. Vieira and L. C. Freitas, "A three phase PWM boost rectifier with high power factor operation and an acceptable current THD using only three switches", *European Conference on Power Electronics and Applications*, Sept. 1997.

[203] J. Kikuchi, M. D. Manjrekar and T. A. Lipo, "Performance improvement of half controlled three phase PWM boost rectifier", *IEEE Power Electronics Specialists Conference*, pp. 319-324, Aug. 1999.

[204] D. S. Oliveira, M. M. Reis, C. Silva, L. C. Barreto, F. Antunes and B. L. Soares, "A three-phase high-frequency semicontrolled rectifier for PM WECS", I*EEE Transactions on Power Electronics*, vol. 25, no. 3, pp. 677-685, Mar. 2010.

[205] D. Krahenbuhl, C. Zwyssig and J. W. Kolar, "Half-controlled boost rectifier for low-power high-speed permanent-magnet generators", *IEEE Transactions on Industrial Electronics*, vol. 58, no. 11, pp. 5066-5075, Nov. 2011.

[206] W. Yang, P. Debiprasad , T. A. Lipo and P. Di , "Pulsewidth-Modulated Dual-Half-Controlled Converter", *IEEE Transactions on Power Electronics*, vol. 28, no. 2, pp. 959-969, Feb. 2013.

[207] N. Freire and A. J. M. Cardoso, "Fault-tolerant converter for AC drives using vector-based hysteresis current control", *IEEE International Symp. on Diagnostics for Electrical Machines, Power Electronics and Drives*, 8 pp., Sept. 2013.

[208] D. Linzen, S. Buller, E. Karden and R. W. De Doncker, "Analysis and evaluation of charge-balancing circuits on performance, reliability, and lifetime of supercapacitor systems", *IEEE Transactions on Industry Applications*, vol. 41, no. 5, pp. 1135-1141, Sept./Oct. 2005.

[209] J. W. Kolar and F. C. Zach, "A novel three-phase utility interface minimizing line current harmonics of high-power telecommunications rectifier modules", *IEEE Transactions on Industrial Electronics*, vol. 44, no. 4, pp. 456-467, Aug. 1997.

[210] L. Dalessandro, S. D. Round and J. W. Kolar, " Center-point voltage balancing of hysteresis current controlled three-level PWM rectifiers", *IEEE Transactions on Power Electronics*, vol. 23, no. 5, pp. 2477-2488, Sep. 2008.

[211] J. W. Kolar and S. D. Round, "Analytical calculation of the RMS current stress on the DC-link capacitor of voltage-PWM converter systems", *IEE Proceedings - Electric Power Applications*, vol. 153, no. 4, pp. 535-543, July 2006.

Appendix A

Experimental Setup Details

This appendix presents the details of the equipment used to build the experimental prototype. Some pictures of the main components are shown, together with their specifications.

A.1 Experimental Setup Pictures

A.1.1 Autotransformer and Transformer

An autotransformer was used to supply the drive with adjustable voltage (Figure A.1). This way experiments at reduced grid voltage can be performed.

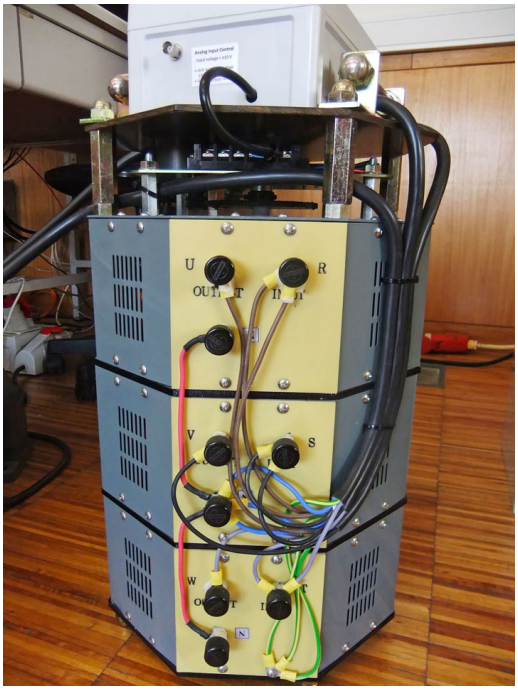

Figure A.1: Autotransformer used to supply the PMSG drive.

A 2 kVA three-phase core-type transformer (Figure A.2) was used for grid connection of the PMSG drive in order to take advantage of the access to the transformer neutral point for fault tolerance purposes.

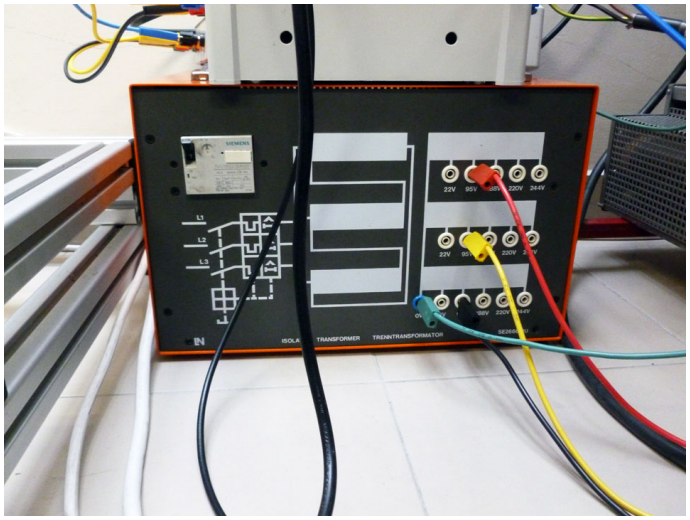

Figure A.2: Transformer for grid connection of the PMSG drive.

A.1.2 Power Converter

The power converter in Figure A.3 comprises two Semikron SKiiP 132GD120-3DUL power modules, two Epcos 400 V 2200 μF capacitors in series with the midpoint accessible, two 2.5 mH inductances in series (Figure A.4), and current and voltage measurement modules (Figure A.5). Some protection components such as fuses and circuit breakers were also included. An additional module was used in order to control a TRIAC and an electromechanical relay (Figure A.6).

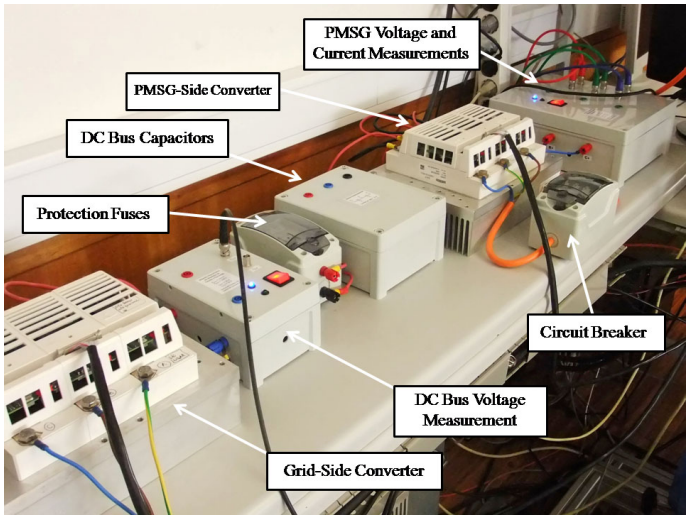

Figure A.3: General view of the power converter.

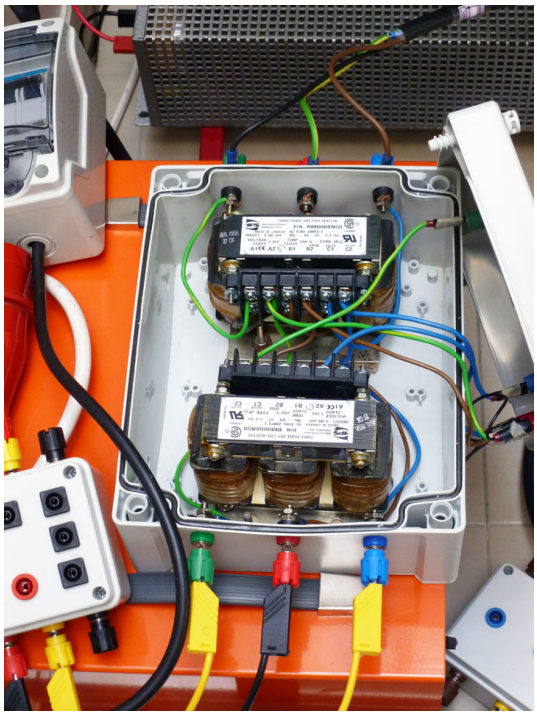

Figure A.4: Detail of the chocke inductance at the output of the grid-side converter.

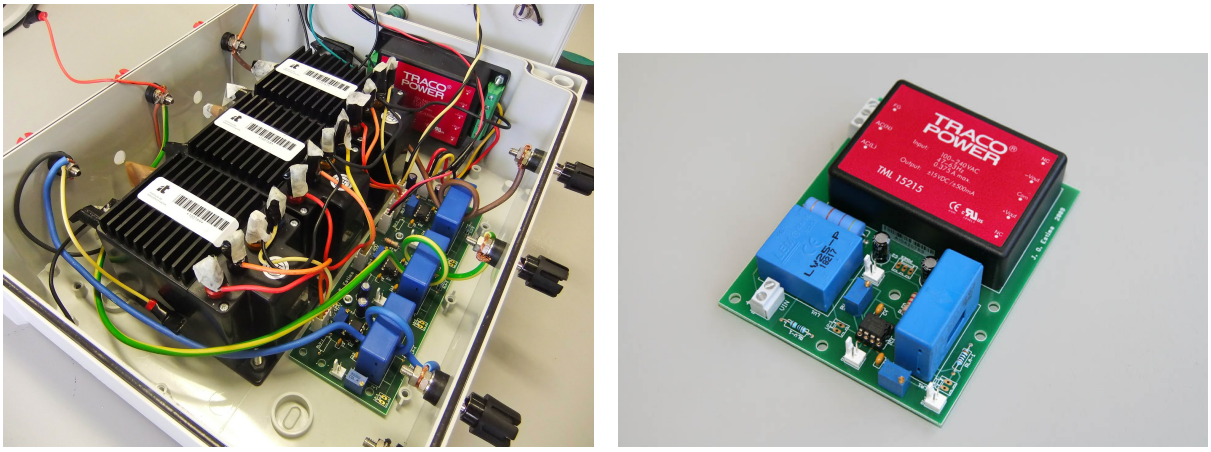

(a) (b)

Figure A.5: Measurement modules: (a) three-phase voltage and current measurement module (LEM sensors: LA-55P and CV3-1000); (b) single-phase voltage and current measurement module (LEM sensors: LA-55P and LV-25P).

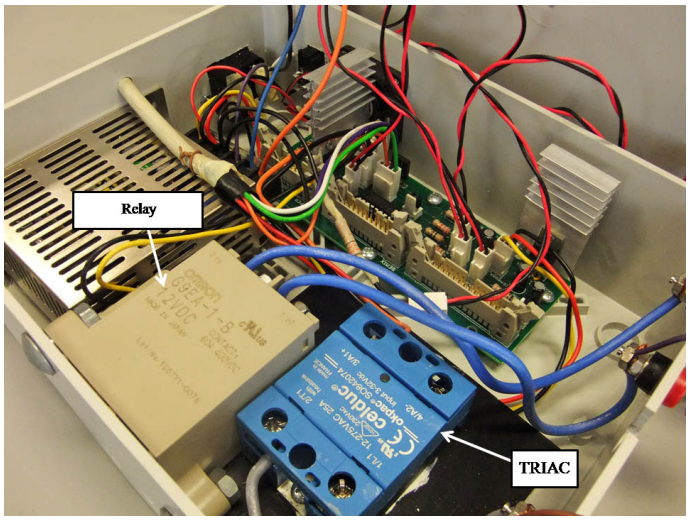

Figure A.6: TRIAC and relay module.

A.1.3 Test Bench

Figure A.7 shows the PMSG coupled to a servomotor that is used as load and operates in torque control mode. The PMSG mechanical speed/position is measured using an incremental encoder from Hengstler, model RI 76TD, with 1024 pulses per revolution.

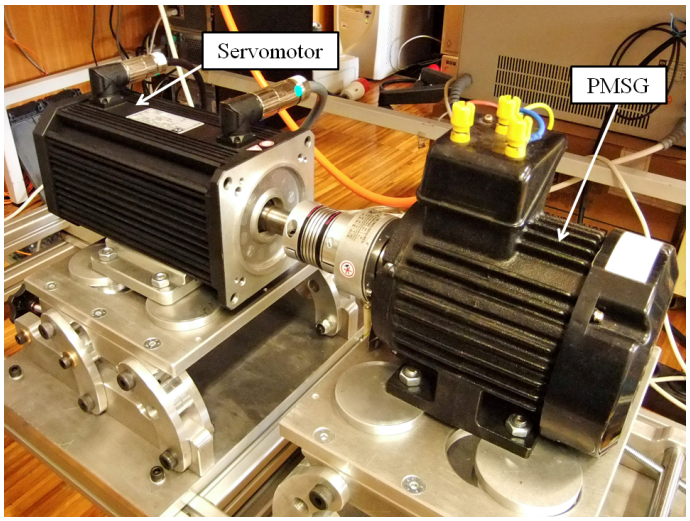

Figure A.7: Detail of the laboratory test bench.

A.1.4 PMSG Parameters

The parameters of the two used Yaskawa PMSGs are shown in Tables A.1 and A.2.

Table A.1: PMSG I parameters.

Power	P	2.2 kW
Speed	N	1750 rpm
Torque	T_n	12 Nm
Voltage	V	146 V
Current	I	10.4 A
Number of pole pairs	p	5
Armature resistance	R_s	0.415 Ω
Magnet flux linkage	ψ_{PM}	0.121 Wb
Synchronous inductance	L_s	5.13 mH

Table A.2: PMSG II parameters.

Power	P	2.2 kW
Speed	N	1750 rpm
Torque	T_n	12 Nm
Voltage	V	316 V
Current	I	5.3 A
Number of pole pairs	p	5
Armature resistance	R_s	1.72 Ω
Magnet flux linkage	ψ_{PM}	0.244 Wb
Synchronous inductance	L_s	20.5 mH